UNIVERSITÀ DEGLI STUDI DI MILANO

PhD Thesis

Chemical Bonding in Metal-Organic Systems: Nature, Structures and Properties

Tutor: Prof. Pierluigi Mercandelli

PhD Candidate: Stefano Racioppi

Dedicated to Emma

Contents

Chapter 1

Introduction

1.1 Theory of Chemical Bonding

The comprehension of interactions between atoms in molecules and rationalization of the concept of chemical bond within the framework of quantum mechanics is one of the main topics of modern quantum chemistry.[1] Indeed, the application of quantum mechanics to chemistry, produced a revolution in the concept of chemical bond.

Nevertheless, the chemical bond is traditionally described using concepts developed from experimental observations and practical intuitions, though not linked directly quantum mechanics.

For example, atomic charges, electronegativity, aromaticity, bond order, charge transfer etc. refers to properties that are not directly connected with an observable, therefore both their prediction and experimental validation remains ambiguous. In fact, one of the greatest challenges in theoretical chemistry is connecting quantum mechanics with those intuitive chemical concepts.

This challenge includes a comprehensive characterization of the nature and strength of chemical bonds. Some applications of quantum chemical approaches will be illustrated in the following paragraphs.

The carbon-carbon bond, corner stone of the organic chemistry, is the prototype of the covalent, homopolar, bond. This interaction is based on the electron-sharing (ES) between two atoms having the same electronegativity, and the electronic charge is necessarily equally distributed. Elements with different electronegativity, instead, produce a displacement of the charge, resulting in a heteropolar bond. Interactions based on the charge transfer from an atom to another are typical in the inorganic and organometallic chemistry. The donor-acceptor (DA) interaction (or dative bond), is indeed the result of the donation of an electron pair from a Lewis base, called “Donor”, to a Lewis acid, the “Acceptor”. A typical example of this kind of interaction is that responsible for the adducts between NH_3 and BH_3. These simple and intuitive schemes, based on the electronegativity and charge transfer can be reconsidered under a quantum mechanics point of view.[2,3]

A covalent bond can be seen as the interaction between two open-shell fragments. In this case, each fragment contributes with one electron to the formation of the covalent interaction. C-C bond in ethane for example, will be the result of the electron sharing of two $CH_3^{\uparrow}$. In this interaction, the electron sharing comes from the mixing of two singly occupied valence orbitals, each localized on one fragment (Figure 1.1).

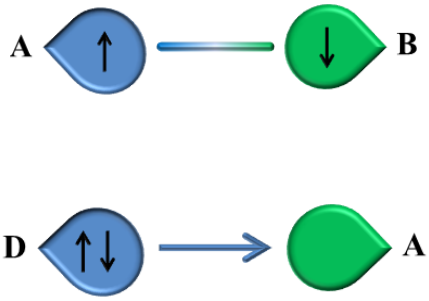

Figure 1.1. Electron-sharing (ES) and donor-acceptor (DA) interactions.

In DA interactions, on the other hand, bond arises from the overlap of frontier orbitals of the two groups of atoms, namely the doubly occupied valence orbital of the donor and the empty valence orbital of the acceptor (Figure 1.1). However, many factors can be involved in the formation and strengthening of this interaction.[4,5] Donor-Acceptor interactions are usually much longer and weaker than pure covalent bond, where the electron-sharing from fragments is involved.

Nevertheless, no correlation was found between bond length and bond strength in DA interactions.[3] To better understand the differences between each kind of interactions, it is common practice to consider the bond's cleavage. In the donor-acceptor like, chemical bond is broken heterolitically, where the electron pair is associated only to one fragment, whereas in the covalent interaction, the breaking is homolitical.

Another special case of this kind of interactions is coordination to transition metals (TM) by organic ligands in organometallic compounds. Metal-carbonyl complexes have been widely adopted as reference systems for the analysis of metal-ligand bonding.[6,7] Many studies in the past years discussed the nature of this interaction, both through experiments and theoretical calculations. The Dewar-Chatt-Duncanson (DCD) model[8] (Figure 1.2) is probably the most used to explain the nature of the interaction between a transition metal and ligands like carbonyl molecules, olefins, etc. DCD model implies a combination of two phenomena: the σ-donation from the highest occupied molecular orbital (HOMO) of the ligand to an empty orbital of the transition metal and the π-back-

donation from filled d-orbitals of metal atom to a vacant orbital of the ligand, which usually is an anti-bonding orbital.

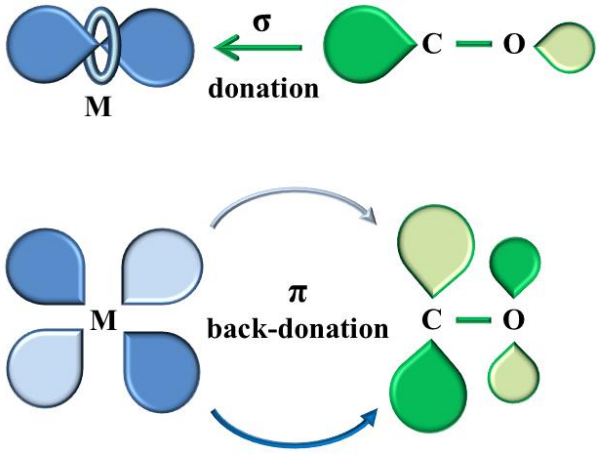

Figure 1.2. DCD model, applied to M-CO interaction.

This qualitative model provides a satisfactory explanation for the bond formation mechanism in metal-carbonyl complexes. Moreover, the effect of back-donation could be directly correlated to the variation of the CO stretching frequency. However, a quantitatively and straightforward distinction between σ-donation and π-back-donation contributions to the M-CO bond is still a matter of discussion.[9]

Obviously, once the chemical bond between two atoms is formed, it is not easy to recognize the individual contribution of A and B and retrieve the "genealogy" of the bond. The question may be tackled by analyzing changes occurring when two atoms/fragments form a new molecule, which implies recognizing these entities inside the newly formed object.

Quantum chemistry and theoretical methods based on quantum mechanics are becoming more and more sophisticated in the calculation and prediction of molecular properties, shortening the gap between pure theory and experimental observations. Geometries and vibrational spectra, nowadays can be computed with high accuracy, reproducing experimental observation and predicting unknown systems. Furthermore, computational methods have been used also to give insight in the electronic structures of molecules and periodic systems. During last decades, a plethora of methodology aiming to reveal the nature behind molecular interactions have been proposed. The great number of these methods reflect in some way the unclearness and complexity of the problem

that they were proposed to solve. Nevertheless, a solid connection with macroscopic observations and general intuitive concepts is as well a very important point to deal with. A number of methods exists, that focus either on the partition of the electronic energy or of the electronic charges in specific region of the space (mostly atomic domains), or on the direct analysis of the molecular wavefunction or electron density distribution without any explicit partition. Some of the most relevant methods are: the energy decomposition analysis (EDA) by Morokuma and Kitaura[10], the extended transition state (ETS) by Ziegler and Rauk[7], the natural bond orbital method (NBO) by Weinhold[11], its consequent combination with EDA, the natural energy decomposition analysis (NEDA) by Glendening and Streitwieser[12], the charge decomposition analysis (CDA) by Dapprich and Frenking[13], the constrained space orbital variation (CSOV) by Bagus[14], the symmetry adapted perturbation theory (SAPT)[15], the quantum theory of atoms in molecules (QTAIM) by Bader[16], the energy decomposition based QTAIM partition, the interacting quantum atoms (IQA) by Pendás *et al.*[17], and many others.

When so many methods for the analysis the chemical bond are present, because of sharing the common purpose and often the same terminology, but differing in the theoretical derivation, contradictions and discrepancies emerge. Indeed, a major issue is brought by using different definitions to refer to general and common terms. One clear example is the definition of ionic or covalent character of a bond, which differs significantly from one method to the others.[17,18,19]

In next paragraphs we will introduce the models and the methodologies used to analyze chemical bonds and interactions in our systems. Those have been divided in two main groups, concerning 1) the analysis of the electron density and 2) the analysis of the energy. Even if IQA would belong to both groups, its information are of energetic character, so it was put in the second group. Then, the applications of those methodologies to study chemical systems will be showed and analyzed during next chapters.

1.2 Electron and Charge Density Analysis

The terms Electron Density and Charge Density are frequently interchanged, with the latter usually (but improperly) used to address the former when obtained *via* X-ray diffraction experiments. However, for the sake of clarity, it is important to point out that the two terms are not synonima.[20] In fact, in a molecular system made of n electrons, the one-electron probability function $\rho(\mathbf{r})$ is defined as

$$\rho(\mathbf{r}) = n \int \Psi^*[\mathbf{r}(1), \mathbf{r}(2) \dots \mathbf{r}(n)]\Psi[\mathbf{r}(1), \mathbf{r}(2) \dots \mathbf{r}(n)]d\mathbf{r}(2) \dots d\mathbf{r}(n) \quad (1.1)$$

Ψ is the electronic wave-function and $\rho(\mathbf{r})d\mathbf{r}$ is the probability of finding one electron in the element of volume d**r**. Whereas, the charge density is the sum of both electron and nuclear densities in position space.

1.2.1 Quantum Theory of Atoms in Molecules (QTAIM)

The Quantum Theory of Atoms in Molecules (QTAIM), developed by Bader[16], has been extensively adopted both by theoreticians and experimentalists because based on a quantum mechanical observable $\rho(\mathbf{r})$ (1.1). Indeed, $\rho(\mathbf{r})$ can be obtained *via* quantum chemical calculations as well as from x-ray diffraction experiments[21,22]. Based on the partition of the electron density, this method defines an atom as an entity constituted by a nucleus and its electronic distribution, enclosed in a volume called basin Ω. The atomic basin is the region of space where the electron density is connected to the nucleus through gradient vectors. Each nucleus is necessarily an attractor in each basin. The electron density is indeed a scalar quantity, but its gradient, $\nabla\rho$, is a vector. The boundary condition of the atomic basin is defined by the *zero-flux* surface $S(\mathbf{r},\Omega)$

$$\nabla\rho(\mathbf{r}) \cdot \mathbf{n}(\mathbf{r}) = 0 \quad (1.2)$$

Where $\mathbf{n}(\mathbf{r})$ is the normal to the surface. Basins do not overlap with each other and atomic regions are well defined. To each basin, is associated one and only one atom, and the position of the nucleus correspond to a maximum of the electron density in the real space (Figure 1.3).

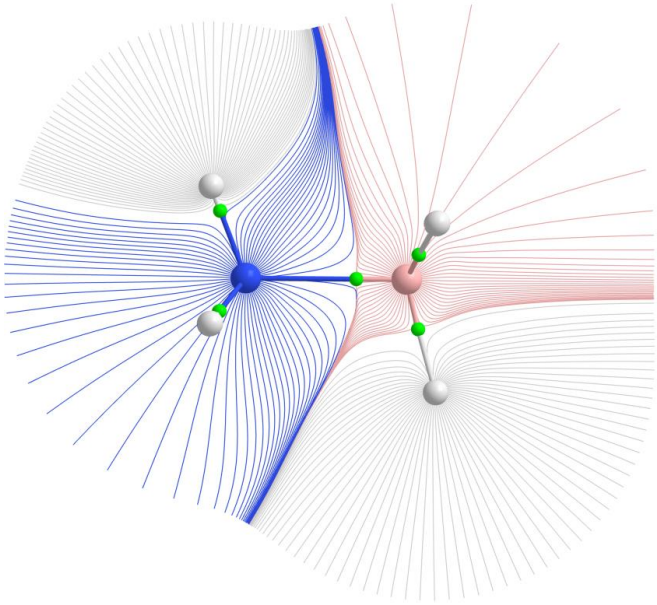

Figure 1.3. Gradient paths, basins and bond critical points (green spheres) of the adduct NH_3-BH_3.

QTAIM analyze the electron density using topological objects and descriptors, in particular the critical points. A critical point occurs when the gradient of a function is zero.

$$\nabla\rho(\mathbf{r}) = \mathbf{i}\frac{\partial\rho(\mathbf{r})}{\partial x} + \mathbf{j}\frac{\partial\rho(\mathbf{r})}{\partial y} + \mathbf{k}\frac{\partial\rho(\mathbf{r})}{\partial z} = 0 \qquad (1.3)$$

In the QTAIM, the function under examination is the electron density of a chemical system. It is possible to assign a rank *w* and signature σ to each critical point, based on the Hessian matrix computed at that point. The Hessian is a 3×3 matrix containing all the second derivatives of ρ with respect to the position defined in the Cartesian coordinates x, y and z.

The rank is the number of nonzero eigenvalues (λ_i, i=1,2,3) of the Hessian matrix, meanwhile di signature is the sum of the sign of each eigenvalue (Figure 1.4). So critical points are characterized by the curvature of the electron density at that point. A critical point (3,-3), which means rank = 3, and signature = -3, is a local maximum, corresponding to nuclear positions.

However, peculiar examples exist of non-nuclear attractors (NNAs),[23,24] corresponding to point of electron density concentration, often located in metallic systems between two (or more) atoms. The (3,-1) is a saddle point corresponding to an accumulation of electron density in two dimension, and a depletion in the third one. It is called *bond critical point*s (bcp) because found along the line of connection between two atoms (*bond path*), although they do not necessarily address the

occurrence of a two-center chemical bond[25]. The network of all the bond paths is called *molecular graph*. In Figure 1.3 it is represented the molecular graph of the adduct NH_3-BH_3.

Finally, (3,+1) is a *ring critical point* (rcp) and (3,+3) are local minima (*cage critical points*, ccp), occurring within cages.

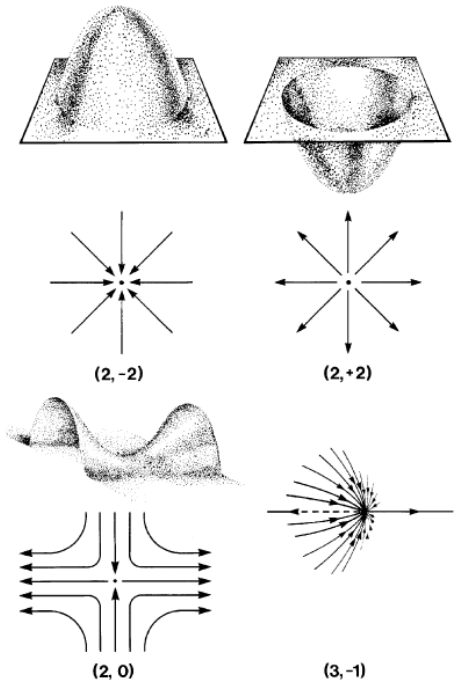

Figure 1.4. Picture from reference[16].

The numbers of critical points in a molecular system are related by the Poincaré-Hopf equation, whereas if a periodic system is considered, the relation is defined by the Morse equation.

$$N(\text{nuclei}) - N(\text{bonds}) + N(\text{rings}) - N(\text{cages}) = n \qquad \begin{cases} n = 1 \text{ in molecular system} \\ n = 0 \text{ in periodic system} \end{cases} \qquad (1.4)$$

Based on Bader's partition, many topological descriptors were developed in order to extract useful and meaningful chemical information.[6,26,27] In particular, many of these descriptors are used to analyze bond critical points. The value of the electron density at the bond critical point $\rho_b(\mathbf{r})$ is the first indicator of the strength of the corresponding interaction. The higher the value of $\rho_b(\mathbf{r})$, the stronger is supposed to be the bond. This may be true for covalent interactions (only if a homogeneous series of bonds is compared), being the electron sharing more relevant, but $\rho_b(\mathbf{r})$ is not directly proportional to the bond order. Moreover, the correlation between electron density at

the bcp and dissociation energy is not always univocal, as it will be discussed in the rest of the thesis.

The bond ellipticity is another descriptor, defined as

$$\varepsilon = \left(\frac{\lambda_1}{\lambda_2} - 1\right) \tag{1.5}$$

and it represents the deviation of the electron density distribution at the bond critical point from the cylindrical symmetry, generating a relation with the character of a chemical bond, like σ or π.[16]

Indeed, it has a value of zero for bonds having cylindrical symmetry, like C-C bond in ethane. In the case of ethylene, ε increases to 0.3, result of the concomitance of both σ and π bond. Another relevant topological descriptor is the delocalization index δ(A,B)[28], which measures the number of electron pairs shared between two atoms. Electron sharing is a fundamental aspect of covalent bond, and so, δ(A,B) gives information also on the covalent character of a two-atoms interaction. One of the greatest advantage of this descriptor is that it does not require a bond critical point between atoms. In fact, electron sharing (hence interactions) can be present even in absence of a bcp.[29,30] Indeed, δ(A,B) is extremely useful for elusive interactions, such as metal-metal bond[31]. So far, descriptors focused mainly on the analysis of the electron density have been proposed. However, many important information concerning chemical bond are still hidden in $\rho(\mathbf{r})$. The analysis of the curvature of the electron density, also called Laplacian, $\nabla^2\rho(\mathbf{r})$ defined as

$$\nabla^2\rho(\mathbf{r}) = \frac{\partial^2\rho(\mathbf{r})}{\partial x^2} + \frac{\partial^2\rho(\mathbf{r})}{\partial y^2} + \frac{\partial^2\rho(\mathbf{r})}{\partial z^2} = -L(\mathbf{r}) \tag{1.6}$$

can reveal these hidden aspects. The Laplacian of a scalar function shows regions of local concentration or depletion. Applied to the electron density, it provides a useful representation of the electronic distribution around an atom, defining regions of charge concentrations ($\nabla^2\rho(\mathbf{r}) < 0 \equiv L(\mathbf{r}) > 0$) and charge depletion ($\nabla^2\rho(\mathbf{r}) > 0 \equiv L(\mathbf{r}) < 0$).[27] It is useful also to use the function $L(\mathbf{r})$, defined in (1.6), because it is positive in regions of local concentrations, and negative in depletions.

The Laplacian is amenable to a topological analysis as the electron density and critical points in the space of $\nabla^2\rho(\mathbf{r})$ are of particular interest in the analysis of atomic coordination. Regions of space coinciding with outer (valence) shell are of particular interest. Minima of $\nabla^2\rho(\mathbf{r})$ are called valence shell charge concentrations (VSCCs) while maxima of $\nabla^2\rho(\mathbf{r})$ are called valence shell charge depletions (VSCDs). The formers can be associated with the localization of electron-pairs,

providing a physical connection with the VSEPR theory.[32,33] If a charge concentration point lies on a bond path, it is called bonding charge concentration (bonding CC). It corresponds to the electron-pair shared by two atoms. If not, it is a nonbonding charge concentration (nonbonding CC), associable with s lone pair. In Figure 1.5 the four VSCC points of the oxygen atom in the molecule of H_2O are reported, corresponding with two bonding and two nonbonding electron pairs.

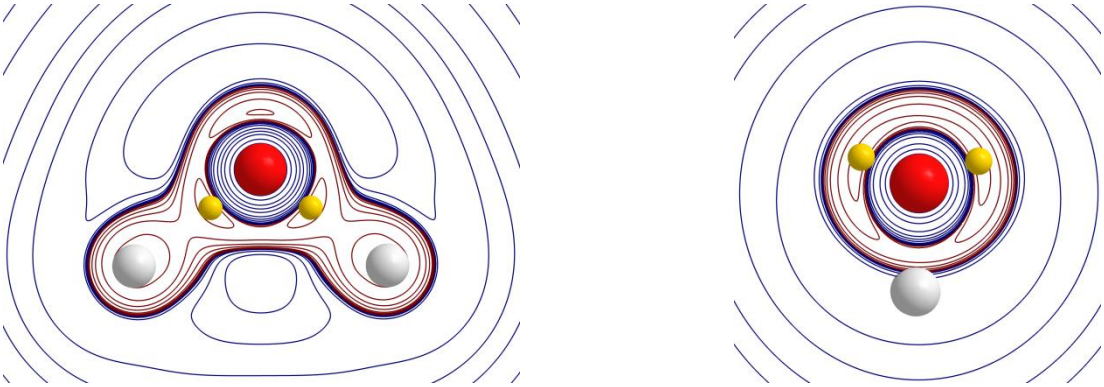

Figure 1.5. Red concentration, blue depletion, yellow points VSCC (left bonding, right nonbonding).

Moreover, thanks to the local expression of the virial theoreom

$$\left(\frac{\hbar^2}{4m}\right)\nabla^2\rho(\mathbf{r}) = 2G(\boldsymbol{r}) + V(\boldsymbol{r}) \tag{1.7}$$

which relates the Laplacian of the electron density to the kinetic energy density $G(\boldsymbol{r})$ and the potential energy density $V(\boldsymbol{r})$, a direct relationship between the electron density and the energy exists. The first term is always positive, whereas the potential energy is always negative.

The total energy density $H(\boldsymbol{r})$, defined as

$$H(\boldsymbol{r}) = V(\boldsymbol{r}) + G(\boldsymbol{r}) \tag{1.8}$$

tells if an interaction is dominated by potential energy, like in covalent interactions, or by kinetic energy, as in more ionic interactions.[34] In this way, the total energy measured at the bond critical points, $H_b(\boldsymbol{r})$, gives information about the bond's character.

Further, the energy density at the bcp's has been widely adopted to characterize chemical bonds and elusive interactions like metallophilicity.[35–37] The ratio between the

module of potential energy density at the bond critical point $|V_b|$ and the kinetic energy density at the bcp G_b can be particularly informative. If $|V_b|/G_b > 2$, the interaction is typically covalent, whereas for a ratio smaller than 1 the nature of the interaction is mainly closed-shell type. For $1 < |V_b|/G_b < 2$, the character is classified as intermediate.[35,37]

QTAIM offers a unique and exact partition of the space and atomic properties (*e.g.* atomic charges, but also atomic energies) can be calculated from the integration over atomic basins. Having defined atoms in a molecule, it is possible to determine any atomic property. This bring to the concept that molecular properties are the sum of the individual atomic properties. For example, the charge Q of a topological atom can be defined as the difference of its electronic population N with the nucleus charge Z. The electron population is obtained by the integration of all the volume elements dτ over all the atomic basin Ω.

$$N(\Omega)= \int_{\Omega} q d\tau \qquad (1.9)$$

Others atomic properties can be defined in the same way, like atomic dipole moments, quadrupole moments, etc. One of the greatest advantages of topological analysis proposed by Bader is indeed that it is applied on a physical observable, and so, it can be carried out also on the electron density obtained from single crystal x-ray diffraction experiment, as shown in the next section.

1.2.2 Electron density from X-ray diffraction

As anticipated, theoretical computation is not the only way to obtain the electron density of a chemical system. This information can be extracted from the scattered intensities of a single crystal x-ray diffraction experiment. The measured intensities are proportional to the square of the modulus of the structure factors F(**H**). Then, a Fourier transform (FT) relation exists between structure factors and thermal averaged electron density of the unit cell

$$F(\mathbf{H}) = \int_{V_{unit\ cell}} \langle \rho(\boldsymbol{r}) \rangle^{2\pi i \mathbf{H}\boldsymbol{r}} d\boldsymbol{r} \qquad (1.10)$$

H is the scattering vector defined in the reciprocal space and the integration is computed over all the volume of the unit cell. However, it is not possible to completely derive the thermal averaged electron density from the structure factors, because of several practical problems.[21]

Nevertheless, measured structure factors can be used to refine the parameters of a model of the electron density through a least-square method. In this way, one obtains an "experimental electron density". In order to refine a model from X-ray scattering intensities, the electron density is considered as the sum of atomic electron densities:

$$\rho_{unit\ cell}(\mathbf{r}) = \sum_i \rho_i(\mathbf{r} - \mathbf{r}_i) \tag{1.11}$$

$\mathbf{r}_i$ is the position of the atomic nucleus *i*. The independent atom model (IAM) is typically adopted to obtain crystal structures. In IAM, only atomic coordinates and displacement parameters are refined against the experimental structure factors, without considering the electronic redistribution due to interactions. This refinement does not return any information about chemical bonds, apart from interatomic distances. To overcome this problem, the experimental charge density can be modeled using aspherical terms. In the Hansen & Coppens formalism,[38] each atomic electron density is further expanded as follow:

$$\rho_i(\mathbf{r}) = P_{i,core}\rho_{i,core}(r) + P_{i,val}\kappa_i^3\rho_{i,val}(\kappa_i\mathbf{r}) + \sum_{l=0,l_{max}}\sum_{m=0,l} P_{i,lm\pm}y_{lm\pm}(\mathbf{r}/r)\kappa'^3_{i,lm\pm}R_{i,lm\pm}(\kappa'_{i,lm\pm}\mathbf{r}) \tag{1.12}$$

P_i are population parameters, κ are contraction/expansion parameters, $\rho(\mathbf{r})$ are spherically averaged Hartree-Fock or Dirac-Fock density functions of the free atom for core and valence. The first two terms describe the core and valence electron density as spherical functions, that can be expanded or contracted by the κ parameter. The last term in the equation represents the so called *deformation density*, which is the main contribution to the deviation from the classic independent atom model. It is a summation of deformation functions described by a radial term $R(\mathbf{r})$, typically a normalized single Slater-type density function, multiplied by density-normalized spherical harmonics $y(\mathbf{r}/r)$ up to a given order (in our models $l_{max} = 4$). The radial function of the last term has to describe the bond region, therefore they are more diffuse.

$$R_l(r) = \kappa'^3\frac{\zeta^{n_l+3}}{(n_l+2)!}(\kappa' r)^{n(l)}e^{(-\kappa'\zeta_l r)} \tag{1.13}$$

Note that κ' and κ parameters, used respectively to scale the spherical and aspherical densities are numerically different. κ-formalism is a consequence of using Slater-type radial functions[39],

provides notable flexibility to the radial density. When $\kappa > 1$, the valence shell results contracted, therefore the same charge density is found at smaller value of r. Consequently, values of $\kappa < 1$ produces an expansion. κ_i^3 satisfies the normalization requirement[38]. The contraction/expansion parameters act exclusively on the valence shell, because the core is considered unperturbed.

Nevertheless it is possible to give the same flexibility al to the inner charge density, however either extremely high resolution or theoretical data are required[40]. In the multipolar formalism, the atomic charge deformation density is expressed as product of radial functions and angular functions.

Spherical harmonic $y_{lm\pm}(\mathbf{r}/\mathrm{r})$ are real functions able to describe dipoles (l = 1), quadrupoles (l = 2), octupoles (l = 3) and hexadecapoles (l = 4) (Figure 1.6).

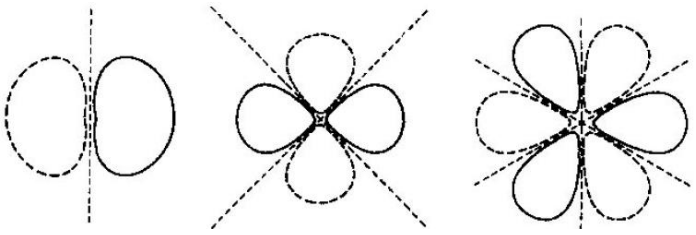

Figure 1.6. Representation of multipolar functions with l = 1,2 and 3.[38]

In general, the expansion is truncated at the hexadecapoles, but in principle it could continue for higher values of l. Spherical harmonics are necessary to model the valence electron density involved in the formation of chemical bond. Quadrupoles and hexadecapoles are essential to model d-orbitals in transition metals.[41,42] Combination of monopoles and octupoles, on the other hand, can describe hybridization in organic molecules.[43,44]

The multipolar expansion can be formulated also in reciprocal space for the atomic contribution to the unit cell structure factors |F(**H**)|. If experimentally measured x-ray diffraction intensities are available, they can be used to refine the population coefficients of the atomic charge density using a least-square minimization of the differences between observed and computed aspherical structure factors.[45] Multipolar refinement is obviously sensitive to the data quality, indeed extremely accurate intensities measured up to high resolution are needed. Information about valence electrons comes from low-angle scattering, meanwhile at high-angle only core's electrons scattering persist. Notable number of data are required to deal with the great amount of parameters generated by multipolar expansion. Low temperature is crucial to attenuate the blurring due to thermal motions and highlight deformations due to chemical bonding. From the multipolar expansion model, all atomic or molecular electrostatic moments and topological indices become easily available.[21] Information

about chemical bonding, strength and interatomic interactions are now reachable. Even the electronic configuration of d-orbital in transition metals can be known.[46]

Structure factors can be obtained thought periodic calculations. Theoretical data avoid problems induced by thermal motion. Moreover, a direct comparison of model made by experimental and computed charge densities becomes possible.

1.3 Interaction Energy

1.3.1 Interacting Quantum Atoms (IQA)

In this section, the theoretical aspects of the Interacting Quantum Atoms (IQA) developed by Blanco *et al.*[17], an energy partition based on QTAIM[16], is reported.

The first step is the partition of the first-order and second-order density matrix, generated from a N-electrons wave function Ψ, defined in the spatial and spin space by the vectors **x**:

$$\rho_1(1:1') = \mathrm{N}\int \Psi(1,\dots,\ \mathrm{N})\Psi^*(1',2,\dots,\mathrm{N})\mathrm{d}\mathbf{x}_2 \dots \mathrm{d}\mathbf{x}_\mathrm{N} \quad (1.14)$$

$$\rho_2(1:2) = \mathrm{N}(\mathrm{N}-1)\int \Psi(1,\dots,\mathrm{N})\Psi^*(1,\dots,\mathrm{N})\mathrm{d}\mathbf{x}_3 \dots \mathrm{d}\mathbf{x}_\mathrm{N} \quad (1.15)$$

From these defined density matrices, it is possible to calculate the energy of the system described by the multi-electrons wave function Ψ as expectation value Hamiltonian operator $\hat{\mathrm{H}}$.

$$\hat{\mathrm{H}} = \hat{T} + \hat{U} + V_{NN} + V_{ee} \quad (1.16)$$

Where $\hat{T}$ is the mono-electronic kinetic energy operator, $\hat{U}$ the mono-electronic nuclear attraction to a nucleus of charge Z^X. V_{NN} describes the inter-nuclear repulsion, derived applying the Born-Oppenheimer approximation, and finally V_{ee} is the inter-electronic repulsion. Considering two nuclei, A and B, the last two terms are defined as follow:

$$\mathrm{V_{NN}} = \frac{\mathrm{Z^A Z^B}}{2\mathrm{R_{AB}}} \quad (1.17)$$

$$\mathrm{V_{ee}} = \frac{1}{2\mathrm{r_{12}}} \quad (1.18)$$

Where Z^A and Z^B are the charges of the nuclei A and B respectively, R_{AB} is the inter-nuclei distance and r_{12} is the inter-electrons distance. The total energy of a multi-body system, expectation value of $\hat{H}$, is named E. At this point, the partition of the density matrices will follow, and then that it is possible, after some arrangement, to separate the one-atom and two-atoms energy contributions.[47] QTAIM provides an exhaustive real space partition of any multi-body system into so called atomic basins Ω_A, and because each basin contains one nucleus, $\Omega_A \equiv A$, and it is possible to partition the first order density matrix into atomic contributions

$$\rho_1(1:1') = \sum_A \rho_1(1:1')\,\Theta_A \tag{1.19}$$

Where $\Theta_\Omega(1)$ equal to 1 if $r_1 \in \Omega$ and 0 elsewhere, then $\sum_A \Theta_A = 1$. Mono-electronic properties are partitioned as well in this way, moreover, any mono-electronic operator, like $\hat{T}$ and $\hat{U}$, can be seen as sum of single basin-acting operators.

$$O = \sum_A \int_{\Omega_A} \hat{O}\,\rho_1(1:1')d\boldsymbol{x}_1 = \sum_A \hat{O}^A \tag{1.20}$$

Following the notation proposed by Blanco[17], the electron-nucleus attraction, previously named $\hat{U}$, from now on will be named V_{en}^{AA} if the electrons in basin A are interacting with the nucleus in basin A (intra-atomic electrostatic interaction), or V_{en}^{AB} if the electrons in basin A are interacting with the nucleus in basin B (inter-atomic electrostatic interaction). Care must be taken not to confuse V_{en}^{AB} with V_{en}^{BA}, because in the second one, electrons in basin B are interacting with the nucleus in basin A, but V_{en}^{AB} coincides with V_{ne}^{BA}. In Figure 1.7 this distinction schematically is represented.

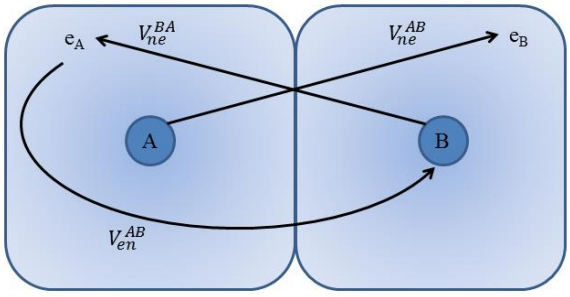

Figure 1.7. Energy term from the interaction of basins A with B.

The partition of the second-order density matrix is less intuitive then the one for $\rho_1(1:1')$, but possible as well.[48] Li and Parr demonstrated that

$$\rho_2^{AB}(1:2) = \rho_2(1:2)\Theta_A(1)\Theta_B(2) \tag{1.21}$$

allowing the partition of the two-electrons inter-basins energy. Finally, it becomes possible to write the expression

$$V_{ee} = \sum_A V_{ee}^{AA} + \frac{1}{2}\sum_A \sum_{B\neq A} V_{ee}^{AB} \tag{1.22}$$

where V_{ee}^{AA} is the intra-basin energy and V_{ee}^{AB} the inter-basin energy between basin A and B.

The Interacting Quantum Atoms partition method, produces in this way a straightforward real space partition of the total energy into one-body (AA) and two-body (AB) contributions:

$$E = \sum_A (T^A + V_{en}^{AA} + V_{ee}^{AA}) + \frac{1}{2}\sum_{A\neq B} (V_{nn}^{AB} + V_{en}^{AB} + V_{ne}^{AB} + V_{ee}^{AB})$$
$$= \sum_A E_{self}^A + \frac{1}{2}\sum_{A\neq B} E_{int}^{AB} \tag{1.23}$$

where T^A is its atomic kinetic energy; and V_{en}, V_{ne}, V_{ee}, and V_{nn} are the potential energies describing the pairwise interactions between the electrons and nuclei of basin A and B. The sum of all the intra-basin terms (A) defines the *self-energy* of a quantum atom (E_{self}^A) or a group of atoms $\mathcal{H}$ ($E_{self}^{\mathcal{H}}$), whereas the inter-basin ones correspond to the interaction energy between atom pairs, E_{int}^{AB}. A further partition of E_{int}^{AB} is possible into a classical term V_{cl}^{AB} and an exchange-correlation term V_{xc}^{AB}:

$$E_{int}^{AB} = V_{cl}^{AB} + V_{xc}^{AB} \tag{1.24a}$$

$$V_{xc}^{AB} = V_{ee}^{AB} - V_C^{AB} \tag{1.24b}$$

$$V_{cl}^{AB} = V_{nn}^{AB} + V_{en}^{AB} + V_{ne}^{AB} + V_C^{AB} \tag{1.24c}$$

where V_C^{AB} is the Coulombic part of V_{ee}. It appears from (1.24c) that V_{cl}^{AB} refers to the classic (or quasi-classic) component of the interaction energy, meanwhile V_{xc}^{AB} describes the quantum-mechanics part, the so called exchange-correlation (XC) energies. Those have no classical equivalent, and so, it is easy to extract them as the difference in (1.24b). Moreover, V_{cl}^{AB} and V_{xc}^{AB} can be associated with the classical notions of ionicity and covalency respectively.[49]

1.3.2 Energy Decomposition Analysis (EDA)

The Energy Decomposition Analysis (EDA) is based on the formalism introduced by Morokuma and Kitaura[10] and by Ziegler and Rauk[50], who realized a procedure to partition the energy of a chemical bond into well define contributions. EDA extracts bonding information from a molecule, that will be named $\mathcal{M}$, as results of the interaction between fragments $\mathcal{G}$ and $\mathcal{H}$, that are used as reference state. The wave function $\Psi_{\mathcal{M}}$, which coincide with the wave function Ψ_{GH}, having energy $E_{\mathcal{M}}$, is the result of the interaction between fragments $\mathcal{G}^0$ and $\mathcal{H}^0$, referring to their relaxed geometry at the electronic ground states Ψ_G^0 and Ψ_H^0, with energies E_G^0 and E_H^0.[19] The resulting total bond energy ΔE depends on two major components:

$$\Delta E = E_{\mathcal{M}} - (E_G^0 + E_H^0) = -D_e = \Delta E_{prep} + \Delta E_{int} \tag{1.25}$$

Where D_e is the dissociation energy. ΔE_{prep}, the preparation energy, is the energy necessary to promote fragments ($\mathcal{G}$ and $\mathcal{H}$) from their equilibrium geometry and electronic ground state to the geometry and electronic state which they display in the assembled molecule (Ψ_G and Ψ_H, with energies E_G and E_H). ΔE_{prep} is so expressed as:

$$\Delta E_{prep} = (E_G + E_H) - (E_G^0 + E_H^0) \tag{1.26}$$

The preparation energy is a destabilizing contribution, and it quantifies the effort necessary to "prepare" the fragments for their final state in $\mathcal{M}$.

ΔE_{int}, on the other hand, is the interaction energy between the two fragments forming the molecule.

$$\Delta E_{int} = E_{\mathcal{M}} - (E_G + E_H) \tag{1.27}$$

It is the stabilizing contribution to the total energy ΔE, associated with the gain of energy resulting from the interaction of the two *prepared* fragments. The EDA formalism enables a further partition of this term as a sum of energy contributions:

$$\Delta E_{int} = \Delta E_{els} + \Delta E_{Pauli} + \Delta E_{orb} \quad (1.28)$$

$$\Delta E^{\circ} = \Delta E_{els} + \Delta E_{Pauli} \quad (1.29)$$

ΔE_{els} is the electrostatic interaction energy between the prepared fragments which are calculated with a frozen electron density distribution calculated for the same geometry that they assume in the complex. The interaction of the two fragments $\mathcal{G}$ and $\mathcal{H}$, combined in the final geometry $\mathcal{M}$ from infinite distance is the quasi-classic Coulomb energy, which is usually an attractive term. ΔE_{Pauli} gives the destabilizing energy caused by exchange (often called Pauli repulsion, because ascribed to the Pauli exclusion principle, although this is not a true potential).

The exchange energy is calculated from the wave function orthogonalization and antisymmetrization:

$$\Psi^0_{\mathcal{M}} = \mathrm{N}\hat{\mathrm{A}}\{\Psi_G \Psi_H\} \quad (1.30a)$$

$$E^0_{\mathcal{M}} = \langle \Psi^0_{\mathcal{M}} | \hat{\mathrm{H}} | \Psi^0_{\mathcal{M}} \rangle \quad (1.30b)$$

$\hat{\mathrm{A}}$ is the antisymmetrizing operator and N the normalization factor. ΔE_{els} and ΔE_{Pauli} are frequently added to give the so-called *steric* energy ΔE°, but it should not be confused with the loosely defined *steric interaction* between substituents in a molecule. ΔE_{orb} gives the stabilization which arises from the orbital interactions when the wave function is fully relaxed. In this model, the orbitals of the wave function $\Psi^0_{\mathcal{M}}$ are relaxed by mixing with SCF computation the virtual orbitals to generate orbitals of the final, exact wave function $\Psi_{\mathcal{M}}$. It is always stabilizing and it can be further broken down into orbital contributions with different symmetry, which refers to the irreducible representations Γ of the point group of $\mathcal{M}$.[51]

$$\Delta E_{orb} = E_{\mathcal{M}} + E^0_{\mathcal{M}} \quad (1.31a)$$

$$\Delta E_{orb} = \sum_{\Gamma} \Delta E^{\Gamma} \quad (1.31b)$$

ΔE_{orb} can be associated with the covalent contributions to the bond whereas the electrostatic term with the ionic bonding,[8] that means that the ratio between ionic/covalent character of the bond can be obtained.[19,52] In this way, ΔE_{els} can used to estimate the strength of the electrostatic bonding, while ΔE_{orb} for the covalent bonding[53,54].

1.4 Conclusions

In this introductory chapters, the theoretical background necessary to read this thesis has been discussed. This includes important tools for the investigation of the nature of the chemical bond.

The purpose of this work is connecting these interpretative tools (grounded on mathematics and physics) with chemistry and material science, that make use of simple models to describe the features of a compound (like chemical bonding, properties, etc.) and exploit its functionalities. A typical problem is the apparently different response coming from various theoretical approaches, that however require homogeneity. For example, for partition methods like QTAIM, IQA and EDA, one of the main differences, apart from the function which is analyzed (electron density or energy), is the necessity to define a reference state or not. In EDA the formalism is necessarily based on a reference state, so the interacting fragments must always be defined. On the other hand, in QTAIM, the partition of the electron density occurs directly on the system under investigation and provides an unbiased perspective, without the need to define a fragment. However, a reference is often useful, even if no necessary. Only the introduction of e reference in QTAIM enables a proper comparison with EDA of energy contribution to the chemical bond.

Each of these methods has strengths and weaknesses. QTAIM for example, has the advantage to analyze an observable and therefore can straightforwardly compare theoretical and experimental results[6,22] revealing the modification and redistribution of the electron density both in molecular and periodic systems. This method takes advantage of topological descriptors to connect quantum-mechanical expectation values (for example, critical points of the Laplacian of the electron density $\nabla^2\rho$) and a theory, (for example, the valence shell electron pair repulsion (VSEPR).[55,33] Moreover, the relationship between the topological bond path with the chemical bond concept is not always possible. Bond order based on this partition produced as well many ambiguities and disagreement: a value of almost 1.5 for the carbon monoxide molecule, in contrast with the traditional picture of the weak triple bond.[56] On the other hand, energy partition analysis,[7,52] which so far belong solely to the theoretical methods, but that in principle could be carried out also on experimental data[57], can be combined with fragment molecular orbital analysis and separated into irreducible representation

contributions to the total bonding, according to the considered point group. Indeed it is possible to separate the energy contributions in O_h metal carbonyl complexes with respect to the irreducible representations e_g and t_{2g}, enabling the qualitative and quantitative quantification[58] of the σ-donation and π-back-donation, within the framework of the DCD model.[7] Anyhow, generation of meaningful fragments, *i.e.* reference states, is not trivial except for simple molecules. The analysis of periodic systems can be particularly tricky. Moreover, the interaction between two fragments do not always correspond to the interaction between two specific atoms. Even in simple adducts, like NH_3---BH_3, calculating the energy difference of the final molecule with the respect of two independent molecules NH_3 and BH_3 does not strictly coincide to calculate the specific interaction energy between nitrogen and boron.

1.5 Aim of the Thesis

Our major purposes were:

- to show how energy decomposition methods based on different space partition; *i.e.*, Hilbert space (EDA) and real space (IQA), can bear to the very same conclusions.
- to investigate elusive chemical bonds by combining different theoretical methodologies.
- to find structure/properties correlations induced by emerging inter-atomic interactions.
- to use accurate X-ray diffraction experiments under various conditions, *i.e.* low temperature or high pressure, to investigate complex systems.

1.6 References

(1) Schwarz, W. H. E. Chemical Bonding: State of the Art in Conceptual Quantum Chemistry An Introduction. *Theor. Chem. Accounts Theory, Comput. Model. (Theoretica Chim. Acta)* **2001**, *105* (4–5), 271–275.

(2) Haaland, A. Covalent versus Dative Bonds to Main Group Metals, a Useful Distinction. *Angew. Chemie Int. Ed. English* **1989**, *28* (8), 992–1007.

(3) Bessac, F.; Frenking, G. Chemical Bonding in Phosphane and Amine Complexes of Main Group Elements and Transition Metals. *Inorg. Chem.* **2006**, *45* (17), 6956–6964.

(4) Spackman, M. A.; Maslen, E. N. Chemical Properties from the Promolecule. *J. Phys. Chem.* **1986**, *90* (10), 2020–2027.

(5) Krapp, A.; Bickelhaupt, F. M.; Frenking, G. Orbital Overlap and Chemical Bonding. *Chem. - A Eur. J.* **2006**, *12* (36), 9196–9216.

(6) Macchi, P.; Sironi, A. Chemical Bonding in Transition Metal Carbonyl Clusters: Complementary Analysis of Theoretical and Experimental Electron Densities. *Coordination Chemistry Reviews*. 2003, pp 383–412.

(7) Frenking, G.; Fröhlich, N. The Nature of the Bonding in Transition-Metal Compounds. *Chem. Rev.* **2000**, *100* (2), 717–774.

(8) Frenking, G. Understanding the Nature of the Bonding in Transition Metal Complexes: From Dewar's Molecular Orbital Model to an Energy Partitioning Analysis of the Metal-Ligand Bond. *J. Organomet. Chem.* **2001**, *635* (1–2), 9–23.

(9) Bistoni, G.; Rampino, S.; Scafuri, N.; Ciancaleoni, G.; Zuccaccia, D.; Belpassi, L.; Tarantelli, F. How π Back-Donation Quantitatively Controls the CO Stretching Response in Classical and Non-Classical Metal Carbonyl Complexes. *Chem. Sci.* **2016**, *7* (2), 1174–1184.

(10) Kitaura, K.; Morokuma, K. A New Energy Decomposition Scheme for Molecular Interactions within the Hartree-Fock Approximation. *Int. J. Quantum Chem.* **1976**, *10* (2), 325–340.

(11) Reed, A. E.; Curtiss, L. A.; Weinhold, F. Intermolecular Interactions from a Natural Bond Orbital, Donor—Acceptor Viewpoint. *Chem. Rev.* **1988**, *88* (6), 899–926.

(12) Glendening, E. D.; Streitwieser, A. Natural Energy Decomposition Analysis: An Energy Partitioning Procedure for Molecular Interactions with Application to Weak Hydrogen Bonding, Strong Ionic, and Moderate Donor-Acceptor Interactions. *J. Chem. Phys.* **1994**, *100* (4), 2900–2909.

(13) Dapprich, S.; Frenking, G. Investigation of Donor-Acceptor Interactions: A Charge Decomposition Analysis Using Fragment Molecular Orbitals. *J. Phys. Chem.* **1995**, *99* (23), 9352–9362.

(14) Bagus, P. S.; Hermann, K.; Bauschlicher, C. W. On the Nature of the Bonding of Lone Pair Ligands to a Transition Metal. *J. Chem. Phys.* **1984**, *81* (4), 1966–1974.

(15) Jeziorski, B.; Moszynski, R.; Szalewicz, K. Perturbation Theory Approach to Intermolecular Potential Energy Surfaces of van Der Waals Complexes. *Chem. Rev.* **1994**, *94* (7), 1887–1930.

(16) Bader, R. F. W. Atoms in Molecules. *Acc. Chem. Res.* **1995**, *18* (1), 9–15.

(17) Blanco, M. A.; Pendás, A. M.; Francisco, E. Interacting Quantum Atoms: A Correlated Energy Decomposition Scheme Based on the Quantum Theory of Atoms in Molecules. *J. Chem. Theory Comput.* **2005**, *1* (6), 1096–1109.

(18) Martin Pendás, A.; Francisco, E.; Blanco, M. A. Binding Energies of First Row Diatomics in the Light of the Interacting Quantum Atoms Approach. *J. Phys. Chem. A* **2006**, *110* (47), 12864–12869.

(19) Von Hopffgarten, M.; Frenking, G. Energy Decomposition Analysis. *WIREs Comput Mol Sci* **2012**, *2*, 43–62 doi: 10.1002/wcms.71.

(20) Gatti C, Macchi P, Editors. Modern Charge Density Analysis. Dordrecht: Springer; 2012.

(21) Macchi, P. Modern Charge Density Studies: The Entanglement of Experiment and Theory. *Crystallogr. Rev.* **2013**, *19* (2), 58–101.

(22) Farrugia, L. J.; Evans, C. Experimental X-Ray Charge Density Studies on the Binary Carbonyls $Cr(CO)_6$, $Fe(CO)_5$, and $Ni(CO)_4$. *J. Phys. Chem. A* **2005**, *109* (39), 8834–8848.

(23) Gatti, C.; Fantucci, P.; Pacchioni, G. Charge Density Topological Study of Bonding in Lithium Clusters. *Theor. Chim. Acta* **1987**, *72* (5–6), 433–458.

(24) Cao, W. L.; Gatti, C.; MacDougall, P. J.; Bader, R. F. W. On the Presence of Non-Nuclear Attractors n the Charge Distributions of Li and Na Clusters. *Chem. Phys. Lett.* **1987**, *141* (5), 380–385.

(25) Foroutan-Nejad, C.; Shahbazian, S.; Marek, R. Toward a Consistent Interpretation of the QTAIM: Tortuous Link between Chemical Bonds, Interactions, and Bond/Line Paths. *Chem. - A Eur. J.* **2014**, *20* (32), 10140–10152.

(26) Gatti, C. Chemical Bonding in Crystals: New Directions. *Zeitschrift fur Krist.* **2005**, *220* (5–6), 399–457.

(27) Popelier, P. On the Full Topology of the Laplacian of the Electron Density. *Coord. Chem.*

Rev. **2000**, *197* (1), 169–189.

(28) Bader, R. F. W.; Stephens, M. E. Spatial Localization of the Electronic Pair and Number Distributions in Molecules. *J. Am. Chem. Soc.* **1975**, *97* (26), 7391–7399.

(29) Macchi, P.; Garlaschelli, L.; Sironi, A. Electron Density of Semi-Bridging Carbonyls. Metamorphosis of CO Ligands Observed via Experimental and Theoretical Investigations on $[FeCo(CO)_8]$-. *J. Am. Chem. Soc.* **2002**, *124* (47), 14173–14184.

(30) Foroutan-Nejad, C.; Badri, Z.; Marek, R. Multi-Center Covalency: Revisiting the Nature of Anion–π Interactions. *Phys. Chem. Chem. Phys.* **2015**, *17* (45), 30670–30679.

(31) Ponec, R.; Gatti, C. Do the Structural Changes Defined by the Electron Density Topology Necessarily Affect the Picture of the Bonding? *Inorg. Chem.* **2009**, *48* (23), 11024–11031.

(32) Bader, R. F. W.; Macdougall, P. J.; Lau, C. D. H. Bonded and Nonbonded Charge Concentrations and Their Relation to Molecular Geometry and Reactivity. *J. Am. Chem. Soc.* **1984**, *106* (6), 1594–1605.

(33) Gillespie, R. J. Electron Densities and the VSEPR Model of Molecular Geometry. *Can. J. Chem.* **1992**, *70*, 742–751.

(34) Cremer, V. D.; Kraka, E. Chemische Bindungen Ohne Bindungselektronendichte - Reicht Die Differenzdichteanalyse Zur Bindungsbeschreibung Aus? *Angew. Chem.* **1984**, *96* (8), 612–614.

(35) Lepetit, C.; Fau, P.; Fajerwerg, K.; Kahn, M. L.; Silvi, B. Topological Analysis of the Metal-Metal Bond: A Tutorial Review. *Coord. Chem. Rev.* **2017**, *345*, 150–181.

(36) Varadwaj, P. R.; Marques, H. M. The Physical Chemistry of Coordinated Aqua-, Ammine-, and Mixed-Ligand Co^{2+} Complexes: DFT Studies on the Structure, Energetics, and Topological Properties of the Electron Density. *Phys. Chem. Chem. Phys.* **2010**, *12* (9), 2126.

(37) Dinda, S.; Samuelson, A. G. The Nature of Bond Critical Points in Dinuclear Copper(I) Complexes. *Chem. - A Eur. J.* **2012**, *18* (10), 3032–3042.

(38) Coppens, P. *X-Ray Charge Densities and Chemical Bonding*; Oxford University Press: New York, 1997.

(39) Slater, J. C. Analytic Atomic Wave Functions. *Phys. Rev.* **1932**, *42*, 33–43.

(40) Fischer, A.; Tiana, D.; Scherer, W.; Batke, K.; Eickerling, G.; Svendsen, H.; Bindzus, N.; Iversen, B. B. Experimental and Theoretical Charge Density Studies at Subatomic Resolution. *J. Phys. Chem. A* **2011**, *115*, 13061–13071.

(41) Hansen, N. K.; Koz, J.; Fuess, H. Nucleophilic Addition Reaction in Coordinated Non-Linear Pseudohalides: Experimental Charge Density Analysis in *Trans*-Bis(

Cyanamidonitrato- N:O) Bis-(Imidazole- N^3) Copper(II) Complex. *Acta Crystallogr. Sect. B Struct. Sci. Cryst. Eng. Mater.* **2002**, *B58*, 463–470.

(42) Poulsen, R. D.; Bentien, A.; Graber, T.; Iversen, B. B. Synchrotron Charge-Density Studies in Materials Chemistry: 16 K X-Ray Charge Density of a New Magnetic Metal-Organic Framework Material, $[Mn_2(C_8H_4O_4)_2(C_3H_7NO)_2]$. *Acta Crystallogr. Sect. A Found. Crystallogr.* **2004**, *A60*, 382–389.

(43) Chen, Y. S.; Stash, A. I.; Pinkerton, A. A. Chemical Bonding and Intermolecular Interactions in Energetic Materials: 1,3,4-Trinitro-7,8-Diazapentalene. *Acta Crystallogr. Sect. B Struct. Sci.* **2007**, *63* (2), 309–318.

(44) Scheins, S.; Messerschmidt, M.; Luger, P. Submolecular Partitioning of Morphine Hydrate Based on Its Experimental Charge Density at 25 K. *Acta Crystallogr. Sect. B Struct. Sci.* **2005**, *61* (4), 443–448.

(45) Erba, A.; Ferrabone, M.; Orlando, R.; Dovesi, R. Accurate Dynamical Structure Factors from Ab Initio Lattice Dynamics : The Case of Crystalline Silicon. *J. Comput. Chem.* **2013**, *34*, 346–354.

(46) Li, N.; Su, Z.; Coppens, P.; Landrum, J. X-Ray Diffraction Study of the Electronic Ground State of (*Meso*-Tetraphenylporphinato)Iron(II). *J. Am. Chem. Soc.* **1990**, *112* (20), 7294–7298.

(47) Pendás, A. M.; Francisco, E. B. Chemical Fragments in Real Space: Definitions, Properties, and Energetic Decomposition. *J. Comput. Chem.* **2009**, *28* (1), 73–86.

(48) Li, L.; Parr, R. G. The Atom in a Molecule: A Density Matrix Approach. *J. Chem. Phys.* **1986**, *84* (3), 1704–1711.

(49) Tiana, D.; Francisco, E.; Blanco, M. A.; Macchi, P.; Sironi, A.; Martı, A. Bonding in Classical and Nonclassical Transition Metal Carbonyls: The Interacting Quantum Atoms Perspective. *J. Chem. Theory Comput.* **2009**, 1064–1074.

(50) Ziegler, T.; Rauk, A. Calculation of Bonding Energies by Hartree-Fock Slater Method .1. Transition-State Method. *Theor. Chim. Acta* **1977**, *46* (1), 1–10.

(51) Bickelhaupt, F. M.; Baerends, E. J. Kohn-Sham Density Functional Theory: Predicting and Understanding Chemistry; Wiley-VCH, John Wiley and Sons, I., Ed.; Kenny B. Lipkowitz and Donald B. Boyd: New York, 2000; Vol. 15, pp 1–86.

(52) Frenking, G.; Wichmann, K.; Fröhlich, N.; Loschen, C.; Lein, M.; Frunzke, J.; Rayón, V. M. Towards a Rigorously Defined Quantum Chemical Analysis of the Chemical Bond in Donor-Acceptor Complexes. *Coordination Chemistry Reviews*. 2003, pp 55–82.

(53) Lein, M.; Szabó, A.; Kovács, A.; Frenking, G. Energy Decomposition Analysis of the Chemical Bond in Main Group and Transition Metal Compounds. *Faraday Discuss.* **2003**, *124* (1), 365–378.

(54) Diefenbach, A.; Bickelhaupt, F. M.; Frenking, G. The Nature of the Transition Metal-Carbonyl Bond and the Question about the Valence Orbitals of Transition Metals. A Bond-Energy Decomposition Analysis of $TM(CO)_6^q$ (TM^q = Hf^{2-}, Ta^-, W, Re^+, Os^{2+}, Ir^{3+}). *J. Am. Chem. Soc.* **2000**, *122* (27), 6449–6458.

(55) Bader, R. F. W.; Gillespie, R. J.; MacDougall, P. J. A Physical Basis for the VSEPR Model of Molecular Geometry. *J. Am. Chem. Soc.* **1988**, *110* (22), 7329–7336.

(56) Cioslowski, J.; Mixon, S. T. Covalent Bond Orders in the Topological Theory of Atoms in Molecules. *J. Am. Chem. Soc.* **1991**, *113* (11), 4142–4145.

(57) Rahm, M.; Hoffmann, R. Toward an Experimental Quantum Chemistry: Exploring a New Energy Partitioning. *J. Am. Chem. Soc.* **2015**, *137* (32), 10282–10291.

(58) Mitoraj, M. P.; Michalak, A.; Ziegler, T. A Combined Charge and Energy Decomposition Scheme for Bond Analysis. *J. Chem. Theory Comput.* **2009**, *5* (4), 962–975.

Chapter 2

Comparing Energy Partition Methods

2.1 Interacting Quantum Atoms with Reference States

As suggested by Cukrowski[1], the contribution of a molecular fragment, consisting of interacting atoms, can be quantified through the so-called fragment attributed molecular system energy change (FAMSEC). Generalizing the idea of Pendás *et al.*[2] reported in Chapter 1, we define the deformation self-energy $\Delta E^{\mathcal{H}}_{def,self}$ of a given fragment $\mathcal{H}$, belonging to a molecule ($\mathcal{M}$) as the difference between the fragment self-energy in the final state $E^{\mathcal{H}}_{self}$, *i.e.* interacting with the other fragments in the molecule $\mathcal{M}$, and the self-energy in the reference state $E^{\mathcal{H}}_{self,vac}$, *i.e.* the isolated fragment, but with the very same geometry as in the molecule.

$$\Delta E^{\mathcal{H}}_{def,self} = E^{\mathcal{H}}_{self} - E^{\mathcal{H}}_{self,vac} = \sum_{A\in\mathcal{H}} E^{A}_{self} - E^{A}_{self,vac} = \sum_{A\in\mathcal{H}} \Delta E^{A}_{self} \quad (2.1)$$

The reference electronic state is not constrained to the final one. $\Delta E^{\mathcal{H}}_{def,self}$ is typically positive (destabilizing) and it accounts for the change of the self-energy of a given fragment during the interaction. Because of the variation of the intra-fragment interaction E^{AB}_{int}, of a fragment $\mathcal{H}$ composed by one or more atomic basins (A, B $\in \mathcal{H}$), from its reference state $E^{AB}_{int,vac}$, which still exhibit the geometry in the final molecule ($\mathcal{M}$), we need a definition of a deformation energy also for this term, $\Delta E^{\mathcal{H}}_{def,int}$.

$$\Delta E^{\mathcal{H}}_{def,int} = \frac{1}{2}\sum_{\substack{\mathrm{A}\neq\mathrm{B}\\ A,B\in\mathcal{H}}} E^{\mathrm{AB}}_{int} - E^{AB}_{int,vac} \quad (2.2)$$

If a fragment is generated by only one atomic basin, the $\Delta E^{\mathcal{H}}_{def,int}$ will obviously vanish. With $\Delta E^{\mathcal{H}}_{def,self}$ and $\Delta E^{\mathcal{H}}_{def,int}$ it is possible to describe the global intra-fragment energy deformation, but another term is necessary, namely the sum of inter-fragment interactions:

$$E^{frg}_{int} = \frac{1}{2}\sum_{\substack{\mathcal{H}\neq\mathcal{G}\\ \mathcal{H},\mathcal{G}\in\mathcal{M}}} E^{\mathcal{G},\mathcal{H}}_{int} = \frac{1}{2}\sum_{\substack{\mathcal{H}\neq\mathcal{G}\\ \mathcal{H},\mathcal{G}\in\mathcal{M}}} \left(\sum_{A\in\mathcal{H}}\sum_{B\in\mathcal{G}} E^{AB}_{int}\right) \tag{2.3}$$

$E^{\mathcal{G},\mathcal{H}}_{int}$ is not a deformation energy, as in equations (2.1) and (2.2); instead it is total interaction-energy between fragments $\mathcal{G}$ and $\mathcal{H}$. In general, when *n* fragments are present, E^{frg}_{int} is the sum of *n*(*n*-1)/2 inter-fragment interactions. Coupling equations (2.3) with (2.1) and (2.2), and summing over all the fragments ($\mathcal{F}$) of the molecule ($\mathcal{M}$), one obtains the global energy binding contribution ΔE^{frg}_{bind} of many interacting fragments (Scheme 2.1).

$$\Delta E^{frg}_{bind} = E^{frg}_{int} + \sum_{\mathcal{F}}\left(\Delta E^{\mathcal{F}}_{def,self}\right) + \sum_{\mathcal{F}}\left(\Delta E^{\mathcal{F}}_{def,int}\right) \tag{2.4}$$

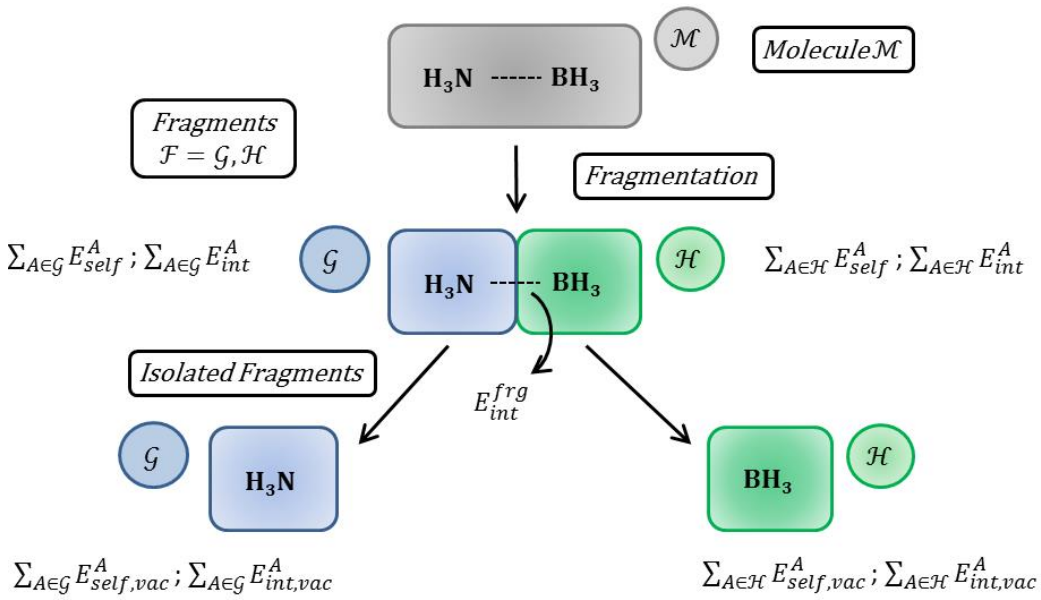

Scheme 2.1 Fragmentation of the adduct H_3N---BH_3 and corresponding energy terms.

In the simple case of only two fragments $(\mathcal{H},\mathcal{G})$:

$$\Delta E_{int}^{\mathcal{G},\mathcal{H}} = \frac{1}{2}\sum_{\substack{\mathrm{A}\neq\mathrm{B}\\ A,B\in\mathcal{M}}} E_{int}^{\mathrm{AB}} - \frac{1}{2}\sum_{\substack{\mathrm{A}\neq\mathrm{B}\\ A,B\in\mathcal{H}}} E_{int,vac}^{AB} - \frac{1}{2}\sum_{\substack{\mathrm{A}\neq\mathrm{B}\\ A,B\in\mathcal{G}}} E_{int,vac}^{AB} \tag{2.5}$$

which takes into account both the intra-fragment and inter-fragment energy contributions, generating a more compact equation for the fragments binding energy:

$$\Delta E_{bind}^{\mathcal{G},\mathcal{H}} = \Delta E_{def,self}^{\mathcal{H}} + \Delta E_{def,self}^{\mathcal{G}} + \Delta E_{int}^{\mathcal{G},\mathcal{H}} \tag{2.6}$$

According to (1.23) and using (1.24a), (1.24b) and (1.24c), it is possible to decompose the self-energy deformation $\Delta E_{def,self}^{\mathcal{H}}$ and the fragment's interaction-energy $\Delta E_{int}^{\mathcal{G},\mathcal{H}}$ into kinetic and potential energy contributions, in order to gather them together in a more chemical intuitive way:

$$\Delta E_{def,self}^{\mathcal{H}} + \Delta E_{def,self}^{\mathcal{G}} = \sum_{\mathcal{F}}\left(\sum_{A\in\mathcal{F}} \Delta T^{A} + \Delta V_{en}^{AA} + \Delta V_{ee}^{AA}\right)$$
$$= \Delta T_{def}^{\mathcal{H}} + \Delta V_{def,en}^{\mathcal{H}\mathcal{H}} + \Delta V_{def,ee}^{\mathcal{H}\mathcal{H}} + \Delta T_{def}^{\mathcal{G}} + \Delta V_{def,en}^{\mathcal{G}\mathcal{G}} + \Delta V_{def,ee}^{\mathcal{G}\mathcal{G}} \tag{2.7}$$

$$\Delta V_{def,ee}^{\mathcal{H}\mathcal{H}} = \Delta V_{def,C}^{\mathcal{H}\mathcal{H}} + \Delta V_{def,xc}^{\mathcal{H}\mathcal{H}} \tag{2.8a}$$

$$\Delta V_{def,ee}^{\mathcal{G}\mathcal{G}} = \Delta V_{def,C}^{\mathcal{G}\mathcal{G}} + \Delta V_{def,xc}^{\mathcal{G}\mathcal{G}} \tag{2.8b}$$

$$\Delta E_{int}^{\mathcal{G},\mathcal{H}} = \frac{1}{2}\sum_{\substack{\mathrm{A}\neq\mathrm{B}\\ A,B\in\mathcal{F}}} (V_{nn}^{AB} + V_{en}^{AB} + V_{ne}^{AB} + V_{ee}^{AB}) -$$
$$\sum_{\mathcal{F}}\left(\frac{1}{2}\sum_{\substack{\mathrm{A}\neq\mathrm{B}\\ A,B\in\mathcal{F}}} V_{nn,vac}^{AB} + V_{en,vac}^{AB} + V_{ne,vac}^{AB} + V_{ee,vac}^{AB}\right)$$
$$= \Delta V_{nn}^{\mathcal{G},\mathcal{H}} + \Delta V_{en}^{\mathcal{G},\mathcal{H}} + \Delta V_{ne}^{\mathcal{G},\mathcal{H}} + \Delta V_{ee}^{\mathcal{G},\mathcal{H}} \tag{2.9}$$

$$\Delta V_{ee}^{\mathcal{G},\mathcal{H}} = \Delta V_{C}^{\mathcal{G},\mathcal{H}} + \Delta V_{xc}^{\mathcal{G},\mathcal{H}} \tag{2.10}$$

With these equations it is possible to define two main potential energy terms: a classical one $\Delta V_{classic}^{\mathcal{G},\mathcal{H}}$, and a quantum-mechanical one $\Delta V_{xc}^{\mathcal{G},\mathcal{H}}$.

$$\Delta V_{classic}^{\mathcal{G},\mathcal{H}} = \Delta V_{def,en}^{\mathcal{H}\mathcal{H}} + \Delta V_{def,C}^{\mathcal{H}\mathcal{H}} + \Delta V_{def,en}^{\mathcal{G}\mathcal{G}} + \Delta V_{def,C}^{\mathcal{G}\mathcal{G}} + \Delta V_{nn}^{\mathcal{G},\mathcal{H}} + \Delta V_{en}^{\mathcal{G},\mathcal{H}} + \Delta V_{ne}^{\mathcal{G},\mathcal{H}} + \Delta V_{C}^{\mathcal{G},\mathcal{H}} \quad (2.11)$$

$$\Delta V_{xc}^{\mathcal{G},\mathcal{H}} = \Delta V_{def,xc}^{\mathcal{H}\mathcal{H}} + \Delta V_{def,xc}^{\mathcal{G}\mathcal{G}} + \Delta V_{xc}^{\mathcal{G},\mathcal{H}} \quad (2.12)$$

Equations (2.11) and (2.12), together with the kinetic energy terms, result in the fragments binding energy.

$$\Delta E_{bind}^{\mathcal{G},\mathcal{H}} = \Delta T_{def}^{\mathcal{H}} + \Delta T_{def}^{\mathcal{G}} + \Delta V_{classic}^{\mathcal{G},\mathcal{H}} + \Delta V_{xc}^{\mathcal{G},\mathcal{H}} \quad (2.13)$$

Which coincides with equations (2.4) and (2.6).

Noteworthy, this formalism, that introduces reference states in the evaluation of the interaction energy, enables to compare the IQA results with those obtained with energy decomposition analysis (EDA) (see next paragraph).

In practice, the attainment of these energy contributions is only the final step of the procedure that will be explained. A real space density matrix partition needs a density matrix, which can be computed either from Hartree-Fock (HF), post-HF (MP2, CCSD, etc.) or from Kohn-Sham Density Functional Theory (KS-DFT). For this last case, only some DFT exchange-correlation models are supported for IQA partition in AIMALL software (see below), *i.e.* LSDA, B3LYP and M06-2X.[3,4]

The first operation is to compute a single point calculation of the molecule $\mathcal{M}$. For the following examples, KS-DFT calculation with B3LYP exchange-correlation functional[5,6], carried out on Gaussian09 package[7], will be considered. It is important to underline that usually the geometry is previously fully optimized, but this is not strictly required for this kind of energy decomposition. It means that it can be carried out on geometries that are not a minimum of the potential energy surface (PES), like transition states. Once that the convergence of the self-consistent-field (SCF) cycles is reached, one can use the wave function based on Gaussian-type orbitals (GTO) to produce the Bader's partition of the charge density. For this purpose, the software AIMALL can be used. Moreover, AIMALL allows the partition of the density matrix and the obtainment of the energy contributions, *i.e.*, IQA analysis can be done simultaneously. The

drawback of Interacting Quantum Atoms partition is the time consuming and the computational cost required for the integrations when transition metals are present and if the system is quite extended.

Once that the real-space integration is correctly concluded, *i.e.* that all the electron density have been assigned to the basins, the atomic partition of the energy is straightforward.

As recently pointed out[4], many terms comes out from this procedure, in particular for the two-atoms terms. One of these term is the so-called AA' energy, which refers to the calculation over all the atoms in the system, but A. So, it coincides with the equivalence

$$\sum_B V_{int}^{AB} \equiv V_{int}^{AA'} \tag{2.14}$$

Accordingly, the total interaction energy of the molecular system becomes

$$E_{int} = \sum_A \sum_B V_{int}^{AB} \tag{2.15}$$

The calculation over A' has the advantage of being more accurate and less time consuming.Summation over B should produce the same results of working with A', but typically small differences appear, particularly errors associated with semi-analytical integration or the grid quadrature.[4] In Table 2.1 the energy terms of IQA partition from AIMALL package are reported, highlighting the mutual correspondence between terms from procedure above and those found from the software.

Table 2.1. Nomenclature of IQA energy terms computed with AIMALL.

E	Partition terms	AIMALL terms
E_{self}^{A}	V_{ne}^{AA}	$V_{ne}(A,A)$
	V_{C}^{AA}	$V_{eeC}(A,A)$
	V_{xc}^{AA}	$V_{eeXC}(A,A)$
	T^{A}	$T(A)$
	V_{nn}^{AB}	$V_{nn}(A)$
E_{int}^{AB}	$V_{neen}^{AB} = V_{en}^{AB} + V_{ne}^{AB}$	$V_{neen}^{AB}(A,A')$
	V_{C}^{AB}	$V_{eeC}(A,A')$
	V_{xc}^{AB}	$V_{eeXC}(A,A')$

The second step for the attainment of $\Delta E_{bind}^{\mathcal{G},\mathcal{H}}$ and the terms $\Delta V_{xc}^{\mathcal{G},\mathcal{H}}$ (ΔE_{XC}) and $\Delta V_{classic}^{\mathcal{G},\mathcal{H}}$ ($\Delta E_{Classic}$) is the calculation of energy contributions of the reference states for two fragments $\mathcal{G}$ and $\mathcal{H}$. This is the typical fragmentation used to study interactions occurring between two sub-systems forming a molecule, like coordination of a ligand to the metal center, donor-acceptor interaction, bond dissociation, etc.

The procedure is therefore very similar to the one described above for $\mathcal{M}$, in fact just a single point calculations on fragments $\mathcal{G}$ and $\mathcal{H}$ is needed. It is very important, anyhow, to keep the same geometry that $\mathcal{G}$ and $\mathcal{H}$ have in $\mathcal{M}$, on the other hand, no restriction is imposed to the electronic state. Once the gas-phase wave functions are obtained, IQA analysis can be done. Then, the energy differences from equations (2.1) and (2.2) can be easily computed, and so $\Delta E_{bind}^{\mathcal{G},\mathcal{H}}$ from equation (2.13), as well as its energy terms. Following this procedure, it is possible to calculate not only the fragments binding energy, which accounts for the stabilization coming from the interaction, but more important, the variation of the kinetic, classic and exchange-correlation energy terms. As already mentioned, classic and exchange-correlation terms can be associated with to the ionic and covalent character respectively.[8] In particular the ratio $\Delta V_{classic}^{\mathcal{G},\mathcal{H}}/(\Delta V_{classic}^{\mathcal{G},\mathcal{H}} + \Delta V_{xc}^{\mathcal{G},\mathcal{H}})$ intuitively assesses the major character contribution. Hereinafter, we will refer to $\Delta V_{xc}^{\mathcal{G},\mathcal{H}}$ and $\Delta V_{classic}^{\mathcal{G},\mathcal{H}}$ as ΔE_{XC} and $\Delta E_{Classic}$ respectively.

2.2 Energy Decomposition Analysis

From the Energy Decomposition Analysis (Chapter 1) it is possible to extract general energy terms which constitute the total bonding energy ΔE_{int}[9]. Those terms are of course the same of above coming from application of the Hamiltonian operator to the wave function, *i.e.*, the electrostatic energy, the kinetic energy, the coulomb energy and the exchange-correlation energy (XC).

$$\Delta E_{int} = \Delta E_{kinetic} + \Delta E_{electrostatic} + \Delta E_{Coulomb} + \Delta E_{XC} = \Delta E_{kinetic} + \Delta E_{Classic} + \Delta E_{XC} \quad (2.16)$$

Being the same kind of energy contribution of IQA, in principle one can compare them directly. For this purpose, we will gather together the electrostatic and the coulomb terms in a so called **Classic term**, as shown in equation (2.16). These general energy terms from EDA come from

all the three main steps of the bonding analysis. For example, the kinetic energy will be the sum of the kinetic energy contributions to ΔE_{els}, ΔE_{Pauli} and ΔE_{orb}, and so on for the other terms.

The practical procedure one has to follow in order to extract the energy terms of (1.28) according to EDA (Ziegler and Rauk) is implemented in the software ADF2014.[10,11] The energy decomposition analysis is automatically calculated for the atomic contributions, however, it is possible to carry out an energy decomposition defining molecular fragments $\mathcal{G}$ and $\mathcal{H}$ (or more).

The computed energy terms will refer to the interaction between fragments. It is important that reference states of $\mathcal{G}$ and $\mathcal{H}$ are the same in IQA and EDA to compare the same sub-systems interactions. Moreover, ADF uses Slater type orbitals (STOs) as basis functions for the SCF calculations.

The comparison between IQA and EDA partition methods is summarized in scheme 2.2. In the next section, examples on typical donor-acceptor interactions will be proposed and analyzed in order to validate this procedure. In this context, hereinafter we will refer to our protocol of reference states for all the IQA results.

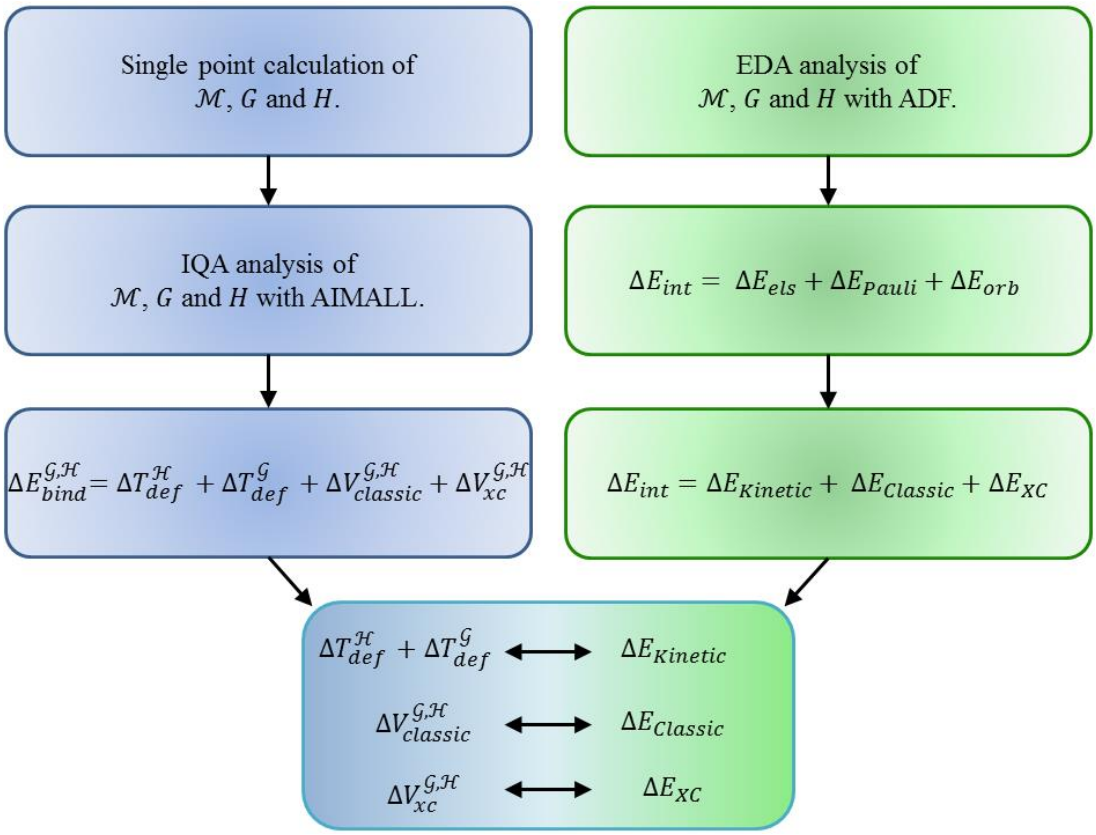

Scheme 2.2. Schematic procedure to compare reference-states-IQA with EDA.

2.3 Methods

IQA: The program package AIMALL was used for carry out the Bader's partition and the IQA energy analysis of the molecular systems. The wave functions were calculated with Gaussian09[7], using the level of theory B3LYP/6-311+G(d,p).[5,6] B3LYP is one of the few DFT models supported by AIMALL for the correct evaluation V_{xc}^{AB} in the IQA analysis[4]. The molecular geometries were optimized and the nature of the minima have been verified by calculation of the vibrational frequencies.

EDA: DFT calculations have been performed with the program package ADF2014[11], using the level of theory B3LYP/ATZ2P (augmented triple-ζ with double polarization functions Slater type orbitals (STOs) basis functions) for the SCF calculations. All the structures have been optimized and verified as minima on the potential energy surface by calculation of the vibrational frequencies.

2.4 Results and discussion

2.4.1 Donor-Acceptor interaction in H_3E---ZH_3 (E = N, P, As ;Z = B, Al)

The donor-acceptor interactions between Lewis bases (H_3E; E = N, P, As) and Lewis acids (ZH_3; Z = B, Al) will be analyzed. H_3E and ZH_3 were treated as close-shell fragments. Because all electrons are paired, the resulting interaction will involve the HOMO of the donor (H_3E) with the LUMO of the acceptor (ZH_3). The analysis of the energy terms of EDA and IQA using our protocol of comparison is reported in Figure 2.1 and Table 2.2. The same reference states were used for the two decomposition methods.

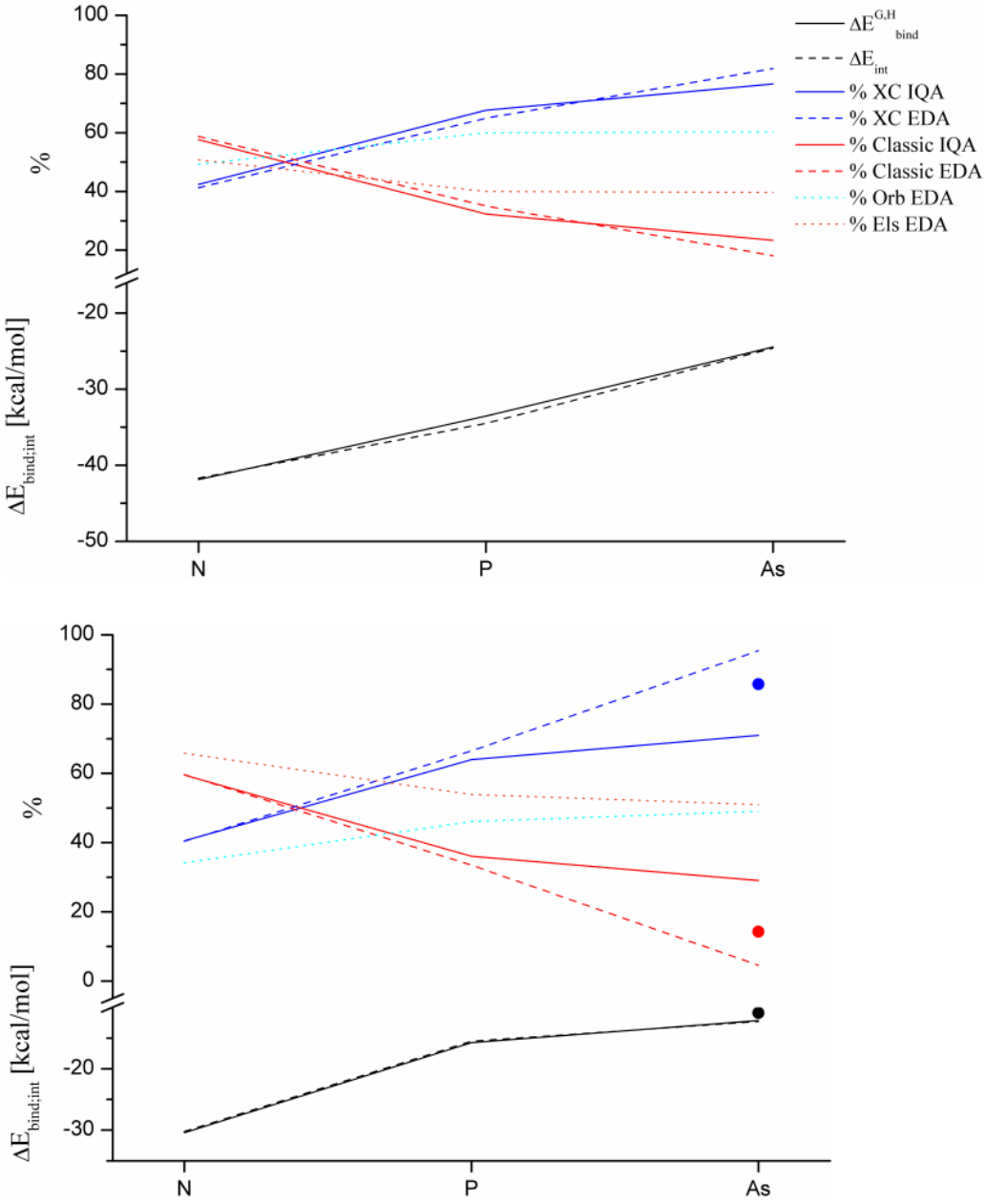

Figure 2.1. Energy terms and interaction energies in donor-acceptor complexes, upper side: Z=B, lower side: Z=Al; ●=level of theory BLYP/TZP.

Table 2.2. Energy terms form EDA and IQA for the H_3E---ZH_3 donor-acceptor interaction.

		BH_3			AlH_3		
		NH_3	PH_3	AsH_3	NH_3	PH_3	AsH_3[a]
EDA	ΔE_{pauli}	110.2	119.7	90.3	58.6	41.2	33.0 (34.5)
	ΔE_{els}	-77.1	-61.7	-45.6	-58.5	-30.6	-23.1 (-23.0)
	ΔE_{steric}	33.1	58.0	44.7	0.1	10.6	9.9 (11.6)
	ΔE_{orb}	-74.8	-92.5	-69.3	-30.4	-26.1	-22.2 (-22.4)
	$\%\Delta E_{els}$	50.8	40.0	39.7	65.8	53.9	50.9 (50.6)
	$\%\Delta E_{orb}$	49.2	60.0	60.3	34.2	46.1	49.1 (49.4)
	ΔE_{int}	-41.7	-34.5	-24.6	-30.2	-15.5	-12.3 (-10.9)
	$\Delta E_{Kinetic}$	77.6	44.6	22.0	58.9	16.9	5.5 (7.0)
	$\Delta E_{Classic}$	-70.1	-27.7	-8.5	-53.1	-10.9	-0.8 (-2.5)
	ΔE_{XC}	-49.2	-51.3	-38.1	-36.0	-21.5	-17.0 (-15.3)
	%Classic	58.8	35.1	18.2	59.6	33.5	4.4 (14.3)
	%XC	41.2	64.9	81.8	40.4	66.5	95.6 (85.7)
IQA	ΔE_{bind}	-41.9	-33.5	-24.4	-30.4	-15.8	-12.2
	$\Delta E_{Kinetic}$	70.4	37.9	24.4	49.2	15.4	11.0
	$\Delta E_{Classic}$	-64.7	-23.1	-11.4	-47.4	-11.2	-6.7
	ΔE_{XC}	-47.6	-48.4	-37.4	-32.3	-19.9	-16.4
	%Classic	57.6	32.3	23.4	59.5	36.1	29.0
	%XC	42.4	67.7	76.6	40.5	63.9	71.0

[a] Values in parenthesis refer to energy terms computed with the level of theory BLYP/TZP

Several terms are reported in Figure 2.1, in particular the total interaction (or binding) energy, as defined in equations (2.13) and (2.16), the electrostatic and orbitalic terms from EDA and the ratio $[\mathrm{XC}/(\mathrm{Classic} + \mathrm{XC})]\%$ and $[\mathrm{Classic}/(\mathrm{Classic} + \mathrm{XC})]\%$, both from IQA or EDA, that well represent the main energy variation during the formation of the interaction. Our results reveal an excellent agreement between the energy terms computed with the two partition methods. The energy differences $\Delta E_{bind}^{\mathcal{G},\mathcal{H}}$ and ΔE_{int} have the same values, as well as the ratio between Classic and XC energies. Analyzing the case with Z=B, an excellent agreement is observed, not only regarding ΔE of interaction, but also in the ratio XC/Classic. Both methods show that H_3N---BH_3, the most stabilized donor-acceptor interaction has dominant Classic character. Moreover, EDA electrostatic and orbitalic terms well reproduce previous studies carried out by Bessac and Frenking.[12] $\%\Delta E_{els}$ in our work (50.8%, with ΔE_{els}= -77.1 kcal/mol) is almost identical to the one of previous works (50.4%, with ΔE_{els}= -77.3 kcal/mol)[12,13], which is associated with the degree of ionic character for the interaction. Nevertheless, $V_{Classic}$, instead of $\Delta E_{Classic}$, has the meaning of "degree of ionicity" in IQA. The main difference in the definition of covalent or ionic bond for IQA and EDA are

indeed in the terms $V_{XC}/V_{Classic}$ and $\Delta E_{orb}/\Delta E_{els}$ respectively. The electrostatic term in EDA comes from the interaction between two frozen (non-interacting) charge density (G and H), at the geometry of the final system $\mathcal{M}$. On the other hand, Classic term in IQA arise from all the mono- and multi-electronic interactions which do not have a pure quantum mechanical nature, indeed associated with the exchange-correlation. Even if a disagreement on what is considered as ionic or covalent exists in the terminology, the energy is consistent and the very same values are reached using the two methods. However, with these results it is not possible, and we do not want, to judge terminologies for the bond character, but we want to highlight that the variations of the interaction energy are the same. Similar results are found also for H_3N---AlH_3, with even better agreement, differing for just 0.2 kcal/mol in $\Delta E_{int/bind}$, and 0.1% in %Classic (or %XC). Classic and electrostatic terms are again the main energy contributions to the interaction, nevertheless, the ratio Classic/XC almost unchanged from B to Al, whereas electrostatic/orbitalic ratio changes from 50.8%/49.2% to 65.8%/34.2%, this implies more EDA's ionic character in H_3N---AlH_3 interaction. Moving to phosphane and arsane, the energy contributions change. $\Delta E_{int/bind}$ decrease almost linearly, becoming less stabilizing, meaning that PH_3 and AsH_3 in this interaction are weaker Lewis bases than NH_3. Then XC term is the main energy contribution. Concerning H_3P---ZH_3 complexes, a good agreement with previous work is found, both for the $\%\Delta E_{els}$ and $\%\Delta E_{orb}$ trends.[12] From our analysis, Classic and XC trends of Z=B, Al are very similar, revealing the same inversion of main contributions from N to P. This inversion reveals a significant difference between NH_3 and PH_3 in the donor-acceptor interaction with borane and alane. Nevertheless, the relative increment of XC is not only due to an higher value of ΔE_{XC}, but to a drop of $\Delta E_{Classic}$ (Table 2.2).

Only in H_3P---BH_3 a slight increment of the XC energy is observed and then it decreases again for AsH_3. In the alane complexes, on the other hand, exchange-correlation energy decreases constantly, but the classic term drops even more severely. The most relevant discrepancy was found for H_3As---AlH_3. According to EDA, the XC reaches 96% of the total energy, mainly because the Classic term contribute with just 0.8 kcal/mol to the stabilization. However, this low $\Delta E_{Classic}$, is not observed in IQA, for which H_3As---AlH_3 is similar to H_3As---BH_3. Also in this case the Classic term is smaller than for the other complexes of the series, anyway it still contributes with 6.7 kcal/mol to the total interaction energy. Our first hypothesis to explain the EDA's out of trend was based on the numerical issue that ADF has with hybrid functional due to part of the exchange energy calculated as pure Hartree-Fock (HF), emphasized when a large and diffuse basis set is used[14] (see also https://www.scm.com/doc/ADF/Input/Hartree-Fock_RI.html). However, for this specific example, it is unlikely that the error is due to a bad treatment of the HF exchange energy

introduced by the B3LYP functional, because ΔE_{XC} is rather similar in EDA and IQA. Moreover, $\Delta E_{bind}^{\mathcal{G},\mathcal{H}}$ and ΔE_{int} differ only by 0.1 kcal/mol, so the total energy is well computed. The main difference is indeed in the kinetic and Classic terms. Decreasing the level of theory to a GGA functional (BLYP), but retaining the basis-set, for the calculation with ADF, the XC energy slightly decreases to -15.9 kcal/mol, whereas the kinetic term increases to 6.7 kcal/mol and the Classic energy becomes more negative by 1 kcal/mol, changing the percentage of Classic/XC to 10.4% and 89.6% respectively. Decreasing even more the level of theory to BLYP/TZP, the ratio turns to 14.3% and 85.7%. So, an issue in the treatment of heavy atoms with large basis-set appears quite clear, in particular in the evaluation of kinetic and Coulombic terms.

2.4.2 Bonding in transition metal carbonyl compounds

To further test our protocol, we analyzed the dissociation of a carbonyl molecule in a series of tetrahedral isoelectronic transition metal complexes $[M(CO)_4]^n$ (n= +1, 0, -1, -2) (Figure 2.2, Table 2.3). The metal ion in the $[M(CO)_4]^n$ and $[M(CO)_3]^n$ fragment is taken as closed–shell d^{10}, so the charge is adjusted in order to occupy all the d-orbitals. The series moves from the cationic specie $[Cu(CO)_4]^+$ to the di-anionic $[Fe(CO)_4]^{2-}$ complex, increasing of the π-back-donating character of the metal center. Tiana *et al.*[8] showed that the net Bader's charges on the metal ions in these complexes are close to zero or slightly positive, meaning that the electrons flow mainly through the carbonyl molecules. Consequently, the higher the negative charge, the more the π-back-donation to the anti-bonding orbital of the ligands. The energy terms of the interaction between one carbonyl molecule with the unsaturated fragment $[M(CO)_3]^n$ and Bader's atomic charges for the metal centers calculated for the complex $[M(CO)_4]^n$ are reported in Figure 2.2 and Table 2.3.

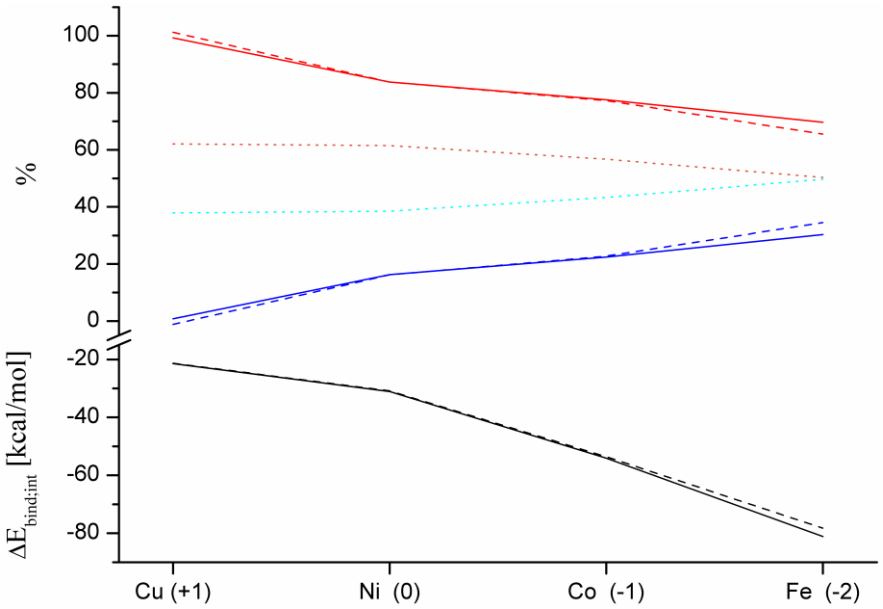

Figure 2.2. Energy terms and interaction energies in transition metal carbonyl $[M(CO)_4]^n$.

Table 2.3. Energy terms form EDA and IQA for the $M^n(CO)_4$transition metal carbonyl compounds.

		$[Cu(CO)_4]^+$	$Ni(CO)_4$	$[Co(CO)_4]^-$	$[Fe(CO)_4]^{2-}$
EDA	ΔE_{pauli}	60.2	116.1	154.4	169.9
	ΔE_{els}	-50.6	-90.4	-117.9	-124.8
	ΔE_{steric}	9.5	25.7	36.5	45.0
	ΔE_{orb}	-30.9	-56.6	-90.1	-123.3
	$\%\Delta E_{els}$	62.1	61.5	56.7	50.3
	$\%\Delta E_{orb}$	37.9	38.5	43.3	49.7
	ΔE_{int}	-21.4	-30.8	-53.6	-78.2
	$\Delta E_{Kinetic}$	8.2	64.8	136.8	227.4
	$\Delta E_{Classic}$	-29.9	-80.1	-147.0	-200.1
	ΔE_{XC}	0.3	-15.5	-43.3	-105.5
	%Classic	101.2	83.8	77.2	65.5
	%XC	-1.2	16.2	22.8	34.5
IQA	ΔE_{bind}	-21.5	-31.1	-54.1	-81.2
	$\Delta E_{Kinetic}$	7.3	69.3	138.9	214.7
	$\Delta E_{Classic}$	-28.5	-84.1	-149.7	-206.2
	ΔE_{XC}	-0.2	-16.3	-43.4	-89.7
	%Classic	99.2	83.8	77.5	69.7
	%XC	0.8	16.2	22.5	30.3
	Q(M)	0.67	0.48	0.46	0.55

$\Delta E_{bind}^{\mathcal{G},\mathcal{H}}$ and ΔE_{int} values are again the very same, with a minor difference of 3 kcal/mol only in the iron complex. The interaction becomes more and more stabilizing as the charge becomes more negative, in agreement with an increase of π-back-donation.[8,15,16] The dominant role in the $(CO)_3$M-CO bond formation comes from the Classic term, although it decreases gradually. Along the series, a drop in %Classic occurs from $[Cu(CO)_4]^+$ to $Ni(CO)_4$, due to a notable increment of exchange-correlation contribution. However, the Classic term not only remains the main contribution to the total energy, but actually becomes stronger and stronger. The stabilization given by the XC term becomes than more relevant, reaching the 30-35% of the total interaction energy in $[Fe(CO)_4]^{2-}$. Indeed, Tiana *et al.* showed that the electron correlation increases the π-back-donation effect.[8] The results from EDA and IQA are very well in agreement. The largest discrepancy is found for the iron complex, where %Classic and %XC differ for just 4% from one method to the other.

Absolute values of the energy terms in this complex are also interesting to analyze: ΔE_{XC} from EDA and IQA terms differs by 15.8 kcal/mol, whereas $\Delta E_{Classic}$ by just 6 kcal/mol. Also the kinetic energy term has a discrepancy of 12.7 kcal/mol. Very likely, this is due to numerical errors caused by the higher charge in combination with an irksome level of theory for ADF. In fact, difficulties in SCF convergence were observed for this system. Some peculiarities appear also in $[Cu(CO)_4]^+$: ΔE_{XC} (EDA) is slightly destabilizing, producing a %Classic higher than 100%, while ΔE_{XC} (IQA) has the opposite sign, so it is stabilizing. Nevertheless, the difference between these two terms is less than 0.5 kcal/mol, and both methods agree in addressing the metal-carbonyl interaction in $[Cu(CO)_4]^+$, as almost completely supported by the Classic energy term. This result well describes the representation of Cu^+ d^{10}as a closed-shell cation, which interacts electrostatically with carbon atoms. Indeed, the calculated Bader's charge of the metal ion is equal to +0.67, the most positive computed for these complexes, and very close to the ideally oxidation state +1. In the other three cases, with the increment of the negative charge, there is more intense flow of electron density towards the carbonyl molecules, on which the LUMO is mainly localize, corresponding to the DCD picture of the π-back-donation. Moreover, the charge of the metal atom is almost +0.5 for Ni, Co and Fe, which is quite far from the expected oxidation state of -1 and -2 for Co and Fe.

According to these results, the σ-donation of carbonyl molecules to the metals doesn't seem to be relevant, otherwise more negative charge should appear on the metals centers. Because the electrons move towards the ligands, the π-back-donation becomes the dominant character. Indeed, metal charges remain positive and almost constant, even in $[Fe(CO)_4]^{2-}$, the most stable tetrahedral complex. Finally, $\%\Delta E_{els}$ and $\%\Delta E_{orb}$ from pure EDA treatment, the main character of the bond would be electrostatic and that the orbitalic contribution increases with the negativity of the charge.

However, their ratio is less unbalanced than the Classic/XC one, reaching 50% each in $[Fe(CO)_4]^{2-}$. Compared with previous works by Frenking *et al.*[16] on octahedral carbonyl complexes, trends are very similar, revealing the same strengthening of the orbitalic term in the bond character with the increasing of the negative charge of the metal center.

2.4.3 Homolytic cleavage of covalent bond

So far we tested our protocol on donor-acceptor closed-shell fragments, obtaining excellent agreements between the two partition methods. In this paragraph, covalent bonds will be investigated, in particular, systems like $X_3C\text{-}CX_3$ (X=H, F, Cl) and $H_3E\text{-}EH_3$ (E=C, Si, Ge). All fragments were generated in order to break homolytically the single C-C or E-E bond. However, in this context, some additional approximations had to be introduced. In EDA, the spatial part of the wave-functions of the two interacting fragments and the final system is required to be the same. For doing so, the reference states has to be considered as Restricted Open-Shell fragments during the computation. Such constrain on the spatial part is not required in IQA, being the interaction energy calculated in two different steps. It means that the spatial part of the reference states is allowed to relax upon the effect of the unpaired spin electrons. This is done considering the fragments as Unrestricted Open-Shell. In order to address the drawbacks of comparing energy terms from Restricted and Unrestricted calculations, the molecule of ethane will be used as test (Figure 2.3 and Table 2.4).

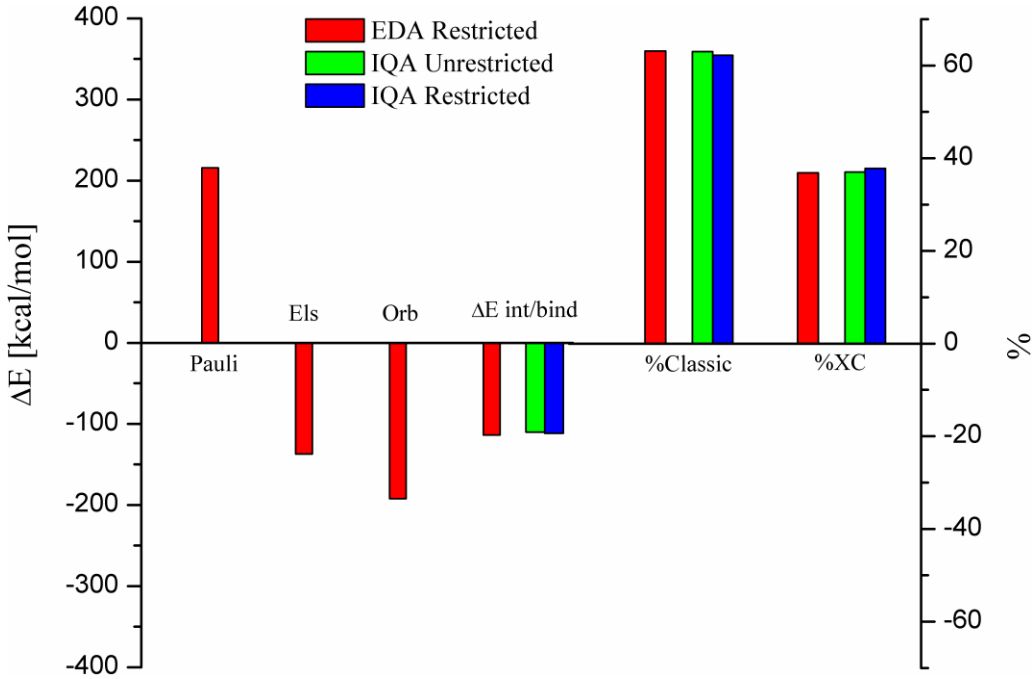

Figure 2.3. Representation of the energy term contributions from the open-shell calculation computed with EDA and IQA.

Table 2.4. Energy terms form EDA and IQA for the molecule of ethane (H_3C-CH_3).

H_3C-CH_3			
		Restricted	
EDA	ΔE_{pauli}	215.7	
	ΔE_{els}	-137.0	
	ΔE_{steric}	78.6	
	ΔE_{orb}	-192.4	
	$\%\Delta E_{els}$	41.6	
	$\%\Delta E_{orb}$	58.4	
	ΔE_{int}	-113.8	
	$\Delta E_{Kinetic}$	160.8	
	$\Delta E_{Classic}$	-173.4	
	ΔE_{XC}	-101.2	
	%Classic	63.1	
	%XC	36.9	
		Restricted	Unrestricted
IQA	ΔE_{bind}	-111.5	-110.2
	$\Delta E_{Kinetic}$	99.9	97.6
	$\Delta E_{Classic}$	-131.5	-130.9
	ΔE_{XC}	-79.9	-76.9
	%Classic	62.2	63.0
	%XC	37.8	37.0

In the IQA analysis, the comparison between a Restricted Open-shell and an Unrestricted Open-shell computation of the electronic energy produced some differences. However, being the system under examination relatively small, results are overall very similar. The main discrepancy by just 3 kcal/mol is found in ΔE_{XC} (Table 2.4). The fragments binding energy is more stabilizing when restricted fragments are considered. Obviously, starting from more destabilized fragments, a greater stabilization will be produced in the final step. $\Delta E_{Classic}$ doesn't seem to suffer the initial spin-state, the difference in IQA between restricted and unrestricted is by 0.6 kcal/mol. Whereas the difference in ΔE_{XC} is greater. Indeed, spin-state affects more the electrons correlation than the quasi-classic electron-electron and electron-nuclei interactions.

ΔE_{Int} and $\Delta E_{bind}^{\mathcal{G},\mathcal{H}}$, as well as %Classic and $\%XC$ in IQA and EDA are again extremely similar, in particular comparing unrestricted fragments (IQA) with the results from EDA. On the other hand, a notable discrepancy between terms $\Delta E_{Kinetic}$, $\Delta E_{Classic}$ and ΔE_{XC} arises. Particularly, the kinetic energy is almost 61 kcal/mol more stable in the real space partition, meanwhile Classic and XC are found to be roughly 42 kcal/mol and 21 kcal/mol more unstable (their sum almost equals the gain in kinetic energy). In EDA, the kinetic energy contribution comes mainly from the renormalization of the two frozen electron densities, corresponding to ΔE_{Pauli}. Probably, the excess observed is an effect of this step, which anyhow disappears during the final relaxation, where more stable Classic and XC terms are produced. Indeed, the ratio between $\Delta E_{Classic}$ and ΔE_{XC} is not affected. Moreover, imposing the restricted space surely affect the kinetic energy. In fact, according to IQA results, allowing the relaxation of the spatial part, the kinetic energy decreases, though just 2.3 kcal/mol. Even if the singular energy term from the two partition methods are no longer directly comparable, the total interaction/binding energy and the ratio of the main stabilizing terms still bring to the very same conclusion. This intriguing aspect needs further investigation in the future.

Considering all these observations, only the results from Unrestricted Open-shell fragments for IQA will be presented for next examples $X_3C\text{-}CX_3$ (X=H, F, Cl) and $H_3E\text{-}EH_3$ (E=C, Si, Ge), reported in Figure 2.4 and in Table 2.5. The choice of using an Unrestricted Open-shell instead of Restricted-Open shell is because the latter is not a needed constrain in IQA, contrary to EDA.

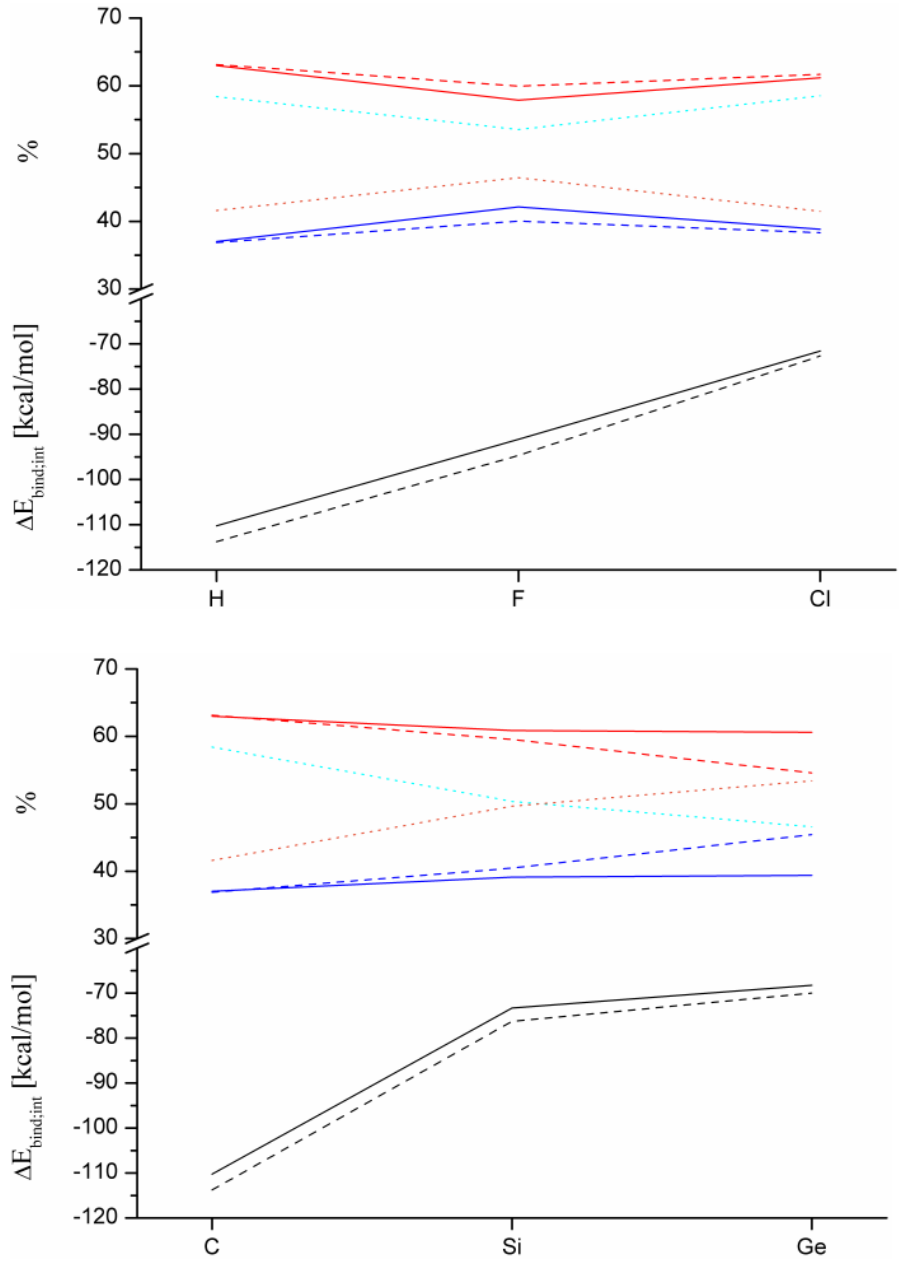

Figure 2.4 Energy terms and interaction energies in covalent bonds, upper side: $X_3C\text{-}CX_3$ (X=H, F, Cl), lower side $H_3E\text{-}EH_3$ (E=C, Si, Ge).

Table 2.5. Energy terms form EDA and IQA for the molecule $X_3C\text{-}CX_3$ (X=F, Cl) and $H_3E\text{-}EH_3$ (E=Si, Ge)

		$F_3C\text{-}CF_3$	$Cl_3C\text{-}CCl_3$	$H_3Si\text{-}SiH_3$	$H_3Ge\text{-}GeH_3$
EDA	ΔE_{pauli}	271.7	302.3	113.8	121.3
	ΔE_{els}	-170.1	-155.5	-94.4	-102.2
	ΔE_{steric}	101.6	146.8	19.4	19.1
	ΔE_{orb}	-196.2	-219.4	-95.7	-89.1
	$\%\Delta E_{els}$	46.4	41.5	49.7	53.4
	$\%\Delta E_{orb}$	53.6	58.5	50.3	46.6
	ΔE_{int}	-94.7	-72.7	-76.3	-70.0
	$\Delta E_{Kinetic}$	214.7	250.9	94.5	57.4
	$\Delta E_{Classic}$	-185.5	-199.5	-101.7	-69.5
	ΔE_{XC}	-123.9	-124.0	-69.1	-57.9
	%Classic	60.0	61.7	59.5	54.6
	%XC	40.0	38.3	40.5	45.4
IQA	ΔE_{bind}	-91.1	-71.6	-73.4	-68.3
	$\Delta E_{Kinetic}$	124.7	189.7	57.3	45.9
	$\Delta E_{Classic}$	-124.9	-159.8	-79.5	-69.2
	ΔE_{XC}	-90.9	-101.4	-51.1	-45.0
	%Classic	57.9	61.2	60.9	60.6
	%XC	42.1	38.8	39.1	39.4

As in the previous examples, the total interaction energies from the two partition methods produce very similar values, within a maximum difference of just 3.6 kcal/mol. Focusing on the alkyl halides, the discrepancy between the percentage of Classic and XC terms increases with the electronegativity of the halide. In fact, in C_2Cl_6 their difference is just of 0.5%, whereas for the fluorinate alkane this reaches the 2.1%. %XC increases as well with the electronegativity of X substituents. Stabilization of ΔE_{XC} follows the trend Cl> F> H, both for IQA and EDA, even if the latter shows no difference between Cl and F. On the other hand, $\Delta E_{Classic}$ has two different trends for the two decomposition methods: Cl> F> H for EDA and Cl> H> F for IQA. Differences in the Classic energy contribution do not affect much the final character of the C-C bonds, which remains comparable.

Indeed, it arises that the interactions in X_3C-CX_3 (X=H, F, Cl), which are universally considered as covalent bonds, have the Classic term as main contribution. This aspect was already observed by Frenking *et al.*[17], indeed even non-polar bond can have strong electrostatic character.

Canonical terms from EDA, on the other hand, suggest that the main character of the X_3C-CX_3 and H_3E-EH_3 interactions is covalency, coming from the dominant orbitalic term. Analyzing the energy contributions to the orbitalic energy ΔE_{Orb}, the only stabilizing term is the kinetic energy, and all the other terms (XC, Coulomb, etc.) are actually slightly destabilizing. The covalent character is referred to the sharing of electron in the region between the two atoms, this expansion of the electron could in the inter-atomic region produces a relevant stabilization of the kinetic energy. In conclusion, both EDA and IQA agree that the typical C-C covalent bond has actually a dominant Classic nature, in terms of ΔE computed using the reference-states formalism

Finally, we analyze the results for the group 14 E-E bond(E=C, Si, Ge). Si-Si interaction energy is much weaker than the one of ethane, but comparable to Cl_3C-CCl_3. Indeed, both XC and Classic terms are smaller, but their ratio is still the very same found for the other covalent bonds, revealing the Classic term as the main one. EDA and IQA, are in excellent agreement. However, some differences appear for E=Ge. According to IQA, the character of the interaction energy do not change compared to C and Si, however, the energy terms from EDA suggest a slight increment of the XC character. Nevertheless, the difference in %Classic and %XC between the two methods is just 5%. Differences in the kinetic energies are still present between EDA and IQA, showing higher values (in module) of all the energy terms computed in ADF. Canonical EDA terms reveal an inversion of the bond character from C to Ge, from dominant orbitalic term to dominant electrostatic term. ΔE terms from our protocol do not reveal any inversion or displacement of the bond's character, indeed, %Classic remains almost constantly the 60% of the total energy.

2.5 Conclusions

The protocol here reported proved to work well, meaning that it returns a substantially compatible interpretation of interactions from two very different partitioning schemes, especially when dealing with donor-acceptor adducts. In fact, for the first time, we have shown that energy terms calculated from real and Hilbert space partitions coincide. EDA and IQA are energy decomposition methods with solid and deep roots in quantum mechanics and are physically consistent but differ in the way fragments and individual energy contributions are defined. Indeed, energy is uniquely defined as the expectation value of the Hamiltonian but its partition depends on the way in which borders are calculated and on the reference framework. By introducing a reference state in the IQA formalism, a direct comparison with EDA was enabled, which allowed to prove that both interaction energies and their contribution terms are consistent and reproducible.

2.6 References

(1) Cukrowski, I. IQA-Embedded Fragment Attributed Molecular System Energy Change in Exploring Intramolecular Interactions. *Comput. Theor. Chem.* **2015**, *1066*, 62–75.

(2) Martín Pendás, A.; Blanco, M. A.; Francisco, E. The Nature of the Hydrogen Bond: A Synthesis from the Interacting Quantum Atoms Picture. *J. Chem. Phys.* **2006**, *125* (18), 184112.

(3) Francisco, E.; Casals-Sainz, J. L.; Rocha-Rinza, T.; Martín Pendás, A. Partitioning the DFT Exchange-Correlation Energy in Line with the Interacting Quantum Atoms Approach. *Theor. Chem. Acc.* **2016**, *135* (7), 1–8.

(4) Maxwell, P.; Pendás, Á. M.; Popelier, P. L. A. Extension of the Interacting Quantum Atoms (IQA) Approach to B3LYP Level Density Functional Theory (DFT). *Phys. Chem. Chem. Phys.* **2016**, *18* (31), 20986–21000.

(5) Becke, A. D. Density-Functional Thermochemistry.III. The Role of Exact Exchange. *J. Chem. Phys.* **1993**, *98* (7), 5648.

(6) Lee, C.; Yang, W.; Parr, R. G. Development of the Colle-Salvetti Correlation-Energy Formula into a Functional of the Electron Density. *Phys. Rev. B* **1988**, *37* (2), 785–789.

(7) Frisch, M. J.; Trucks, G. W.; Schlegel, H. B.; Scuseria, G. E.; Robb, M. A.; Cheeseman, J. R.; Scalmani, G.; Barone, V.; Mennucci, B.; Petersson, G. A.; *et al.* Gaussian09 Revision B.010. Gaussian, Inc.: Wallingford CT 2010.

(8) Tiana, D.; Francisco, E.; Blanco, M. A.; Macchi, P.; Sironi, A.; Martı, A. Bonding in Classical and Nonclassical Transition Metal Carbonyls: The Interacting Quantum Atoms Perspective. *J. Chem. Theory Comput.* **2009**, 1064–1074.

(9) Bickelhaupt, F. M.; Baerends, E. J. Kohn-Sham Density Functional Theory: Predicting and Understanding Chemistry; Wiley-VCH, John Wiley and Sons, I., Ed.; Kenny B. Lipkowitz and Donald B. Boyd: New York, 2000; Vol. 15, pp 1–86.

(10) Te Velde, G.; Bickelhaupt, F. M.; Baerends, E. J.; Fonseca Guerra, C.; van Gisbergen, S. J. A.; Snijders, J. G.; Ziegler, T. Chemistry with ADF. *J. Comput. Chem.* **2001**, *22* (9), 931–967.

(11) E.J. Baerends, T. Ziegler, J. Autschbach, D. Bashford, A. Bérces, F.M. Bickelhaupt, C. Bo, P. M.; Boerrigter, L. Cavallo, D.P. Chong, L. Deng, R.M. Dickson, D.E. Ellis, M. van Faassen, L. Fan, T. H.; Fischer, C. Fonseca Guerra, M. Franchini, A. Ghysels, A. Giammona, S.J.A. van Gisbergen, A. W. G.; J.A. Groeneveld, O.V. Gritsenko, M. Grüning, S. Gusarov,

F.E. Harris, P. van den Hoek, C.R. Jacob, H.; Jacobsen, L. Jensen, J.W. Kaminski, G. van Kessel, F. Kootstra, A. Kovalenko, M.V. Krykunov, E. van; Lenthe, D.A. McCormack, A. Michalak, M. Mitoraj, S.M. Morton, J. Neugebauer, V.P. Nicu, L.; Noodleman, V.P. Osinga, S. Patchkovskii, M. Pavanello, P.H.T. Philipsen, D. Post, C.C. Pye, W.; Ravenek, J.I. Rodríguez, P. Ros, P.R.T. Schipper, H. van Schoot, G. Schreckenbach, J. S. S.; M. Seth, J.G. Snijders, M. Solà, M. Swart, D. Swerhone, G. te Velde, P. Vernooijs, L. Versluis, L.; Visscher, O. Visser, F. Wang, T.A. Wesolowski, E.M. van Wezenbeek, G. Wiesenekker, S.K. Wolff, T. K.; *et al.* ADF2014, SCM, Theoretical Chemistry, Vrije Universiteit, Amsterdam, The Netherlands.

(12) Bessac, F.; Frenking, G. Chemical Bonding in Phosphane and Amine Complexes of Main Group Elements and Transition Metals. *Inorg. Chem.* **2006**, *45* (17), 6956–6964.

(13) Von Hopffgarten, M.; Frenking, G. Energy Decomposition Analysis. *WIREs Comput Mol Sci* **2012**, *2*, 43–62 doi: 10.1002/wcms.71.

(14) Watson, M. A.; Handy, N. C.; Cohen, A. J. Density Functional Calculations, Using Slater Basis Sets, with Exact Exchange. *J. Chem. Phys.* **2003**, *119* (13), 6475–6481.

(15) Diefenbach, A.; Bickelhaupt, F. M.; Frenking, G. The Nature of the Transition Metal-Carbonyl Bond and the Question about the Valence Orbitals of Transition Metals. A Bond-Energy Decomposition Analysis of $TM(CO)_6^q$ (TM^q = Hf^{2-}, Ta^-, W, Re^+, Os^{2+}, Ir^{3+}). *J. Am. Chem. Soc.* **2000**, *122* (27), 6449–6458.

(16) Frenking, G. Understanding the Nature of the Bonding in Transition Metal Complexes: From Dewar's Molecular Orbital Model to an Energy Partitioning Analysis of the Metal-Ligand Bond. *J. Organomet. Chem.* **2001**, *635* (1–2), 9–23.

(17) Kovács, A.; Esterhuysen, C.; Frenking, G. The Nature of the Chemical Bond Revisited: An Energy-Partitioning Analysis of Nonpolar Bonds. *Chem. - A Eur. J.* **2005**, *11* (6), 1813–1825.

Chapter 3

Chemical Bonding in Semi-Interstitial Metal Carbonyl Clusters

In this chapter, the effect of interstitial pnictogen elements on molecular structures and chemical bonding of metal carbonyl clusters will be analyzed. The ability of group V atoms to expand metal cages and generate high nuclearity clusters is well known. However, the nature of chemical bond between interstitial atom and the metallic cage, as well as its effect on the molecular properties, is not completely understood yet. Particularly, the class of metal carbonyl clusters presenting semi-interstitial atoms have been poorly investigated so far, especially from the theoretical point of view. In this context, the systems $[Co_6X(CO)_{16}]^-$ with X=P,As have been analyzed. Moreover, two different conformers differing for the length of just one Co-Co distance, have been isolated for the cluster with As, but not for P. The factors which may trigger this unprecedented case of conformational polymorphism and the nature of X-Co and Co-Co interactions have been studied through DFT computations and analyzed with decomposition methods (AIM, EDA, IQA) in combination with high resolution x-ray diffraction, refined with the Hansen&Coppens multipolar model.

Section 1

Periodic Trends in $[Co_6X(CO)_{16}]^-$ Clusters: Structural, Synthetic and Energy Changes Produced by Substitution of P with As

3.1.1 Introduction

Thanks to their tendency to catenation, the heavier elements of group V (As, Sb, Bi) are particularly useful to construct molecular architectures, in combination with transition metals. The concern about this chemistry reached its highest point in the '80-'90 years, and scientists focused essentially on structural aspects. Owing to this wide interest and this structural complexity, the field was synthetically illustrated by Greenwood[1] and was thoroughly reviewed by Whitmire.[2]

Depending on the number of substituents (and the number of orbitals available for bonding), the main group element may act simply as an *exo*-skeleton ligand, be a well-defined vertex of the cluster skeleton, or occupy an interstitial position. Accordingly, AsR_3 are typical ligands in organometallic chemistry,[3] AsR fragments mimic $M(CO)_n$ moieties as vertices of the cage,[4,5] and As atoms may be fully surrounded by metals in clusters like $[Rh_{10}As(CO)_{22}]^{3-}$.[6] Transition and main group elements may play interchangeable roles, as shown by the complete series $As_{4-n}\{Co(CO)_3\}_n$ (n = 0,[1] 1,[7] 2,[8] 3 ,[9] 4[10,11]), which nicely illustrate the isolobal principle.[12] Moreover, the construction of molecular architectures with different structural elements can be relevant for catalysis, since the formation of strong E-M bonds can confer extra stability to the molecules.[2] Accordingly, the quoted $[Rh_{10}As(CO)_{22}]^{3-}$ was self-assembled in conditions suitable for the homogeneous catalytic conversion of CO-H_2 mixtures into oxygenated compounds, and proved to be stable at partial pressures of CO as high as 260 atm.[6] More recently, this class of compounds has been used as single source for the preparation of binary and ternary phases which,[13] on turn, can find application for magnetic nanoparticles,[14] for the deposition of thin films[15] or for electrocatalysis.[16,17] In the latter field, the presence of the main group element helps in forming amorphous layers which are

more catalytically active than bulk metal. In particular cobalt phosphides emerged as materials extremely active for both the hydrogen and oxygen evolution reactions (HER and OER).[18,19,20,21]

For all these reasons, we devoted our attention to the synthesis of new Co-As clusters, trying to incorporate As atoms into small simple molecular compounds, to be exploited as precursors of larger clusters, possibly with interstitial As atoms. The first result in this field is the isolation of the anion $[Co_6As(CO)_{16}]^-$, whose formula exactly matches that of the corresponding $[Co_6P(CO)_{16}]^-$ phosphide,[22] but differs from it for several structural and chemical aspects.

3.1.2 Experimental section and computational details

All the solvents were purified and dried by conventional methods and stored under nitrogen. All the reactions were carried out under oxygen-free nitrogen atmosphere using the Schlenk-tube technique.[23] Infrared spectra in solution were recorded on a Nicolet iS10 spectrophotometer, using calcium fluoride cells previously purged with N_2. A batch of $Na[Co(CO)_4]$ was prepared by dissolving 20 g of $Co_2(CO)_8$ in anhydrous THF (50 mL), and allowing it to react with small pieces of Na, until the IR bands of the reactant disappeared (2-3 days). The pale solution was filtered, and the THF was dried in vacuum, under moderate heating, to remove all traces of solvent. ν(CO) in THF : 2010vw, 1887vs, 1857 m cm^{-1}

3.1.2.1 Synthesis of $Na[Co_6As(CO)_{16}]$

$Na[Co(CO)_4]$ (960 mg, 4.4 mmol) and $As_2O_5 \cdot xH_2O$ (480mg; 1.75 mmol) were suspended in THF (25 mL) and stirred at room temperature. A brown solution was formed, and some CO evolution was observed. After 1 day of stirring, the solution was filtered and the solvent was partially removed in vacuum. 30 mL of heptane were added dropwise and the solution furtherly concentrated, until most of the product precipitated. The suspended solid was collected by filtration, washed with 10 mL of heptane, and dried. ν(CO) in MeOH : 2075vw, 2027vs, 2014s, 1975w, 1809 m cm^{-1} (Figure 3.1.1).

3.1.2.2 Synthesis of $(PPh_4)[Co_6As(CO)_{16}]$

3.1.2.2.1

The crystals used for X-ray diffraction were obtained dissolving $Na[Co_6As(CO)_{16}]$, obtained as above, in the minimum amount of Methanol, and layering with a solution of PPh_4Cl in 2-propanol (ca. 0.5 mg/mL). After diffusion was completed, the mother liquors were eliminated by syringe.

The solid residue was washed with 2-propanol and dried.

3.1.2.2.2

To obtain larger amounts of compound, $Na[Co_6As(CO)_{16}]$ was dissolved in Methanol and treated with a concentrated solution of PPh_4Cl in 2-propanol. After complete precipitation occurred, the solid was collected by filtration, washed with 2-propanol and dried. Typical yields 45-50% (calculated on Co). Calc for $C_{40}H_{20}AsCo_6O_{16}P$ C 39.51 ; H 1.66 %; found C 39.7 ; H 1.4 %. ν(CO) in THF : 2074vw, 2027vs, 2012s, 1975w, 1954w, 1809 m cm^{-1} (Figure 3.1.1)

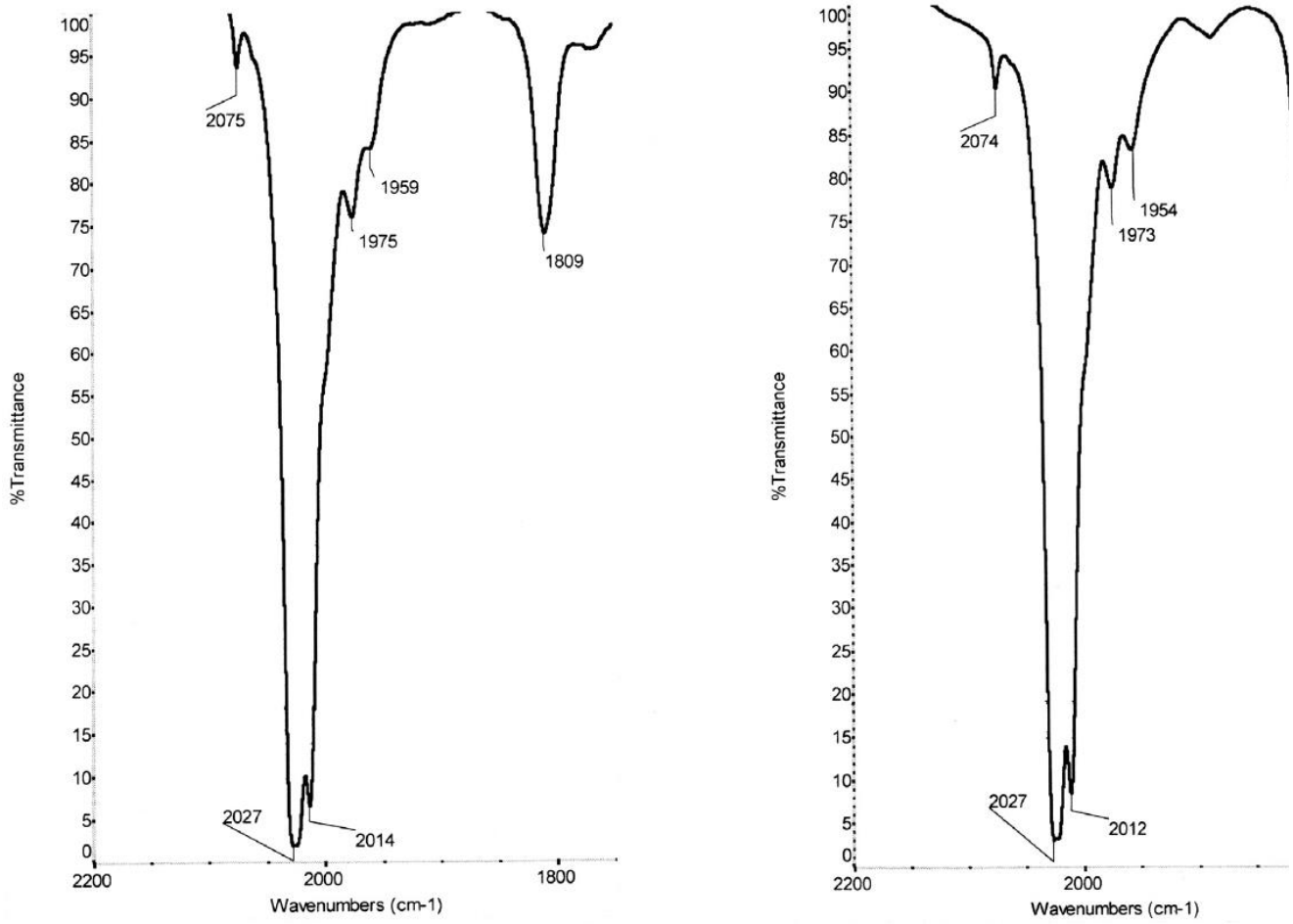

Figure 3.1.1. The IR spectra of $Na[Co_6As(CO)_{16}]$ in MeOH (left) and $PPh_4[Co_6As(CO)_{16}]$ in THF (right)

3.1.2.3 Single crystal X-ray diffraction

Crystal data are summarized in Table 3.1.1. An oblique prismatic crystal of compound (α-**1**[PPh_4], see below) of dimensions 0.33 × 0.18 × 0.17 mm and an irregular-shaped crystal of compound (β-**1**[PPh_4], see below) of dimensions 0.13 × 0.12 × 0.12 mm, both mounted on glass fibers in the air, were transferred to an Enraf-Nonius CAD4 automated diffractometer. Graphite-monochromated Mo-Kα, radiation was used. In both cases the setting angles of 25 random reflections ($16 < 2\theta < 22°$) were used to determine by least-squares fit accurate cell constants and orientation matrices. The two data collections were performed by the ω-scan method, within the limits $3 < 2\theta < 25°$, using a variable scan speed (from 3 to 20° min^{-1}) and a variable scan range of *(*α+0.35tanθ)" [α= 1.0°(α-**1**[PPh_4]) and 1.2°(β-**1**[PPh_4])], with a 25% extension at each end for

background determination. Reflections corresponding to the ±*h, +k, +l* and *+h, +k, +l* indices were collected for compounds (α-**1**[PPh_4]) and (β-**1**[PPh_4]), respectively. The total numbers of reflections measured were 7788 (α-**1**[PPh_4]) and 7946 (β-**1**[PPh_4]). Three standard reflections were measured every 3 h and no significant crystal decay was observed in both data collections. The intensities were corrected for Lorentz and polarization effects. An empirical absorption correction was applied in both cases based on ψ scans [24] (ψ 0-360° every 10°) of suitable reflections with χ values close to 90°; the maximum, minimum, and average relative transmission values were 1.00, 0.55, and 0.84 for complex (α- **1**[PPh_4]) and 1.00, 0.72, and 0.85 for (β-**1**[PPh_4]), respectively. Two sets of 3897 (α-**1**[PPh_4]) and 2168 *(*β-**1**[PPh_4]*)* independent significant reflections, with $I > 3\,\sigma(I)$, were used in the structure solutions and refinements. Both structures were solved by direct methods (SHELXS). The refinements were carried out by full-matrix least-squares methods using SHELXL-2014/7.[25] Anisotropic thermal parameters were assigned only to phosphorous and the anionic atoms. Phenyls have been treated as rigid bodies with hydrogen atoms riding on their carbon atoms on idealized positions. Final Fourier difference maps showed residual peaks not exceeding *ca.* 0.8 e/ A^{-3}. The final values of the conventional agreement indices R_1 and wR_2 [$I > 2\sigma(I)$] were 0.0414 and 0.0828 for compound α-**1**[PPh_4] and 0.0483 and 0.0923 for compound β-**1**[PPh_4]**,** respectively. The final positional parameters are listed in Tables 3.1.4 and 3.1.5 for α-**1**[PPh_4] and β-**1**[PPh_4]**,** respectively.

Table 3.1.1. Crystal data and experimental details for α-**1**[PPh_4] and β-**1**[PPh_4]

Identification code	α-**1**[PPh_4]	β-**1**[PPh_4]
Empirical formula	C_{40} H_{20} As Co_6 O_{16} P	C_{40} H_{20} As Co_6 O_{16} P
Formula weight	1216.03	1216.03
Temperature	298(2) K	298(2) K
Wavelength	0.71073	0.71073
Crystal system	Monoclinic	Orthorhombic
Space group	P 2_1/c	P b c a
a/Å	10.082(3)	21.191(5)
b/Å	21.266(5)	20.370(5)
c/Å	20.791(5)	21.284(5)
α/°	90.0	90.0
β/°	91.05(2)	90.0
γ/°	90.0	90.0
V/Å^3	4457(3)	9187(4)
Z, Calculated density /Mg m^{-3}	4, 1.812	8, 1.758
Absorption coefficient /mm^{-1}	3.023	2.933
F(000)	2392	4784
Crystal size /mm	0.33 × 0.18 × 0.17	0.13 × 0.12 × 0.12
θ-range/°	2.998 to 24.974	3.189 to 24.898
Limiting indices	-11≤ h ≤11, 0≤ k ≤25, 0≤ l ≤24	0≤ h ≤25, 0≤ k ≤24, 0≤ l ≤25
Reflections collected/unique	7788 / 7788	7946 / 7946
Completeness to *θ*-max	99.8 %	99.4 %
Absorption correction	Psi-scan	
Max. and min. transmission	1.0 and 0.78	1.00 and 0.91
Refinement method	Full-matrix least-squares on F^2	
Data / restraints / parameters	7788 / 0 / 409	7946 / 0 / 409
Goodness-of-fit (F^2)	0.995	0.902
R_1, wR_2 [$I > 2\sigma(I)$]	0.0414, 0.0828	0.0483, 0.0923
R_1, wR_2 (all data)	0.1476, 0.1010	0.2961, 0.1329
Largest diff. peak and hole/e Å^{-3}	0.705, -0.504	0.804, -1.024

3.1.2.4. Computational details

All the calculations were performed with GAUSSIAN 09 package.[26] Initial structures were taken from single crystal X-ray diffraction results. Full geometry optimizations of the isomers were carried out considering C_2 point group, followed by frequency calculation to confirm the nature of the minima and to obtain thermochemical data. The functional M06[27] was chosen with 6-311+G(d,p) basis for all the atoms. The same level of theory (M06/6-311+G(d,p)) was used for both geometry optimizations and frequencies calculations. Solvent effect was accounted for subsequent geometry optimizations using the Polarizable Continuum Model (PCM)[28]. A standard cavity was used, and the dielectric constant of tetrahydrofuran (THF) was 7.4257, and the initial structures were taken from the optimizations in gas phase. Simulated IR spectra are given in the Supporting information of this chapter (Figure 3.2.9).

3.1.3 Results and discussions

3.1.3.1 Synthesis of $[Co_6As(CO)_{16}]^-$

As(I) and As(III) compounds such as $(AsPh)_6$ [4,5] or $(AsMe)_5$,[7] $AsCl_3$,[8] AsH_3 [9] or $AsPh_3$[6] are typically used as sources of As. Conversely, we used PCl_5 as a source of P atoms in molecular cobalt clusters.[29] Since arsenic pentahalide are unstable and not commercially available, we tested the condensation of arsenic acid, (the hydrated $As_2O_5 \cdot 2H_2O$) with the sodium salt of $[Co(CO)_4]^-$.

The reaction in THF at room temperature is smooth, as clearly evidenced by the darkening of the reaction mixture and the CO evolution. After about 1 day of stirring, the infrared spectrum of the reaction mixture shows the presence of new carbonyl compounds, together with some unreacted $[Co(CO)_4]^-$. When the As/Co is lower than 1, the most intense bands are located at 2025, 2011 and 1808 cm^{-1}, assignable to the anion $[Co_6As(CO)_{16}]^-$; minor bands at higher wavenumbers denote the presence of neutral clusters, possibly the trimer $As_3Co_9(CO)_{24}$.[9] Conversely, if the As/Co is increased to about 2, different uncharacterized species are formed, presumably richer in As and similar to the known $[Co_4Sb_2(CO)_{11}]^{2-}$ [30] and $[Co_4Bi_2(CO)_{11}]^{2-}$ anions.[31] Neutral and anionic species can be easily separated, by extracting the former with hydrocarbon solvents. After repeated washing with hexane, the salt $Na[Co_6As(CO)_{16}]$ is left behind. It is dissolved in methanol, and layered with a dilute solution of PPh_4Cl in 2-propanol. Diffusion of the two solutions allowed crystal growth.

Alternatively, the compound can be isolated by precipitation with ammonium or phosphonium salt, and used for further studies. Among these, we are currently investigating the pyrolysis of $[Co_6As(CO)_{16}]^-$, in different solvents and at different temperatures.

3.1.3.2 Solid state structure

The samples obtained from methanol (method *3.1.2.2.1* in the experimental) contained crystals featuring two different morphologies (larger oblique prisms or smaller irregular chunks) both affording reasonable X-ray diffraction patterns (though, of different quality). Conventional single crystal X-ray diffraction analysis afforded a full structural characterization of both species. They resulted to be two *conformational polymorphs* of the $[Co_6As(CO)_{16}][PPh_4]$ salt (α-**1**$[PPh_4]$ and β-**1**$[PPh_4]$). In fact, the two structures differ not only in the packing of the cationic and anionic moieties in the crystal (they feature, in fact, different space group types and lattice parameters) but also in the stereochemistry of the anionic cluster units (**1a** in α-**1**$[PPh_4]$ and **1b** in β-**1**$[PPh_4]$, respectively). Actually, **1a** and **1b** are constitutional isomers rather than conformers, given the presence or the absence of a weak Co-Co bond (*vide infra*). Thus, strictly speaking, the term 'conformational polymorphs' could be questionable here. However, we find this terminology substantially correct because **1a** and **1b** easily interconvert in solution (*vide infra*) and, more generally, metal carbonyl clusters often display ligands (and even metal-cage) fluxionalities in solution.[32] α-**1**$[PPh_4]$, which crystallizes in the monoclinic space group P21/c, has a significantly higher density (1.812 *vs.* 1.758 g/cm3) and a better crystallinity than β-**1**$[PPh_4]$, which crystallizes in the orthorhombic Pbca space group. As a matter of facts, eight small 'cavities' (each of ca. 10 $Å^3$) can be computed in β-**1**$[PPh_4]$. However, they are too small to host solvent molecules and, within the limits due to poor sample diffraction, do not contain any residual electron density. Thus, the packing in β-**1**$[PPh_4]$ appears to be truly less efficient than that in α-**1**$[PPh_4]$ and must be correlated to the slightly different molecular geometries of **1a** and **1b**. α-**1**$[PPh_4]$ is isomorphous to the known $[Co_6P(CO)_{16}][PPh_4]$ salt[22]; accordingly, the stereochemistry of **1a** resembles that of $[Co_6P(CO)_{16}]^-$ (hereinafter, **2**) but for the differences inherent to the larger semi-interstitial atom (As *vs.* P). Thus, one may describe the anionic cluster cage as a folded chain of four edge-sharing triangles surrounding a "semi-interstitial" arsenic atom (see the folding angles Table 3.1.2). The anions are close to the idealized C_2 symmetry, with the twofold axis passing through the heteroatom and the middle of the Co1-Co2 edge. However, the metal cage has an approximate C_{2v} symmetry.

Accordingly, the Co-E bonds belong to two classes: the bonds to Co5 and Co6 atoms are significantly shorter than the other four. The Co-Co interactions can be divided into three classes: the four edges involving the external Co5 and Co6 atoms, the four shorter edges involving the central quadrilateral and the very long Col-Co2 edge, (see Table 3.1.2). All Co-Co bond distances are comparable to those found in many cobalt carbonyl clusters but the very long Col-Co2 interactions. Of the sixteen CO groups, fourteen are terminal and two symmetric edge-bridging. The cobalt atoms Co5 and Co6 bear three terminal carbonyls, whereas each of the other metal atoms is connected to one edge-bridging and to two terminal carbonyls. The main difference between **1b** and **1a** concerns atoms Co1 and Co2 (see Figure 3.1.2 for a comparison between the two geometries). In fact, in **1b** the weak Co1-Co2 bond has an even longer distance, exceeding the limit to classify it as a bond. This elongation implies a rotation of ca. 20° about the pseudo three-fold axis of the Co(CO)3 moieties of Co1 and Co2. Quite evident is especially the different orientation of the C15 and C16 carbonyls, bridging Co1-Co3 and Co2-Co4 bonds respectively (see Figure 3.1.2). This rearrangement preserves the overall C_2 symmetry of the anion but lowers (from C_{2v} to C_2) that of the cage.

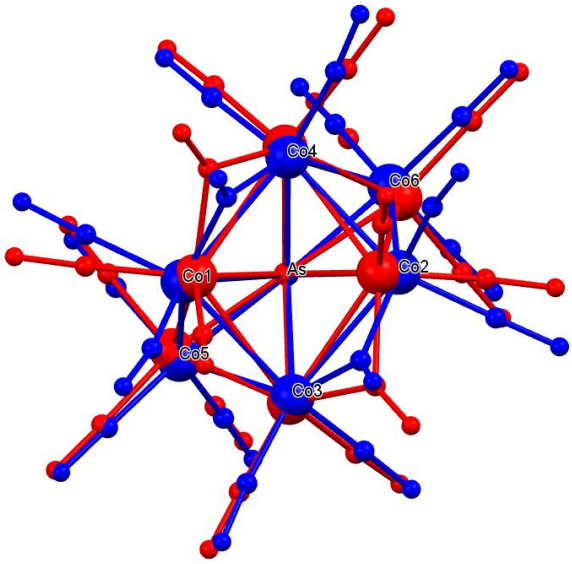

Figure 3.1.2. The overlay between structures **1a** (red) and **1b** (blue) as obtained from the corresponding α-**1** and β-**1** salts. Note in particular the longer Co1-Co2 contact in **1b** and the rotation of $Co(CO)_3$ moieties for Co1 and Co2. The root mean square deviation between the two geometries is 0.6 Å.

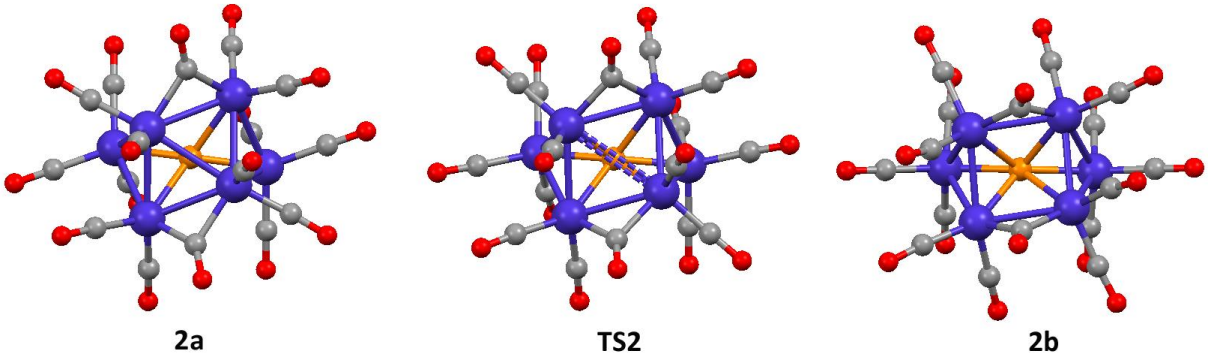

Figure 3.1.3. The isomer **2a**, **2b** and the transition state **TS2**, from M06/6-311+G(d,p) calculations.

Table 3.1.2. Selected bond distance and angles of isomers **1a**, **1b**, **2a**, **2b** and of the transition states **TS1** and **TS2** for $[Co_6X(CO)_{16}]^-$ (X = As, P) from X-ray diffraction or from theoretical calculations (M06/6-311+G(d,p)). The theoretical calculations are in C_2 symmetry.

	X = P				**X = As**				
	Expt.		**Theor.**		**Expt.**		**Theor.**		**Expt.**
	2a[22]	**2a**	**TS2**	**2b**	**1a**	**1a**	**TS1**	**1b**	**1b**
Selected Co-Co averaged distances									
Co1-Co2	2.935	2.801	3.150	3.487	2.944	2.800	3.045	3.489	3.457
Co5-Co(1,3), Co6-Co(2,4)	2.664	2.673	2.628	2.602	2.720	2.724	2.678	2.634	2.660
	2.646	2.680	2.644	2.623	2.703	2.728	2.687	2.658	2,672
Co1-Co(3,4), Co2-Co(3,4)	2.574	2.670	2.660	2.631	2.607	2.695	2.682	2.671	2.636
	2.575	2.570	2.555	2.538	2.595	2.564	2.564	2.544	2.579
Co5-Co6	4.105	4.153	4.107	4.092	4.385	4.441	4.436	4.408	4.364
Selected E-Co (E = P, As) averaged distances									
X-Co(1,2,3,4)	2.263	2.255	2.274	2.287	2.371	2.378	2.392	2.400	2.390
X-Co(5,6)	2.170	2.193	2.181	2.181	2.265	2.283	2.281	2.279	2.266
Dihedral angles (°) between edge sharing triangles									
Co(1,2,3)/Co(1,2,4)	143.4	135.4	145.3	159.9	145,0	137.5	144.2	159.3	159.7
Co(1,2,3)/Co(1,3,5)	122.9	123.8	120.1	115.4	125.1	126.0	124.3	118.9	119.1
Co(1,2,4)/Co(2,4,6)	122.0	123.8	120.1	115.4	124.3	126.0	124.3	118.9	118.4
Dihedral angles (°) between E, Co1,Co3 plane and carbonyls									
E,Co(1,3),C(1)	105.7	112.3	112.4	88.9	105.0	111.1	109.6	87.7	85.2
E,Co(1,3),C(2)	-156.9	-148.7	-151.7	-176.1	-159.2	-152.2	-155.0	-176.5	-179.5
E,Co(1,3),C(15)	-64.8	-36.7	-63.1	-84.4	-69.8	-46.6	-64.4	-86.0	-86.7

3.1.3.3 Computational results

We have simulated the structures of anions **1a** and **1b**, as well as of the already known **2a** and of the not yet isolated **2b**. Moreover, we searched for energy pathways interconnecting the isomers and found the transition states **TS1** and **TS2** (Figure 3.1.3). All geometry optimizations and frequency calculations were performed using density functional theory (DFT) (see experimental section for more details). The calculated geometries of **1a**, **1b** and **2a** are in good qualitative and quantitative agreement with the experimental results (Table 3.1.2). Co1-Co2 distance is not very sensitive to the change of semi-interstitial atom, in fact **1a**/**2a** and **1b**/**2b** show similar lengths.

Compared with X-ray data, the gas phase DFT calculations underestimate the Co1-Co2 distance in anions **a**, which further confirms the flexibility of this bond, very likely sensitive to the data collection conditions (such as P or T) when determined in the solid state. We tested also the possible role of the dielectric medium surrounding the anion and therefore optimized the geometries in various polarizable continuum model (PCM)[28], simulating solvents with different dielectric constant. However, this variable did not affect much the computed molecular geometries. The computed transition states show that the Co1-Co2 distance is in fact intermediate between **2a** and **2b** for the phosphide, whereas it results closer to **1a** for the arsenide. The bond distances and angles confirm that **TS1** is an early transition state (see Scheme 3.1.1). In Table 3.1.3, we report energy differences between isomers **a** and **b**. ΔE is the electronic energy difference which is independent from the medium (*in vacuo* or PCM returns the same value). From frequency calculations, we derived the corresponding enthalpies and Gibbs free energy differences (ΔH, ΔG), using thermal corrections at 1 atm and 298 K. ΔG_{PCM} represents the difference between free energy of solvation in THF obtained through PCM.

Table 3.1.3. The energy differences between isomers **a** and **b** for both **1** and **2**. Results are in kcal/mol

X	ΔE	ΔH	ΔG	ΔG_{PCM}
As	4.9	4.8	2.4	5.1
P	2.8	2.6	0.1	2.9

For both As and P derivatives, the isomers **b** are the most stable, however the thermodynamic driving force is certainly more pronounced for the As-derivative, whereas the Gibbs free energy difference (in pure gas phase) is negligible for the P-derivative. We also analyzed the potential energy surface of these clusters. We carried out linear transit calculations *in vacuo*, by constraining various values of the Co1-Co2 distance, and computed the local transition states using the Synchronous Transit-Guided Quasi-Newton method.[33] Only **TS2** features a single imaginary frequency, corresponding to the stretching of Co1-Co2, whereas **TS1** shows an additional negative, albeit small, eigenvalue (-10.4 cm^{-1}), which corresponds to a real frequency in **TS2**. The discrepancy between anions **1** and **2** is probably due to the size of the integration grid, as for example observed by Ding and co-workers.[34] The overall reaction paths can be summarized as in scheme 3.1.1.

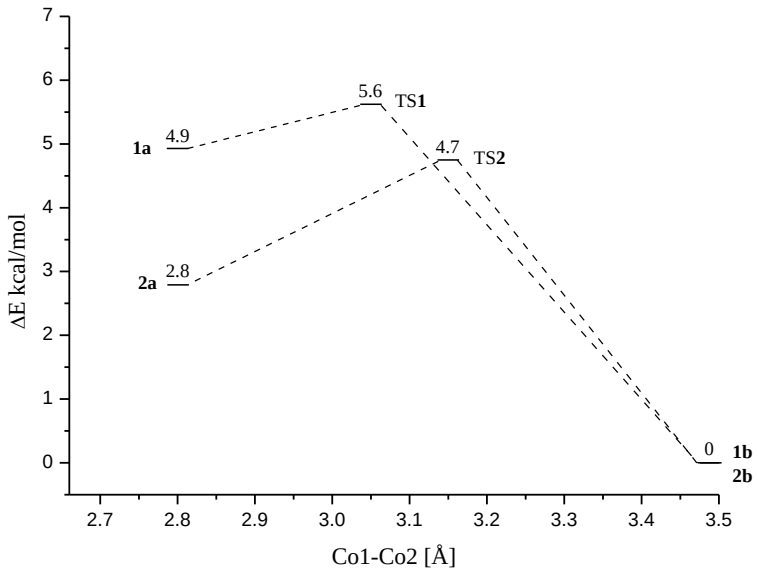

Scheme 3.1.1. Calculated energy [kcal/mol] Pathway for isomerization.

Here we note that the early transition state of **1** implies a much smaller barrier $\Delta E_{(\mathbf{TS1},\ \mathbf{1a})}$ compared with $\Delta E_{(\mathbf{TS1},\ \mathbf{1a})}$. From these data, we conclude that: 1) in both cases, the isomer with the longest Co1-Co2 bond is the most stable, but the reaction equilibrium in the As derivative is certainly more shifted towards the "open" isomer **1b** (of course, this preference is fully consistent with the larger atomic radius of As); 2) the kinetic barrier for this interconversion is higher for the P derivative, but anyway not very high and one should expect both species to be present in solution.

These conclusions should be merged with what previously observed on the crystal structure of the two isomers: isomers **a**, although less stable in isolation, are better stabilized by packing forces

that counterbalance the unfavorable form of the cluster in polymorphs **α**. This may explain the reason why isomers **a** are always observed for both As and P, although being only the kinetic products. The calculated ΔE and ΔG may, in part, explain the reason why isomer **b** has not been isolated (yet) for the P derivative. In fact, the thermodynamic driving force toward **2b** is weaker than for **1b** and a higher kinetic barrier is present. Nevertheless, it is sensible to anticipate that an isomer of type **2b** should exist and could be in principle isolated.

3.1.4 Conclusions

The reaction between $Na[Co(CO)_4]$ and arsenic acid yields $[Co_6As(CO)_{16}]^-$, which is the first known anionic Co-As derivative, and other uncharacterized species. $[Co_6As(CO)_{16}]^-$ and $[Co_6P(CO)_{16}]^-$ share a quite similar geometry, however we observed for the As derivative an additional isomer (featuring one absent Co-Co bond), not yet known for the P-substituted species.

Theoretical calculations predict for both species that the larger cage is the more stable isomer, although the experimentally observed packing for this species is much less efficient, which may explain its more elusive behavior.

Table 3.1.4. Atomic coordinates ($x10^4$) and equivalent isotropic displacement parameters (A^2x10^3) for α-**1**[PPh_4]. U(eq) is defined as one third of the trace of the orthogonalized U_{ij} tensor.

Atom	x	y	z	U(eq)
Co(1)	9810(1)	2567(1)	9671(1)	46(1)
Co(2)	10899(1)	3140(1)	10857(1)	50(1)
Co(3)	9387(1)	3727(1)	10020(1)	50(1)
Co(4)	10162(1)	1980(1)	10760(1)	45(1)
Co(5)	7269(1)	2985(1)	9770(1)	47(1)
Co(6)	9064(1)	2698(1)	11684(1)	54(1)
C(1)	9075(7)	2142(3)	9031(3)	64(2)
O(1)	8655(6)	1841(3)	8615(3)	103(2)
C(2)	11006(8)	2998(3)	9257(3)	73(2)
O(2)	11865(6)	3214(3)	8975(3)	105(2)
C(3)	12497(8)	2832(3)	10717(4)	70(2)
O(3)	13549(5)	2661(3)	10624(3)	99(2)
C(4)	11168(7)	3532(4)	11584(4)	74(2)
O(4)	11470(5)	3819(3)	12021(3)	115(2)
C(5)	9493(8)	4169(3)	9288(4)	75(2)
O(5)	9561(7)	4467(3)	8836(3)	126(3)
C(6)	8578(7)	4288(3)	10515(4)	71(2)
O(6)	8071(6)	4630(3)	10847(3)	113(2)
C(7)	11493(7)	1659(3)	11235(3)	62(2)
O(7)	12305(5)	1435(3)	11545(3)	91(2)
C(8)	9039(7)	1332(3)	10682(3)	62(2)
O(8)	8335(6)	924(3)	10612(3)	100(2)
C(9)	7322(7)	3262(3)	8951(4)	60(2)
O(9)	7315(6)	3418(3)	8430(2)	92(2)
C(10)	6403(7)	2250(3)	9746(3)	60(2)
O(10)	5848(6)	1790(3)	9741(3)	108(2)
C(11)	6103(7)	3498(3)	10140(3)	61(2)
O(11)	5382(5)	3822(3)	10385(3)	92(2)
C(12)	10254(8)	2414(4)	12264(3)	83(2)
O(12)	10970(6)	2238(4)	12653(3)	137(3)
C(13)	7793(8)	2117(4)	11783(3)	65(2)
O(13)	6974(6)	1755(3)	11839(3)	94(2)
C(14)	8363(6)	3399(4)	12035(3)	64(2)
O(14)	7929(6)	3831(3)	12263(3)	95(2)
C(15)	10921(7)	1881(3)	9930(3)	58(2)
O(15)	11711(5)	1559(3)	9692(2)	90(2)
C(16)	11115(7)	3898(3)	10368(3)	59(2)
O(16)	11921(5)	4287(2)	10318(3)	92(2)
As	8678(1)	2837(1)	10614(1)	38(1)
P	5812(2)	-383(1)	12095(1)	42(1)
C(111)	5652(4)	-1219(2)	12185(2)	47(2)
C(112)	5862(4)	-1605(2)	11657(2)	66(2)
C(113)	5775(5)	-2254(2)	11721(2)	84(2)
C(114)	5477(5)	-2518(2)	12312(2)	88(2)
C(115)	5266(4)	-2132(2)	12841(2)	83(2)

C(116)	5353(4)	-1483(2)	12777(2)	63(2)
C(121)	7509(3)	-170(2)	11986(2)	41(1)
C(122)	8059(4)	342(2)	12310(2)	56(2)
C(123)	9390(4)	491(2)	12234(2)	73(2)
C(124)	10171(3)	127(2)	11834(2)	75(2)
C(125)	9621(4)	-384(2)	11510(2)	88(2)
C(126)	8290(4)	-533(2)	11586(2)	67(2)
C(131)	4832(3)	-149(2)	11410(2)	46(2)
C(132)	5152(3)	396(2)	11079(2)	62(2)
C(133)	4345(4)	601(2)	10571(2)	78(2)
C(134)	3219(4)	261(2)	10396(2)	69(2)
C(135)	2899(3)	-285(2)	10728(2)	63(2)
C(136)	3706(4)	-489(2)	11235(2)	55(2)
C(141)	5227(4)	13(2)	12792(2)	45(2)
C(142)	5874(3)	-55(2)	13383(2)	53(2)
C(143)	5388(4)	247(2)	13923(2)	64(2)
C(144)	4255(4)	617(2)	13871(2)	74(2)
C(145)	3607(3)	685(2)	13280(2)	78(2)
C(146)	4093(4)	383(2)	12740(2)	63(2)

Table 3.1.5. Atomic coordinates ($x10^4$) and equivalent isotropic displacement parameters ($A^2 x10^3$) for β-**1**[PPh_4]. U(eq) is defined as one third of the trace of the orthogonalized U_{ij} tensor.

Atom	x	y	z	U(eq)
Co(1)	-915(1)	617(1)	2579(1)	45(1)
Co(2)	16(1)	-776(1)	2543(1)	48(1)
Co(3)	-262(1)	105(1)	1679(1)	45(1)
Co(4)	-370(1)	-75(1)	3474(1)	45(1)
Co(5)	9(1)	1318(1)	2079(1)	51(1)
Co(6)	869(1)	-179(1)	3270(1)	56(1)
As	209(1)	392(1)	2639(1)	42(1)
C(1)	-1542(5)	535(5)	2044(5)	66(3)
O(1)	-1990(4)	511(5)	1745(4)	116(3)
C(2)	-1187(4)	1318(5)	3007(5)	55(3)
O(2)	-1383(4)	1756(4)	3275(4)	84(3)
C(3)	-371(5)	-1398(5)	2965(5)	58(3)
O(3)	-629(4)	-1847(4)	3185(4)	100(3)
C(4)	603(5)	-1274(5)	2157(5)	56(3)
O(4)	983(4)	-1588(4)	1927(4)	111(3)
C(5)	441(5)	-70(5)	1250(5)	61(3)
O(5)	900(4)	-170(4)	979(4)	91(3)
C(6)	-764(5)	253(5)	1020(5)	58(3)
O(6)	-1045(4)	338(4)	582(3)	85(3)
C(7)	-528(5)	-682(6)	4072(5)	64(3)
O(7)	-641(4)	-1028(4)	4464(4)	103(3)
C(8)	-349(5)	614(6)	3999(5)	72(3)
O(8)	-339(5)	1043(4)	4334(4)	116(3)
C(9)	81(5)	1920(5)	2685(5)	56(3)
O(9)	117(4)	2305(4)	3079(4)	87(3)

C(10)	-601(5)	1623(5)	1572(5)	62(3)
O(10)	-976(4)	1830(4)	1241(4)	97(3)
C(11)	714(5)	1405(5)	1650(5)	62(3)
O(11)	1172(4)	1487(4)	1366(4)	96(3)
C(12)	1534(5)	-279(6)	2783(6)	90(4)
O(12)	1966(4)	-357(6)	2466(5)	157(5)
C(13)	841(5)	-912(6)	3733(6)	78(4)
O(13)	864(4)	-1375(4)	4037(5)	118(3)
C(14)	1109(5)	452(6)	3807(6)	76(4)
O(14)	1271(4)	862(4)	4126(4)	112(3)
C(15)	-1209(4)	-38(5)	3154(4)	48(3)
O(15)	-1698(3)	-294(3)	3253(3)	69(2)
C(16)	-572(5)	-772(5)	1868(5)	55(3)
O(16)	-965(3)	-1121(3)	1657(3)	76(2)
P	1942(1)	2865(1)	4616(1)	45(1)
C(111)	2202(3)	2212(3)	5108(3)	50(3)
C(112)	2703(3)	1815(3)	4925(2)	63(3)
C(113)	2942(2)	1347(3)	5337(3)	72(3)
C(114)	2680(3)	1276(3)	5932(3)	62(3)
C(115)	2179(3)	1673(3)	6115(2)	68(3)
C(116)	1940(2)	2141(3)	5703(3)	60(3)
C(121)	2351(3)	3605(3)	4808(3)	46(3)
C(122)	2323(3)	4134(3)	4396(2)	61(3)
C(123)	2603(3)	4728(3)	4557(3)	73(3)
C(124)	2911(3)	4793(3)	5130(3)	86(4)
C(125)	2939(3)	4264(4)	5542(3)	95(4)
C(126)	2659(3)	3671(3)	5381(3)	77(4)
C(131)	2100(3)	2677(3)	3817(3)	46(3)
C(132)	2695(3)	2801(3)	3570(3)	82(4)
C(133)	2832(3)	2627(4)	2954(4)	98(4)
C(134)	2374(4)	2328(4)	2584(3)	105(4)
C(135)	1778(4)	2204(4)	2831(4)	133(6)
C(136)	1641(3)	2378(4)	3448(4)	98(4)
C(141)	1114(2)	2984(3)	4750(3)	48(3)
C(142)	874(3)	3615(3)	4814(3)	50(3)
C(143)	228(3)	3711(3)	4881(3)	70(3)
C(144)	-178(2)	3174(3)	4884(3)	72(3)
C(145)	63(3)	2543(3)	4820(3)	84(4)
C(146)	709(3)	2448(2)	4753(3)	67(3)

Section 2

Electron Density Analysis of Metal Clusters with Semi-Interstitial Main Group Atoms. Chemical Bonding in $[Co_6X(CO)_{16}]^-$ Species

3.2.1 Introduction

Since the discovery of the first high nuclearity ($n \geq 6$) metal carbonyl cluster, $[Co_6(CO)_{15}]^{2-}$ in 1967 by Chini,[35] many investigations on these intriguing species have been carried out in order to understand and rationalize the chemical bonding, to predict molecular structures and to investigate their potential catalytic activity. Even before the characterization of $[Co_6(CO)_{15}]^{2-}$, the nuclearity of a cluster could be increased using p-block atoms, following the discovery of $[Fe_5C(CO)_{15}]$.[36]

Afterwards, Vidal synthesized and characterized the first high nuclearity clusters featuring interstitial elements of group V, namely $[Rh_9P(CO)_{21}]^{2-}$,[37] $[Rh_{10}P(CO)_{22}]^{3-}$,[38] and $[Rh_{10}As(CO)_{22}]^{3-}$.[6]

Finally, using the relatively large atomic radius of pnictogens, combined with their ability to stabilize unusual geometry, Chini *et al.*[22] isolated semi-interstitial anionic clusters, like $[Co_6(CO)_{16}P]^-$. The organometallic chemistry community recently rehashed the interest on these compounds, when other high nuclearity clusters have been reported.[39,40,41] Some carbonyl clusters with semi-interstitial, exposed group V atoms have shown high catalytic performance in the C-H activation of 3-picoline.[42] Moreover, cobalt-phosphide materials are extremely efficient in both hydrogen and oxygen evolution reactions (HER, OER),[19,21] whereas some metal-As carbonyls were found to be promising for magnetic properties.[14]

Transition-metal clusters have always attracted the curiosity of theoretical chemists because of the elusive nature of the metal-metal bonds and the cooperative σ-donation/π-back-donation mechanism of the metal-ligand interactions. The research studies published in the last twenty years made use of different theoretical approaches in order to rationalize the nature of chemical bonding, including charge density analysis[43] or energy decomposition analysis.[44] From some of these studies, it emerged, for example, that the radial W-Au bonds, the aurophilic interactions and relativistic

effects stabilize the icosahedral WAu_{12} cluster,[45] a molecule that was theoretically predicted by Pyykkö before its observation in the gas-phase. Hopffgarten and Frenking[46] studied a number of icosahedral $[M(EH)_{12}]$ compounds, using theoretical tools for an accurate analysis of the nature of the M-E and E-E interactions and for quantifying the atomic contributions to the stability of the molecular structure.

The nature of bonding between metals and interstitial or semi-interstitial main group atoms is still largely unexplored, especially from the point of view of charge density analysis. This prompted us to investigate theoretically and experimentally a class of semi-interstitial carbonyl clusters, namely $[Co_6X(CO)_{16}]^-$ (X = As, P; hereinafter **1** and **2** respectively). As we recently reported,[41] this cluster has two conformers,[i] differing for the presence or absence of a short Co-Co distance (namely Co1-Co2). Hereinafter, the isomers are named **a** and **b**, respectively. For X = As, both isomers (**1a** and **1b**) have been isolated and structurally characterized[41] as salts of tetraphenylphosphonium. For X = P only isomer **2a**, with short Co-Co distance, has been isolated, so far.[22] The species **2b**, *i.e.*, $[Co_6P(CO)_{16}]^-$ with long Co1-Co2 distance, has not been observed yet, at least in the form of a single crystal. In fact, from X-ray diffraction studies, α-**1**$[PPh_4]$ and α-**2**$[PPh_4]$, containing **1a** and **2a** cluster units respectively, crystallize in the P $2_1/c$ space group and are isomorphous whereas β-**1**$[PPh_4]$, having **1b** unit, is a polymorph which crystallizes in the Pbca space group. This intriguing stereochemical flexibility and the promising applications of this class of compounds (catalysis, HER/OER, magnetic nanomaterials, etc.), motivated us to carry out an in-depth investigation on the nature of X-Co and Co-Co interaction, using both charge density and energy partition approaches: Quantum Theory of Atoms in Molecules (QTAIM)[47], Energy decomposition Analysis (EDA)[48], Interacting Quantum Atoms (IQA)[49] and Wiberg Bond Indices (WBI)[50]. For species **2a**, a high resolution X-ray diffraction experiment was also possible, that enabled an experimental model[51] of the charge density distribution, in order to complement and validate the theoretical analysis.

[i] Because in both cases a clear Co-Co bond cannot be identified (as discussed in the rest of this paper), we prefer using here the term "conformational isomers", which are in fact due to different rotation of some $Co(CO)_3$ groups, leading to a short or a long Co1-Co2 distance.

3.2.2 Experimental section and computational details

3.2.2.1 Single crystal X-ray diffraction

The single crystal **2a_1** (dimension 0.1, 0.1, 0.2 mm) was collected on a Bruker-APEX-II X-ray diffractometer, using Mo Kα graphite-monochromatized radiation, with generator working at 50 kV and 30 mA. Data were collected at T = 100 K using an Oxford cryosystem series 600; ω-scans of 0.3° were adopted and a total of 5354 frames with exposure times of 40, 80 and 120 seconds were collected. The data were integrated using SAINT (version V7.23A[52]), and corrected analytically for absorption and empirically (with SADABS[53]) for the other anisotropies of the diffraction. The single crystal **2a_2** was mounted on an Agilent SuperNova diffractometer, equipped with a MoKα microsouce (50 kV and 0.8 mA), Al-filtered[54]. Data were collected at T = 110 K using an Oxford cryosystem 700, with ω-scans of 1.0° were adopted and a total of 4282 frames with exposure times of 20, 30 and 120 seconds were collected. The software CrysAlisPro Version 1.171.37.35g[55], was used to perform data collection and reduction. Data were corrected for absorption (analytically) and diffraction anisotropies using ABSPACK[55] routine of Crysalis. More information about the two experiments are reported in Table 3.2.1.

Table 3.2.1. Crystallographic Data and Structure Refinement Parameter for 2a_1 and 2a_2

Identification code	α-**2a_1**	α-**2a_2**
Empirical formula	C_{40} H_{20} Co_6 O_{16} P_2	C_{40} H_{20} Co_6 O_{16} P_2
Formula weight	1172.08	1172.08
Temperature	100 K	110 K
Wavelength	0.71073	0.71073
Crystal system	Monoclinic	Monoclinic
Space group	$P2_1/c$	$P2_1/c$
a/Å	10.0109(4)	10.0180(1)
b/Å	20.8610(8)	20.8737(1)
c/Å	20.4255(8)	20.4382(1)
β/°	92.176(2)	92.1609(4)
V/Å^3	4262.5(3)	4270.85(5)
Z, Calculated density /Mg m^{-3}	4, 1.826	4, 1.823
Absorption coefficient /mm^{-1}	2.428	2.423
Θ-range/°	1.952 to 45.294	1.951 to 45.506
Reflections collected/unique	121109 / 32541	329282 / 36061
R_{merge}	0.0345	0.0461
R_{rim}	0.0403	0.0488
Multiplicity (inf-0.5 Å)	3.7	9.1
Multiplicity (inf-0.7 Å)	7.0	12.1
Spherical Atom Refinement		
Data / restraints / parameters	32541 / 0 / 577	36061 / 0 / 577
Goodness-of-fit (F^2)	1.003	1.028
R_1, wR_2 [$I > 2\sigma(I)$]	0.0382, 0.0704	0.0296, 0.0678
R_1, wR_2 (all data)	0.0784, 0.0812	0.0450, 0.0736
Multipolar Refinement		
Data / restraints / parameters	21540 / 0 / 1917	28825 / 0 / 1917
Goodness-of-fit (F^2)	1.1405	1.2502
R_1, wR_2 [$I > 2\sigma(I)$]	0.0289, 0.0407	0.0211, 0.0500
R_1 (all data)	0.0393	0.0233

3.2.2.1.1 Multipolar expansion

In Table 3.2.1, we report the results of conventional and multipolar refinements for the salt $[Co_6P(CO)_{16}]^-[PPh_4]^+$ (**2a_1, 2a_2**), carried out with ShelX[25,56] and XD[57] programs, respectively (Table 3.2.1). The multipolar refinement was carried out using data with $I > 2\sigma(I)$, using the Hansen and Coppens model, as showed in equation (1.12). For Co and P atoms, the multipolar expansion was truncated at the hexadecapole level, for O and C at the octupole level. The scattering factors of cobalt atoms was constructed from the $4s^2 3d^7$ configuration of the isolated atom, but the population of the 4s valence orbitals was not refined and all the deformation density of Co atoms was constructed from 3d orbitals for all atoms. The Volkov and Macchi atomic functions[58] were employed to describe the radial densities of all atoms. The positions of H atoms were kept fixed at a C-H distance equal to 1.079 Å, according to average neutron diffraction data for tetraphenylphosphonium cation. The H thermal motion was considered isotropic and only the monopole and the C-H oriented dipole parameters were refined. Expansion/contraction parameters κ and κ' were refined for each kind of element: two different sets were assigned to phosphorus (to discriminate the phosphide from the phosphonium atoms) and carbon (to distinguish carbonyl carbons and phenyl carbons). For all expansion/contraction parameters, κ' were constrained to κ, in order to avoid divergence of the refinement. For hydrogen atoms, κ and κ' were kept equal to the standard value of 1.2. Third- and fourth- Gram-Charlier coefficients of anharmonicity (Table S3.2) were refined for Co and P (phosphide) atoms. The residual distribution and normal probability plots of diffraction intensities discrepancies and other parameters are reported in Figures 3.2.1- 3.2.3 and inTables S3.1-S3.3.

The two experimental charge densities of the anion $[Co_6P(CO)_{16}]^-$ were analyzed using the QTAIM routine implemented in the module XDPROP. In Figure 3.2.4 and Table 3.2.2 we report the main topological indices, the charges of the semi-interstitial atom Q(X). The Lagrangian function integrated within an atomic basin, $L(\Omega)$, should vanish and therefore it is an indicator of accuracy of the integration. With our models, for P atom this value resulted equal to $-2.01\cdot10^{-3}$ au in **2a_1** and $-3.83\cdot10^{-3}$ au in **2a_2**, for metal atoms, from Co1 to Co6 respectively, $L(\Omega)$ values resulted $1.52\cdot10^{-2}$, $1.62\cdot10^{-2}$, $2.74\cdot10^{-2}$, $4.38\cdot10^{-2}$, $1.15\cdot10^{-1}$ and $1.22\cdot10^{-1}$ au in **2a_1** and $-2.72\cdot10^{-4}$, $1.10\cdot10^{-3}$, $2.22\cdot10^{-2}$, $1.74\cdot10^{-2}$, $1.03\cdot10^{-1}$, $2.83\cdot10^{-2}$ au in **2a_2**.

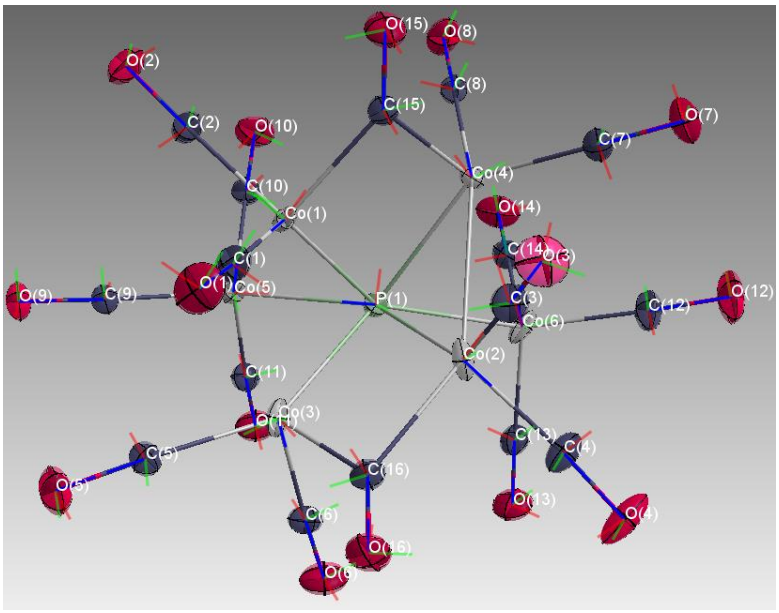

Figure 3.2.1. The local coordinate system adopted for all multipolar models. For each atom, blue is Z axis, green is Y axis and red is X axis.

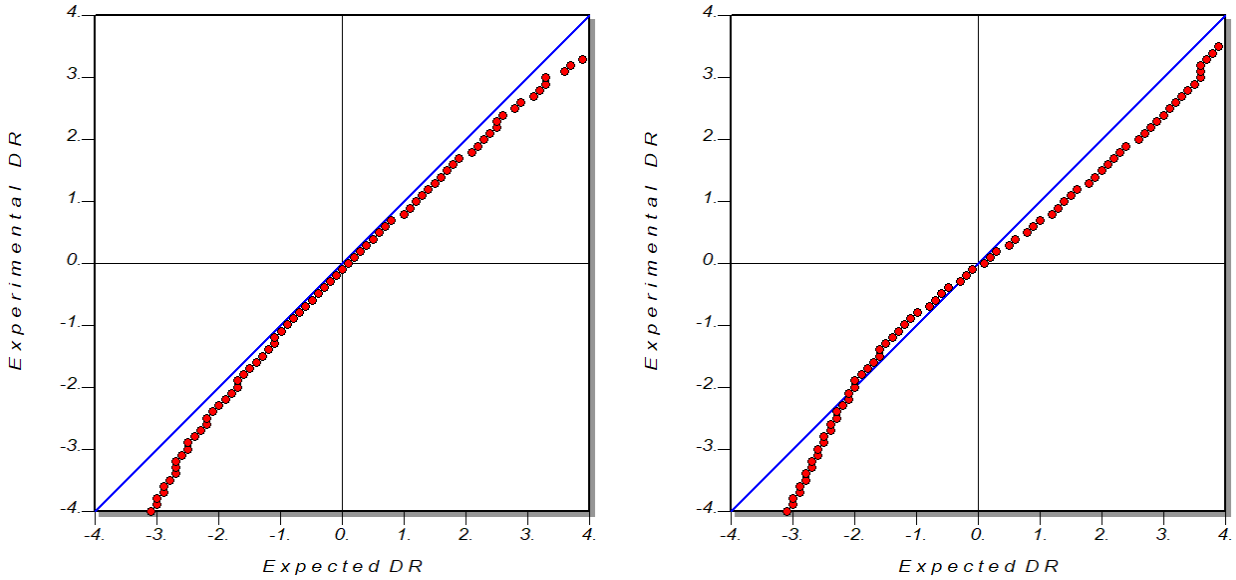

Figure 3.2.2. The normal probability plots[ii] of the intensities residuals for **2a_1** (left) and **2a_2** (right) refinements.

[ii] Abrahams, S. C.; Keve, E. T. Normal probability plot analysis of error in measured and derived quantities and standard deviations. *Acta Cryst.*, **1971**, *A27*, 157-165.

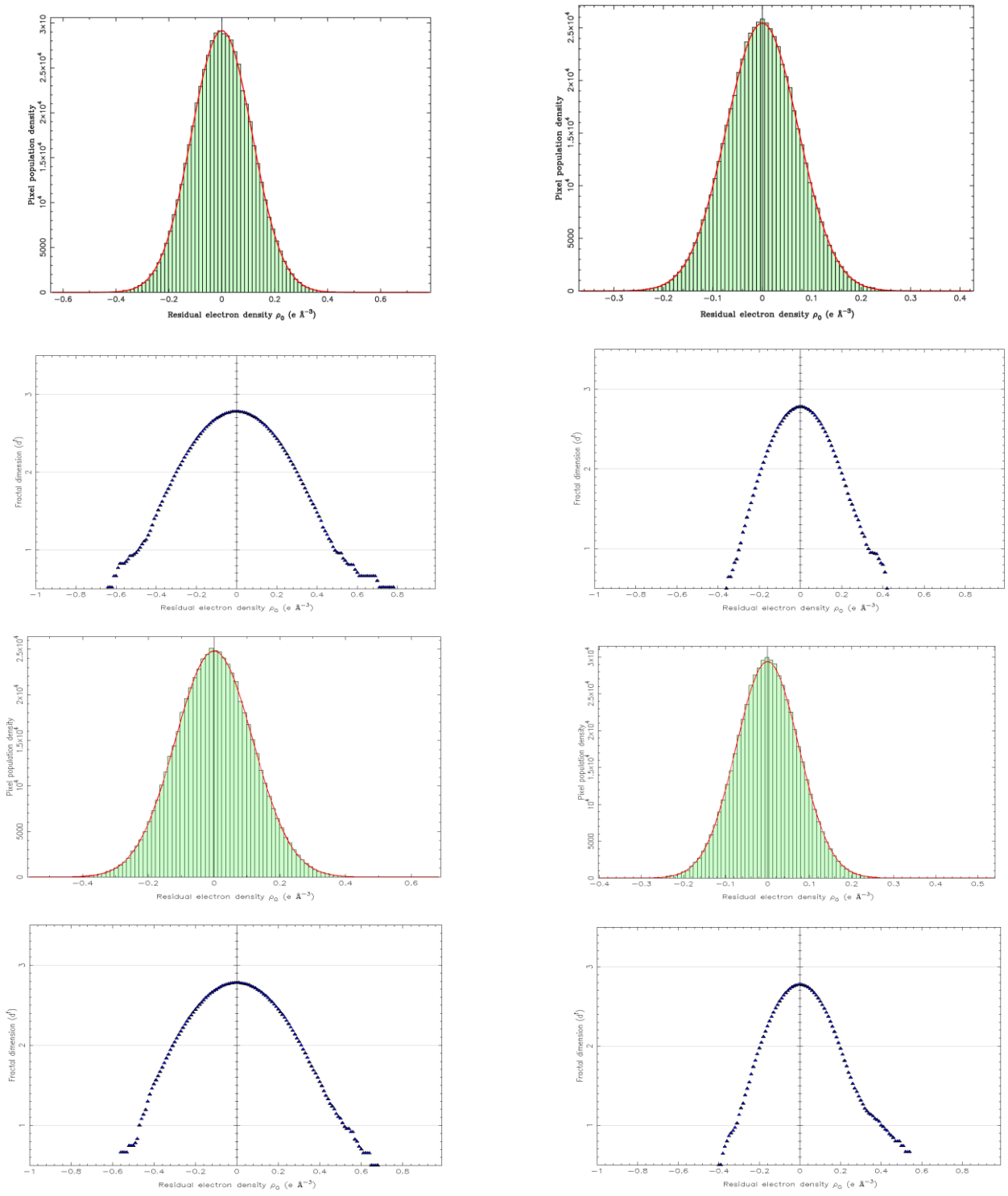

Figure 3.2.3. Residual distributions for **2a_1** (left) and **2a_2** (right) models. First line: normal probability plot for anharmonic models; Second line: fractal plot of the residual distribution for the two anharmonic motions; Third line normal probability plot for harmonic models; Fourth line normal probability plot for harmonic models.

3.2.2.2 Computational details

EDA: DFT calculations have been performed with the program package ADF2014[59], using the functional B3LYP and the triple zeta with double polarization functions (TZ2P) Slater type orbitals (STOs) as basis functions for the SCF calculations. All the structures have been optimized and verified as minima on the potential energy surface by calculation of the vibrational frequencies.

QTAIM/IQA: The program package AIMALL was used. The wave functions were calculated with Gaussian09 [26], using the B3LYP functional and *correlation-consistent* triple zeta (cc-PVTZ) basis set. B3LYP is one of the few DFT models supported by AIMALL for the correct evaluation V_{xc}^{AB} in the IQA analysis[60]. The molecular geometries were optimized and the nature of the minima have been verified by calculation of the vibrational frequencies.

Wiberg bond indices: they were computed on the B3LYP/cc-PVTZ optimized geometries using the NBO3.1 program linked to Gaussian09.

3.2.3 Results and discussions

3.2.3.1 The molecular structures and the crystal packing

As we reported in a previous Section,[41] the salt $[Co_6As(CO)_{16}]^-[PPh_4]^+$ (**1**[PPh_4]) is known in two different conformational polymorphs, **α-1a**[PPh_4] and **β-1b**[PPh_4]. The solid state form α (space group, $P2_1/c$) is similar for **1a** and **2a** (*i.e.* $[Co_6P(CO)_{16}]^-[PPh_4]^+$, [22]), whereas the form β (space group, Pbca) has been observed for **1b** only and never obtained for the phosphide analogue.

Both anionic isomers feature a cluster cage (an 'unfolded' octahedron), made of a folded chain of four edge-sharing triangles surrounding a "semi-interstitial" heteroatom. The idealized symmetry is C_2, with the two-fold axis going through the heteroatom and the midpoint of the Co1-Co2 edge.

The most striking difference between the isomers **a** and **b** is the Co1-Co2 distance, which is shorter for **a** (2.944(1) in **1a**, 2.935(2) Å in **2a**) and longer for **b** (3.457(2) Å in **1b**). Theoretical calculations predict that in gas phase and in solution the isomers of type **b** would be the most stable forms for the $[Co_6X(CO)_{16}]^-$ anions. In the solid state, however, polymorphs type α (hence, the isomers type **a**) have a much more efficient type of packing, as revealed by the mass densities of the arsenides polymorphs (1.812 for α-**1a** and 1.758 g/cm^{-3} for β-**1b**). The quality of the crystal samples is also much better for the α-**1b** polymorph, compared to β-**1b**; this may be an indication (together with the higher density of α-**1a** and the missing β-**2b**) of β-type polymorphs being only kinetic products, not always isolable. The higher quality of samples α-**2a** enabled us to carry out extensive

data collections with the purpose of an experimental determination of the charge density, not possible for α-1**a** or β-**1b**. For sake of improving the precision of the measured quantities, two different crystals of $[Co_6P(CO)_{16}]^-[PPh_4]^+$ (Table 3.2.1), hereinafter **2a_1** and **2a_2**, respectively, were measured. The two structure determinations (all carried out at low T) provide very similar values of the "critical" Co1-Co2 distance, namely 2.8901(2) Å for **2a_1** and 2.8922(1) Å for **2a_2** (from spherical atom refinement), but they significantly differ from the characterization by *Chini et al.*[22], carried out at room temperature, 2.935(2) Å. Indeed, multi temperature diffraction shows that Co1-Co2 is quite flexible and it significantly contract as the sample is cooled.

3.2.3.2 Charge Density Analysis

QTAIM enable to gain, from the electron density distribution only, important insight into the nature of the chemical bonding, which is especially useful when dealing with non-standard kind of bonding, especially metal-metal bonding and metal-interstitial atoms bonding[43], both present in species **1** and **2**. As anticipated, the crystal sample quality enabled the experimental determination only for isomer **2a**, whereas **1a**, **1b** and, obviously, the elusive **2b** are determined only by theoretical simulations.

In Figure 3.2.4, we report the topological indices for the main interactions in the anionic clusters. This enables a comparison between the two kinds of isomers (**a** vs **b**) and the two kinds of semi-interstitial atoms (P vs. As). From theoretical calculations, one may also obtain quantities related to the electron pair distribution, as for example the electron delocalization indices[61,62] that are very useful, especially to characterize the electron-donor ability of interstitial atoms. In keeping with all bridged metal-metal bonds[63], the molecular graphs of all clusters lack of direct Co-Co bond paths, with the exception of Co1-Co3 (and the symmetry equivalent Co2-Co4) in **1b**. If optimized with the basis set 6-311+G(d,p), **1a** also features the same bond path, although with almost overlapping bond and ring critical points. As we previously discussed for carbonyl bridges, the lack of a bond path does not necessarily imply the absence of a Co---Co interaction, but simply the dominance of the *through-bond* interaction over the direct *through-space* one.[64] Therefore, the main feature of the molecular graphs is the connection of all Co atoms to the semi-interstitial atom. Given the C_2 symmetry of the gas phase molecules and the pseudo-symmetry in the solid state, the Co-X paths can be grouped into three symmetry independent interactions, namely to Co1 (= Co2), Co3 (= Co4) and Co5 (= Co6) (Figure 3.2.4, 3.2.5).

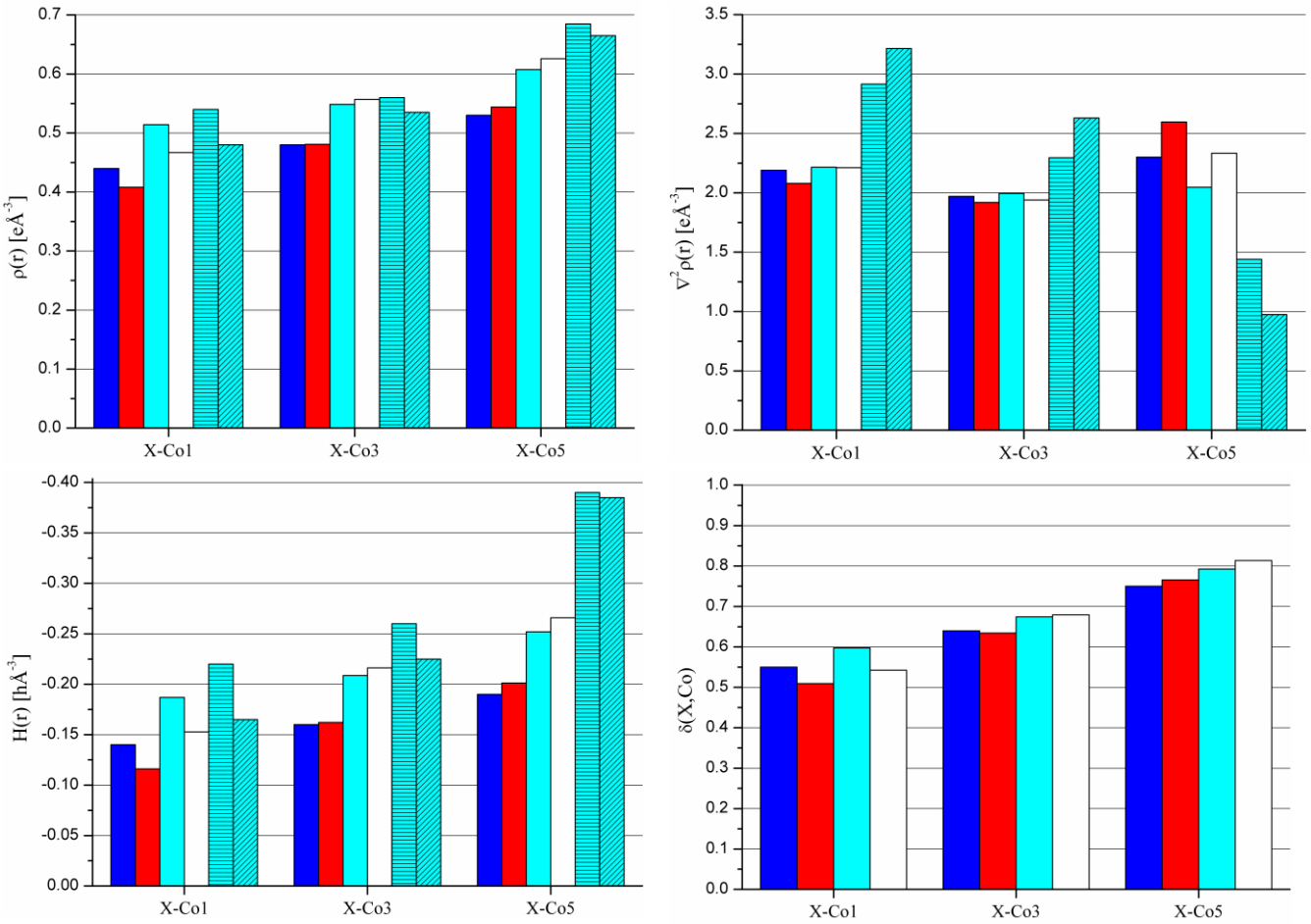

Figure 3.2.4. Results of the Theoretical and Experimental Topological Analysis. Theoretical calculations refer to the point group symmetry C_2, meaning that X-Co1 = X-Co2, X-Co3 = X-Co4, X-Co5 = X-Co6, Co1-Co3 = Co2-Co4. Theoretical values of $\int_{A\square B}\rho(r)$ are reported in Table 3.2.2. Experimental values of $Q(Co_n)$ and $\delta(Co_n,Co_m)$ are reported in Table 3.2.3. **1a**= Blue; **1b**=Red; **2a**=Cyan; **2b**= White. α-**2a_1,2** = Cyan -weft (**1**= horizontal strings, **2**= diagonal strings).

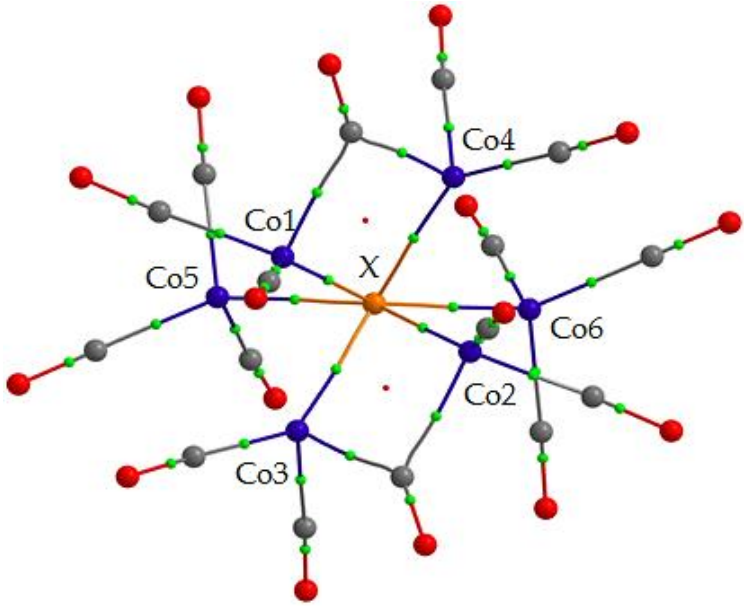

Figure 3.2.5. Molecular graph of the system $[Co_6X(CO)_{16}]^-$ (for type-**a** conformer**)**.

Table 3.2.2. Results of the Theoretical and Experimental Topological Analysis [a,b,c]

	BCP	$\rho(\mathbf{r})$ [e Å^{-3}]	$\nabla^2\rho(\mathbf{r})$ [e Å^{-5}]	$G(\mathbf{r})$ [he^{-1}]	$H(\mathbf{r})$ [hÅ^{-3}]	ε	r_1 [Å]	r_2 [Å]
1a	As-Co1	0.44	2.19	0.29	-0.14	0.17	1.244	1.149
	As-Co3	0.48	1.97	0.30	-0.16	0.02	1.238	1.135
	As-Co5	0.53	2.30	0.35	-0.19	0.08	1.211	1.103
	Q(As) =	-0.24						
1b	As-Co1	0.41	2.07	0.27	-0.12	0.36	1.284	1.163
	As-Co3	0.50	1.84	0.31	-0.18	0.19	1.238	1.130
	AsX-Co5	0.56	2.64	0.40	-0.22	0.08	1.203	1.092
	Co1-Co3	0.29	1.00	0.14	-0.07	1.47	1.307	1.295
	Q(As) =	-0.22						
2a	P-Co1	0.51	2.22	0.34	-0.19	0.16	1.164	1.118
	P-Co3	0.55	1.99	0.35	-0.21	0.01	1.167	1.105
	P-Co5	0.61	2.05	0.40	-0.25	0.07	1.140	1.079
	Q(P) =	-0.37						
2b	PCo1	0.47	2.21	0.31	-0.15	0.26	1.213	1.132
	P-Co3	0.56	1.94	0.35	-0.22	0.16	1.165	1.098
	P-Co5	0.63	2.33	0.43	-0.27	0.07	1.133	1.069
	Q(P) =	-0.35						
2a_1	P-Co1	0.54	2.91	0.42	-0.22	0.50	1.1611	1.084
	P-Co2	0.54	2.92	0.42	-0.22	0.43	1.1709	1.0815
	P-Co3	0.53	1.97	0.38	-0.24	0.30	1.2024	1.0623
	P-Co4	0.59	2.62	0.46	-0.28	0.13	1.1903	1.0971
	P-Co5	0.68	1.10	0.47	-0.39	0.15	1.1324	1.0297
	P-Co6	0.69	1.78	0.52	-0.39	0.22	1.1246	1.0717
	Q(P) =	-0.52						
2a_2	P-Co1	0.52	3.05	0.41	-0.20	0.59	1.185	1.081
	P-Co2	0.44	3.38	0.36	-0.13	0.30	1.187	1.092
	P-Co3	0.52	3.01	0.41	-0.20	0.10	1.186	1.082
	P-Co4	0.55	2.25	0.41	-0.25	0.14	1.210	1.073
	P-Co5	0.66	0.56	0.43	-0.39	0.27	1.161	0.988
	P-Co6	0.67	1.39	0.48	-0.38	0.09	1.159	1.033
	Q(P) =	-0.45						

[a] In theoretical calculation it was considered the point group symmetry C2, meaning that values in cp X-Co1 = X -Co2, X -Co3 = X -Co4, X -Co5 = X -Co6, Co1-Co3 = Co2-Co4. [b] Theoretical values of $\delta(X,Y)$ and $\int_{A\square B}\rho(\mathbf{r})$ are reported in Table S3.1. [c]

Table 3.2.3. Charges and delocalization indexes for not bonded Cobalt atoms

	Q(Co1) Q(Co2)	Q(Co3) Q(Co4)	Q(Co5) Q(Co6)	δ(Co1,Co2)	δ(Co1,Co3) δ(Co2,Co4)	δ(Co1,Co4) δ(Co2,Co3)	δ(Co1,Co5) δ(Co2,Co6)	δ(Co4,Co6) δ(Co3,Co5)
1a	0.43	0.40	0.42	0.22	0.37	0.23	0.33	0.24
1b	0.43	0.42	0.37	0.04	0.49	0.25	0.33	0.32
2a	0.45	0.42	0.43	0.20	0.35	0.23	0.34	0.27
2b	0.44	0.44	0.39	0.04	0.48	0.25	0.34	0.33
2a_1	0.45	0.51	0.38					
	0.49	0.46	0.46					
2a_2	0.66	0.57	0.51					
	0.74	0.57	0.57					

From the calculated and experimental molecular graphs (Figure 3.2.4, Table 3.2.2), Co-X interactions are in general quite strong, because they feature a relatively large amount of electron density at the bond critical points, significantly negative values of the energy density, low values of the kinetic energy density and large electron delocalization indices. A *caveat* is necessary, though, because the valence shell electrons of the metals are shared among all 6 Co atoms, which implies only a much smaller amount of electron pair delocalization per each Co-Co interaction. The main differences between X= P and X = As are the larger negative charge of P and the larger delocalization of the electrons in Co-P bonds. The theoretical charges are in agreement with the experimental values for **2a**, in both samples we measured (see Table 3.2.2, 3.2.3). On the other hand, it seems that the type of isomer does not affect so significantly the charge of the main group atom, despite the rather different set of Co-X bonds.

Given the absence of direct Co-Co bond paths (apart from **1b**), only delocalization indices can shed light on these interactions (Table 3.2.3). The electron sharing between Co atoms is in general slightly weaker than with the semi-interstitial atoms (Figure 3.2.4), in keeping with general trends of bridged metal-metal interactions [43]. In addition, Co1-Co4 (equivalent to Co2-Co3), which is also supported by a carbonyl bridge, is even weaker with an electron sharing down to less than 0.3 pairs.

Given the rather distorted nature of the Co cages in both kinds of isomers, it is very important to characterize the hybridization state of the interstitial atoms. From electron density distribution, this can be achieved through the analysis of the Laplacian distribution within the atomic basin. In fact, $L(\mathbf{r}) = -\nabla^2\rho(\mathbf{r})$, has been widely used to characterize electron pair distribution and therefore atomic hybridization and interatomic interactions, because the Laplacian enhances the features of

the charge distribution and the electron pair localization. *Valence shell charge concentrations* (VSCC), *i.e.* (3,+3) critical points of L(**r**), for the semi-interstitial atoms have been searched and located both theoretically and experimentally, Figure 3.2.6. All values are reported in Table 3.2.4.

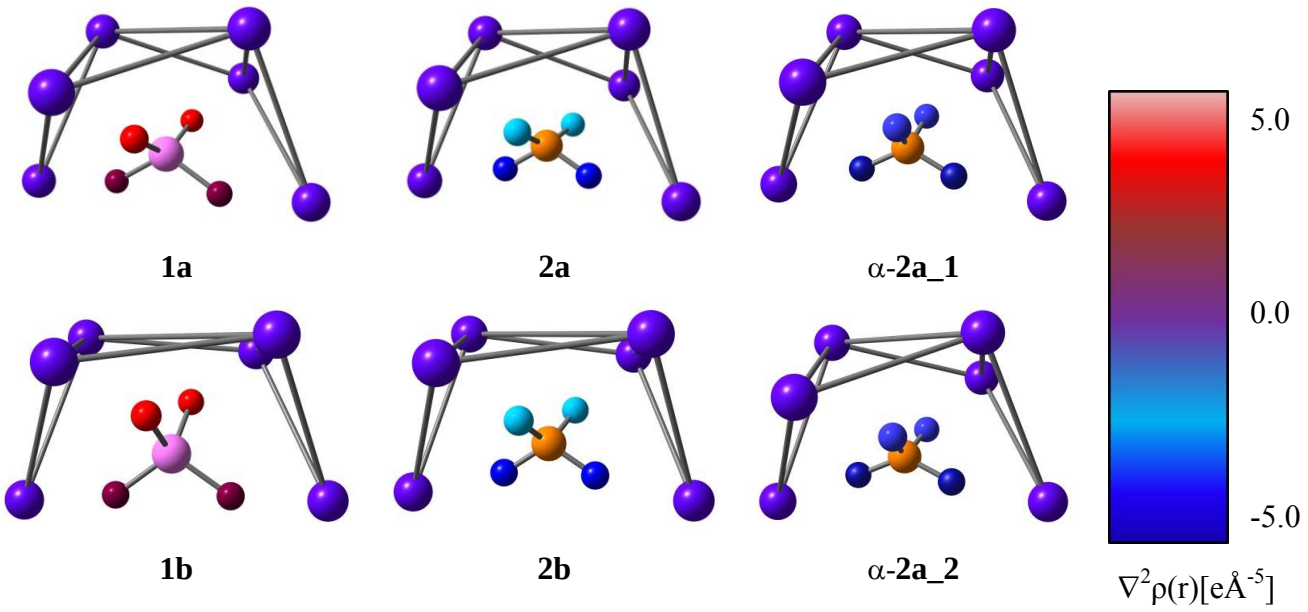

Figure 3.2.6. Experimental and Theoretical Atomic Graph of P and As atom. Color coding follows the $\nabla^2\rho(\mathbf{r})$ [e Å^{-5}] scale on the right.

Table 3.2.4. Theoretical and Experimental (3,+3) cps values of L(r) in the Atomic Graph of semi-interstitial atoms[a]

		CP type	distance r [Å]	$\nabla^2\rho(r)$ [e Å^{-5}]
1a	1,2	(3,+3)	1.04	0.159
	3,4	(3,+3)	1.07	0.438
1b	1,2	(3,+3)	1.03	0.153
	3,4	(3,+3)	1.08	0.327
2a	1,2	(3,+3)	0.80	-4.767
	3,4	(3,+3)	0.81	-3.59
2b	1,2	(3,+3)	0.79	-5.029
	3,4	(3,+3)	0.81	-3.694

		CP type	distance r [Å]	$\nabla^2\rho(r)$ [eÅ^{-5}]
2a_1	1	(3,+3)	0.817	-4.885
	2	(3,+3)	0.815	-5.658
	3	(3,+3)	0.819	-4.467
	4	(3,+3)	0.818	-4.929
2a_2	1	(3,+3)	0.808	-4.715
	2	(3,+3)	0.805	-6.497
	3	(3,+3)	0.807	-5.097
	4	(3,+3)	0.808	-4.620

[a] In theoretical calculation it was considered the point group symmetry C2, meaning that values of cp1 = cp2 (Co5, Co6), cp3 = cp4 (Co3, Co4).

The distribution and the number of VSCCs reflects the stereochemistry of an atom, better than its connectivity. In fact, the bonds to a given atom may be elusive or differ in nature and therefore not usable to ascertain the hybridization state. Here, this is very important for the semi-interstitial atoms. From the theoretical calculations, P features four VSCC's in the third (valence) shell suggesting a distorted tetrahedral coordination. Similarly, in the fourth shell, As has four maxima at $L(\mathbf{r}) < 0$. Strictly speaking, they are not charge concentrations. However, one should take into account that, even in the isolated atom, As has a vanishing maximum of the spherically averaged Laplacian in the fourth shell, which occurs at $L(\mathbf{r}) < 0$[3]. Thus the local maxima in the fourth shell, albeit with $L(\mathbf{r}) < 0$, can be taken as representative of the valence orbital state of As, as they are for P. Both VSCC's distributions (and especially for X = P) clearly differ from what expected with the geometrical hexa-coordination of the semi-interstitial atoms. In **2a** and **2b**, the maxima are directed towards Co3, Co4, Co5 and Co6, with uneven values of $\rho(\mathbf{r})$ and $\nabla^2\rho(\mathbf{r})$ (Table 3.2.4), bringing a higher charge concentration to Co5 and Co6, which increases going from **2a** to **2b**. Analogously, the four maxima in **1a** and **1b** point towards Co3, Co4, Co5 and Co6, with a trend in the Laplacian values that reflects the behavior of $\nabla^2\rho(\mathbf{r})$ in the phosphide isomers (*i.e.* more negative towards Co5 and Co6). Thus, in keeping with distances and electron density sharing, the interaction of the interstitial atom is stronger with the two Co atoms for which the hypothetical edge of an octahedron

is clearly broken (Co5-Co6 is in excess of 4 Å in all isomers). Instead, the interactions with the two atoms involved in the short or long Co-Co bond (*i.e.* Co1, Co2) are anyway weak in both isomers.

So weak, that the atomic graph of P does not show any charge localization in that direction. The experimental atomic graphs are in good agreement with the theoretical values. In both cases, there are four charge concentrations. Together with the distances of the critical points from the P nucleus and $\nabla^2\rho(r)$ values (Table 3.2.4), this confirm the computational prediction. Therefore, when X = P, one can speak of a distorted tetrahedral stereochemistry for the interstitial atom, better than a distorted octahedral one. Although weaker, and based on theoretical calculations only, the same conclusion holds for the As clusters.

3.2.3.3 Energy breakdown

While the charge density partition inform on the hybridization states, and could take advantage of experimental confirmation, even more insight could be obtained from an energy decomposition.

Therefore, for this analysis we rely only on theoretical values and we present here two kinds of analysis, the interacting quantum atom (where the charge density is used to define the atomic basins) and the energy decomposition analysis (where atoms are pre-defined by their atomic basis sets).

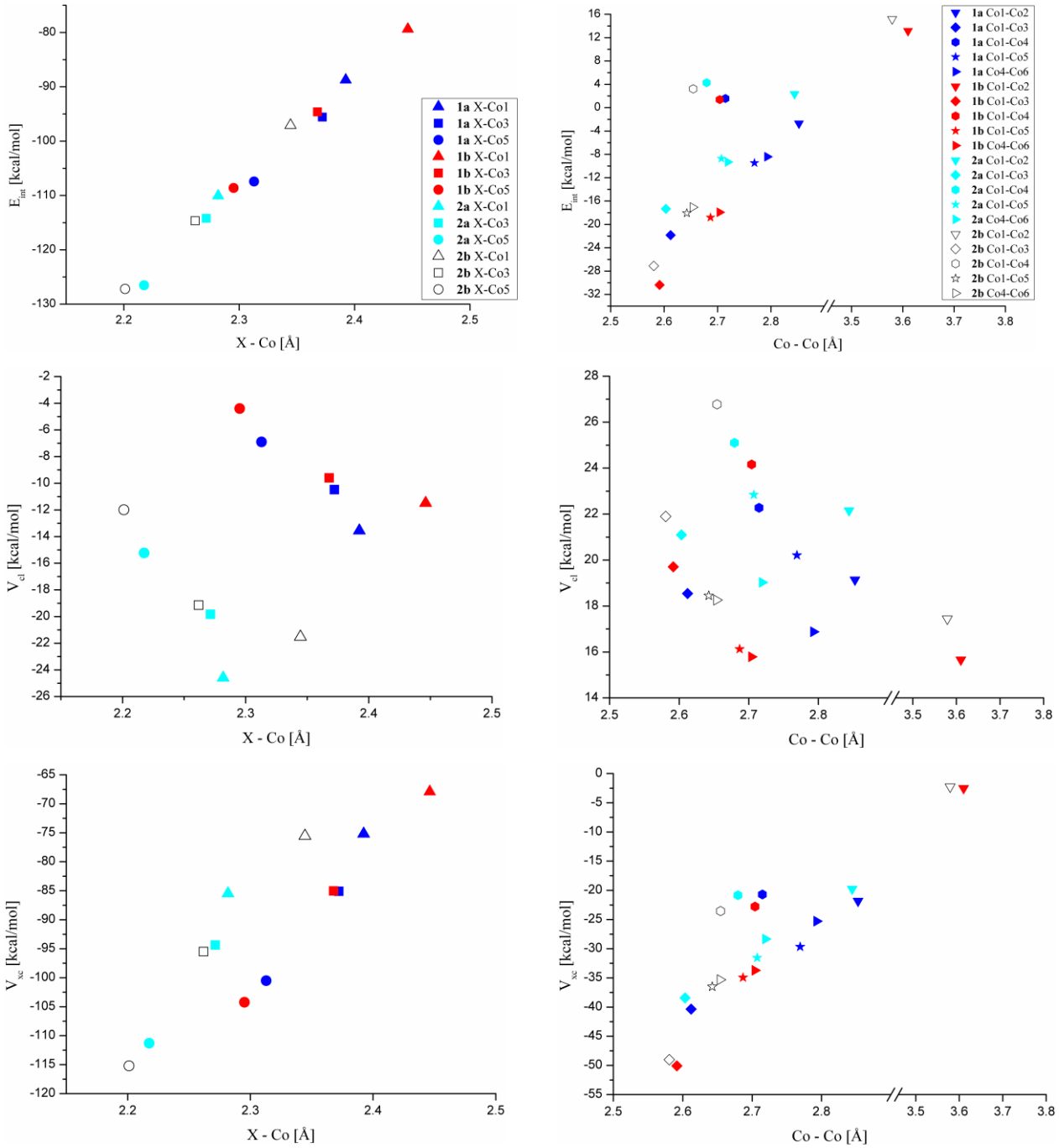

Figure 3.2.7. Interaction Energy E_{int}^{AB}, classic term V_{cl}^{AB} and exchange-correlations term V_{xc}^{AB} from IQA decomposition; **1a**= Blue; **1b**=Red; **2a**=Cyan; **2b**= White; The terms for Co1-Co2 of **1b** and **2b** have been omitted because the long distance produced too weak interactions.

3.2.3.3.1 Interacting Quantum Atoms

The IQA energy terms are reported in Figure 3.2.7 and Table 3.2.5. The interaction energies between semi-interstitial atoms and Co atoms are always larger than the Co-Co ones. Of course, this is favored by the cooperation between the electron-sharing (exchange) and the columbic term. For Co-X, both are favorable, at variance from Co-Co, that are of course associated with strongly destabilizing columbic terms. Nevertheless, the exchange is quite large and clearly dominating, confirming that the X-Co strength decreases along the series X-Co5 > X-Co3 > X-Co1. The trend is more pronounced for the **b** isomers. The P atom gives rise not only to a larger orbital overlap with the metal atoms (Table 3.2.5; see in particular the high values of V_{xc}^{AB}), but also to a stronger electrostatic interaction, V_{cl}^{AB}, caused by its more negative charge. Overall, the interaction of P with the cage is stronger than that of As, in terms of both covalency and ionicity. The higher ratio between covalency and ionicity for X=As is simply due to the lower negative charge of As and it should not be misinterpreted. Indeed, an interaction like Co-P can be simultaneously more covalent and more electrostatic[65] (Table 3.2.5). Ongoing from **a** to **b,** V_{xc}^{AB} becomes more negative for X-Co5, whereas X-Co3 remains almost constant and X-Co1 becomes more positive. The classical potential energy V_{cl}^{AB} doesn't follow the same trend, in fact it always increases from **a** to **b**, particularly for X-Co1 and X-Co5.

The energy decomposition of the Co-Co bonds show that they are dominated by the exchange-correlation interaction, as expected for metal-metal bonds[66]. The strongest interaction is Co1-Co3, though highly dependent on both the cage conformation and the semi-interstitial atom. The interactions of Co1 with Co4 and Co5 depend mainly on the conformation of the cluster and Co1-Co4, which is bridged by a carbonyl, is poorly stabilizing or even destabilizing. Co1-Co2 has a considerable elongation on going from isomers **a** to **b**, producing a large difference in the interaction energy. Even if V_{xc}^{AB} has almost the same value for the two semi-interstitial atoms, V_{cl}^{AB} is much more destabilizing in the phosphide clusters. An overall stabilizing energy for this interaction (Table 3.2.5) was found only for **1a**. As expected, Co4-Co6 is similar to Co1-Co5 but weaker, except for **2a**.

Table 3.2.5. Theoretical IQA values X-Co and Co-Co [kcal/mol]

		E_{int}	V_{cl}	V_{xc}	% ionicity	% covalency
1a	As-Co1	-88.7	-13.6	-75.2	15.3	84.7
	As-Co3	-95.6	-10.5	-85.1	11.0	89.0
	As-Co5	-107.4	-6.9	-100.5	6.4	93.6
	Co1-Co2	-2.7	19.1	-21.8		
	Co1-Co3	-21.8	18.5	-40.3		
	Co1-Co4	1.6	22.3	-20.7		
	Co1-Co5	-9.5	20.2	-29.7		
	Co4-Co6	-8.4	16.9	-25.3		
1b	As-Co1	-79.4	-11.5	-67.9	14.5	85.5
	As-Co3	-94.6	-9.6	-85.0	10.1	89.9
	As-Co5	-108.6	-4.4	-104.2	4.0	96.0
	Co1-Co2	13.1	15.7	-2.5		
	Co1-Co3	-30.4	19.7	-50.1		
	Co1-Co4	1.4	24.2	-22.8		
	Co1-Co5	-18.8	16.1	-35.0		
	Co4-Co6	-17.9	15.8	-33.7		
2a	P-Co1	-110.1	-24.6	-85.5	22.3	77.7
	P-Co3	-114.2	-19.8	-94.4	17.4	82.6
	P-Co5	-126.5	-15.2	-111.3	12.0	88.0
	Co1-Co2	2.3	22.2	-19.8		
	Co1-Co3	-17.3	21.1	-38.4		
	Co1-Co4	4.3	25.1	-20.8		
	Co1-Co5	-8.7	22.8	-31.6		
	Co4-Co6	-9.3	19.0	-28.3		
2b	P-Co1	-97.1	-21.5	-75.6	22.2	77.8
	P-Co3	-114.6	-19.1	-95.5	16.7	83.3
	P-Co5	-127.2	-12.0	-115.2	9.4	90.6
	Co1-Co2	15.2	17.4	-2.3		
	Co1-Co3	-27.1	21.9	-49.0		
	Co1-Co4	3.2	26.8	-23.6		
	Co1-Co5	-18.1	18.4	-36.5		
	Co4-Co6	-17.1	18.3	-35.3		

The most evident change due to the isomerization is the elongation (or shortening) of Co1-Co2. However, less evident are the changes of the other interactions. We can pinpoint the following correlation: the longer is Co1-Co2, the weaker becomes X-Co1 (=X-Co2), whereas, as reported in Figure 3.2.7, E_{int}^{AB} of Co1-Co3 (Co2-Co4) increases in modulus. The above discussed trends are confirmed also by the Wiberg indices, see Table 3.2.6.

Table 3.2.6. Wiberg Bond Index of X-Co and Co-Co

	X-Co1	X-Co3	X-Co5	Total WBI (X)	Co1-Co2	Co1-Co3	Co1-Co4	Co1-Co5	Co4-Co6
1a	0.456	0.524	0.671	3.998	0.190	0.309	0.234	0.320	0.202
1b	0.408	0.530	0.712	3.961	0.063	0.441	0.241	0.294	0.273
2a	0.484	0.537	0.669	4.075	0.173	0.298	0.224	0.329	0.222
2b	0.428	0.553	0.708	4.047	0.053	0.437	0.232	0.303	0.282

The total WBI values for the semi-interstitial atoms are almost constant in all isomers but the individual interactions have different strength. The WBI reflects also what it was obtained in the atomic graph analysis: the values of X-Co5 are the largest and very similar in all the isomers. **2b** has the highest value of X-Co3, which is quite close X-Co5, and a much lower value of X-Co1, in agreement with the previously discussed tetracoordination. Bond index for Co1-Co3 features the very same value for both **1b** and **2b**, meaning that also for the phosphide isomer the presence of a metal-metal interaction cannot be not excluded. All the other Co-Co indexes follow the trend outlined by the IQA analysis, in particular in the low sensitive values for Co4 and Co5, but also in the behavior with Co2.

3.2.3.3.2 Energy Decomposition and Fragment Interaction Analysis

The traditional EDA implies the definition of two closed- or open-shell fragments, whose interaction is evaluated in terms of the classical Morokuma's scheme[67]. The identification of the fragments and the assignment of their electronic configuration are essential and may bias the interpretation.[68,69] The atomic charges, the stereochemistries and the stability of known metal clusters, imply that the fragments to consider are $^{1}X^{-1}$ and $[Co_6(CO)_{16}]^0$. ΔE_{prep} implies a) the excitation of the semi-interstitial atom (X^{-1}) from its ground state triplet to the singlet excited state and b) the deformation of the $Co_6(CO)_{16}$[70] cluster geometry to produce the distorted geometries of **a** and **b** (See Table 3.2.7).

Table 3.2.7. Preparation Energies [kcal/mol] for the cluster $[Co_6X(CO)_{16}]^-$

	$^3X^{-1} \rightarrow {}^1X^{-1}$	$Co_6(CO)_{16} \rightarrow [Co_6(CO)_{16}]^0$(**a**)	$Co_6(CO)_{16} \rightarrow [Co_6(CO)_{16}]^0$(**b**)
ΔE_{prep}(P)	26.9	103.7	113.4
ΔE_{prep}(As)	24.3	111.9	116.7

The deformation necessary to reach conformation **a** is less energy demanding than for **b**. In the phosphide isomers, this difference is even larger because of the smaller (Pauli) repulsion occurring in **a** (see Figure 3.2.8). The ionic radius of As^{-1} is so large that the energy required to form either **a**- or **b**-shape metal cages differs by less than 5 kcal/mol.

In Table 3.2.8, we compare the "classical" partitions for EDA and IQA, reporting the terms from equation (1.28) and (2.6), respectively. For the fragment partition, and in particular for the reference fragments, the very same scheme used for the calculation of ΔE_{int} in EDA was used for IQA, *i.e.*, the semi-interstitial atom in the electronic state $^1X^{-1}$ as one fragment and the cage $[Co_6(CO)_{16}]^0$ presenting the same geometry in the final molecule as second fragment. Moreover, we carried out a so called "Energy Terms Partition", (see Chapter 2) which in the case of EDA it is automatically done during the bond energy decomposition by ADF; for IQA, we adopted the formalism presented in the introduction (equation (17)).

ΔE_{els} and ΔE_{orb}, both stabilizing, are larger for isomers **a**, particularly X = P. The ΔE_{Pauli} term addresses isomers phosphide isomers as less stable and conformer **a** as less stable than **b**.

According to Hopffgarten and Frenking[46], ΔE_{els} could be used to estimate the degree of electrostatic character of a bond (which not necessarily coincides with the ionicity), whereas ΔE_{orb} would represent the covalent character. The electrostatic term slightly overwhelms the orbitalic one (55%:45% for the arsenides, 53%:47% for the phosphides). For a deeper understanding of the X−cage bond, in Table 3.2.9 an analysis is reported of the main contribution to the orbital interaction provided by the valence orbitals of the semi-interstitial atom.

Table 3.2.8. EDA/IQA Classical and Energetic Components Partition [kcal/mol] of $^1X^{-1}$ + $[Co_6(CO)_{16}]^0$

	EDA					IQA			
	1a	**1b**	**2a**	**2b**		**1a**	**1b**	**2a**	**2b**
				Classical Partition					
ΔE_{pauli}	1313.2	1219.8	1415.5	1317.4	$\Delta E^{\mathcal{H}}_{def,self}$	329.0	245.6	311.0	336.4
ΔE_{els}	-882.3	-835.4	-915.2	-872	$\Delta E^{\mathcal{G},\mathcal{H}}_{int}$	-607.5	-531.6	-611.3	-647.5
ΔE_{steric}	430.8	384.4	500.2	445.4	$\Delta E^{\mathcal{G},\mathcal{H}}_{bind}$	-278.5	-285.9	-300.3	-311.1
ΔE_{orb}	-716.3	-676.5	-804.4	-761.1					
ΔE_{int}	-285.5	-292.2	-304.2	-315.7					
$\%\Delta E_{els}$	55.2	55.3	53.2	53.4					
$\%\Delta E_{orb}$	44.8	44.7	46.8	46.6					
				Energy Terms Partition					
Classic	-569.1	-566.4	-599.4	-593.4	Classic	-452.6	-476.7	-611.9	-622
Electrostatic	-882.3	-835.4	-915.2	-872					
Coulomb	313.2	269	315.9	278.6					
XC	-385.3	-355.1	-404.7	-373	XC	-331.5	-302.8	-334.4	-302.7
Kinetic	668.9	629.4	700	650.6	Kinetic	505.6	493.6	646.1	613.5
%Classic	59.6	61.5	59.7	61.4	%Classic	57.7	61.2	64.7	67.3
%XC	40.4	38.5	40.3	38.6	%XC	42.3	38.8	35.3	32.7

Table 3.2.9. ΔE_{MO} [kcal/mol] stabilization of $^1X^{-1}$ p-valence orbitals in the MO

I.R.[a]	**1a**	**1b**	**2a**	**2b**
B	-165.4 ($4p_x$: 28.0%; $5p_x$: 4.1%; 4s: 0.0%)[b]	-166.2 ($4p_x$: 29.0%; $5p_x$: 2.7%; 4s: 0.0%)[b]	-172.4 ($3p_x$: 23.2%; $4p_x$: 7.8%; 3s: 0.0%)[b]	-172.9 ($3p_x$: 25.8%; $4p_x$: 6.1%; 3s: 0.0%)[b]
A	-176.7 ($4p_z$: 29.1%; $5p_z$: 3.9%; 4s: 2.2%)[b]	-173.7 ($4p_z$: 27.0%; $5p_z$: 3.5%; 4s: 2.1%)[b]	-182.3 ($3p_z$: 23.2%; $4p_z$: 7.3%; 3s: 1.5%)[b]	-178.7 ($3p_z$: 21.7%; $4p_z$: 6.8%; 3s: 1.6%)[b]
B	-191.4 ($4p_y$: 25.7%; $5p_y$: 8.0%; 4s: 0.0%)[b]	-191.8 ($4p_y$: 25.5%; $5p_y$: 7.9%; 4s: 0.0%)[b]	-199.3 ($3p_y$: 15.4%; $4p_y$: 14.6%; 3s: 0.0%)[b]	-199.5 ($3p_y$: 15.0%; $4p_y$: 15.0%; 3s: 0.0%)[b]

[a] Irreducible Representation; [b] The p_y orbital points towards Co5 and Co6, p_z is coaxial with C2 axis; $E_{4p\ orbital}(^1As^{-1})$ = 30.3 kcal/mol, $E_{3p\ orbital}(^1P^{-1})$ = 30.7 kcal/mol.

$\Delta E^{\mathcal{H}}_{def,self}$ is positive and describes the energetic deformation of a fragment upon the molecular formation[71]. The stabilizing contribution $\Delta E^{\mathcal{G},\mathcal{H}}_{int}$, on the other hand, is indicative of the constructive interaction between the fragments $^1X^{-1}$ and $[Co_6(CO)_{16}]^0$. $\Delta E^{\mathcal{H}}_{def,self}$ follows the same trend of ΔE_{Pauli} and ΔE_{steric} for the isomers **1a** and **1b**, meanwhile for **2a** and **2b** it produces very similar values, slightly more destabilizing for the open isomer. The same behavior is seen again for $\Delta E^{\mathcal{G},\mathcal{H}}_{int}$ *i.e.*, **1a** is more stabilized than **1b**, and the opposite for the phosphides isomers. ΔE_{int} and $\Delta E^{\mathcal{G},\mathcal{H}}_{bind}$, on the other hand, are very well in agreement, with a difference of just few kcal/mol, this result tells us that both the partition methods and bonding analysis produce the same total bonding energy for interacting fragments. Moreover, now the trends are in perfect agreement, producing higher (more stabilizing) bonding energy for open isomers **b**, in favor of X=P. Energy terms partition produced interesting results. By isolating the Classic, Kinetic and XC term from both ΔE_{int} and $\Delta E^{\mathcal{G},\mathcal{H}}_{bind}$ it emerges that proportions and trends are the very same.

Quantitatively, EDA produces higher absolute values compared to IQA. However, the ratio between Classic and XC energies of the two decomposition methods are very similar. The Classic term clearly overwhelms the XC (ca. 60% *vs*. 40%), in particular for **b** isomers. In EDA, no difference appears on moving from As to P, whereas in IQA the Classic term is clearly larger, in percentage, for P isomers. This may strongly depend on the definition of the atomic charges, and the fact that in IQA they are not predetermined.

According to the above bonding analysis, we can confirm that, even if the individual X-Co interaction is mainly covalent, the energy that keeps together the metal-carbonyl cage with pnictogen semi-interstitial atoms (P,As) has a more electrostatic nature. In other words, the interaction between the carbonyls and the interstitial atoms plays an important role, although invisible in the charge density.

In Figure 3.2.8, we report the ΔE_{prep} and ΔE_{int} terms of the energy decomposition for the fragments $^1X^{-1}$ and $[Co_6(CO)_{16}]^0$ (see also Table 3.2.7 and 3.2.8) and the total bonding energy ΔE (see also Table 3.2.10. The trend followed by ΔE is the same of ΔE_{int}, confirming that the most stabilized species are the **b** isomers and that P has the strongest binding. Even if isomers **a** produce the most stabilizing contributions of ΔE_{els} and ΔE_{orb}, the higher destabilization of the Pauli term inverts this trend, and **b** results as the most stable conformation (in isolation).

For the phosphides the effect of the cage's conformation is much more relevant that for the arsenides (Figure 3.2.8), because of both the destabilizing (ΔE_{prep}) and stabilizing (ΔE_{int}) contribution. All these mechanisms are anyhow "hidden" in the final energy difference (ΔΔE), due

to mutual cancellation. ΔΔE results to be the very same for **1** and **2**, meaning that even if there is an energy difference between isomers of the same chemical nature (same semi-interstitial atom)[41], the preparation energy has the effect of cancelling this discrepancy. If this is correct, the hypothesis of the existence of **2b**, at least in solution, is reinforced, although its isolation may not be possible and so far, despite our repeated attempts, has always failed.

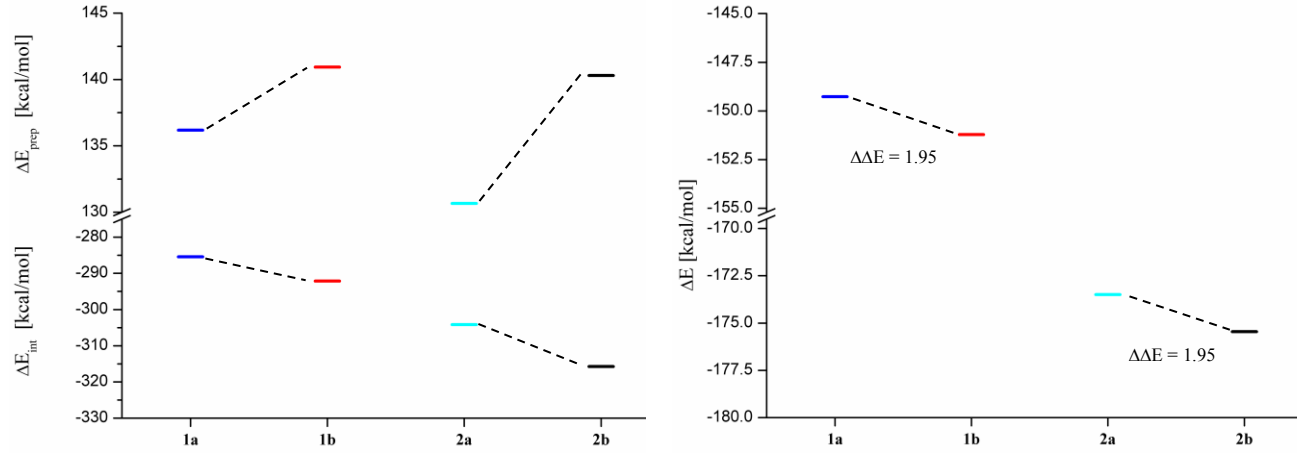

Figure 3.2.8. ΔE_{prep}, ΔE_{int} (left), the total bonding energy ΔE (right); **1a**= Blue; **1b**=Red; **2a**=Cyan; **2b**= Black. ΔΔE are the total bonding energy differences.

Table 3.2.10. Total Bonding Energies [kcal/mol] (1) and their difference (2)[a]

	1a	**1b**	**2a**	**2b**
ΔE	-149.27	-151.22	-173.50	-175.45

1

	(1a – 1b)	**(2a – 2b)**
ΔΔE	1.95	1.95

2

[a] Difference of the electronic energy obtained from the geometry optimization with ADF, with the level of theory B3LYP/TZ2P.

3.2.4 Conclusions

In this chapter, we have analyzed the chemical bonding in high nuclearity transition metal carbonyl clusters with semi-interstitial main group atoms, focusing on the species $[Co_6X(CO)_{16}]^-$.

The study involved both charge density and energy partitioning, adopted to characterize the ratios between covalent and electrostatic terms of the interactions, the hybridization and oxidation states of the main group atoms and the behavior of two semi-interstitial atoms of the same group (namely P and As). The stereochemistry of the clusters under investigation is quite peculiar, because of the two possible conformers that differ mainly in the distortion of the metal cages (and corresponding conformation of CO ligands). The charge density analysis revealed the larger atomic charge of the phosphide compared to the arsenide, anyway smaller than the formal oxidation state of -1. The stronger electrostatic interactions of the phosphide derivative does not hamper a larger covalency of the P-Co interactions, compared to the As-Co ones, which is addressed both by charge and energy partition methods. The hybridization of the semi-interstitial atom remains sp^3-like in the phosphide and in the arsenide. Co-Co interactions are globally quite weak, even if the electronic exchange and the energy stabilization in Co1-Co3 (= Co2-Co4) interactions is enough to produce a bond critical point of the theoretical electron density distribution of **1b**, the overall structure is supported mainly by the more robust X-Co bonds, which according to IQA partition have quite larger interaction energies and bond orders.

EDA and IQA agree in finding the interaction between the semi-interstitial atoms and the overall cages mainly electrostatic, although Co-X interactions, alone, are mainly shared interactions.

For one of the species, $[Co_6P(CO)_{16}]^-[PPh_4]^+$ α-**2a**, the accurate low temperature X-ray diffraction was measured on different crystal samples, in order to obtain an experimental charge density to be compared with the theoretical ones, calculated for all the four $[Co_6X(CO)_{16}]^-$ (X=As,P) isomers. This study is the first comprehensive analysis of chemical bonding in these species, merging the complementary viewpoints of energy and charge density partitioning in order to gain insight into the stereochemistry of these clusters. This enabled to pinpoint the role and the stereochemistry of the main group semi-interstitial atoms.

3.2.5 References

(1) N.N.Greenwood, A.Earnshaw, Chemistry of the Elements , (2nd Ed.) - Butterworth-Heinemann, Oxford, 1997. 19.

(2) Whitmire, K. H. *Main Group-Transition Metal Cluster Compounds of the Group 15 Elements*; Elsevier Masson SAS, 1998; Vol. 42.

(3) Macchi, P.; Proserpio, D. M.; Sironi, A. Experimental Electron Density in a Transition Metal Dimer : Metal–Metal and Metal–Ligand Bonds. *J. Am. Chem. Soc.* **1998**, *120* (51), 13429–13435.

(4) De Silva, R. M.; Mays, M. J.; Davies, J. E.; Raithby, P. R.; Rennie, M. A.; Shield, G. P. New Organoarsino-Bridged Cobalt Carbonyl Complexes Derived from Reactions of $[Co_2(CO)_8]$ or $[Co_2(\mu\text{-Alkyne})(CO)_6]$ with Cyclo-$(AsPh)_6$. *J. Chem. Soc. - Dalt. Trans.* **1998**, *2* (3), 439–446.

(5) Rheingold, A. L.; Sullivan, P. J. X-Ray Crystal and Molecular Structure of $[Co_8(\mu_6\text{-As})(\mu_4\text{-As})(\mu_4\text{-AsPh})_2\text{-}(CO)_{16}]_2$. *J. Chem. Soc., Chem. Commun.* **1983**, *8*, 39–40.

(6) Vidal, J. L. $[Rh_{10}As(CO)_{22}]^{3-}$. Example of Encapsulation of Arsenic by Transition-Metal Carbonyl Clusters As Illustrated by the Structural Study of the Benzyltriethylammonium Salt. *Inorg. Chem* **1981**, *20* (1), 243–249.

(7) Foust, A. S.; Foster, M. S.; Dahl, L. F. Organometallic Pnicogen Complexes. III. Preparation and Structural Characterization of the Triarsenic-Cobalt Atom Cluster System $As_3Co(CO)_3$. The First Known X_3-Transition Metal Analog of Group Va Tetrahedral X_4 Molecules. *J. Am. Chem. Soc.* **1969**, *91* (20), 5631–5633.

(8) Foust, A. S.; Foster, M. S.; Dahl, L. F. Organometallic Pnicogen Complexes. IV. Synthesis, Structure, and Bonding of New Organometallic Arsenic-Metal Atom Clusters Containing a Metal-Bridged Multiply Bonded As_2 Ligand: $Co_2(CO)_6As_2$ and $Co_2\{(CO)_5P(C_6H5)_3\}As_2$. *J. Am. Chem. Soc.* **1969**, *91* (20), 5633–5635.

(9) Arnold, L. J.; Mackay, K. M.; Nicholson, B. K. Reaction of Arsane with Cobalt or Iron Carbonyls, and the X-Ray Crystal Structures of $[Fe_2(CO)_8(\mu_4\text{-As})]_2[Fe_2(CO)_6]$ and $[\mu_4\text{-}AsCo_3(CO)_8]_3$. *J. Organomet. Chem.* **1990**, *387* (2), 197–207.

(10) Hsuan Wei, C. Structural Analyses of Tetracobalt Dodecacarbonyl and Tetrarhodium Dodecacarbonyl. Crystallographic Treatments of a Disordered Structure and a Twinned Composite. *Inorg. Chem.* **1969**, *8* (11), 2384–2397.

(11) Farrugia, L. J.; Braga, D.; Grepioni, F. A Structural Redetermination of $Co_4(CO)_{12}$: Evidence

for Dynamic Disorder and the Pathway of Metal Atom Migration in the Crystalline Phase1. *J. Organomet. Chem.* **1999**, *573* (1–2), 60–66.

(12) Hoffmann, R. Building Bridges Between Inorganic and Organic Chemistry. *Angew. Chem. Int. Ed. Engl.* **1982**, *21*, 711–724.

(13) Schipper, D. E.; Young, B. E.; Whitmire, K. H. Transformations in Transition-Metal Carbonyls Containing Arsenic: Exploring the Chemistry of $[Et_4N]_2[HAs\{Fe(CO)_4\}_3]$ in the Search for Single-Source Precursors for Advanced Metal Pnictide Materials. *Organometallics* **2016**, *35* (4), 471–483.

(14) Desai, P.; Ashokaan, N.; Masud, J.; Pariti, A.; Nath, M. Synthesis and Magnetic Properties of Superparamagnetic CoAs Nanostructures. *Mater. Res. Express* **2015**, *2* (3), 036102.

(15) Klingan, F. R.; Miehr, A.; Fischer, R. A.; Herrmann, W. A. Thin Films of CoAs from Low-Temperature Metalorganic Chemical Vapor Deposition of a Novel Single-Source Precursor Compound. *Appl. Phys. Lett.* **1995**, *67* (1995), 822.

(16) Rabis, A.; Rodriguez, P.; Schmidt, T. J. Electrocatalysis for Polymer Electrolyte Fuel Cells : Recent Achievements and Future Challenges. *ACS Catal.* **2012**, *2*, 864–890.

(17) Vante, N. A.; Jaegermann, W.; Tributsch, H.; Hönle, W.; Yvon, K. Electrocatalysis of Oxygen Reduction by Chalcogenides Containing Mixed Transition Metal Clusters. *J. Am. Chem. Soc.* **1987**, *109* (11), 3251–3257.

(18) Wang, J.; Cui, W.; Liu, Q.; Xing, Z.; Asiri, A. M.; Sun, X. Recent Progress in Cobalt-Based Heterogeneous Catalysts for Electrochemical Water Splitting. *Adv. Mater.* **2016**, *28* (2), 215–230.

(19) Wang, P.; Song, F.; Amal, R.; Ng, Y. H.; Hu, X. Efficient Water Splitting Catalyzed by Cobalt Phosphide-Based Nanoneedle Arrays Supported on Carbon Cloth. *ChemSusChem* **2016**, *9* (5), 472–477.

(20) Jiang, N.; You, B.; Sheng, M.; Sun, Y. Electrodeposited Cobalt-Phosphorous-Derived Films as Competent Bifunctional Catalysts for Overall Water Splitting. *Angew. Chemie - Int. Ed.* **2015**, *54* (21), 6251–6254.

(21) Popczun, E. J.; Read, C. G.; Roske, C. W.; Lewis, N. S.; Schaak, R. E. Highly Active Electrocatalysis of the Hydrogen Evolution Reaction by Cobalt Phosphide Nanoparticles. *Angew. Chemie - Int. Ed.* **2014**, *53* (21), 5427–5430.

(22) Chini, Paolo; Martinengo, S.; Ciani, Gianfranco; Sironi Angelo; Longhetti, L.; Heaton, B. T. Synthesis and X-Ray Crystal Structure of the Anion $[Co_6(CO)_{14}(\mu\text{-}CO)_2P]^-$; an Example of a 'Semi-Interstitial Phosphide.' *J. Chem. Soc., Chem. Comm.* **1979**, No. 4, 188–189.

(23) Shriver, D. F.; Drezdzon, M. A. The Manipulation of Air-Sensitive Compounds , 2nd Ed. (1986) Wiley New York.

(24) North, A. C. T.; Phillips, D. C.; Mathews, F. S. A Semi-empirical Method of Absorption Correction. *Acta Crystallogr. Sect. A* **1968**, *24* (3), 351–359.

(25) Sheldrick, G. M. Crystal Structure Refinement with SHELXL. *Acta Crystallogr. Sect. C Struct. Chem.* **2015**, *71* (Md), 3–8.

(26) Frisch, M. J.; Trucks, G. W.; Schlegel, H. B.; Scuseria, G. E.; Robb, M. A.; Cheeseman, J. R.; Scalmani, G.; Barone, V.; Mennucci, B.; Petersson, G. A.; *et al.* Gaussian09 Revision B.010. Gaussian, Inc.: Wallingford CT 2010.

(27) Zhao, Y.; Truhlar, D. G. The M06 Suite of Density Functionals for Main Group Thermochemistry, Thermochemical Kinetics, Noncovalent Interactions, Excited States, and Transition Elements: Two New Functionals and Systematic Testing of Four M06-Class Functionals and 12 Other Function. *Theor. Chem. Acc.* **2008**, *120*, 215–241.

(28) Tomasi, J.; Mennucci, B.; Cammi, R. Quantum Mechanical Continuum Solvation Models. *Chem. Rev.* **2005**, *105* (8), 2999–3093.

(29) Ciani, G.; Sironi, A.; Martinengo, S.; Garlaschelli, L.; Della Pergola, R.; Zanello, P.; Laschi, F.; Masciocchi, N. Synthesis and X-Ray Characterization of the Phosphido−Carbonyl Cluster Anions $[Co_9(\mu_8\text{-}P)(CO)_{21}]^{2-}$ and $[Co_{10}(\mu_8\text{-}P)(CO)_{22}]^{3-}$. *Inorg. Chem.* **2001**, *40* (16), 3905–3911.

(30) Albright, T. A.; Yee, K. A.; Saillard, J. Y.; Kahlal, S.; Halet, J. F.; Leigh, J. S.; Whitmire, K. H. Capping Considerations in Main-Group/Transition-Metal Clusters: Synthetic, Structural, and Theoretical Discussions of $[E_2Co_4(CO)_{10}(\mu\text{-}CO)]^{-/2-}$ (E = Sb, Bi). *Inorg. Chem.* **1991**, *30* (6), 1179–1190.

(31) Martinengo, S.; Ciani, G. Bismuth-Cobalt Heteronuclear Carbonyl Cluster Compounds . Synthesis and X-Ray And. *J. Chem. Soc., Chem. Comm.* **1987**, No. 20, 1589–1591.

(32) Heaton, B. T.; Strona, L.; Della Pergola, R.; Vidal, J. L.; Schoening, R. C. Multinuclear Variable-Temperature Nuclear Magnetic Resonance Study of Rhodium Carbonyl Clusters Containing Encapsulated Heteroatoms: Ligand and Metal Polyhedral Rearrangements. *J. Chem. Soc. Dalt. Trans.* **1983**, No. 9, 1941–1947.

(33) Peng, C.; Ayala, P. Y.; Schlegel, H. B.; Frisch, M. J. Using Redundant Internal Coordinates to Optimize Equilibrium Geometries and Transition States. *J. Comput. Chem.* **1996**, *17* (1), 49–56.

(34) Ding, H.; Lu, Y.; Xie, Y.; Liu, H.; Schaefer, H. F. The Energy Difference between the

Triply-Bridged and All-Terminal Structures of $Co_4(CO)_{12}$, $Rh_4(CO)_{12}$, and $Ir_4(CO)_{12}$: A Difficult Test for Conventional Density Functional Methods. *J. Chem. Theory Comput.* **2015**, *11* (3), 940–949.

(35) Chini, P. A New Cluster Carbonylcobaltate. *Chem. Commun.* **1967**, No. 1, 29.

(36) Braye, E.; Dahl, L.; Hubel, W.; Wampler, D. L. The Preparation, Properties and Structure of the Iron Carbonyl Carbide $Fe_5(CO)_{15}C$. *J. Am. Chem. Soc.* **1962**, *84* (24), 4633–4638.

(37) Vidal, J. L.; Walker, W. E.; Pruett, R. L.; Schoening, R. C. $[Rh_9P(CO)_{21}]^{2-}$. Example of Encapsulation of Phosphorus by Transition-Metal-Carbonyl Clusters. *Inorg. Chem.* **1979**, *18* (1), 129–136.

(38) Vidal, J. L. ; Walker, W. E., Schoening, E. C. $[Rh_{10}P(CO)_{22}]^{3-}$. A Transition-Metal Carbonyl Cluster with a Metal Polyhedron Based on the Bicapped Square Antiprism As Illustrated by the Structural Study of the Benzyltriethylammonium Salt. **1981**, *7* (3), 238–242.

(39) Hong, C. S.; Berben, L. A.; Long, J. R. Synthesis and Characterization of a Decacobalt Carbonyl Cluster with Two Semi-Interstitial Phosphorus Atoms. *Dalt. Trans.* **2003**, *505* (11), 2119–2120.

(40) Dreher, C.; Zabel, M.; Bodensteiner, M.; Scheer, M. $[(CO)_4W(PH_3)_2]$ as Source of Semi-Interstitial Phosphorus Ligands in Cobalt Carbonyl Clusters. *Organometallics* **2010**, *29* (21), 5187–5191.

(41) Della Pergola, R.; Sironi, A.; Colombo, V.; Garlaschelli, L.; Racioppi, S.; Sironi, A.; Macchi, P. Periodical Trends in $[Co_6E(CO)_{16}]^-$ Clusters: Structural, Synthetic and Energy Changes Produced by Substitution of P with As. *J. Organomet. Chem.* **2017**, *849–850*, 130–136.

(42) Adams, R. D.; Chen, M.; Elpitiya, G.; Potter, M. E.; Raja, R. Iridium−Bismuth Cluster Complexes Yield Bimetallic Nano-Catalysts for the Direct Oxidation of 3-Picoline to Niacin. *ACS Catal.* **2013**, *3*, 3106–3110.

(43) Macchi, P.; Sironi, A. Chemical Bonding in Transition Metal Carbonyl Clusters: Complementary Analysis of Theoretical and Experimental Electron Densities. *Coordination Chemistry Reviews*. 2003, pp 383–412.

(44) Frenking, G.; Fröhlich, N. The Nature of the Bonding in Transition-Metal Compounds. *Chem. Rev.* **2000**, *100* (2), 717–774.

(45) Pyykkö, P.; Runeberg, N. Icosahedral WAu_{12}: A Predicted Closed-Shell Species, Stabilized by Aurophilic Attraction and Relativity and in Accord with the 18-Electron Rule. *Angew. Chemie - Int. Ed.* **2002**, *41* (12), 2174–2176.

(46) Von Hopffgarten, M.; Frenking, G. Building a Bridge between Coordination Compounds and

Clusters: Bonding Analysis of the Icosahedral Molecules [$M(ER)_{12}$] (M = Cr, Mo, W; E = Zn, Cd, Hg). *J. Phys. Chem. A* **2011**, *115* (45), 12758–12768.

(47) Bader, R. F. W. Atoms in Molecules. *Acc. Chem. Res.* **1995**, *18* (1), 9–15.

(48) Kitaura, K.; Morokuma, K. A New Energy Decomposition Scheme for Molecular Interactions within the Hartree-Fock Approximation. *Int. J. Quantum Chem.* **1976**, *10* (2), 325–340.

(49) Blanco, M. A.; Pendás, A. M.; Francisco, E. Interacting Quantum Atoms: A Correlated Energy Decomposition Scheme Based on the Quantum Theory of Atoms in Molecules. *J. Chem. Theory Comput.* **2005**, *1* (6), 1096–1109.

(50) Wiberg, K. B. Application of the Pople-Santry-Segal CNDO Method to the Cyclopropylcarbinyl and Cyclobutyl Cation and to Bicyclobutane. *Tetrahedron* **1968**, *24* (3), 1083–1096.

(51) Coppens, P. *X-Ray Charge Densities and Chemical Bonding*; Oxford University Press: New York, 1997.

(52) SAINT, Version V7.23A, Bruker. SAINT, version V7.23A, Bruker (2003), Bruker AXS Inc., Madison, Wisconsin, USA.

(53) Krause, L.; Herbst-Irmer, R.; Sheldrick, G. M.; Stalke, D. Comparison of Silver and Molybdenum Microfocus X-Ray Sources for Single-Crystal Structure Determination. *J. Appl. Crystallogr.* **2015**, *48* (1), 3–10.

(54) Macchi, P.; Bürgi, H. B.; Chimpri, A. S.; Hauser, J.; Gál, Z. Low-Energy Contamination of Mo Microsource X-Ray Radiation: Analysis and Solution of the Problem. *J. Appl. Crystallogr.* **2011**, *44* (4), 763–771.

(55) Agilent Technologies: CrysAlisPRO Software System, Version 1.171.37.35g, Agilent Technologies UK Ltd, Oxford, UK,(2014).; Agilent Technologies: CrysAlisPRO Software system, version 1.171.37.35g, Agilent Technologies UK Ltd, Oxford, UK, (2014).

(56) Sheldrick, G. M. SHELXT - Integrated Space-Group and Crystal-Structure Determination. *Acta Crystallogr. Sect. A Found. Crystallogr.* **2015**, *71* (1), 3–8.

(57) Volkov, A.; Macchi, P.; Farrugia, L.; Gatti, C.; Mallinson, P.; Richter, T.; Koritsanszky, T. XD2016 - A Computer Program Package for Multipole Refinement, Topological Analysis of Charge Densities and Evaluation of Intermolecular Energies from Experimental and Theoretical Structure Factors, 2016.

(58) Volkov, A.; Macchi, P.; Farrugia, L.; Gatti, C.; Mallinson, P.; Richter, T.; Koritsanszky, T. XD2006 - a Computer Program for Multipole Refinement, Topological Analysis of Charge

Densities and Evaluation of Intermolecular Energies from Experimental or Theoretical Structure Factors., 2006.

(59) E.J. Baerends, T. Ziegler, J. Autschbach, D. Bashford, A. Bérces, F.M. Bickelhaupt, C. Bo, P. M.; Boerrigter, L. Cavallo, D.P. Chong, L. Deng, R.M. Dickson, D.E. Ellis, M. van Faassen, L. Fan, T. H.; Fischer, C. Fonseca Guerra, M. Franchini, A. Ghysels, A. Giammona, S.J.A. van Gisbergen, A. W. G.; J.A. Groeneveld, O.V. Gritsenko, M. Grüning, S. Gusarov, F.E. Harris, P. van den Hoek, C.R. Jacob, H.; Jacobsen, L. Jensen, J.W. Kaminski, G. van Kessel, F. Kootstra, A. Kovalenko, M.V. Krykunov, E. van; Lenthe, D.A. McCormack, A. Michalak, M. Mitoraj, S.M. Morton, J. Neugebauer, V.P. Nicu, L.; Noodleman, V.P. Osinga, S. Patchkovskii, M. Pavanello, P.H.T. Philipsen, D. Post, C.C. Pye, W.; Ravenek, J.I. Rodríguez, P. Ros, P.R.T. Schipper, H. van Schoot, G. Schreckenbach, J. S. S.; M. Seth, J.G. Snijders, M. Solà, M. Swart, D. Swerhone, G. te Velde, P. Vernooijs, L. Versluis, L.; Visscher, O. Visser, F. Wang, T.A. Wesolowski, E.M. van Wezenbeek, G. Wiesenekker, S.K. Wolff, T. K.; *et al.* ADF2014, SCM, Theoretical Chemistry, Vrije Universiteit, Amsterdam, The Netherlands.

(60) Maxwell, P.; Pendás, Á. M.; Popelier, P. L. A. Extension of the Interacting Quantum Atoms (IQA) Approach to B3LYP Level Density Functional Theory (DFT). *Phys. Chem. Chem. Phys.* **2016**, *18* (31), 20986–21000.

(61) Daudel, R.; Bader, R. F. W.; Stephens, M. E.; Borrett, D. S. The Electron Pair in Chemistry. *Can. J. Chem.* **1974**, *52* (8), 1310–1320.

(62) Bader, R. F. W.; Stephens, M. E. Spatial Localization of the Electronic Pair and Number Distributions in Molecules. *J. Am. Chem. Soc.* **1975**, *97* (26), 7391–7399.

(63) Macchi, P.; Garlaschelli, L.; Sironi, A. Electron Density of Semi-Bridging Carbonyls. Metamorphosis of CO Ligands Observed via Experimental and Theoretical Investigations on $[FeCo(CO)_8]^-$. *J. Am. Chem. Soc.* **2002**, *124* (47), 14173–14184.

(64) Foroutan-Nejad, C.; Shahbazian, S.; Marek, R. Toward a Consistent Interpretation of the QTAIM: Tortuous Link between Chemical Bonds, Interactions, and Bond/Line Paths. *Chem. - A Eur. J.* **2014**, *20* (32), 10140–10152.

(65) Francisco, E.; Blanco, M. A.; Pendás, A. M. An Electron Number Distribution View of Chemical Bonds in Real Space. *Phys. Chem. Chem. Phys.* **2007**, *9*, 1087–1092.

(66) Tiana, D.; Francisco, E.; Macchi, P.; Sironi, A.; Martín Pendás, A. An Interacting Quantum Atoms Analysis of the Metal–Metal Bond in $[M_2(CO)_8]^n$ Systems. *J. Phys. Chem. A* **2015**, *119* (10), 2153–2160.

(67) Von Hopffgarten, M.; Frenking, G. Energy Decomposition Analysis. *WIREs Comput Mol Sci* **2012**, *2*, 43–62 doi: 10.1002/wcms.71.

(68) Bickelhaupt, F. M.; Baerends, E. J. Kohn-Sham Density Functional Theory: Predicting and Understanding Chemistry; Wiley-VCH, John Wiley and Sons, I., Ed.; Kenny B. Lipkowitz and Donald B. Boyd: New York, 2000; Vol. 15, pp 1–86.

(69) Te Velde, G.; Bickelhaupt, F. M.; Baerends, E. J.; Fonseca Guerra, C.; van Gisbergen, S. J. A.; Snijders, J. G.; Ziegler, T. Chemistry with ADF. *J. Comput. Chem.* **2001**, *22* (9), 931–967.

(70) Chini, P.; Longoni, G.; Albano, V. G. High Nuclearity Metal Carbonyl Clusters. In *Advances in Organometallic Chemistry*; Edited by F.G.A. Stone, R. W., Ed.; 1976; Vol. 14, pp 285–344.

(71) Martín Pendás, A.; Blanco, M. A.; Francisco, E. The Nature of the Hydrogen Bond: A Synthesis from the Interacting Quantum Atoms Picture. *J. Chem. Phys.* **2006**, *125* (18), 184112.

3.2.6 Supporting information

Table S3.1. Bond lengths [Å] for **2a_1** and **2a_2** with and without anharmonic model.

	2a_1 harmonic	**2a_1** anharmonic	**2a_2** harmonic	**2a_2** anharmonic
CO(1)-P(1)	2.2526(3)	2.245(3)	2.2521(2)	2.2646(14)
CO(1)-C(1)	1.7643(13)	1.772(3)	1.7673(9)	1.7673(16)
CO(1)-C(2)	1.7684(14)	1.775(3)	1.7701(8)	1.7571(17)
CO(1)-C(15)	1.9148(13)	1.907(4)	1.9161(8)	1.9089(17)
CO(2)-P(1)	2.2649(4)	2.252(3)	2.2656(2)	2.2652(16)
CO(2)-C(3)	1.7755(14)	1.773(4)	1.7747(10)	1.7742(18)
CO(2)-C(4)	1.7618(15)	1.779(4)	1.7607(10)	1.7604(17)
CO(2)-C(16)	1.9248(13)	1.938(3)	1.9276(8)	1.9318(17)
CO(3)-P(1)	2.2670(4)	2.258(3)	2.2674(2)	2.2636(15)
CO(3)-C(5)	1.8037(15)	1.811(4)	1.8057(9)	1.8062(17)
CO(3)-C(6)	1.7939(15)	1.797(4)	1.7978(10)	1.8045(17)
CO(3)-C(16)	1.9071(13)	1.912(3)	1.9071(9)	1.9094(17)
CO(4)-P(1)	2.2734(4)	2.284(3)	2.2738(2)	2.2811(15)
CO(4)-C(7)	1.7952(14)	1.786(3)	1.7956(9)	1.7882(17)
CO(4)-C(8)	1.7878(14)	1.784(3)	1.7907(9)	1.7866(17)
CO(4)-C(15)	1.8976(12)	1.902(3)	1.8991(8)	1.9031(15)
CO(5)-P(1)	2.1667(4)	2.162(3)	2.1676(2)	2.1465(16)
CO(5)-C(9)	1.8087(13)	1.815(3)	1.8094(8)	1.8269(17)
CO(5)-C(10)	1.7927(14)	1.793(3)	1.7970(9)	1.7959(17)
CO(5)-C(11)	1.7952(14)	1.792(3)	1.7965(10)	1.8021(17)
CO(6)-P(1)	2.1791(4)	2.196(3)	2.1796(2)	2.1900(15)
CO(6)-C(12)	1.8186(17)	1.798(4)	1.8156(10)	1.8070(19)
CO(6)-C(13)	1.8192(15)	1.842(4)	1.8202(10)	1.8185(19)
CO(6)-C(14)	1.7924(16)	1.772(4)	1.7917(12)	1.791(2)
P(2)-C(51)	1.7978(12)	1.7977(13)	1.7965(7)	1.7966(7)
P(2)-C(21)	1.7898(11)	1.7896(12)	1.7900(7)	1.7902(7)
P(2)-C(31)	1.7943(11)	1.7941(12)	1.7951(7)	1.7952(8)
P(2)-C(41)	1.7908(12)	1.7907(13)	1.7903(7)	1.7903(7)
O(1)-C(1)	1.153(2)	1.153(2)	1.1488(14)	1.1487(14)
O(2)-C(2)	1.148(3)	1.148(2)	1.1499(12)	1.1503(12)
O(3)-C(3)	1.149(2)	1.149(2)	1.1477(16)	1.1478(16)
O(4)-C(4)	1.149(3)	1.150(3)	1.1464(15)	1.1474(15)
O(5)-C(5)	1.144(3)	1.144(3)	1.1413(14)	1.1417(14)
O(6)-C(6)	1.144(3)	1.144(3)	1.1393(16)	1.1397(15)
O(7)-C(7)	1.150(3)	1.150(3)	1.1487(13)	1.1487(13)
O(8)-C(8)	1.149(2)	1.149(2)	1.1442(14)	1.1443(14)
O(9)-C(9)	1.146(2)	1.146(2)	1.1452(12)	1.1451(12)
O(10)-C(10)	1.145(3)	1.145(3)	1.1427(14)	1.1426(13)
O(11)-C(11)	1.144(3)	1.144(3)	1.1462(15)	1.1467(15)
O(12)-C(12)	1.142(3)	1.143(3)	1.1442(16)	1.1440(16)

O(13)-C(13)	1.144(3)	1.145(3)	1.1417(14)	1.1417(14)
O(14)-C(14)	1.141(3)	1.141(3)	1.1438(18)	1.1439(18)
O(15)-C(15)	1.181(2)	1.181(2)	1.1785(13)	1.1785(13)
O(16)-C(16)	1.177(2)	1.177(2)	1.1775(13)	1.1779(13)
C(51)-C(52)	1.4016(17)	1.4009(18)	1.4022(10)	1.4018(10)
C(51)-C(56)	1.3965(17)	1.3958(18)	1.3992(10)	1.3993(11)
C(52)-C(53)	1.3910(19)	1.390(2)	1.3915(12)	1.3914(12)
C(53)-C(54)	1.397(3)	1.398(3)	1.3940(19)	1.3941(19)
C(54)-C(55)	1.391(3)	1.392(3)	1.3928(19)	1.3927(19)
C(55)-C(56)	1.3933(19)	1.392(2)	1.3919(12)	1.3913(12)
C(21)-C(22)	1.3986(15)	1.3978(16)	1.3979(10)	1.3977(10)
C(21)-C(26)	1.4037(16)	1.4034(17)	1.4037(10)	1.4036(10)
C(22)-C(23)	1.3899(16)	1.3883(17)	1.3917(11)	1.3913(11)
C(23)-C(24)	1.389(2)	1.390(2)	1.3925(14)	1.3925(14)
C(24)-C(25)	1.397(2)	1.396(2)	1.3971(14)	1.3971(14)
C(25)-C(26)	1.3912(15)	1.3900(16)	1.3906(10)	1.3904(10)
C(31)-C(32)	1.3958(16)	1.3956(17)	1.3949(9)	1.3946(9)
C(31)-C(36)	1.3967(15)	1.3957(16)	1.3963(10)	1.3961(10)
C(32)-C(33)	1.3958(16)	1.3949(17)	1.3961(12)	1.3961(12)
C(33)-C(34)	1.391(2)	1.391(2)	1.3896(14)	1.3894(15)
C(34)-C(35)	1.392(2)	1.393(2)	1.3942(15)	1.3944(16)
C(35)-C(36)	1.3879(18)	1.3865(19)	1.3832(13)	1.3828(14)
C(41)-C(42)	1.3965(16)	1.3958(17)	1.3982(10)	1.3980(10)
C(41)-C(46)	1.3997(15)	1.3986(16)	1.4003(10)	1.4001(10)
C(42)-C(43)	1.3924(19)	1.392(2)	1.3953(12)	1.3952(12)
C(43)-C(44)	1.397(2)	1.396(2)	1.3880(13)	1.3879(14)
C(44)-C(45)	1.3887(19)	1.389(2)	1.3899(12)	1.3900(12)
C(45)-C(46)	1.3893(17)	1.3891(18)	1.3892(10)	1.3893(10)

Table S3.2. Refined Gram-Charlier parameters.

2a_1	**Co1**	**Co2**	**Co3**	**Co4**	**Co5**	**Co6**	**P1**
C_{111}	0.000034	-0.000267	-0.000006	0.000300	-0.000044	0.000033	-0.000058
C_{222}	-0.000030	-0.000171	-0.000085	-0.000040	0.000012	-0.000260	0.000005
C_{333}	0.000050	-0.000044	0.000007	0.000058	0.000018	0.000045	-0.000015
C_{112}	-0.000073	-0.000074	-0.000075	-0.000084	-0.000057	-0.000194	0.000006
C_{122}	0.000035	-0.000042	-0.000018	0.000019	-0.000007	0.000058	-0.000012
C_{113}	0.000207	-0.000077	-0.000022	0.000076	0.000150	0.000065	0.000002
C_{133}	0.000014	-0.000060	-0.000049	-0.000036	0.000024	0.000013	0.000001
C_{223}	0.000007	-0.000055	0.000019	0.000013	0.000007	0.000101	-0.000008
C_{233}	-0.000011	-0.000050	-0.000005	-0.000019	-0.000001	-0.000069	-0.000001
C_{123}	-0.000025	-0.000029	-0.000034	0.000023	-0.000015	-0.000032	0.000010
D_{1111}	0.001449	-0.000029	-0.000256	0.000156	0.001450	-0.000003	0.000209
D_{2222}	0.000002	0.000078	0.000134	-0.000012	-0.000005	0.000067	0.000015
D_{3333}	-0.000009	-0.000007	-0.000002	0.000065	-0.000006	-0.000007	0.000020
D_{1112}	-0.000333	0.000027	-0.000006	0.000023	-0.000299	-0.000054	-0.000015
D_{1222}	-0.000039	0.000006	0.000012	-0.000004	-0.000028	-0.000021	-0.000004
D_{1113}	-0.000011	-0.000012	-0.000021	-0.000211	0.000208	0.000044	0.000014
D_{1333}	0.000003	0.000001	-0.000006	-0.000075	0.000016	0.000003	0.000002
D_{2223}	-0.000001	0.000049	0.000004	0.000000	0.000000	-0.000033	-0.000001
D_{2333}	-0.000002	0.000021	0.000003	-0.000007	-0.000003	-0.000016	-0.000001
D_{1122}	0.000077	0.000011	-0.000016	-0.000014	0.000050	0.000019	0.000021
D_{1133}	0.000009	0.000003	-0.000024	0.000097	0.000041	0.000007	0.000022
D_{2233}	-0.000002	0.000020	0.000006	0.000003	-0.000002	0.000017	0.000004
D_{1123}	-0.000014	0.000023	0.000009	-0.000002	-0.000031	-0.000033	-0.000007
D_{1223}	0.000006	0.000003	-0.000005	-0.000014	0.000006	0.000014	-0.000001
D_{1233}	-0.000009	0.000004	0.000001	0.000002	-0.000008	-0.000011	-0.000002
2a_2	**Co1**	**Co2**	**Co3**	**Co4**	**Co5**	**Co6**	**P1**
C_{111}	0.000017	-0.000003	0.000028	0.000075	0.000478	-0.000142	0.000014
C_{222}	-0.000081	-0.000032	-0.000023	-0.000035	-0.000029	-0.000011	-0.000005
C_{333}	-0.000041	0.000018	-0.000021	0.000044	0.000110	0.000074	0.000001
C_{112}	-0.000027	-0.000015	-0.000085	-0.000044	-0.000084	-0.000017	0.000003
C_{122}	0.000014	-0.000014	0.000010	0.000010	0.000042	0.000033	-0.000002
C_{113}	-0.000067	0.000017	-0.000037	0.000014	0.000210	0.000087	-0.000018
C_{133}	0.000002	0.000001	-0.000023	0.000011	0.000154	0.000059	-0.000001
C_{223}	-0.000057	-0.000002	-0.000003	0.000031	0.000026	0.000017	-0.000001
C_{233}	-0.000047	-0.000004	-0.000021	-0.000034	-0.000033	-0.000008	-0.000002
C_{123}	0.000003	-0.000003	-0.000018	-0.000012	-0.000043	-0.000003	0.000007
D_{1111}	-0.000242	-0.000070	0.000233	-0.000207	-0.000084	-0.000090	0.000168
D_{2222}	0.000031	0.000017	-0.000009	0.000007	-0.000004	-0.000008	0.000003
D_{3333}	0.000009	0.000005	0.000031	0.000040	0.000039	0.000043	0.000001
D_{1112}	-0.000026	0.000077	0.000046	-0.000014	-0.000027	-0.000045	-0.000001
D_{1222}	-0.000008	0.000034	0.000003	0.000001	-0.000002	-0.000006	0.000002
D_{1113}	0.000000	0.000062	0.000235	0.000030	0.000121	0.000123	-0.000019
D_{1333}	0.000011	0.000031	0.000072	0.000019	0.000058	0.000065	0.000001
D_{2223}	0.000025	0.000019	0.000000	-0.000023	-0.000006	-0.000003	0.000000

D_{2333}	0.000019	0.000015	0.000000	-0.000032	-0.000009	-0.000011	0.000000
D_{1122}	0.000018	0.000039	0.000008	0.000002	0.000008	0.000003	-0.000004
D_{1133}	-0.000006	0.000022	0.000091	0.000004	0.000047	0.000070	0.000006
D_{2233}	0.000016	0.000014	0.000003	0.000021	0.000007	0.000007	0.000001
D_{1123}	0.000014	0.000035	0.000009	-0.000020	-0.000012	-0.000021	0.000002
D_{1223}	0.000002	0.000021	0.000009	0.000006	0.000013	0.000013	-0.000002
D_{1233}	0.000003	0.000020	0.000005	-0.000008	-0.000009	-0.000012	0.000001

The Kuhs's rule implies [iii] a resolution of 1.1 $Å^{-1}$ for third order coefficients and 1.3 $Å^{-1}$ for fourth order coefficients. Despite the data do not reach 1.3 $Å^{-1}$, the refinement of fourth order coefficients bring to an undoubted improvement of the residual density (Figure 3.2.3). The nuclear probability functions for **2a_2** display less than 5% negative volumes (thus at the precision limit) for all atoms but Co1, which has a negative probability of ca. 10%. In **2a_1**, the negative probability volumes are ca. 10% for all Co atoms. In both experiments, the probability function of P(1) is almost everywhere positive.

[iii] Kuhs, W. F. Generalized atomic displacements in crystallographic structure analysis. *Acta Cryst.*, **1992**, *A48*, 80-98.

Table S3.3. Absolute difference of Mean-Squares Displacement Amplitudes (DMSDA, 10^{-3} Å^2) along interatomic vectors of bonded atoms. Noteworthy, as it is usual for bonds to transition metals, metal-ligand bonds exceed the typical Hirshfeld limit of 1.0 10^{-3} Å^2 expected for covalent bonds of main group atoms.

	2a_1	**2a_2**
Co1-P1	1.2	2.7
Co1-C1	3.4	7.4
Co1-C2	6.3	7.5
Co1-C15	9.4	0.1
Co2-P1	1.3	4.4
Co2-C3	2.6	7.0
Co2-C4	8.2	8.3
Co2-C16	2.8	2.4
Co3-P1	8.0	3.0
Co3-C5	3.5	0.9
Co3-C6	0.4	7.4
Co3-C16	8.1	8.6
Co4-P1	7.1	2.6
Co4-C7	7.7	4.9
Co4-C8	5.2	3.0
Co4-C15	14.1	0.5
Co5-P1	7.8	12.4
Co5-C9	4.4	7.3
Co5-C10	8.2	5.0
Co5-C11	2.8	7.0
Co6-P1	0.9	10.4
Co6-C12	3.8	11.7
Co6-C13	0.2	5.2
Co6-C14	2.3	6.6
P2-C21	0.0	0.6
P2-C31	0.1	0.7
P2-C41	0.4	0.7
P2-C51	0.4	0.5
O1-C1	2.3	0.7
O2-C2	0.8	1.0
O3-C3	2.2	0.1
O4-C4	2.4	0.9
O5-C5	1.8	1.2
O6-C6	2.8	1.9
O7-C7	1.3	0.3
O8-C8	1.9	0.3
O9-C9	3.5	1.1
O10-C10	0.3	1.2
O11-C11	1.2	1.6
O12-C12	1.9	0.3
O13-C13	1.9	1.6
O14-C14	2.8	1.6
O15-C15	3.0	0.4
O16-C16	2.3	0.9
C21-C22	1.4	0.1
C21-C26	1.7	0.2
C22-C23	0.0	0.0
C23-C24	1.0	0.0
C24-C25	0.6	0.3
C25-C26	0.3	0.6
C31-C32	0.5	0.1
C31-C36	0.3	0.3
C32-C33	0.1	0.4
C33-C34	1.2	0.2
C34-C35	1.5	0.1
C35-C36	1.6	0.2
C41-C42	0.1	0.4
C41-C46	0.3	0.1
C42-C43	0.4	0.0
C43-C44	1.3	0.5
C44-C45	1.3	0.1
C45-C46	0.3	0.3
C51-C52	0.9	0.2
C51-C56	0.3	0.4
C52-C53	0.3	0.6
C53-C54	0.2	0.5
C54-C55	0.6	0.0
C55-C56	0.1	0.2

1a

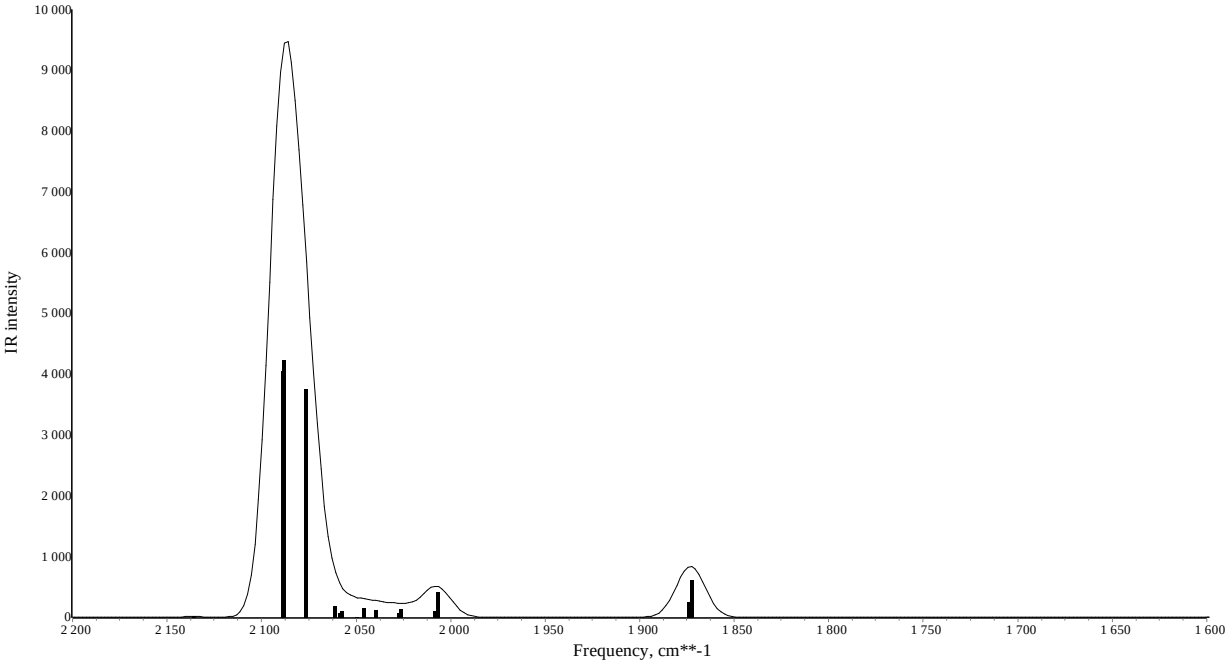
IR intensity
10 000
9 000
8 000
7 000
6 000
5 000
4 000
3 000
2 000
1 000
0
2 200
2 150
2 100
2 050
2 000
1 950
1 900
1 850
1 800
1 750
1 700
1 650
1 600
Frequency, cm**-1

1b

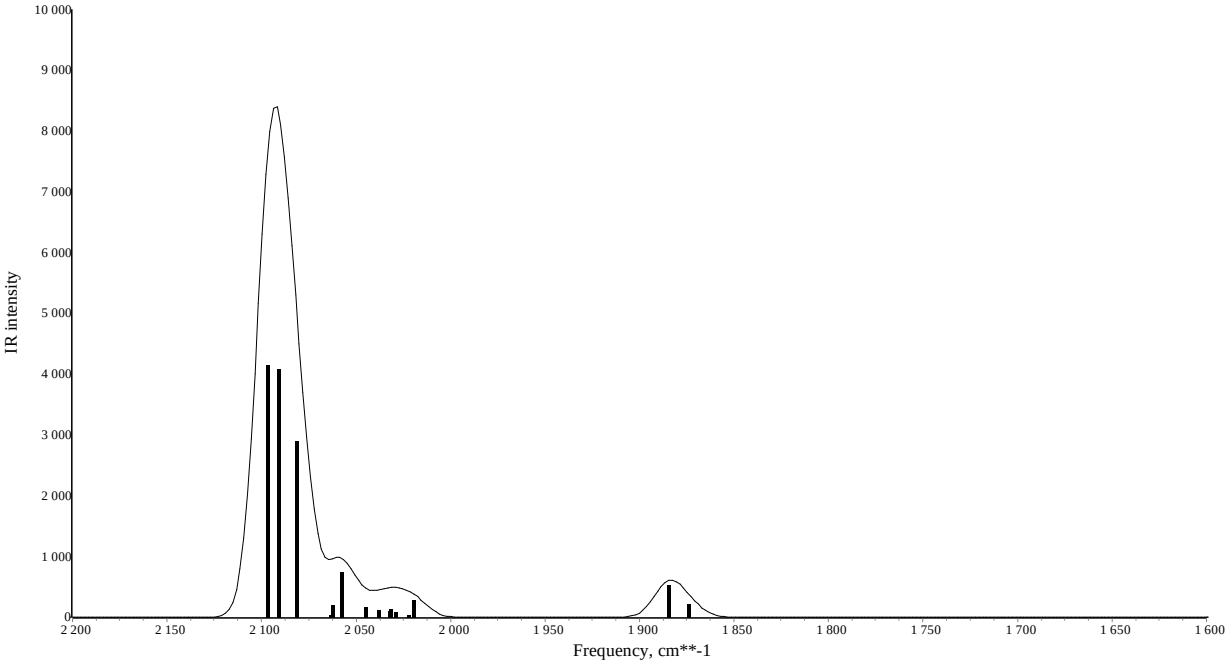
IR intensity
10 000
9 000
8 000
7 000
6 000
5 000
4 000
3 000
2 000
1 000
0
2 200
2 150
2 100
2 050
2 000
1 950
1 900
1 850
1 800
1 750
1 700
1 650
1 600
Frequency, cm**-1

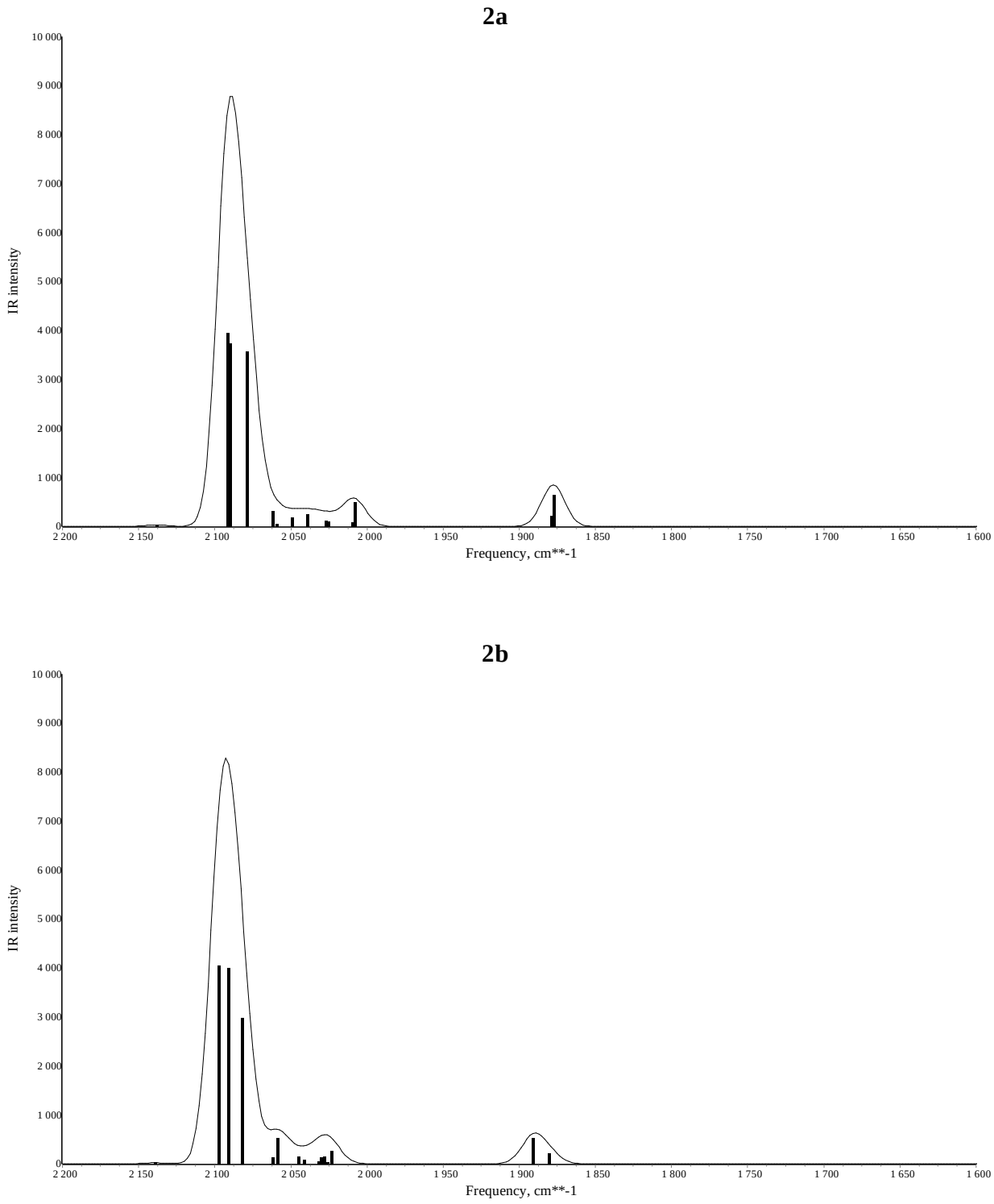

Figure 3.2.9. Simulated IR spectrum of **1a**, **1b**, **2a** and **2b**, level of theory B3LYP/cc-PVTZ, Gaussian09.

Chapter 4

Metallophilic Interactions

The concept of metallophilicity, first introduced by Pyykkö in 1994, was used to denote the specific attraction between two group 11 closed-shell metal ions.[1] Initially, this concept was applied to the Au(I)---Au(I) interactions, called Aurophilic[2], then extended to the others coinage metals.[3,4,5]

However, Cu(I)---Cu(I) and Ag(I)---Ag(I) interactions were already identified by Hoffmann[6] and Jansen[7]. Metallophilicity indicates a type of chemical bonding between metal ions having d^{10} electronic configuration.[8] At the beginning, this interaction was attributed to mixing between (n+1)s and nd orbitals,[6,9] then, it was concluded that metallophilicity was primarily due to electron-correlation and dispersion contributions,[2,10] but many factors affect the occurrence and the strength of this interaction. It is a weak interaction, with a range of energy of the order of weak hydrogen bonds. Even though many studies have been dedicated to explain this interaction during the last decades, it is still considered elusive and unclear. As observed by Mehrotra and Hoffmann, referring to the Cuprophilic interaction:"*It will be difficult to distinguish the effect of direct Cu-Cu interaction and the stereochemical demands of the ligand set around the copper atoms".*[6] Indeed, inter-metallic distance is not a straightforward parameter to denote the presence or not of the methallophilic interaction.[11] The strength of metallophilicity increases on descending group 11, in fact, many systems with Aurophilic interaction were reported in the literature, [10,12,13] whereas Cuprophilic interaction is more elusive.[11,14] Recently, the concept of metallophilicity have been expanded also to other closed-shell ions, like Pt^0, Hg^{2+}, Tl^+, Pb^{2+} and Bi^{3+}.[15]

In the following, an experimental/theoretical work is reported on two isostructural coordination polymers differing only in the coinage metal(I) cations which were compressed with the purpose of testing secondary interactions between polymeric chains, that may trigger metallophilic interactions or otherwise expand the metal coordination. DFT calculations and X-ray diffraction studies at high pressure reveal an extraordinary difference between Ag(I) and Cu(I) in homologous compounds.

Argentophilic interactions are induced just by a mild compression and, at P = 7.94 GPa, Ag---Ag distance matches the value in metallic silver. On the contrary, no cuprophilic interaction is activated even by compression up to 8 GPa. The Cu---Cu distances remain ca. 0.5 Å longer than the sum of van der Waals radii.

4.1 Introduction

Aurophilic[16], argentophilic[17] and cuprophilic[18] interactions have always attracted the curiosity of scientists for both the intriguing nature of this bonding and the high frequency of their occurrence in the solid state, with M(I)---M(I) distances shorter than the sum of the van der Waals radii.

Moreover, recent studies demonstrated that this interaction plays a major role for properties like luminescence[19,20], and in fields like catalysis[21] and life science[22].

The attraction between two cations is of course counterintuitive, especially when the two atoms involved are formally closed-shell and, in principle, cannot share d-electrons and form a covalent bond. However, close-shell d^{10}---d^{10} interaction energies are calculated to be stabilizing (7-11 kcal/mol), depending anyhow on the nature of the metals and their ligand environment.[4,8] It is nowadays established that this stabilization arises from a combination of electron correlation[4], relativistic contraction[23] and other secondary contributions like charge transfer[10]. These effects are not always stabilizing a geometry with shorter metal-metal distance, for example relativistic effect could also weaken it[24]. When compounds featuring metallophilic interactions at ambient conditions were brought to extreme conditions of pressure and temperature, rare mechanical phenomena occurred, such as negative linear compressibility in $Ag_3[Co(CN)_6]$,[25] $KMn[Ag(CN)_2]_3$,[26] negative area compressibility in gold diethyldithiocarbamate[27] and negative thermal expansion in $In[Ag(CN)_2]_3 \cdot xH_2O$.[28] However, to the best of our knowledge, no formation of metallophilic interaction upon compression has ever been reported.

The study here presented was undertaken because the packing of two unprecedented metal(I) 5-(2-fluoro-4-pyridyl)tetrazolate 2D coordination polymers, that we report here for the first time, is such that an interaction between M(I) ions may potentially arise upon compression. Moreover, the isostructural relation between the silver (I) and copper (I) polymers (AgFPT, CuFPT, respectively), may be used to single out the different metallophilic attitude of the two metals (Table 4.1 and 4.2).

The application of pressure is a way to probe the forces acting on atoms, within a crystal: the compression paths reveal either the softness of each bond (intermolecular interactions are typically softer than intra-molecular ones) and ‘hidden’ attractions (of electronic nature) that may favor one compression path over another.

4.2 Experimental section and computational details

4.2.1 Synthesis of CuFPT and AgFPT

To a 25-mL teflon-lined stainless steel vessel was added 0.5 mmol of the metal salt (CuI for CuFPT and $AgNO_3$ for AgFPT, respectively); 1.25 mmol of 4-cyano-2-fluoropyridine and 0.5 mmol of NaN_3 in a CH_3OH/H_2O mixture (5:2, 10 mL). The mixture was than heated at 120 °C for 72 h and cooled to room temperature with cooling ramp of 5 °C/h. The product was filtered and washed thoroughly with CH_3OH (3 * 10 mL).

4.2.1.1 AgFPT

Anal. Calc. for $C_6H_3N_5AgF$ (*fw* = 271.98 $gmol^{-1}$): C, 26.50; H, 1.11; N, 25.75, %. Found: C, 26.48; H, 1.52; N, 26.09, %. IR (ATR) Figure 4.1.

4.2.1.2 CuFPT

Anal. Calc. for $C_6H_3N_5CuF$ (*fw* = 227.66 $gmol^{-1}$): C, 31.65; H, 1.33; N, 30.76, %. Found: C, 31.20; H, 1.45; N, 31.09, %. IR (ATR) Figure 4.1.

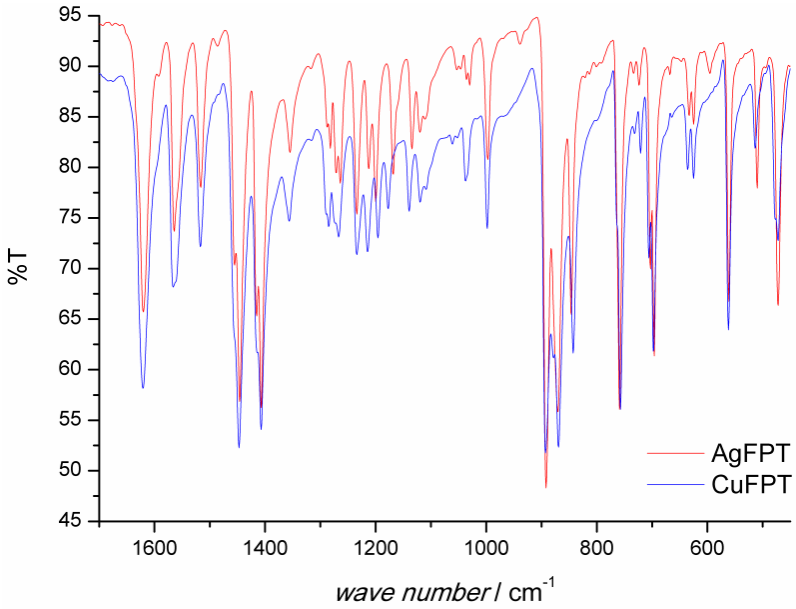

Figure 4.1. ATR spectra of AgFPT (red) and CuFPT (blue) in ambient conditions.

4.2.2 Single crystal X-ray diffraction and high-pressure

Single crystals of AgFPT (Figure 4.2a) and CuFPT (Figure 4.2b) were isothermally compressed in a diamond-anvil cell (DAC)[29] up to 6.15 GPa and 8 GPa, respectively. Additionally, AgFPT was remeasured with synchrotron radiation (λ=0.56371) up to 7.94 GPa. Methanol:ethanol:water mixture (volume ratio 16:3:1) was used as a hydrostatic medium[30] and a ruby sphere to calibrate pressure inside a cell.[31,32] Single-crystal X-ray diffraction data were collected on a Supernova micro-source diffractometer with Mo anode and a CCD detector. Data were collected and reduced using CrysAlis software.[33] Structures were solved and refined using ShelXT and ShelXL,[34] respectively in Olex2 interface.[35] All hydrogen atoms were located from molecular geometry.

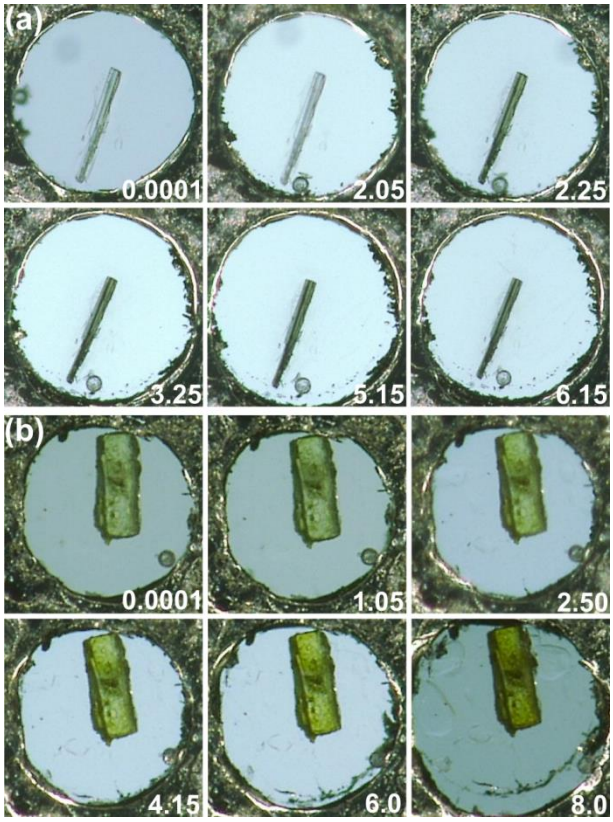

Figure 4.2. Single crystals of (a) AgFPT and (b) CuFPT compressed in a DAC, a ruby sphere is visible by the gasket edge.

4.2.3 Computational details

Optimizations of both atomic coordinates and lattice parameters were calculated with CRYSTAL14[36], at density functional level of theory, using Becke's 3 parameter exchange and the Lee-Yang-Parr non-local correlation functionals[37,38] combined with semi-empirical dispersion correction with a scaling factor s_6 equal to 0.6[39]. The copper [6s5p2d] and the silver [4s2p2d] basis set proposed by Doll and Harrison were used[40,41], combined with relativistic pseudo-potential for Ag atom[42]. Double-zeta polarized Gaussian-type functions were used for the non-metallic atoms.

Topological analysis was computed with TOPOND package implemented in CRYSTAL14[43]. Calculations *in vacuo* of selected crystal fragments were carried out with Gaussian16[44], using the same exchange-correlation functional and dispersion correction, for sake of consistency with solid-state computations. A 6-311G(d,p) basis-set was applied for every kind of atom but Ag, for which the def2TZVP was selected. AIMALL package (version 17.01.25)[45] was used for the topological analysis of *in vacuo* electron densities. The coordinates of the fragments used for calculation *in vacuo* correspond to the geometries optimized in solid state. The terminations of peripheral ligands were capped with H atoms to reproduce electroneutrality.

4.3 Results and discussions

We synthetized AgFPT and CuFPT in solvothermal conditions, exploiting the *in situ* generation of the tetrazolate ligand.[46] Indeed, they precipitate as single crystals from a water/methanol solvent mixture, starting from the 4-cyano-2-fluoropyridine and sodium azide, in the presence of the corresponding Ag(I) or Cu(I) salts. Both coordination polymers crystallize in the monoclinic $P2_1/n$ space group, with two independent cations in the asymmetric unit (Figure 4.3): both are three coordinated to tetrazolate rings but differ in their relation with a fourth nitrogen atom. M(1) being close, but not jet σ-bound, to the π-system of a side-on tetrazolate (N(9)), while M(2) is bound, hence tetra-coordinated, to fluoropyridine (N(1)), both of adjacent ribbons. Actually, forgetting 'bond' distances, the two metals share the very same trigonal pyramidal stereochemistry.

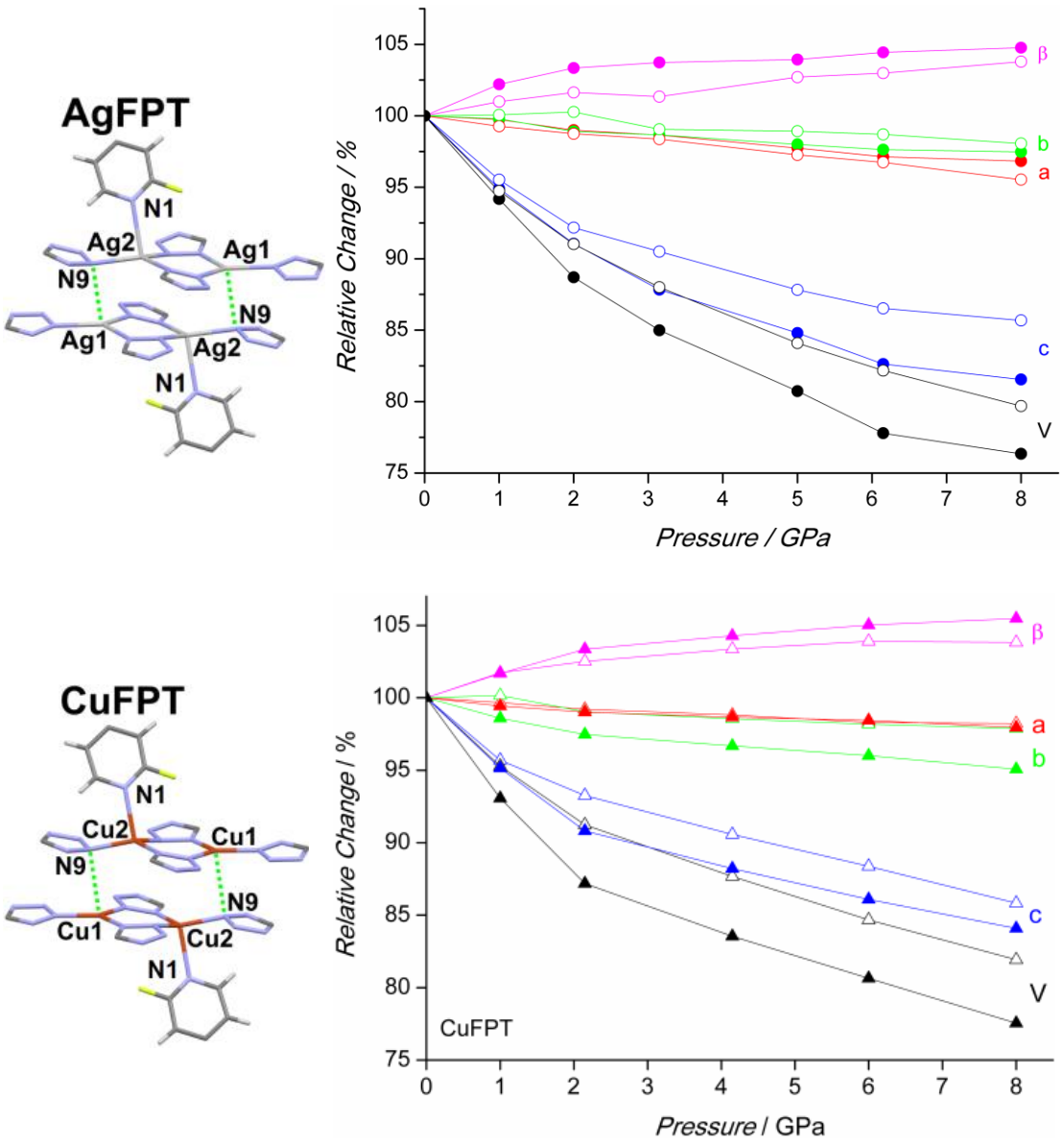

Figure 4.3. Asymmetric part of unit cells of AgFPT and CuFPT (left); relative change of the unit cell parameter (right), filled symbol: experimental value, empty symbol: theoretical value.

Table 4.1. Full crystallographic and experimental data of AgFPT at various temperature, pressure and radiation.

Compound	AgFPT	AgFPT	AgFPT	AgFPT	AgFPT	AgFPT	AgFPT
Formula	$C_{12}H_6F_2N_{10}Ag_2$	$C_{12}H_6F_2N_{10}Ag_2$	$C_{12}H_6F_2N_{10}Ag_2$	$C_{12}H_6F_2N_{10}Ag_2$	$C_{12}H_6F_2N_{10}Ag_2$	$C_{12}H_6F_2N_{10}Ag_2$	$C_{12}H_6F_2N_{10}Ag_2$
Formula weight	544.01	544.01	544.01	544.01	544.01	544.01	544.01
Pressure (GPa)	0.0001	0.0001	1.0	2.0	3.15	5.0	6.15
Temperature (K)	293	110	293	293	293	293	293
Crystal system	monoclinic	monoclinic	monoclinic	monoclinic	monoclinic	monoclinic	monoclinic
Space group	$P2_1/n$	$P2_1/n$	$P2_1/n$	$P2_1/n$	$P2_1/n$	$P2_1/n$	$P2_1/n$
a (Å)	6.2014(14)	5.780(2)	6.1733(9)	6.1291(4)	6.0860(8)	6.0588(5)	6.0170(7)
b (Å)	19.2121(14)	18.847(7)	19.074(4)	18.9185(17)	18.811(2)	18.7747(13)	18.668(2)
c (Å)	12.844(5)	13.045(5)	12.325(14)	11.618(9)	11.228(10)	10.813(6)	10.643(11)
β (°)	93.65(4)	93.725(5)	95.34(3)	96.52(2)	96.76(3)	97.066(18)	97.35(3)
Volume ($Å^3$)	1527.2(6)	1418.2(9)	1444.9(17)	1338.4(11)	1276.5(11)	1220.7(7)	1185.6(12)
Z/Z’	4/1	4/1	4/1	4/1	4/1	4/1	4/1
Calculated density ($g \cdot cm^{-3}$)	2.366	2.548	2.501	2.700	2.831	2.960	3.048
Absorption coefficient (mm^{-1})	2.609	2.809	2.758	2.977	3.121	3.264	3.361
F(000)	1040	1040	1040	1040	1040	1040	1040
Crystal size (max, mid, min)	0.1x0.05x0.02	0.1x0.05x0.02	0.1x0.05x0.02	0.1x0.05x0.02	0.1x0.05x0.02	0.1x0.05x0.02	0.1x0.05x0.02
Radiation (Å)	0.71073	0.71073	0.71073	0.71073	0.71073	0.71073	0.71073
2θ-range for data collection (°)	3.82 – 56.888	3.808 – 55.98	4.27 – 52.77	4.306 – 52.282	4.33 – 56.922	4.338 – 57.084	4.364 – 56.99
Min/max indices: h,k,l	-8/8, -25/25, -17/16	-8/8, -24/24, -17/16	-7/4, -22/14, -4/7	-4/7, -17,13, -5/3	-7/7, -25/25, -5/5	-7/7, -25/25, -4/5	-6/7, -25/25, -4/4
Reflections collected/unique	15585/3829	14405/3426	2757/836	2643/625	6946/1001	6803/950	6555/864
R_{int}	0.0431	0.0398	0.2826	0.1370	0.1859	0.1222	0.1478
Completeness (%)	99.51	99.94	28.27	23.36	31.14	30.57	28.84
Data/parameters/restrains	3829/0/235	3426/0/235	836/161/97	625/160/85	1001/160/43	950/160/85	864/160/85
GooF on F2	1.015	1.022	1.080	1.066	1.128	1.098	1.125
Final R1/wR2 (I>2σ(I))	0.0415, 0.0729	0.0390, 0.0759	0.1457, 0.3142	0.0872, 0.1857	0.1208, 0.2835	0.1179, 0.2581	0.1067, 0.2476
Final R1/wR2 (all data)	0.0754, 0.0820	0.0675, 0.0822	0.2992, 0.4039	0.1694, 0.2386	0.3017, 0.3933	0.2201, 0.3852	0.2489, 0.3688
Weighting parameters w_1, w_2	0.027, 4.18	0.033, 3.12	0.165, 0.0	0.062, 1,01	0.2, 0.0	0.2, 0.0	0.2, 0.0
Largest diff. peak/hole ($eÅ^{-3}$)	2.31, -1.62	2.39, -1.56	1.15, -1.22	1.19, -1.05	1.59/-1.59	2.83/-1.53	2.15, -1.75

Compound	AgFPT	AgFPT	AgFPT	AgFPT	AgFPT	AgFPT
Formula	$C_{12}H_6F_2N_{10}Ag_2$	$C_{12}H_6F_2N_{10}Ag_2$	$C_{12}H_6F_2N_{10}Ag_2$	$C_{12}H_6F_2N_{10}Ag_2$	$C_{12}H_6F_2N_{10}Ag_2$	$C_{12}H_6F_2N_{10}Ag_2$
Formula weight	544.01	544.01	544.01	544.01	544.01	544.01
Pressure (GPa)	1.06	1.83	3.05	4.55	6.28	7.94
Temperature (K)	293	293	293	293	293	293
Crystal system	monoclinic	monoclinic	monoclinic	monoclinic	monoclinic	monoclinic
Space group	$P2_1/n$	$P2_1/n$	$P2_1/n$	$P2_1/n$	$P2_1/n$	$P2_1/n$
a (Å)	6.1859(4)	6.1394(6)	6.1177(5)	6.0604(5)	6.0237(6)	6.0049(5)
b (Å)	19.1704(19)	19.0012(18)	18.9548(18)	18.8292(17)	18.7574(19)	18.7256(17)
c (Å)	12.190(10)	11.694(6)	11.281(5)	10.894(6)	10.613(5)	10.474(7)
β (°)	95.718(18)	96.788(19)	97.145(18)	97.335(6)	97.81(2)	98.12(2)
Volume ($Å^3$)	1438.3(11)	1354.6(7)	1298.0(6)	1232.9(6)	1188.0(6)	1166.0(8)
Z/Z’	4/1	4/1	4/1	4/1	4/1	4/1
Calculated density ($g \cdot cm^{-3}$)	2.512	2.667	2.784	2.931	3.042	3.099
Absorption coefficient (mm^{-1})	1.470	1.561	1.629	1.715	1.780	1.813
F(000)	1040	1040	1040	1040	1040	1040
Crystal size (max, mid, min)	0.1x0.1x0.15	0.1x0.1x0.15	0.1x0.1x0.15	0.1x0.1x0.15	0.1x0.1x0.15	0.1x0.1x0.15
Radiation (Å)	0.56371	0.56371	0.56371	0.56371	0.56371	0.56371
2θ-range for data collection (°)	5.716 – 49.77	4.394 – 50.296	3.408 – 50.5	3.432 – 49.998	3.444 – 49.58	3.45 – 50.31
Min/max indices: h,k,l	-8/8, -28/27, -6/6	-8/7, -26/26, -8/7	-8/8, -26/26, -7/8	-8/8, -25/25, -7/7	-8/8, -26/26, -7/7	-8/8, -27/27, -6/6
Reflections collected/unique	2613/1415	2473/1509	2335/1459	2255/1394	2155/1355	2114/1202
R_{int}	0.0522	0.0481	0.0425	0.0409	0.0399	0.0349
Completeness (%)	42.31	47.98	48.49	48.67	49.19	45.15
Data/parameters/restrains	2613/1415	1509/0/127	1459/0/188	1394/0/127	1355/0/116	1202/0/127
GooF on F2	0.968	1.228	1.056	1.054	1.007	1.105
Final R1/wR2 (I>2σ(I))	0.0673, 0.1822	0.0994, 0.2858	0.0709, 0.1991	0.0851, 0.2347	0.0747, 0.2017	0.0698, 0.1954
Final R1/wR2 (all data)	0.1237, 0.2220	0.1305, 0.3301	0.1038, 0.2291	0.1191, 0.2637	0.1109, 0.2437	0.0935, 0.2246
Weighting parameters w_1, w_2	0.139, 0	0.2, 0	0.152, 0	0.175, 0	0.168, 0	0.149, 0
Largest diff. peak/hole ($eÅ^{-3}$)	0.87/-1.41	1.11/-2.09	0.74/-1.44	0.90/-1.79	0.75/-1.88	0.79/-1.49

Table 4.2. Full crystallographic and experimental data of CuFPT at various temperature and pressure.

Compound	CuFPT	CuFPT	CuFPT	CuFPT	CuFPT	CuFPT	CuFPT
Formula	$C_{12}H_6F_2N_{10}Cu_2$	$C_{12}H_6F_2N_{10}Cu_2$	$C_{12}H_6F_2N_{10}Cu_2$	$C_{12}H_6F_2N_{10}Cu_2$	$C_{12}H_6F_2N_{10}Cu_2$	$C_{12}H_6F_2N_{10}Cu_2$	$C_{12}H_6F_2N_{10}Cu_2$
Formula weight	455.35	455.35	455.35	455.35	455.35	455.35	455.35
Pressure (GPa)	0.0001	0.0001	1	2.5	4.15	6	8
Temperature (K)	293	110	293	293	293	293	293
Crystal system	monoclinic	monoclinic	monoclinic	monoclinic	monoclinic	monoclinic	monoclinic
Space group	$P2_1/n$	$P2_1/n$	$P2_1/n$	$P2_1/n$	$P2_1/n$	$P2_1/n$	$P2_1/n$
a (Å)	5.7705(4)	5.7723(2)	5.7470(2)	5.7227(2)	5.7026(2)	5.6901(3)	5.6617(5)
b (Å)	18.8183(12)	18.761(3)	18.582(2)	18.3687(16)	18.2211(16)	18.095(2)	17.920(4)
c (Å)	13.0141(8)	12.7976(18)	12.413(3)	11.847(2)	11.508(2)	11.230(3)	10.970(4)
β (°)	93.668(1)	94.238(2)	95.296(7)	96.869(7)	97.741(7)	98.434(10)	98.857(17)
Volume ($Å^3$)	1410.32(6)	1382.1(3)	1320.0(3)	1236.4(3)	1184.9(2)	1143.8(3)	1099.8(5)
Z/Z’	4/1	4/1	4/1	4/1	4/1	4/1	4/1
Calculated density ($g \cdot cm^{-3}$)	2.145	2.188	2.291	2.446	2.553	2.644	2.75
Absorption coefficient (mm^{-1})	3.063	3.126	3.273	3.494	3.646	3.777	3.928
F(000)	896	896	896	896	896	896	896
Crystal size (max, mid, min)	0.15x0.08x0.03	0.15x0.08x0.03	0.15x0.08x0.03	0.15x0.08x0.03	0.15x0.08x0.03	0.15x0.08x0.03	0.15x0.08x0.03
Radiation (Å)	0.71073	0.71073	0.71073	0.71073	0.71073	0.71073	0.71073
2θ-range for data collection (°)	3.81 – 60.50	3.802 – 63.1	3.958 – 52.988	4.112 – 52.642	4.214 – 52.402	4.302 – 52.374	4.392 – 51.062
Min/max indices: h,k,l	-8/8, -26/26, -18/18	-8/8, -25/26, -18/18	-6/3, -11/13, -6/7	-6/3, -11/13, -6/7	-6/3, -11/13, -6/7	-6/3, -11/13, -5/6	-6/3, -11/14, -5/6
Reflections collected/unique	20834/4191	15458/4089	2513/682	2363/641	2263/618	2186, 592	2078, 568
R_{int}	0.0391	0.0312	0.0462	0.0453	0.0476	0.0473	0.0488
Completeness (%)	99.53	99.15	24.88	25.51	25.99	25.89	27.75
Data/parameters/restrains	4191/0/235	4089/0/235	682/0/85	641/0/85	618/0/85	592/0/85	568/0/85
GooF on F2	1.037	1.049	1.063	1.11	1.107	1.097	1.089
Final R1/wR2 (I>2σ(I))	0.0556, 0.1102	0.0383, 0.0795	0.0674, 0.1499	0.0628, 0.1374	0.0564, 0.1230	0.0547, 0.1190	0.0532, 0.1262
Final R1/wR2 (all data)	0.0770, 0.1163	0.0486, 0.0821	0.0874, 0.1642	0.0797, 0.1465	0.0735, 0.1332	0.0689, 0.1268	0.0709, 0.1363
Weighting parameters w_1, w_2	0.041, 5.23	0.03, 3.51	0.059, 28.878	0.049, 22.283	0.043, 17.964	0.049, 13.223	0.074, 5.183
Largest diff. peak/hole ($eÅ^{-3}$)	2.07, -2.37	1.67, -1.28	0.6, -0.72	0.51, -0.53	0.46, -0.49	0.56, -0.38	0.59,-0.46

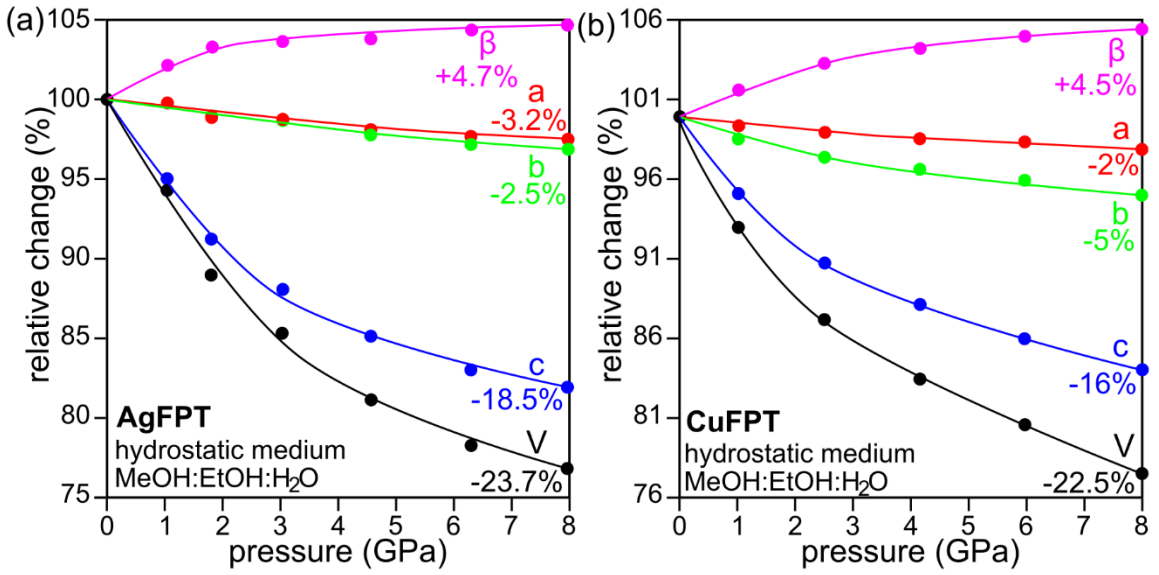

Figure 4.4. Compressibility of unit-cell parameters and volume of (a) AgFPT and (b) CuFPT.

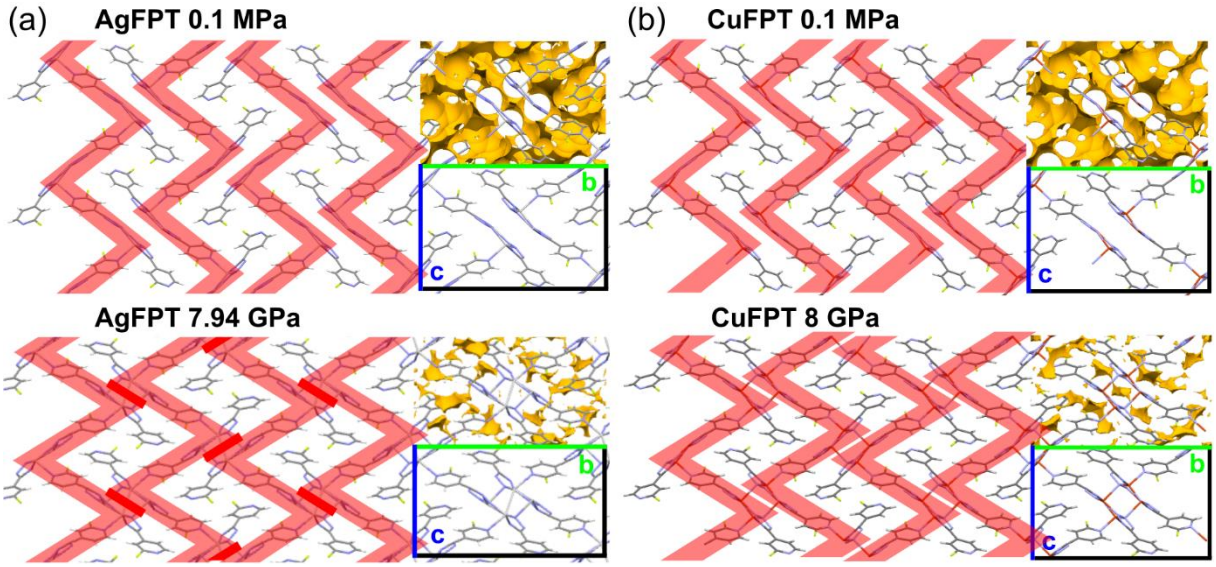

Figure 4.5. Crystal structures of (a) AgFPT and (b) CuFPT projected along [100] at ambient and high pressure. Red zig-zags show ribbons of molecules which approach to form Ag---Ag and Ag---N for AgFPT and Cu---N for CuFPT, respectively. Yellow spheres are voids in structures calculated in Mercury (probe radius 0.2 Å, grid spacing 0.1 Å).

The hydrostatic compression of both species results in a significant contraction along the axis *c*, whereas the other crystallographic directions remain almost unaffected (Figure 4.3 and 4.4). This contraction is slightly more pronounced in AgFPT (18.5% at 7.94 GPa) than in CuFPT (16% at 8 GPa). This response entails a considerably approach of adjacent zig-zag chains inherent to the shortening of inter-ribbon M(2)---M(2) distances (Figure 4.5). Noteworthy, the Ag(2)---Ag(2) distance becomes shorter than the sum of van der Waals radii already at 3.25 GPa[47] eventually, at 7.94 GPa, upon a 29% shortening, reach 2.986(6) Å, being only 0.05 Å longer than in metallic silver[17]. At variance, Cu(2)---Cu(2) contacts shorten by only 13% at 8 GPa, remaining well above the van der Waals limit. The inter-ribbon M(1)---N(9) contacts are also sensitive to compression (Figure 4.6), their shortening occurs simultaneously to that of M(2)---M(2), but competing with it (Figure 4.7), and is definitely stronger in CuFPT than in AgFPT. This is related to a different hardness of unit-cell parameters: *b* is twice softer than *a* in CuFPT, while equally compressible in AgFPT (Figure 4.4). Accordingly, the structural response to compression in the two coordination polymers, while consisting in a substantial ribbons approaching, see a different role of these two contacts: in the Cu derivatives prevails the shortening of M(1)---N(9) while in the Ag one prevails that of M(2)---M(2).

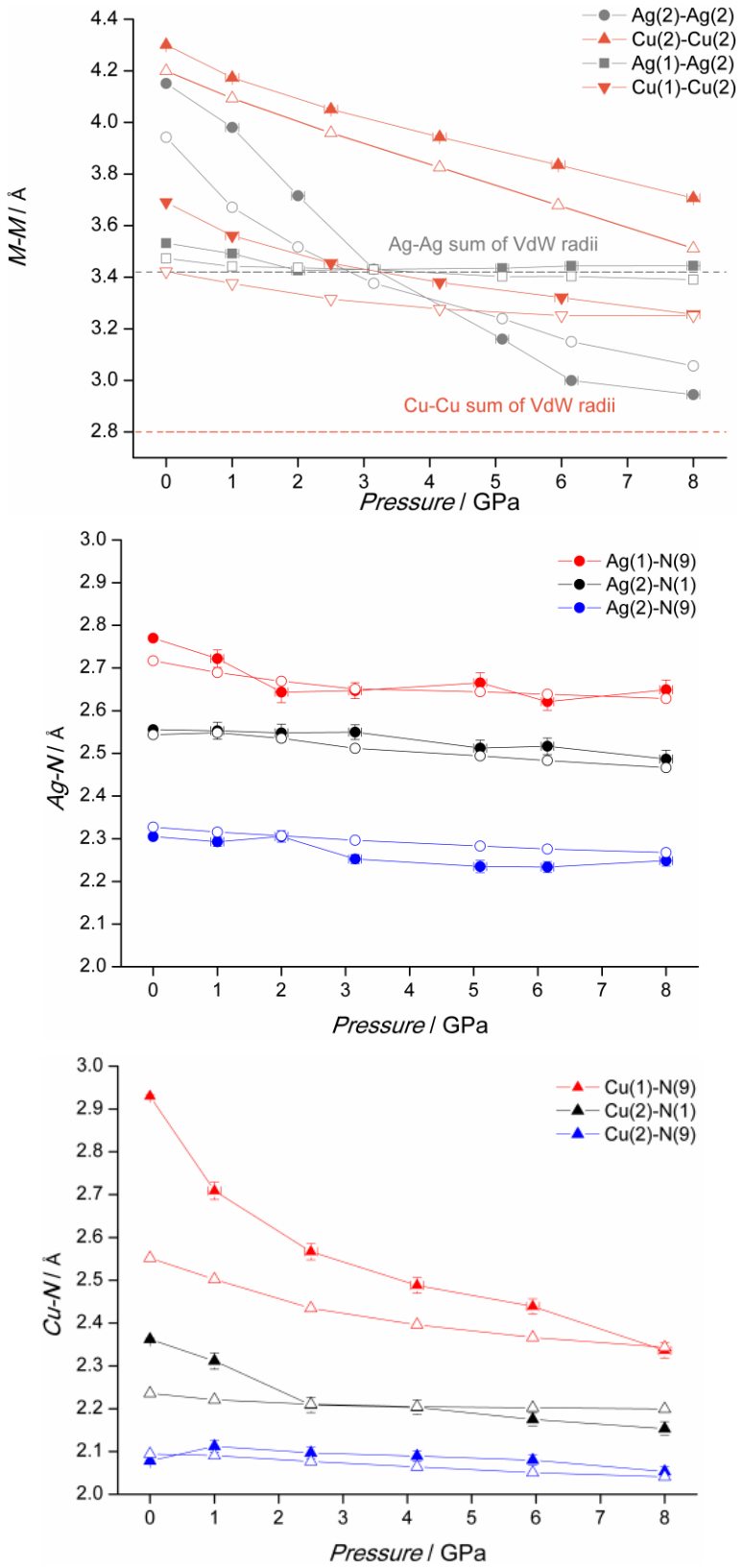

Figure 4.6. Significant experimental (bold symbol) and theoretical (empty symbol) inter-atomic distances. Estimated standard uncertainties are shown.

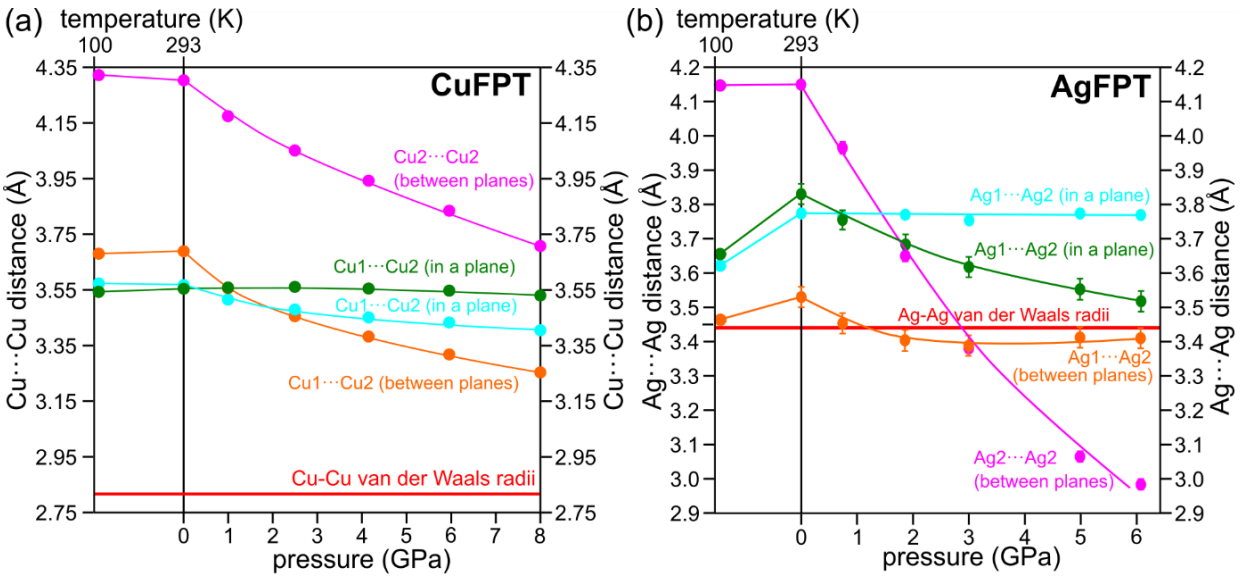

Figure 4.7. Compressibility of (a) Ag---Ag and (b) Cu---Cu interactions in a function of temperature (left) and pressure (right).

Table 4.3. Percentage difference of computed cell parameters.

	Pressure (GPa)	Δa %	Δb %	Δc %	Δβ %	ΔVolume %
AgFPT	1	-0.7	0.1	-4.5	1	-5.3
	2	-1.3	0.3	-7.8	1.6	-9
	3.15	-1.6	-0.9	-9.5	1.3	-12
	5	-2.7	-1.1	-12.2	2.7	-15.9
	6.15	-3.3	-1.3	-13.5	3	-17.8
	8	-4.5	-1.9	-14.3	3.8	-20.3
CuFPT	1	-0.3	0.2	-4.3	1.7	-4.7
	2.5	-0.8	-1	-6.7	2.5	-8.8
	4.15	-1.2	-1.4	-9.4	3.4	-12.3
	6	-1.7	-1.8	-11.6	3.9	-15.3
	8	-1.8	-2.1	-14.2	3.8	-18.1

There are two kind of M(1)---M(2) contacts: the inter-ribbons, which, upon compression, become more and more bridged by the tetrazolate nitrogen atom N(9), and the intra-ribbons which are η^2-bridged to two tetrazolate ligands in a flat six-membered ring. Both undergo significant variation upon compression due to conformational modifications inherent to approaching ribbons and not interpretable as incipient metallophilic interactions. Hence, instead of cuprophilic interactions, M(1) centers show a much stronger affinity for tetrazolate rings (Figure 4.6, Table 4.4 and 4.5).

Plausible metallophilic interactions solely occur between ribbons, involving two M(2) cations. Despite a somewhat low quality of the diffraction, especially that of AgFTP at high pressures, the overall experimental picture is coherent with our periodic DFT calculations (Figure 4.3, 4.6 and Table 4.3). The main discrepancy concerns the Cu(1)-N(9) distances, which are predicted much shorter than experimentally measured, especially at ambient pressure. This is in part due to the temperature, which that softens even more the weaker interactions whereas it is not included in the model. Moreover, Cu atoms are associated with large atomic displacement parameters, prolated perpendicularly to the layers, speaking for a dynamical disorder. On increasing pressure, however, the atomic displacement of Cu atoms decreases, as it is expected by the tighter packing.

DFT calculations enable a detailed analysis of the chemical bonding through the topological analysis of the electron density distribution[48]. In the optimized structures, both M(1) and M(2) form four bond paths. While this is obvious for M(2), it is not surprising for the substantially trigonal M(1) (see Figure 4.3) since also weak intermolecular contacts can afford bond paths. Indeed, M(1)---N(9) is much longer and associated with much smaller electron density at the bond critical point (bcp) and smaller electron delocalization. The ambiguous stereochemistry of M(1) emerges more clearly from the calculated atomic graphs (Figure 4.8) which indicate three valence charge concentrations[49] (CCs) for M(1) (like a trigonal metal) and four ligand opposed concentrations for M(2), in keeping with a distorted trigonal pyramid. The tetrazole nitrogen atom N(9) orients one of its three charge concentrations mainly toward M(2), though slightly shifted in direction of M(1) (Figure 4.8).

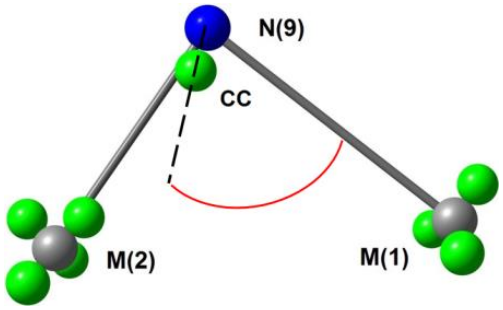

Figure 4.8. Atomic graph of M(1), N(9) and M(2) at ambient and high pressure, green points = critical points in the Laplacian representing positions of charge concentration; the angle M(1)-N(9)-CC, for M=Ag equals to 66.7 ° at 0 GPa and 65.7 ° at 8 GPa, for M=Cu equals to 68.7 ° at 0 GPa and 73.2 ° at 8 GPa.

This behavior is characteristic of semi-bridging atoms,[50] at variance from symmetric bridges, that feature a bisecting CC, or from genuinely bidentate atoms, that form two distinct CCs. The Ag(1)-N(9)-CC angle slightly decreases with pressure whereas Cu(1)-N(9)-CC increases (Figure 4.8). The most interesting analysis concerns the electron density along M(2)---M(2) (Figure 4.9a).

Once again, the two compounds differ: AgFPT features a bcp, whereas CuFPT displays only a ring critical point (rcp) and much lower electron density. The compression induces in AgFPT an even larger electron density at the bcp. At 8 GPa (with a predicted Ag(2)---Ag(2) distance of 3.06 Å), $\rho(\mathbf{r}_{bcp})$ = 0.14 eÅ^{-3}, a value very close to typical electron density associated with covalent M-M (ca. 0.2-0.3 eÅ^{-3})[50,51,52]. On the other hand, Cu(2)---Cu(2) remains longer (3.51 Å at 8 GPa) and the intermediate point remains a rcp with $\rho(\mathbf{r}_{rcp})$ << 0.1 eÅ^{-3} (see Figure 4.9a and Table 4.5).

The Laplacian of the electron density, $\nabla^2\rho$[53,54], does not show enormous difference between the two coinage metals upon compression (see Figure 4.10). On the other hand, the delocalization indexes $\delta(X,Y)$[55] clearly address the Ag(2)---Ag(2) bond formation, associated with the share of 0.1 electron pairs at 8 GPa (Figure 4.9b, 4.10), one order of magnitude larger than Cu(2)---Cu(2) or Cu(1)---Cu(2).

Out of the five different M---N contacts the three within the trigonal plane are harder than the two out of that plane both considering distances and delocalization indexes variations (Table 4.6).

The intra-ribbon Ag(2)---N(1) and, to a lesser extent, Cu(2)---N(1) the distances significantly shorten upon compression. While the three M---N in the trigonal plane are far less affected by compression. However, these variations are due to conformational modifications inherent to the approaching ribbons but not interpretable as significant changes in the nature of the pertinent bonds.

The inter-ribbons M(1)---N(9) is significantly strengthened for M=Cu (Figure 4.9b), confirming the affinity of this metal with nitrogen atoms. On the other hand, the electron delocalization of Ag(1)---N(9) is just slightly increased.

Notably, even if the rotation of the CC (Figure 4.8) could suggest that M(1)---N(9) interaction becomes stronger for Ag than for Cu, the delocalization indices behave oppositely. Indeed, such rotation correlates with (is induced by) the formation of the metallophilic interaction.

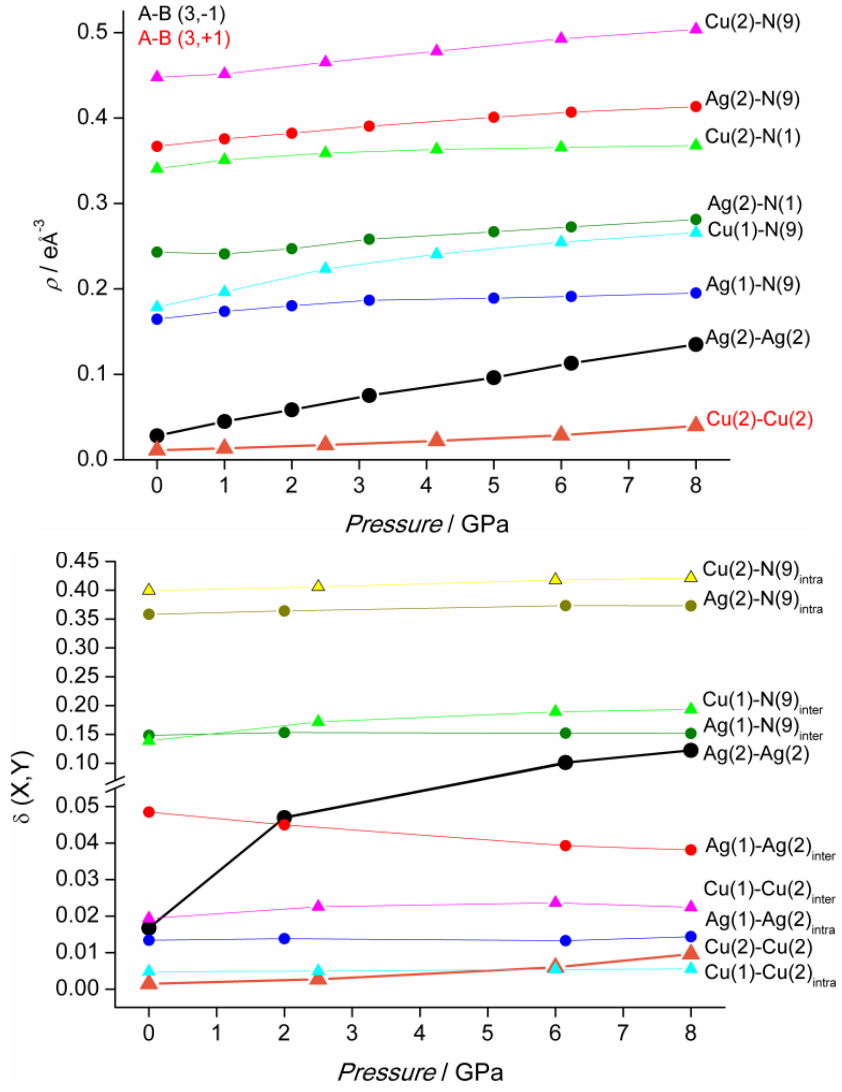

Figure 4.9. Theoretical electron density (a) in significant critical points and delocalization indexes (b) at different pressure; intra= intra-layer, inter=inter-layer.

Table 4.4. Theoretical topological analysis of AgFPT.

Pressure (GPa)	CP	type	ρ (e Å^{-3})	$\nabla^2\rho$ (e Å^{-5})	ε	dX-Y (Å)	dX-bcp (Å)	dY-bcp (Å)
0	Ag(2)-Ag(2)	(3,-1)	0.028	0.27	243[a]	3.942	1.971	1.971
	Ag(2)-Npy	(3,-1)	0.24	3.24	0.07	2.544	1.306	1.238
	Ag(1)-N(9)tz	(3,-1)	0.16	2	0.12	2.718	1.419	1.3
	Ag(2)-N(9)tz	(3,-1)	0.37	5.73	0.02	2.327	1.195	1.132
1	Ag(2)-Ag(2)	(3,-1)	0.04	0.41	1.46	3.671	1.836	1.836
	Ag(2)-Npy	(3,-1)	0.24	3.18	0.07	2.549	1.31	1.238
	Ag(1)-N(9)tz	(3,-1)	0.17	2.14	0.12	2.69	1.406	1.284
	Ag(2)-N(9)tz	(3,-1)	0.38	5.93	0.03	2.315	1.189	1.126
2	Ag(2)-Ag(2)	(3,-1)	0.06	0.53	0.71	3.517	1.758	1.758
	Ag(2)-Npy	(3,-1)	0.25	3.28	0.07	2.535	1.305	1.23
	Ag(1)-N(9)tz	(3,-1)	0.18	2.25	0.12	2.67	1.397	1.274
	Ag(2)-N(9)tz	(3,-1)	0.38	6.07	0.03	2.307	1.185	1.122
3.15	Ag(2)-Ag(2)	(3,-1)	0.08	0.69	0.57	3.376	1.688	1.688
	Ag(2)-Npy	(3,-1)	0.26	3.45	0.06	2.512	1.296	1.216
	Ag(1)-N(9)tz	(3,-1)	0.19	2.35	0.12	2.652	1.388	1.264
	Ag(2)-N(9)tz	(3,-1)	0.39	6.24	0.04	2.296	1.18	1.116
5	Ag(2)-Ag(2)	(3,-1)	0.1	0.88	0.29	3.24	1.62	1.62
	Ag(2)-Npy	(3,-1)	0.27	3.6	0.06	2.494	1.289	1.205
	Ag(1)-N(9)tz	(3,-1)	0.19	2.4	0.13	2.645	1.385	1.26
	Ag(2)-N(9)tz	(3,-1)	0.4	6.46	0.04	2.283	1.175	1.108
6.15	Ag(2)-Ag(2)	(3,-1)	0.11	1.04	0.21	3.15	1.575	1.575
	Ag(2)-Npy	(3,-1)	0.27	3.69	0.06	2.483	1.284	1.199
	Ag(1)-N(9)tz	(3,-1)	0.19	2.44	0.13	2.64	1.383	1.257
	Ag(2)-N(9)tz	(3,-1)	0.41	6.58	0.05	2.276	1.172	1.104
8	Ag(2)-Ag(2)	(3,-1)	0.14	1.24	0.14	3.056	1.528	1.528
	Ag(2)-Npy	(3,-1)	0.28	3.84	0.06	2.467	1.277	1.189
	Ag(1)-N(9)tz	(3,-1)	0.2	2.51	0.13	2.63	1.378	1.252
	Ag(2)-N(9)tz	(3,-1)	0.41	6.71	0.05	2.268	1.169	1.099

[a] Not reasonable value, probably due to the weakness of the Ag-Ag interaction at ambient condition.

Table 4.5. Theoretical topological analysis of CuFPT.

Pressure (GPa)	CP	type	ρ (e Å^{-3})	$\nabla^2\rho$ (e Å^{-5})	ε	dX-Y (Å)	dX-bcp (Å)	dY-bcp (Å)
0	Cu(2)-Cu(2)	(3,+1)	0.01	0.2		4.2	2.1	2.1
	Cu(2)-Npy	(3,-1)	0.34	5.14	0.07	2.236	1.069	1.167
	Cu(1)-N(9)tz	(3,-1)	0.18	1.67	0.11	2.552	1.258	1.294
	Cu(2)-N(9)tz	(3,-1)	0.45	8.05	0.02	2.094	1.008	1.086
1	Cu(2)-Cu(2)	(3,+1)	0.01	0.23		4.094	2.047	2.047
	Cu(2)-Npy	(3,-1)	0.35	5.37	0.07	2.221	1.063	1.158
	Cu(1)-N(9)tz	(3,-1)	0.2	1.91	0.11	2.503	1.23	1.272
	Cu(2)-N(9)tz	(3,-1)	0.45	8.16	0.02	2.09	1.007	1.084
2.5	Cu(2)-Cu(2)	(3,+1)	0.02	0.29		3.959	1.98	1.98
	Cu(2)-Npy	(3,-1)	0.36	5.53	0.07	2.21	1.06	1.151
	Cu(1)-N(9)tz	(3,-1)	0.22	2.32	0.1	2.435	1.193	1.242
	Cu(2)-N(9)tz	(3,-1)	0.47	8.51	0.02	2.077	1.001	1.076
4.15	Cu(2)-Cu(2)	(3,+1)	0.02	0.35		3.825	1.913	1.913
	Cu(2)-Npy	(3,-1)	0.36	5.58	0.06	2.205	1.059	1.146
	Cu(1)-N(9)tz	(3,-1)	0.24	2.62	0.1	2.396	1.173	1.223
	Cu(2)-N(9)tz	(3,-1)	0.48	8.86	0.02	2.064	0.996	1.068
6	Cu(2)-Cu(2)	(3,+1)	0.03	0.43		3.679	1.84	1.84
	Cu(2)-Npy	(3,-1)	0.37	5.59	0.06	2.202	1.059	1.143
	Cu(1)-N(9)tz	(3,-1)	0.25	2.88	0.1	2.367	1.159	1.208
	Cu(2)-N(9)tz	(3,-1)	0.49	9.25	0.02	2.051	0.99	1.06
8	Cu(2)-Cu(2)	(3,+1)	0.04	0.54		3.511	1.756	1.756
	Cu(2)-Npy	(3,-1)	0.37	5.59	0.06	2.2	1.059	1.14
	Cu(1)-N(9)tz	(3,-1)	0.27	3.09	0.1	2.344	1.149	1.195
	Cu(2)-N(9)tz	(3,-1)	0.5	9.56	0.03	2.041	0.986	1.055

Table 4.6. Theoretical delocalization indexes and atomic charges of AgFPT and CuFPT.

δ(X,Y)	Ag				Cu			
Pressure (GPa)	0	2	6.15	8	0	2.5	6	8
M(2)-M(2)	0.017	0.047	0.101	0.122	0.001	0.003	0.006	0.01
M(1)-M(2) interlayer	0.048	0.045	0.039	0.038	0.019	0.023	0.024	0.022
M(1)-M(2) intralayer	0.013	0.014	0.013	0.014	0.005	0.005	0.005	0.006
M(1)-N(9) interlayer	0.148	0.153	0.152	0.152	0.139	0.172	0.189	0.193
M(2)-N(9) interlayer	0.358	0.364	0.373	0.373	0.4	0.406	0.418	0.422

Q	Ag				Cu			
Pressure (GPa)	0	2	6.15	8	0	2.5	6	8
M(1)	0.614	0.618	0.629	0.633	0.766	0.769	0.774	0.776
M(2)	0.638	0.638	0.638	0.64	0.799	0.797	0.795	0.793
N(9)	-0.129	-0.127	-0.127	-0.126	-0.172	-0.176	-0.177	-0.177

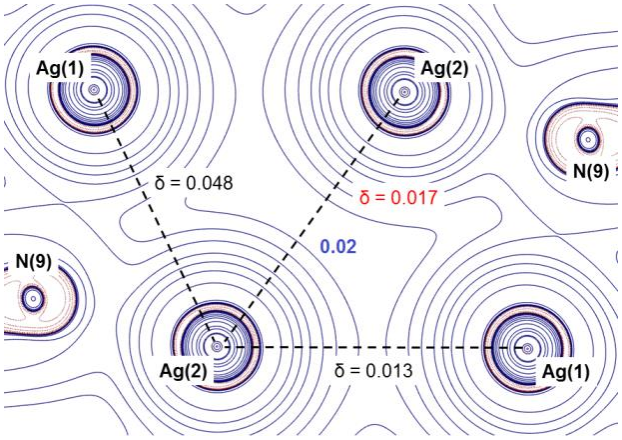

0 GPa

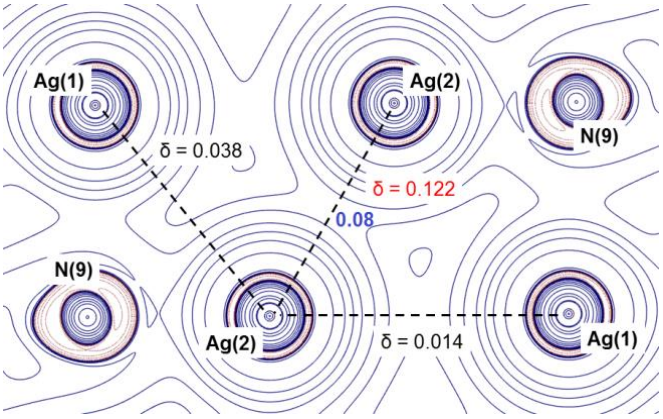

8 GPa

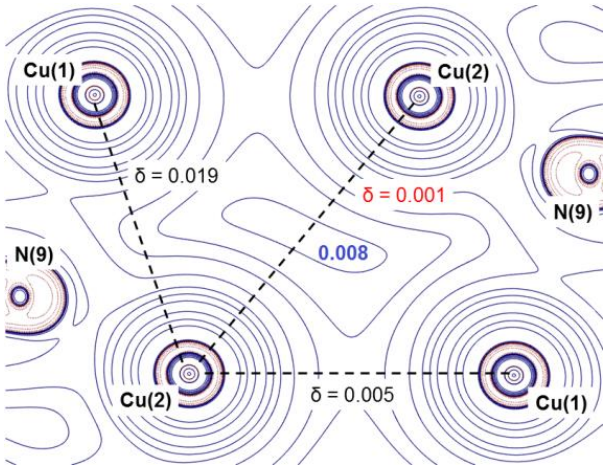

0 GPa

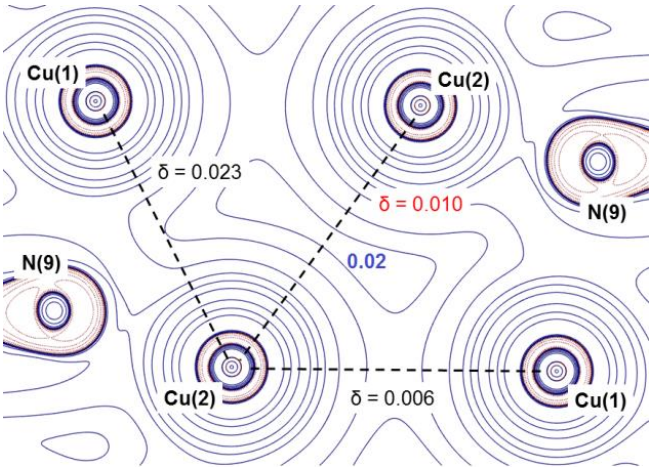

8 GPa

Figure 4.10. Maps of the theoretically calculated Laplacian of the electron density in the plane M(2)-M(1)-M(2) and delocalization indexes for M---M interactions; δ M(2)---M(2) is highlighted in red. Contours value of the Laplacian (in a.u.) are reported in blue.

4.4 Conclusions

In this chapter, we reported the first example of a metallophilic interaction induced by compression and we discuss on the difference between two Cu(I) and Ag(I) isomers, which in spite of forming isostructural polymers at ambient conditions behave differently at high pressure. In keeping with previous studies,[56,57,58] a pressure in the range 0-10 GPa is an extraordinary tool to learn more on the nature of some elusive bonding, like the metallophilic one.

In AgFTP, we observe both the establishing of a metallophilic interaction and the strengthening of the weakest Ag---N coordination (thus expanding the coordination at the metals), whereas in CuFTP only the latter occurs. This trend reveals not only a lower repulsion between Ag(I) cations, compared to Cu(I), but also a favorable repolarization of Ag(I), which enables larger electron sharing with another Ag(I).

Upon all the topological descriptor of the electron density, the delocalization index $\delta(X,Y)$ was crucial to reveal this elusive interaction. The analysis of $\nabla\rho$ and $\nabla^2\rho$ showed a notable difference between the two coinage metals, particularly the M(2)---M(2) are topologically different.

Nevertheless, $\delta(X,Y)$ address and quantify the notable increment in the electron sharing between two Ag(2) atoms. Moreover, the delocalization index could be calculated also for other metal pairs, even if not connected by bcp, and used to reveal their metallophilic attitude.

4.5 References

(1) Pyykkö, P.; Li, J.; Runeberg, N. Predicted Ligand Dependence of the Au(I)...Au(I) Attraction in $(XAuPH_3)_2$. *Chem. Phys. Lett.* **1994**, *218* (1–2), 133–138.

(2) Li, J.; Pyykkö, P. Relativistic Pseudo-Potential Analysis of the Weak Au(I)...Au(I) Attraction. *Chem. Phys. Lett.* **1992**, *197* (6), 586–590.

(3) Pyykkö, P.; Runeberg, N.; Mendizabal, F. Theory of the d^{10}–d^{10} Closed-Shell Attraction: 1. Dimers Near Equilibrium. *Chem. - A Eur. J.* **1997**, *3* (9), 1451–1457.

(4) Pyykkö, P.; Mendizabal, F. Theory of the d^{10}–d^{10} Closed-Shell Attraction: 2. Long-Distance Behaviour and Nonadditive Effects in Dimers and Trimers of Type $[(x\text{-}Au\text{-}L)_n]$ (n = 2, 3; X = Cl, I, H; L = PH_3, PMe_3, -N≡CH). *Chem. Eur. J.* **1997**, *3* (9), 1458–1465.

(5) Pyykkö, P.; Mendizabal, F. Theory of d^{10}–d^{10} Closed-Shell Attraction. III. Rings. *Inorg. Chem.* **1998**, *37* (12), 3018–3025.

(6) Mehrotra, P. K.; Hoffmann, R. Cu(I)-Cu(I) Interactions. Bonding Relationships in d^{10}–d^{10} Systems. *Inorg. Chem.* **1978**, *17* (8), 2187–2189.

(7) Jansen, M. Über Die Silberteilstrukturen in Silberreichen Oxiden*. *J. Less-Common Met.* **1980**, *76*, 285–292.

(8) Sculfort, S.; Braunstein, P. Intramolecular d^{10}–d^{10} Interactions in Heterometallic Clusters of the Transition Metals. *Chem. Soc. Rev.* **2011**, *40* (5), 2741.

(9) Görling, A.; Rösch, N.; Ellis, D. E.; Schmidbaur, H. Electronic Structure of Main-Group-Element-Centered Octahedral Gold Clusters. *Inorg. Chem.* **1991**, *30* (21), 3986–3994.

(10) Pyykkö, P. Theoretical Chemistry of Gold. III. *Chem. Soc. Rev.* **2008**, *37* (9), 1967.

(11) Cotton, F. A.; Feng, X.; Timmons, D. J. Further Study of Very Close Nonbonded Cu(I)-Cu(I) Contacts. Molecular Structure of a New Compound and Density Functional Theory Calculations. *Inorg. Chem.* **1998**, *37* (16), 4066–4069.

(12) Vickery, J. C.; Olmstead, M. M.; Fung, E. Y.; Balch, A. L. Solvent-Stimulated Luminescence from the Supramolecular Aggregation of a Trinuclear Gold(I) Complex That Displays Extensive Intermolecular Au·Au Interactions. *Angew. Chemie Int. Ed. English* **1997**, *36* (11), 1179–1181.

(13) Schmidbaur, H.; Cronje, S.; Djordjevic, B.; Schuster, O. Understanding Gold Chemistry through Relativity. *Chem. Phys.* **2005**, *311* (1–2 SPEC.ISS.), 151–161.

(14) Hermann, H. L.; Boche, G.; Schwerdtfeger, P. Metallophilic Interactions in Closed-Shell Copper (I) Compounds – A Theoretical Study. *Chem. Eur. J.* **2001**, *7* (24), 5333–5342.

(15) Schmidbaur, H.; Schier, A. Mercurophilic Interactions. *Organometallics* **2015**, *34* (11), 2048–2066.

(16) Schmidbaur, H.; Schier, A. Aurophilic Interactions as a Subject of Current Research: An up-Date. *Chem. Soc. Rev.* **2012**, *41* (1), 370–412.

(17) Schmidbaur, H.; Schier, A. Argentophilic Interactions. *Angewandte Chemie - International Edition*. 2015, pp 746–784.

(18) Carvajal, M. A.; Alvarez, S.; Novoa, J. J. The Nature of Intermolecular CuI···CuI Interactions: A Combined Theoretical and Structural Database Analysis. *Chem. - A Eur. J.* **2004**, *10* (9), 2117–2132.

(19) Jia, J.; Wang, Q. Intensely Luminescent Gold(I)-Silver(I) Cluster with Hypercoordinated Carbon. *J. Am. Chem. Soc.* **2009**, *131*, 16634–16635.

(20) Benito, Q.; Baptiste, B.; Polian, A.; Delbes, L.; Martinelli, L.; Gacoin, T.; Boilot, J. P.; Perruchas, S. Pressure Control of Cuprophilic Interactions in a Luminescent Mechanochromic Copper Cluster. *Inorg. Chem.* **2015**, *54* (20), 9821–9825.

(21) Weber, D.; Gagné, M. R. *Aurophilicity in Gold(I) Catalysis: For Better or Worse?. In: Slaughter L. (Eds) Homogeneous Gold Catalysis. Topics in Current Chemistry, Vol 357. Springer, Cham*; 2014.

(22) Schwerdtfeger, P.; Lein, M. *Gold Chemistry: Applications and Future Directions in the Life Sciences, Ed. F. Mohr, Wiley-VCH, Weinheim.*; 2009.

(23) Pyykkö, P. Relativistic Effects in Structural Chemistry. *Chem. Rev.* **1988**, *88* (3), 563–594.

(24) O'Grady, E.; Kaltsoyannis, N. Does Metallophilicity Increase or Decrease down Group 11? Computational Investigations of $[Cl–M–PH_3]_2$ (M = Cu, Ag, Au, [111]). *Phys. Chem. Chem. Phys.* **2004**, *6* (4), 680–687.

(25) Goodwin, A. L.; Keen, D. A.; Tucker, M. G. Large Negative Linear Compressibility of $Ag_3[Co(CN)_6]$. *Proc. Natl. Acad. Sci.* **2008**, *105* (48), 18708–18713.

(26) Cairns, A. B.; Thompson, A. L.; Tucker, M. G.; Haines, J.; Goodwin, A. L. Rational Design of Materials with Extreme Negative Compressibility: Selective Soft-Mode Frustration in $KMn[Ag(CN)_2]_3$. *J. Am. Chem. Soc.* **2012**, *134*, 4454–4456.

(27) Paliwoda, D.; Wawrzyniak, P.; Katrusiak, A. Unwinding $Au^{+}\cdots Au^{+}$ Bonded Filaments in Ligand-Supported Gold(I) Polymer under Pressure. *J. Phys. Chem. Lett.* **2014**, *5* (13), 2182–2188.

(28) Korčok, J. L.; Katz, M. J.; Leznoff, D. B. Impact of Metallophilicity on "Colossal" Positive and Negative Thermal Expansion in a Series of Isostructural Dicyanometallate Coordination

Polymers. *J. Am. Chem. Soc.* **2009**, *131* (13), 4866–4871.

(29) Merrill, L.; Bassett, W. A. Miniature Diamond Anvil Pressure Cell for Single Crystal X-Ray Diffraction Studies. *Rev. Sci. Instrum.* **1974**, *45* (2), 290–294.

(30) Angel, R. J.; Bujak, M.; Zhao, J.; Gatta, G. D.; Jacobsen, S. D. Effective Hydrostatic Limits of Pressure Media for High-Pressure Crystallographic Studies. *J. Appl. Crystallogr.* **2007**, *40* (1), 26–32.

(31) Mao, H. K.; Xu, J.; Bell, P. M. Calibration of the Ruby Pressure Gauge to 800 Kbar under Quasi-Hydrostatic Conditions. *J. Geophys. Res.* **1986**, *91* (B5), 4673.

(32) Piermarini, G. J.; Block, S.; Barnett, J. D.; Forman, R. A. Calibration of the Pressure Dependence of the R1ruby Fluorescence Line to 195 Kbar. *J. Appl. Phys.* **1975**, *46* (6), 2774–2780.

(33) Agilent Technologies: CrysAlisPRO Software System, Version 1.171.37.35g, Agilent Technologies UK Ltd, Oxford, UK,(2014).; Agilent Technologies: CrysAlisPRO Software system, version 1.171.37.35g, Agilent Technologies UK Ltd, Oxford, UK, (2014).

(34) Sheldrick, G. M. A Short History of SHELX. *Acta Crystallogr. Sect. A* **2008**, *64*, 112–122.

(35) Dolomanov, O. V.; Bourhis, L. J.; Gildea, R. J.; Howard, J. A. K.; Puschmann, H. OLEX2: A Complete Structure Solution, Refinement and Analysis Program. *J. Appl. Crystallogr.* **2009**, *42* (2), 339–341.

(36) Dovesi, R.; Orlando, R.; Erba, A.; Zicovich-wilson, C. M.; Civalleri, B.; Casassa, S.; Maschio, L.; Ferrabone, M.; Pierre, M. D. La; Arco, P. D.; *et al.* CRYSTAL 14 : A Program for the Ab Initio Investigation of Crystalline Solids. *Int. J. Quantum Chem.* **2014**, No. 114, 1287–1317.

(37) Becke, A. D. Density-Functional Thermochemistry.III. The Role of Exact Exchange. *J. Chem. Phys.* **1993**, *98* (7), 5648.

(38) Lee, C.; Yang, W.; Parr, R. G. Development of the Colle-Salvetti Correlation-Energy Formula into a Functional of the Electron Density. *Phys. Rev. B* **1988**, *37* (2), 785–789.

(39) Grimme, S. Semiempirical GGA-Type Density Functional Constructed with a Long-Range Dispersion Correction. *J. Comput. Chem.* **2006**, *27* (15), 1787–1799.

(40) Doll, K.; Harrison, N. M. Chlorine Adsorption on the Cu(111) Surface. *Chem. Phys. Lett.* **2000**, *317* (February), 282–289.

(41) Doll, K.; Harrison, N. M. Theoretical Study of Chlorine Adsorption on the Ag(111) Surface. *Phys. Rev. B - Condens. Matter Mater. Phys.* **2001**, *63* (16), 2–7.

(42) Andrae, D.; Häußermann, U.; Dolg, M.; Stoll, H.; Preuß, H. T. Energy-Adjusted Ab Initio

Pseudopotentials for the Second and Third Row Transition Elements. *Theor. Chim. Acta* **1990**, *77* (2), 123–141.

(43) Rabiller, P.; Souhassou, M.; Katan, C.; Gatti, C.; Lecomte, C. Accuracy of Topological Analysis of Gridded Electron Densities. *J. Phys. Chem. Solids* **2004**, *65* (12), 1951–1955.

(44) Gaussian 16, R. B. 0.; Frisch, M. J.; Trucks, G. W.; Schlegel, H. B.; Scuseria, G. E.; Robb, M. A.; Cheeseman, J. R.; Scalmani, G.; Barone, V.; Petersson, G. A.; *et al.* Gaussian16. 2016, p Gaussian, Inc., Wallingford CT.

(45) AIMAll (Version 17.01.25), Todd A. Keith, TK Gristmill Software, Overland Park KS, USA, 2017 (Aim.Tkgristmill.Com).

(46) Zhang, X. M. Hydro(Solvo)Thermal in Situ Ligand Syntheses. *Coord. Chem. Rev.* **2005**, *249* (11–12), 1201–1219.

(47) Bondi, A. Van Der Waals Volumes and Radii. *J. Phys. Chem.* **1964**, *68* (3), 441–451.

(48) Bader, R. F. W. Atoms in Molecules. *Acc. Chem. Res.* **1995**, *18* (1), 9–15.

(49) Bader, R. F. W.; Macdougall, P. J.; Lau, C. D. H. Bonded and Nonbonded Charge Concentrations and Their Relation to Molecular Geometry and Reactivity. *J. Am. Chem. Soc.* **1984**, *106* (6), 1594–1605.

(50) Macchi, P.; Sironi, A. Chemical Bonding in Transition Metal Carbonyl Clusters: Complementary Analysis of Theoretical and Experimental Electron Densities. *Coordination Chemistry Reviews*. 2003, pp 383–412.

(51) Macchi, P.; Proserpio, D. M.; Sironi, A. Experimental Electron Density in a Transition Metal Dimer : Metal–Metal and Metal–Ligand Bonds. *J. Am. Chem. Soc.* **1998**, *120* (51), 13429–13435.

(52) Macchi, P.; Garlaschelli, L.; Sironi, A. Electron Density of Semi-Bridging Carbonyls. Metamorphosis of CO Ligands Observed via Experimental and Theoretical Investigations on $[FeCo(CO)_8]^-$. *J. Am. Chem. Soc.* **2002**, *124* (47), 14173–14184.

(53) Antes, I.; Frenking, G. Structure and Bonding of the Transition Metal Methyl and Phenyl Compounds MCH_3 and MC_6H_5 (M = Cu, Ag, Au) and $M(CH_3)_2$ and $M(C_6H_5)_2$ (M = Zn, Cd, Hg). *Organometallics* **1995**, *14* (6), 4263–4268.

(54) Macchi, P.; Donghi, D.; Sironi, A. The Electron Density of Bridging Hydrides Observed Via. *J. Am. Chem. Soc.* **2005**, *127*, 16494–16504.

(55) Bader, R. F. W.; Stephens, M. E. Spatial Localization of the Electronic Pair and Number Distributions in Molecules. *J. Am. Chem. Soc.* **1975**, *97* (26), 7391–7399.

(56) Scherer, W.; Dunbar, A. C.; Barquera-Lozada, J. E.; Schmitz, D.; Eickerling, G.; Kratzert,

D.; Stalke, D.; Lanza, A.; Macchi, P.; Casati, N. P. M.; *et al.* Anagostic Interactions under Pressure: Attractive or Repulsive? *Angew. Chemie - Int. Ed.* **2015**, *54* (8), 2505–2509.

(57) Casati, N.; Macchi, P.; Sironi, A. Molecular Crystals under High Pressure: Theoretical and Experimental Investigations of the Solid-Solid Phase Transitions in $[Co_2(CO)_6(XPh_3)_2]$ (X = P, As). *Chem. - A Eur. J.* **2009**, *15* (17), 4446–4457.

(58) Macchi, P.; Casati, N.; Evans, S. R.; Gozzo, F.; Simoncic, P.; Tiana, D. An "Off-Axis" Mn–Mn Bond in $Mn_2(CO)_{10}$ at High Pressure. *Chem. Commun.* **2014**, *50* (85), 12824–12827.

Chapter 5

Metal-Organic Frameworks as Low Dielectric Constant Materials

5.1 Introduction

5.1.1 Low dielectric Constant Materials

The constant miniaturization of microelectronic devices towards smaller and smaller scale requires low dielectric constant materials to guarantee performance and reduce unwanted processes.

Increment of transistor density augmented the operating speed and computing performance. However, cross-talk and noise are becoming more and more important issues in transistor technology. The impact of delay is indeed inherently correlated to the miniaturization into nanometer regimes. In this context, the usage of low dielectric constant materials as interlayer materials can reduce the noise.[1] Moreover, interwire dielectrics materials are also crucial in the dynamics of power dissipation.[2,3] The impact of dielectrics on the performance of microelectronics devices is evident and the research in this field is vital.

The dielectric constant or relative permittivity, ε_r (or *k* depending on the convention) is a dimensionless quantity describing the behavior of a material exposed to an external electric field, in particular its polarization. In the following work, we will refer to the relative permittivity of a film, or better, of a disk-shaped pellet, which is expressed as follows:

$$\varepsilon_r = \frac{Cd}{\varepsilon_0 A} \tag{5.1}$$

Where d is the thickness of the film, C is the capacitance, A is the area of the electrode and ε_0 is the dielectric permittivity in vacuum.

The static dielectric constant is related to the polarizability (α) by the equation

$$\varepsilon = 1 + \frac{(4\pi\alpha)}{V} \qquad (5.2)$$

Where V is the considered volume. The polarizability of a molecular system describes the deformability of its electron distribution.

From equation (5.2), it emerges that the higher the polarizability, the higher the dielectric constant. Consequently, an efficient insulator must be poorly polarizable. Because the polarizability of a material roughly depends on the amount of electrons, porous dielectric materials[2] are good candidates for low-dielectric constant materials.

Indeed, a correlation exist between degree of porosity and dielectric constant[2,4] (Figure 5.1). Nevertheless, characterization and evaluation of porosity is not always easy and simplified assumptions have to be introduced.[5]

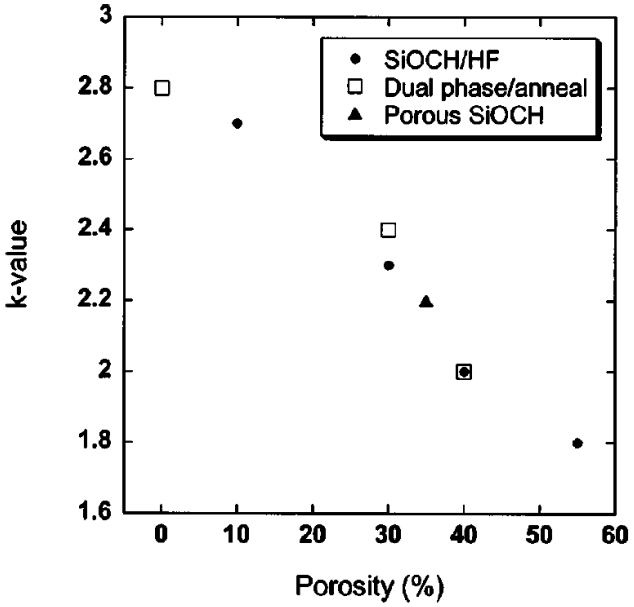

Figure 5.1. Dielectric constant versus total porosity for different SiOCH materials (reference 2).

Silica based systems have been the most used and efficient low dielectric constant materials so far. SiO_2 is chemically and thermally stable, but all kinds of silica feature a quite dense structure.

Indeed, the dielectric constant of quartz is ca. 4. On the other hand, amorphous silicas are much less dense (2.1 – 2.3 g/cm^3) therefore their dielectric constant is spread in a range between 4 and 2.15.

The quite high value of quartz and silica is strictly related to the notable polarizability of Si-O. To overcome this problem and lower the dielectric constant, oxygen have been substitute with fluorine in the so called F doped silica glassed (FSG).[6] The Si-F bond is indeed less polarizable.

Another solution is doping with carbon, introducing for example CH_3 group.[7] Then, the evolution of insulators in microprocessors moved toward organosilicate porous materials SiCOH, having a dielectric constant range of 2.2 – 2.7.[8–10]

Porosity in this class of insulators is anyhow difficult to control and characterize, moreover, porosity weakens mechanical stability.[11,12]

In this context, metal-organic frameworks (MOFs) have been recently proposed as solution in the research of new low dielectric constant materials.[13] Their notable mechanical and thermal stability are fundamental requirements for applications in microelectronic devices.[14] Moreover, the high and uniform porosity, which characterize this class of (crystalline) materials, makes them particularly promising as next generation insulators.[15]

5.1.2 Metal-Organic Frameworks

Metal-organic frameworks (MOFs) are a class of *Porous Coordination Polymer* (PCP) with permanent and uniform porosity[16], widely studied during last decades.[17] They are mainly crystalline materials, hence easily characterizable through single crystal/powder x-ray diffraction. A material in crystal form is normally preferable for a more efficient control of the properties.

MOFs are synthetized by self-assembling of metal ions or clusters (*nodes*) with organic ligands (*linkers*). The combination of metallic nodes and organic linkers induced the definition of hybrid inorganic-organic material. The nature of the node is crucial for the dimensionality of the network. Linkers connect at least two nodes, allowing the formation of polymeric structures.[18,19] An important part of the linker is the *spacer*¸ which determines the size and the rigidity of the frame (Figure 5.2).

An important concept in the chemistry of MOFs is the one of the secondary building units (SBUs).[20] Here is reported the definition given by Eddoudi *et al.*: ”*Molecular complexes and clusters entities in which ligand coordination modes and metal coordination environments can be utilized in the transformation of these fragments into extended porous networks using polytopic linkers*”.[21]

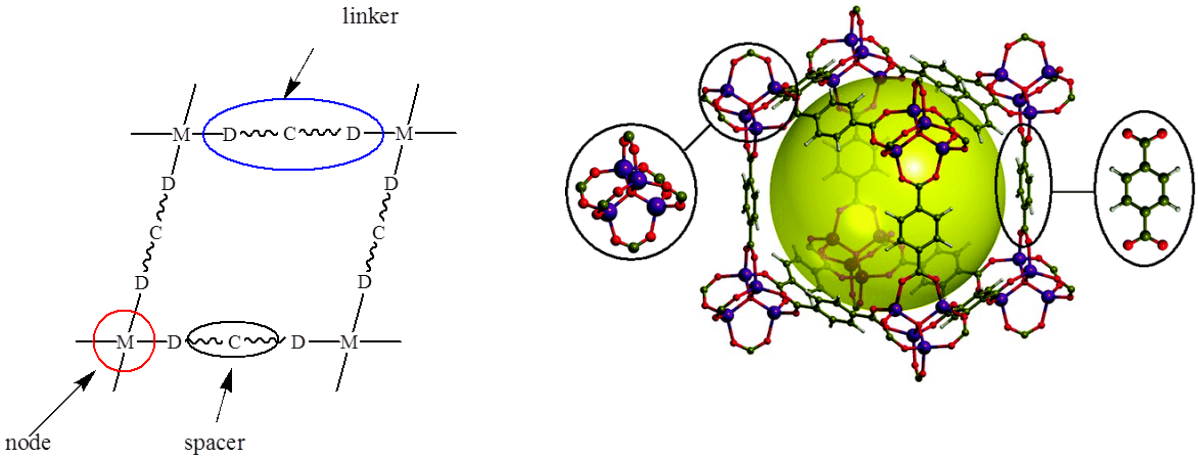

Figure 5.2. Left side, schematic representation of nodes, spacers and linkers; right side, the same representation using balls-and-sticks.

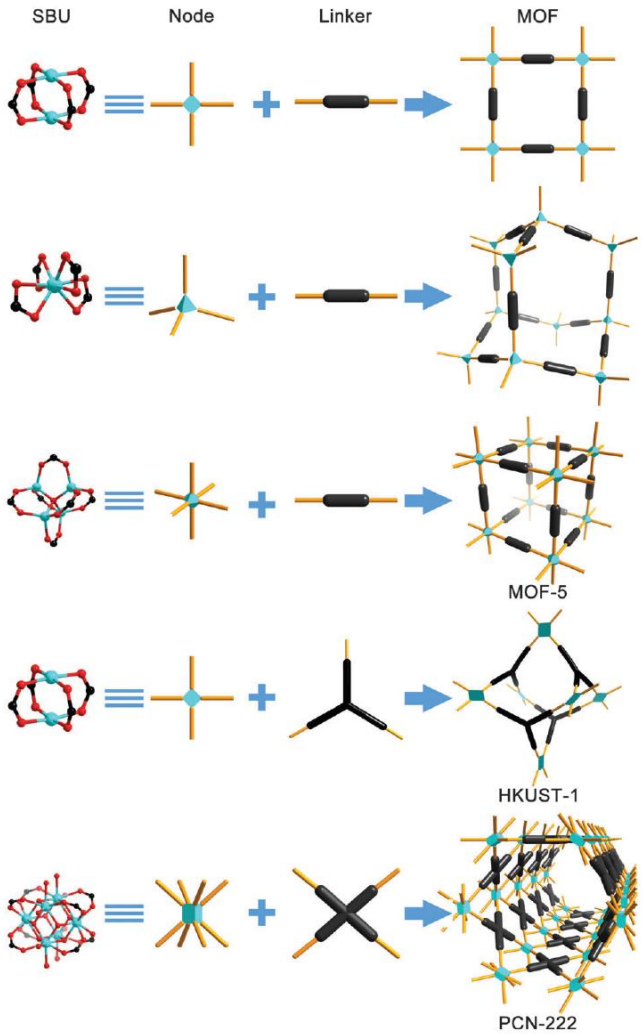

Figure 5.3. Combination of SBUs with linkers.

Three generations of MOFs can be identified based on their behavior upon absorption/desorption of guest molecules.[22] The first generation has cavities, filled with solvent molecules or ions, which collapse when guests are removed. Second generation, combining rigid secondary building units and organic linkers, possesses frameworks able to maintain the porosity even in the absence of guests. In this way, it is possible to design and predict the reticular structure by selecting the appropriate molecular building blocks (Figure 5.3).[23] For example, the combination of the cluster $Zn_4O(CO_2)_6$, which is a SBU with octahedral connection, was used by Eddaodi *et al.* in combination with carboxylate based linkers to synthetize a wide number of isoreticular 3D MOFs (IRMOFs).[24] In Figure 5.4, MOF-5, IRMOF-6 and IRMOF-8 are shown. Guest molecules play as well an important templating role in the building of the network.[25]

Finally, third generation, also known as *breathing MOFs*, has flexible structures with guest dependent pore sizes.[26]

Moreover, four classes of porosity can be identified: 0D or cavities, 1D or channels, 2D or Layers and 3D or intersecting channels (Figure 5.5).[27]

Guests can be evacuated from the framework, in a process called *activation*. MOFs can lose guest molecules without degradation of the frame in some cases.[28] The activation is usually carried out heating the sample and/or applying vacuum. An activated MOF may be ready to host new (perhaps different) molecules. For this reason, MOFs have been extensively studied for applications in fields like gas storage[29], catalysis[30,31], sensing[32,33], biomedicine[34], electronic/opto-electronic[35] and others.[36–39]

Properties like high stability, uniform porosity, extended surface area and low density are central in electronic device's applications. Indeed, many predictions and theoretical studies support the idea of using metal-organic porous materials as insultors[40–42], but from the experimental point of view only few progresses occurred.[43–45]

The use-oriented research for their application as ultra-low dielectric constant materials is indeed still in its infancy.

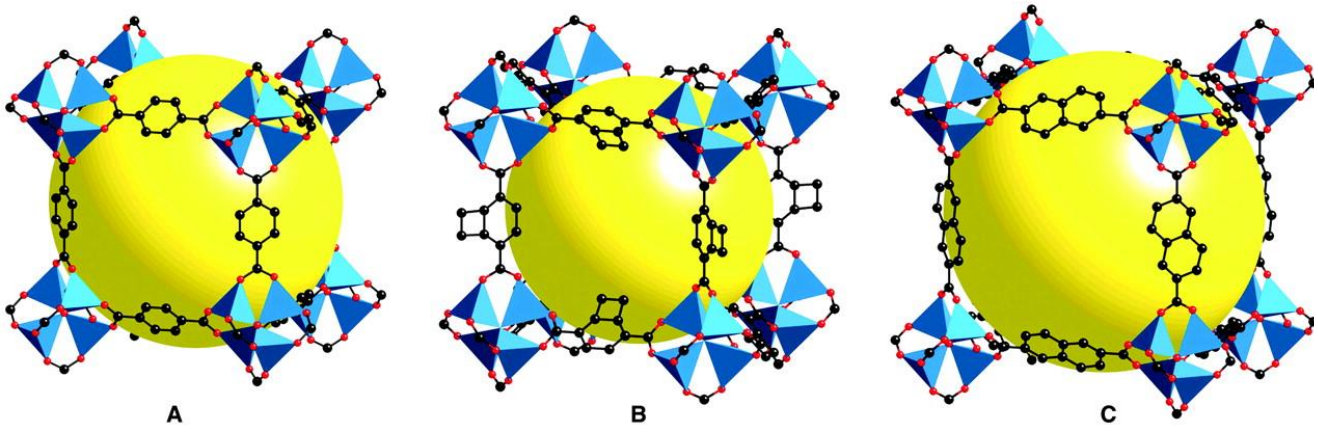

Figure 5.4. Pores size of (A) MOF-5, (B) IRMOF-6 and (C) IRMOF-8.

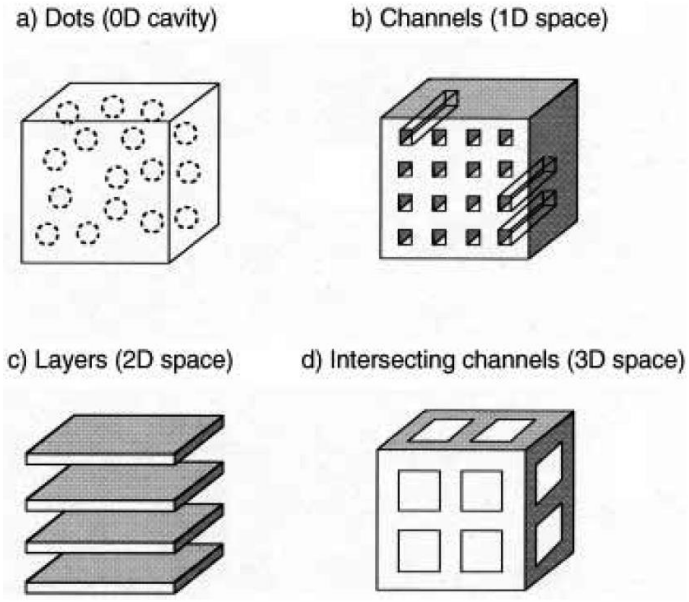

Figure 5.5. Representation of the different dimensionality (0D, 1D, 2D and 3D) of porosity.

5.1.3 Azolate based MOFs

Among the virtually infinite number of MOFs, Metal-Azolate Frameworks (MAFs) are remarkable for their high thermal and chemical stability[46–48], and so, suitable in the microelectronic field of application. In MAFs, the linker is an organic molecule with an azole group, used for the coordination to a metal center. An Azole is a five-member unsaturated N-heterocycle, with up to four nitrogen atoms. In Figure 5.6 are reported azole/azolate rings with increasing number of nitrogen atoms all sharing the sp^2 hybridization.

The more are the nitrogen atoms, the higher is the polytopic character of the linker and the lower its basicity. In particular, tetrazolate ring display a large number of coordination opportunities (figure 5.7). The deprotonation of the ring has the effect of both making one N atom available, thus enhancing the topicity of the ligand, and increasing its basicity, strengthening the coordination with metal ions. Basicity and high number of donor atoms make azolate rings exceptional linkers for coordination polymers and porous materials.[47,49] The acidity of tetrazole is comparable with that of carboxylic acids, so the deprotonation is easily induced. In MAFs, the metal centers are normally saturated by the interactions with the azolate ligands, thus providing exceptional chemical stabilities.[47] This is at variance from carboxylate-based MOFs, where guest molecules often interact with the unsaturated metal center.[50] Moreover, MAFs have usually a weak absorption affinity, due to a notable hydrophobicity of the azolate ligands.[51]

ZIFs (zeolitic imidazolate frameworks) are probably the most famous class of azolate frameworks.[46] The extended surface area (1.810 m^2/g) and notable thermal stability (up to 550 °C) of ZIF-8, combined to its chemical resistance, promoted the investigation of this material for application in microelectronics devices.[45]

Tetrazolate ligands have recently attracted attention in the field of porous coordination polymers because of their coordination behavior and their easy and environment friendly synthesis from nitrile derivates.[46,49] This synthesis allows one to obtain many poly-tetrazolate ligands with different spacers having different stereochemical flexibilities and properties.[53] For example, Long and co-workers obtained several highly porous and stable MOFs based on 1,4-benzeneditetrazolate with interesting hydrogen storage properties.[54] Tetrazolates have flexible and unique coordination modes, which are promising for stable, highly porous materials. In fact, MOFs based on tetrazolate ligands have been recently studied for their luminescence[55–58] and magnetic[59] properties and for application in CO_2 absorption[60], gas separation[61] and catalysis[62].

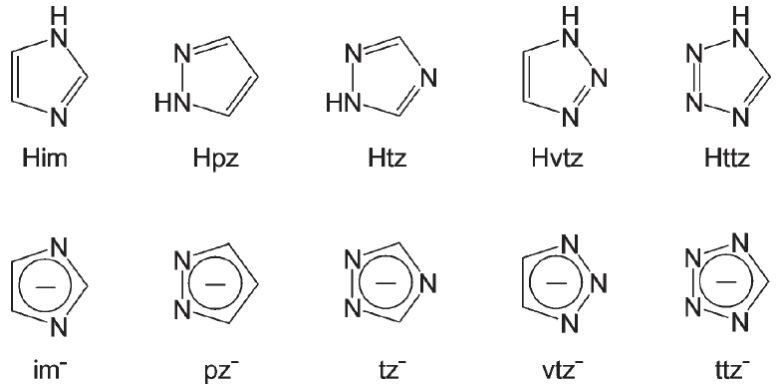

Figure 5.6. Imidazole, pyrazole, 1,2,4-triazole, 1,2,3-triazole, tetrazole and the corresponding deprotonated anion (azolates or azolides).

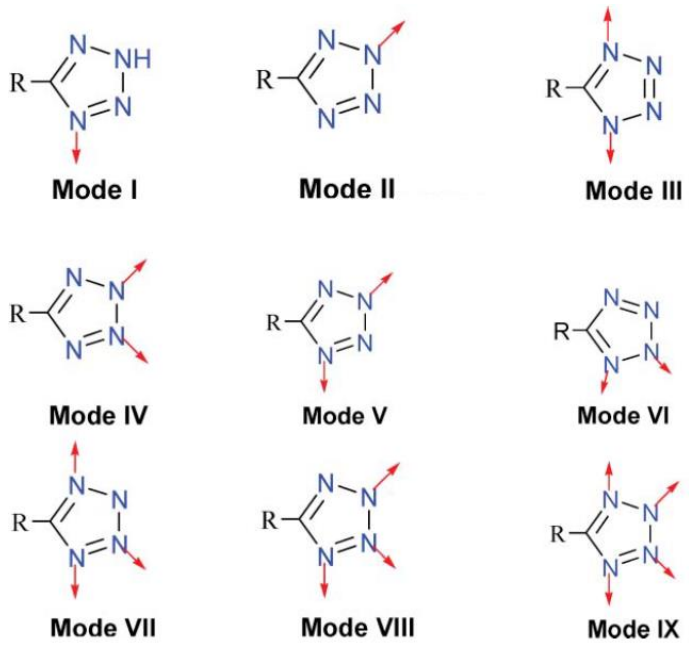

Figure 5.7. Possible coordinative modes of the tetrazolate ring.

5.2 2D network Metal Azolate-Frameworks, a novel low dielectric constant materials

In order to verify and quantify the performances of azolate based MOFs as low dielectric constant materials, we selected a bi-dimensional MOF based on the linker L=5-(4-pyridyl)tetrazolate and solvated with ethanol, Cu(L)·2EtOH (**1**).[55] It presents a network of two-dimensional layers stacked through π-π interactions. Copper atoms are planar-coordinated with three different rings: one pyridine and two tetrazolate. The linkers are planar, which favor the stacking of the layers. One-dimensional pores, filled by ethanol molecules, extend perpendicularly with respect to the layers. Two different kinds ethanol molecules are present: one is hydrogen-bond coordinated to the tetrazolate ring, specifically with the lateral nitrogen not coordinated to a metal center, whereas the second one interacts with the first molecule of ethanol through the hydroxyl group. The interlayer distance is of 3.14 Å (at 100 °K).[56]

The effects of the activation of the MOF on the electronic properties and the nature of the interatomic interactions were investigated both via high resolution x-ray diffraction experiments and theoretical computations. The evaluation of the dielectric constant was carried out through impedance spectroscopy.

5.2.1 Synthesis of 1

1 was synthesized according to an improved procedure with respect to that reported by Wang *et al.*[55]: in a 23-mL Teflon-lined autoclave, a mixture of CuI (0.5 mmol, 0.095 g), HL (1 mmol, 0.147 mg), EtOH (10 ml) and $NH_3 \cdot H_2O$ (25%, 2 ml) was stirred for about 10 min in air, closed, heated at 120 °C for 72 h and cooled to RT in about 20 h (5 °C/h). With this procedure, we were able to enhance the purity of the product, containing mostly yellow crystals, used for single crystal X-ray diffraction. The elemental analysis (H, C, N) for **1** ($C_{28}H_{28}N_{20}O_2Cu_4$, Mw = 930.86 g/mol), was carried out: Anal. Calc. (%) H: 3.03; C: 36.16, N: 30.09. Found (%) H: 2.77, C: 35.69, N: 29.94. All the solvents and the reagents were obtained from commercial suppliers and used as received. Elemental analyses were obtained with a Perkin Elmer CHN Analyzer 2400 Series II.

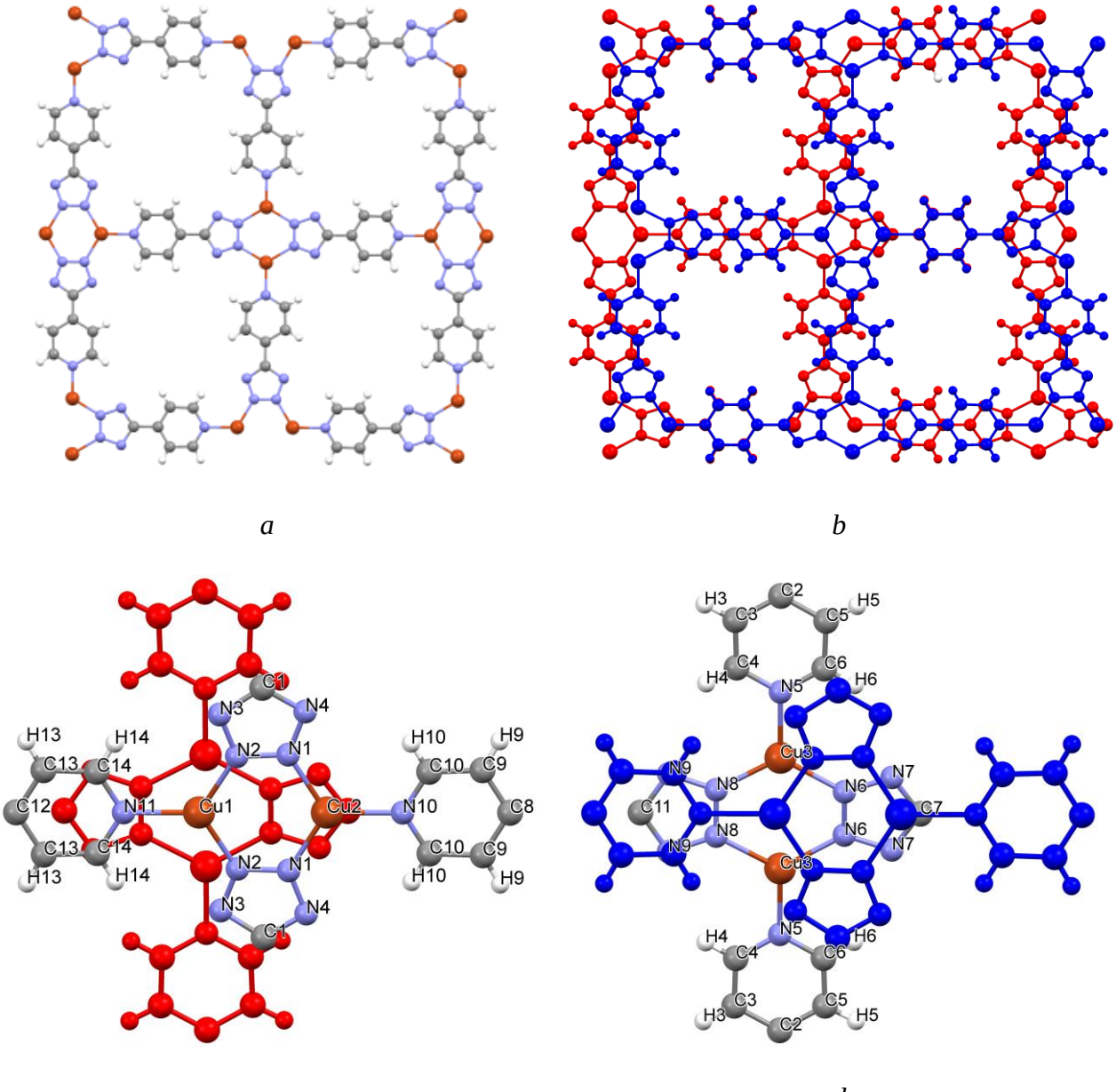

Figure 5.8 *a*=single layer, *b*=packing motif along the *a* cell parameter, *c*=labels of the upper layer, *d*=labels of the lower layer.

5.2.2 Thermogravimetric analysis

The thermogravimetric (TG) analysis on single crystals on **1** (Figure 5.9) showed that the guest molecules of ethanol are released between 50 °K and 280 °K, corresponding to a weight loss of 8.98% (whereas the theoretical value is 9.90%, assuming a site-occupation of 100%). The decomposition started at 280 °C and finished at 340 °C.

A plateau was visible in the range of temperature between 255-280 °C. Thermogravimetric analysis was performed with a TGA/SDTA 851e instrument under N_2, from 30 °C up to 650 °C, increasing the temperature with a rate of 5 °C min^{-1}.

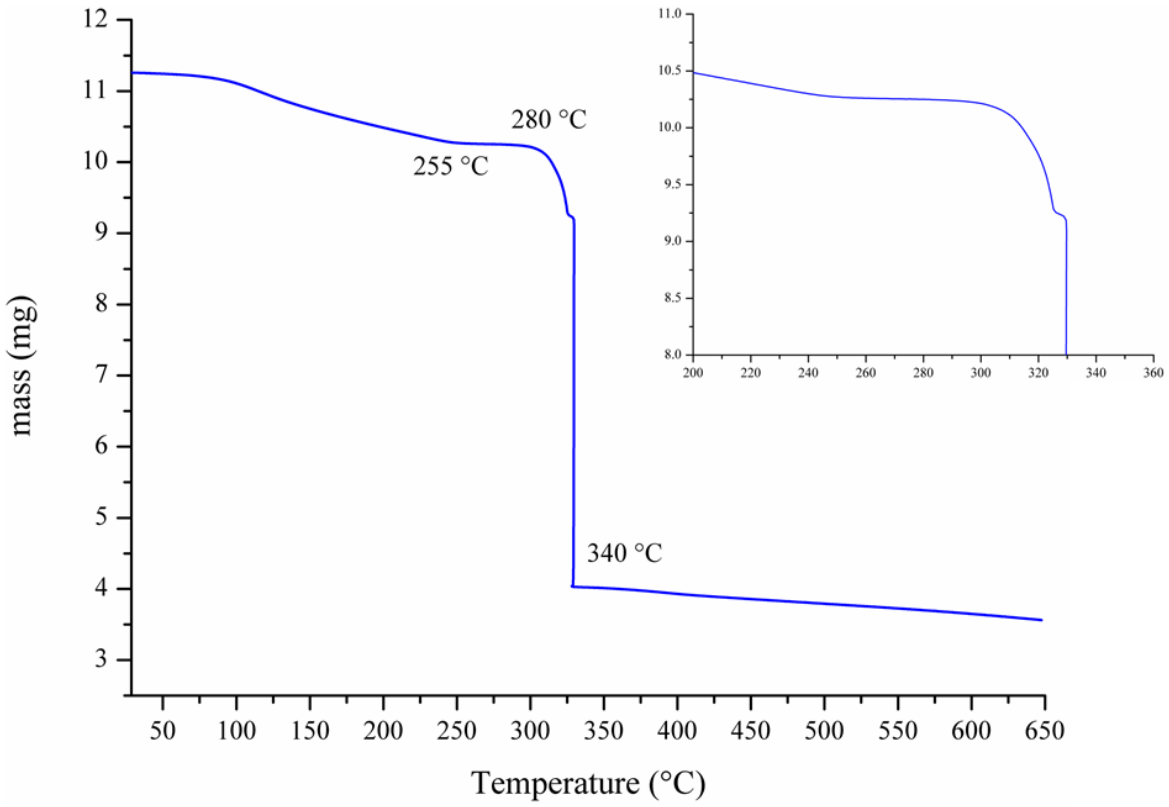

Figure 5.9 TGA of single crystals of **1**.

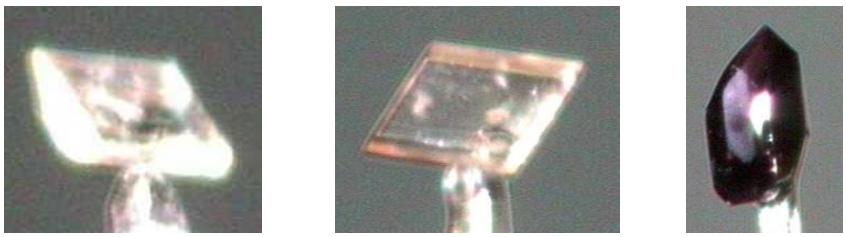

Figure 5.10 From the left, **1**, **2a** and **2b**.

The desolvation of the single crystals of **1** was carried out following two strategies: **a**) the sample was kept in a Büchi for 12 h at the temperature of 200 °C and pressure of $1 \cdot 10^{-2}$ mbar and then 4 h at 230 °C at the same pressure; **b**) the sample was kept for 1 h at 150 °C and then 1.5 h at 265 °C, at the pressure $2 \cdot 10^{-2}$ mbar. Schlenck were open under inert atmosphere of N_2 and the samples were immediately immersed in Parabar 10312 to protect them from refilling of particles present in the atmosphere. After the desolvation, crystals of both samples turned to a darker color, which may depend on the degree of desolvation (Figure 5.10). The crystallinity was retained and the products (hereinafter named **2**) were then characterized *via* single-crystal x-ray diffraction.

5.2.3 Powder X-ray diffraction

Powder diffraction experiments were performed, using Cu-Kα radiation (λ = 1.5418 Å) on a vertical-scan Bruker AXS D8 Advance diffractometer in θ:θ mode, equipped with a Goebel Mirror and a linear Position Sensitive Detector (PSD), with the following optics: primary and secondary Soller slits, 2.3° and 2.5°, respectively; divergence slit, 0.1°; receiving slit, 2.82°. Generator setting: 40 kV, 40 mA. The nominal resolution for the present set-up is 0.08° 2θ (FWHM of the α1 component) for the LaB_6 peak at about 21.3° (2θ).

A pellet of diameter of 25 mm was prepared from grinded single crystals of **1** and pressed of applying a force of $1 \cdot 10^5$ N. The diffraction patterns at RT of the pellet of **1** were acquired in the 5-90° 2θ range, with $\Delta 2\theta$ = 0.02° and exposure time 2 s/step. Le Bail refinements on the collected data have been performed with the aim of monitoring the intensity of the (2,-2,-2) hkl reflection at 27.8 2θ, in order to evaluate possible preferred orientation phenomena. The preferential orientation was indeed confirmed, and the intensity of (2,-2,-2) could be model only assuming the preferential orientation along this plane, and the refinement produced a parameter of 0.27.

5.2.4 Single crystal X-ray diffraction

X-ray diffraction data were collected on an Agilent SuperNova diffractometer, equipped with a MoKα microsouce (50 kV and 0.8 mA), Al-filtered[63]. Data were collected at T = 223 K and 173 K respectively for **2a** and **2b** using an Oxford cryosystem 700, with ω-scans of

1.0° were adopted. A total of 3066 frames with exposure times of 10, 30 and 60 seconds were collected for **2a**, 1810 frames for 5, 10, 17.5 and 25 seconds for **2b**. CrysAlisPro software, Version 1.171.37.35g[64], was used to perform the data collection and reduction, then data were corrected for absorption (analytically) and diffraction anisotropies using ABSPACK[64] routine of Crysalis.

The structure refinement was performed using ShelX package[65] and results are reported in Table 5.1. Some residual electron density was find in the pores of the solved structure, due to an incomplete activation of the MOF. Nevertheless, it was not possible to remove these residuals by modeling solvent molecules in their sites. Therefore, the data were treated with SQUEEZE method[66]. The electron count and the potential solvent accessible void volume were equal to 116 / 817 $Å^3$ and 85/815 $Å^3$ respectively for **2a** and **2b**. It was observed that the degree of desolvation was much more affected by the temperature rather than the time of treatment. Moreover, a potential correlation between color of the crystal and degree of desolvation is visible, probably due to a change of the refractive index.
Conventional and multipolar refinement are reported in Table 5.1. During the experiments we observed that on lowering temperature, many peaks became notably broadened. This phenomenon appeared at different temperature for **2a** and **2b**, but it was reversible, as peaks narrowed upon temperature increase. Because of that, it was not possible to carry out single crystal x-ray diffraction experiments below 223 K for **2a** and 173 K for **2b**, without compromising the quality of the data.

Very few reflections below resolution of 0.7 Å were measured, probably due to a loss of crystallinity during the thermal treatment. ShelX[67] and XD[68] programs were used respectively to generate the spherical and aspherical models. Moreover, because of the notable improvement of residual distribution, aspherical refinement was carried out on structure factors after the treatment with SQUEEZE.[66] This choice was also motivated by the fact that most of the residual density from the retained solvent molecules was spread in the channels, and not localized near to the tetrazolate rings. SQUEEZE[66] modifies the observed structure factors by removing the contribution of unmodeled solvent molecules. The program defines a solvent accessible volume in the unit cell using a probe sphere of fixed radius (usually 1.2 Å). Then decomposes the calculated structure factors in two parts one computed from the main structural model the other computed by considering as many fractional electrons as necessary in the solvent region iteratively extracted from difference-electron density maps. Upon convergence, the electron density of the disordered solvent is

evaluated. This enables to obtain new structure factors free from the solvent contribution. Of course, this correction strongly depends on the way in which the solvent accessible region is estimated. For routine structure determination, this procedure works quite well and it offers in general a more reliable structural model. However, for accurate charge density modeling it can be risky, because some electron density belonging to the atoms close to the solvent region could be truncated, thus affecting the proper refinement of radial functions of the multipolar model.

Table 5.1. Crystal data and structure refinement for **2a** and **2b** after the treatment with SQUEEZE.

	2a	**2b**
Empirical formula	C12 H8 Cu2 N1	C12 H8 Cu2 N1
Formula weight	419.36	419.36
Temperature	223.0(1) K	173.0(1) K
Wavelength	0.71073 Å	0.71073 Å
Crystal system	Monoclinic	Monoclinic
Space group	I 2/a	I 2/a
Unit cell dimensions	a = 7.17560(10) Å	a = 7.1420(2) Å
	b = 23.1347(2) Å	b = 23.1389(2) Å
	c = 20.8684(3) Å	c = 20.8843(3) Å
	β= 99.324(2)°.	β= 99.328(2)°.
Volume	3418.50(8) $Å^3$	3406.53(12) $Å^3$
Z	8	8
Density (calculated)	1.630 Mg/m^3	1.635 Mg/m^3
Absorption coefficient	2.504 mm^{-1}	2.513 mm^{-1}
Crystal size	0.303 x 0.178 x 0.066 mm^3	0.369 x 0.154 x 0.147 mm^3
Reflections collected/ unique	116537 / 14414	72333 / 14311
Data / restraints / parameters	14414 / 0 / 221	14311 / 0 / 221
Goodness-of-fit on (F^2)	1.047	0.978
R_1, wR_2 [$I > 2\sigma(I)$]	0.0407, 0.0987	0.0403, 0.0932
R indices (all data)	0.0907, 0.11131	0.0947, 0.1089
Multipolar Refinement		
Data / restraints / parameters	7059 / 0 / 644	6787 / 0 / 644
Goodness-of-fit (F^2)	1.7875	1.5081
R_1, wR_2 [$I > 3\sigma(I)$]	0.0221, 0.0434	0.0279, 0.0442
R_1 (all data)	0.0292	0.0373

5.2.4.1 Multipolar expansion

The multipolar refinement was carried out according to the Hansen and Coppens formalism (see Chapter 1) using data with $I > 3\sigma(I)$. The Volkov and Macchi atomic functions[69] were employed to describe the radial densities of all atoms.

The electronic configuration of Cu in isolation (*i.e.* $4s^1 3d^{10}$) was used for its scattering factor. The population of 4s was frozen in the multipolar expansion model, whereas d-electron population was enabled to change.

Positions and anisotropic thermal parameters were refined for all the non-hydrogen atoms. Whereas, positions of H atoms were kept fixed at a C-H distance equal to 1.089 Å, according to the average neutron diffraction data for pyridine. Their anisotropic thermal motion were then calculated using SHADE3 from the asymmetric unit.[70]

The multipolar expansion of Cu atoms were treated up to the hexadecapole level (l=4), for N and C up to the octupole level (l=3), whereas for H only the monopole (l=0) and the dipole (l=1) along C-H directions were refined. Two different κ sets were assigned to nitrogen atoms, in order to distinguish pyridine (Py) and tetrazolate (tz) rings. Spherical kappa parameters where refined for each atom species but hydrogen, which was kept equal to 1.2. κ' parameters were not refined and fixed to 1.0 for the non-hydrogen atoms and to 1.2 for H atoms. Multipolar treatment is summarized in Table 5.2. Additional information are reported in Figure 5.11.

Table 5.2. Multipolar and κ refinement.

Element	Refinement
Cu	Hexadecapole; κ
N	Octupole; two different kappas: κ(Py), κ(tz)
C	Octupole; κ
H	Dipole (along C-H); κ fixed to 1.2

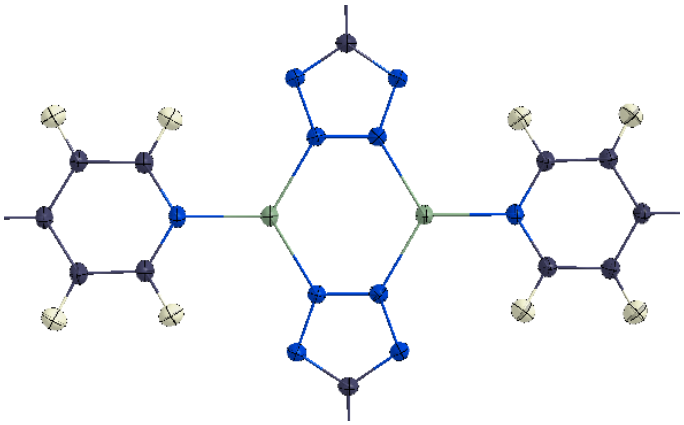

a

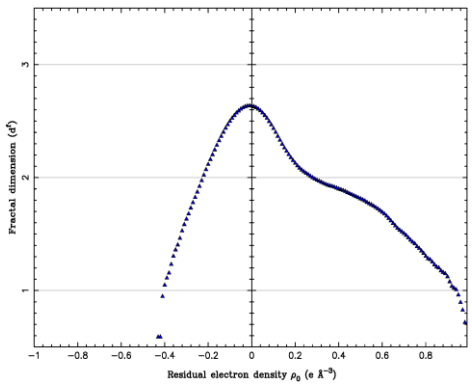
Fractal dimension (d')
Residual electron density ρ_0 (e Å^{-3})

b

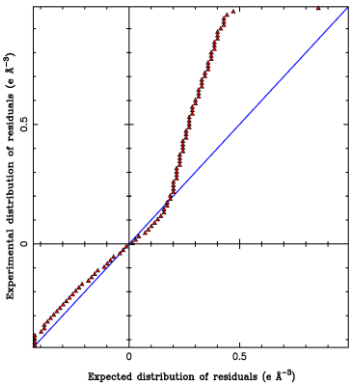
Experimental distribution of residuals (e Å^{-3})
Expected distribution of residuals (e Å^{-3})

c

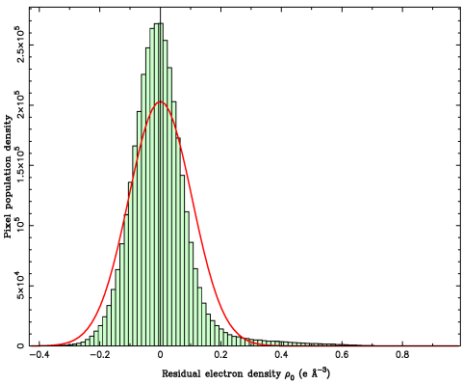
Pixel population density
Residual electron density ρ_0 (e Å^{-3})

d

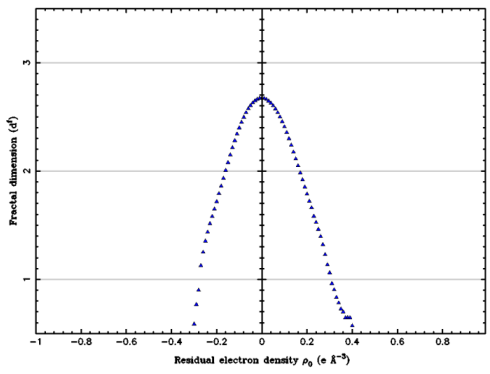
Fractal dimension (d')
Residual electron density ρ_0 (e Å^{-3})

b'

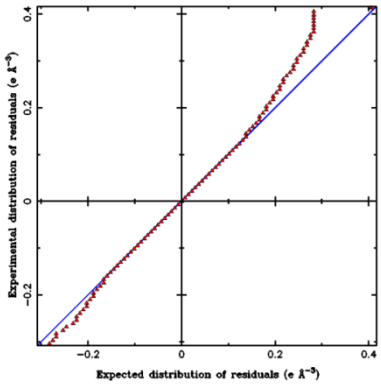
Experimental distribution of residuals (e Å^{-3})
Expected distribution of residuals (e Å^{-3})

c'

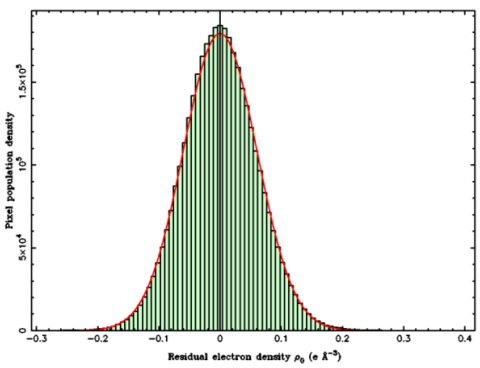
Pixel population density
Residual electron density ρ_0 (e Å^{-3})

d'

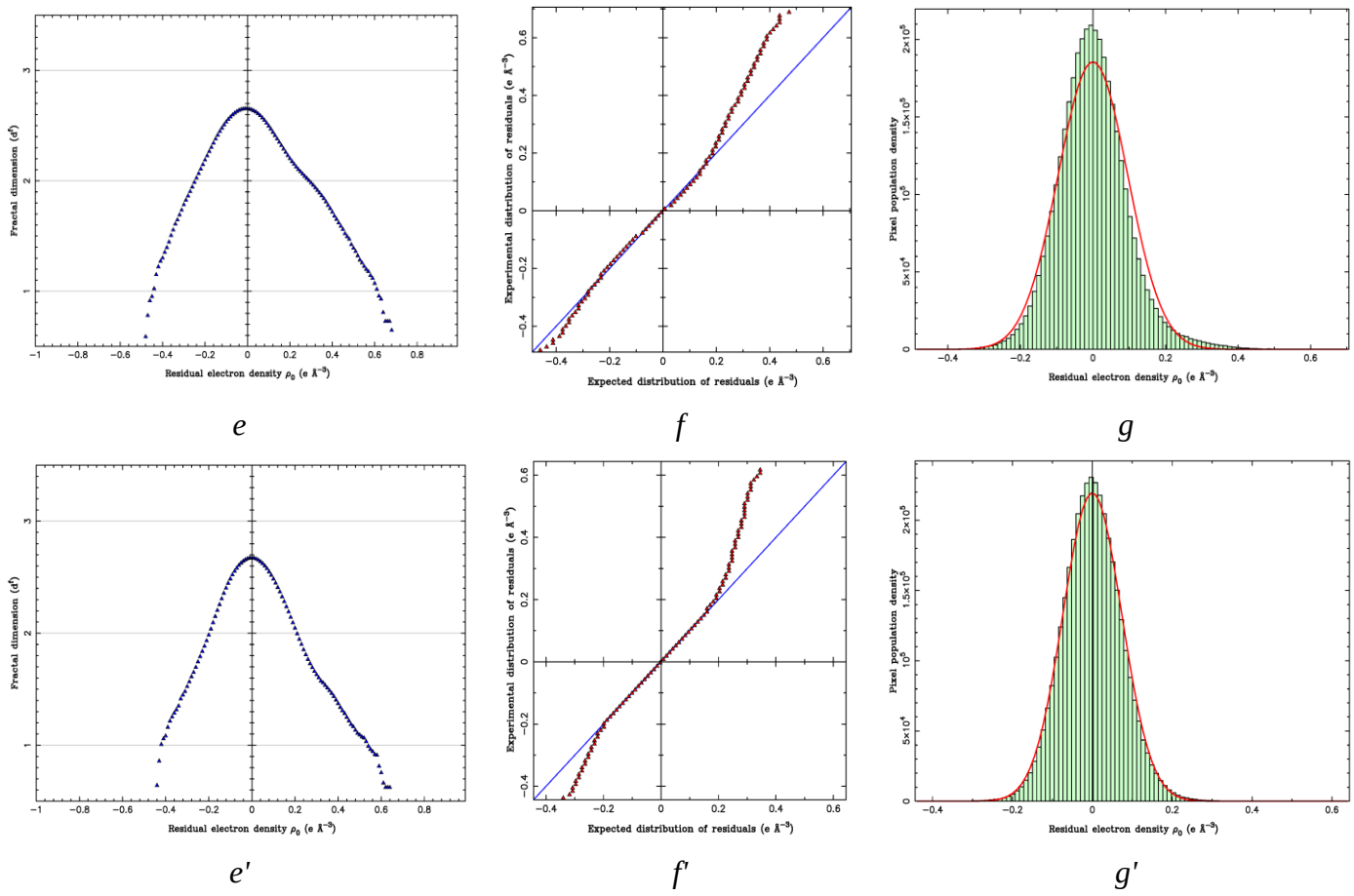

Figure 5.11 *a*= fragment of **2**; *b,c,d*= fractal, normal and statistical histogram residual distribution of **2a** before squeeze; *b',c',d'*= fractal, normal and statistical histogram residual distribution of **2a** after squeeze; *e,f,g*= fractal, normal and statistical histogram residual distribution of **2b** before squeeze; *e',f',g'*= fractal, normal and statistical histogram residual distribution of **2b** after squeeze.

The residual density distributions[71] in Figure 5.11 show some important difference between the two models. In both case there is more positive residual density, revealed by the shift of the Gaussian distribution in *d/g and d'/g'* plots. However, SQUEEZE improved the residual density distributions, removing the positive non-modeled electron density in the pores. Fractal (*b',e'*) linear (*c',f'*) and Henn–Meindl (*d',g'*) plots highlight the better quality of the model in **2a** data, even if collected at higher temperature compared to **2b**. Indeed, because **2a** and **2b** shares the same multipolar model, it appears that the second data set is more affected by systematic errors.

5.2.5 Impedance spectroscopy

The frequency dependence of the dielectric constant of **1**, $\varepsilon_r(\omega)$ was obtained via impedance spectroscopy measurement[45] on pellets of diameter of 25 mm prepared grinding crystals and applying a force of $1 \cdot 10^5$ N. The measured thickness was of 0.393 mm.

Impedance spectroscopy measurement was carried out using **ModuLab® XM MTS system** combined with the 12962A sample holder (electrode diameter 20 mm) in alternate current at room temperature in inert atmosphere of N_2. The frequency range was 1MHz-10mHz with a voltage capacitor range of 0-100 mV. The same pellet was then desolvated at a temperature of 265 °C and pressure of $1 \cdot 10^{-2}$ mbar per 15 h. Color changed to dark brown/black during the thermal treatment, as observed for single crystals (Figure 5.10). A second measurement of the activated pellet, corresponding to the specie **2**, was carried out in the same conditions.

5.2.6 Computational details

Solid state calculations have been carried out using Crystal14 code[72]. Full optimizations of cell parameters and atom positions were computed with B3LYP hybrid-GGA functional[73,74], Grimme's dispersion corrections parameters (scaled to 0.6) were added[75].

This level of theory gave better results compared with other GGA and *meta*-GGA exchange-correlation functionals (Figure 5.12). Cu [6s5p2d] basis set proposed by Doll and Harrison was used[76,77], whereas for non-metallic atoms a triple-zeta polarized functions were chosen. The static dielectric constant and the eigenvalues of the dielectric tensor, were obtained from Couple-Perturbed Kohn-Sham (CPKS) calculations[78].

Gaussian09 package[79] was used for gas-phase calculations. In order to compare as much as possible the solid-state and gas-phase results, the B3LYP/6-311G** level of theory corrected with Grimme semi-empirical dispersion terms was used.

ADF2014 code[80,81] was used for energy decomposition analysis according to the Morokuma, Kitaura, Ziegler and Rauk procedure from gas-phase calculation. As for the other computations, a B3LYP-D functional with semi-empirical corrections for dispersion, combined with a Triple-Zeta Valence Polarized (TZVP) Slater-type Orbital (STO) basis-set, was used.

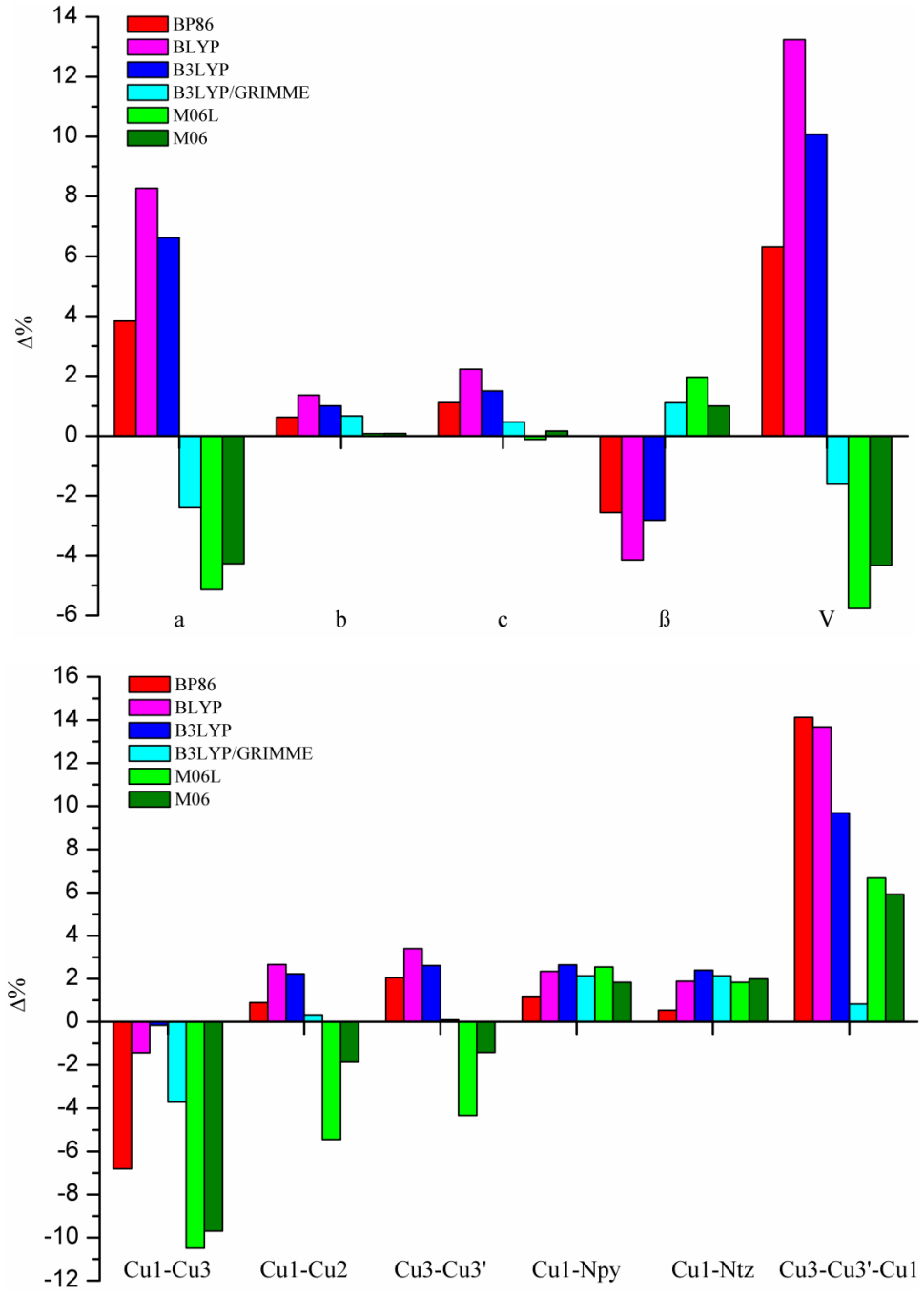

Figure 5.12 Percentage difference between computed and experimental unit cell parameters and inter atomic distances for several functionals.

5.3 Results and discussion

5.3.1 Crystal structure

Due to the evacuation of the pores, it was revealed by single-crystal x-ray diffraction experiment a change in the symmetry of the system: indeed **1**, which is triclinic P-1 and systematically affected by twinning, became monoclinic I2/a and single crystal.

Diffraction at low temperature revealed almost no effect on the cell parameter decreasing from 223 K to 173 K, except a slight contraction for *a* parameter.

The Cu(1)-Cu(3) interlayer distance (Figure 5.8) is equal to 3.140 Å at 223 K (**2a**) and 3.123 Å at 173 K (**2b**) (multipolar models), both still longer than the sum of the Van der Waals radii. The same inter-metallic distances in **1** measured by Wen *et al*[56] , were equal to 3.205 and 3.137 Å respectively at RT and 100 °K. The Cu-Cu distance measured in **1** is very similar to those measured in **2a** and **2b**. The shrinking due to the effect of the temperature is in the range of 0.06÷0.08 Å and we observe no effect on the interlayer Cu-Cu distance due to the presence of guest molecules. The stacking of the layers results unchanged as well, moreover no differences are observed also in the Cu-N distances. The only significant variations concern the stereochemistry of the Cu atoms which in **2** is very close to the ideal trigonal planar one, whereas in **1,** due to the presence of ethanol molecules, angles are quite dissimilar (116 vs. 127 °).

5.3.2 Interlayer interactions

The interlayer interaction energy was computed in gas-phase with Gaussian09. Four fragments were generated from the single-crystal structure of **2b**: a) the single layer, as reference; b) two paired layers; c) three paired layer; d) four paired layer (Figure 5.13). Each fragment is built by circumscribing the shape of the mono-dimensional pore. The electroneutrality of the systems was preserved capping the edging carbon atoms with protons.

The total energy E_L of the fragment is normalized dividing by the number of the constituent layers L (L=4, 3, 2, 1). When L=1, the mono-layer fragment is considered.

Moreover, the interlayers interaction energy ΔE and the relative dispersion energy contribution ΔE_{Disp} were computed as ($E_L/L - E_1$), and then divided by the number of atoms

composing one layer (136 atoms). This value should estimate the atom-contribution to the total pairing stabilization. Results are reported in Figure 5.13.

The interlayer stabilization ΔE reaches the value of 0.80 kcal/atom for L=4, whereas ΔE_{Disp} the value of 0.83 kcal/atom. Notably, ΔE is stabilizing only if dispersion corrections Grimme-like are taken into account, revealing no significant interlayer stabilization induced by electrostatic or polarization effects. Indeed, the forces involved in the stability of this 2D material are quite weak. Noteworthy, with these calculations the dispersion contributions are not properly accounted for, given the level of theory B3LYP-D/6-311G** that necessarily has to be adopted.

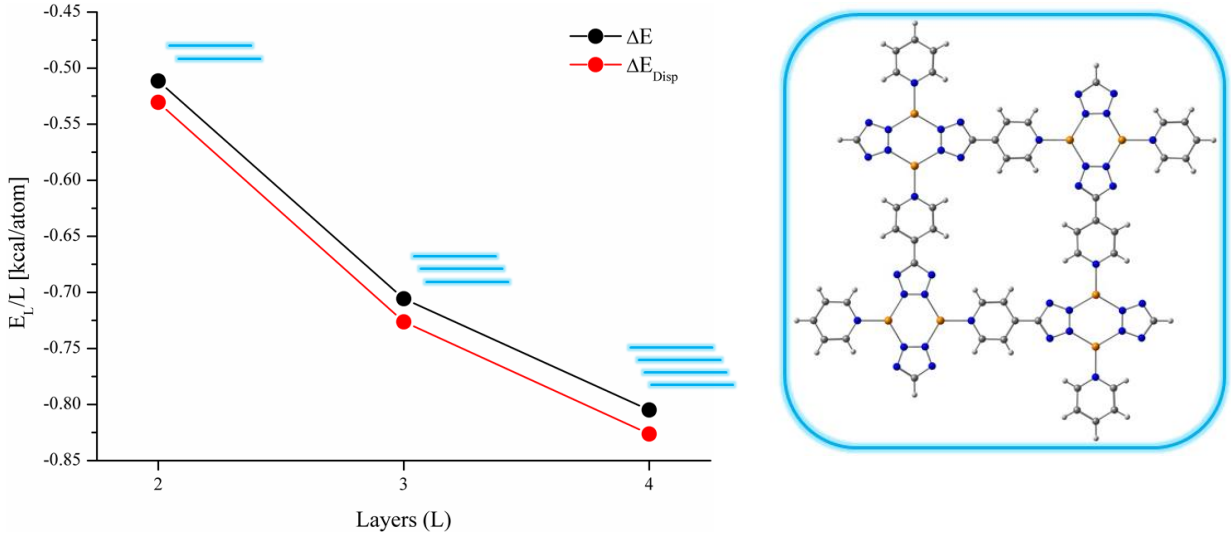

Figure 5.13. Stabilization energy produced by the interlayers interaction, L=number of layers.

5.3.3 Experimental and theoretical topological analysis

The topological analysis (see Chapter 1 for the theoretical background) was carried out on both experimental and theoretical electron densities. For the former, multipolar models of **2a** and **2b** were analyzed using XDPROP module in XD2016, whereas for the latter the TOPOND package[82] implemented in Crystal14 was used.

Attention was focused mainly on the intralayer Cu-N interactions, distinguishing those concerning the tetrazolate (tz) and pyridine (Py) ring and on interlayer's connections Cu(1)-Cu(3) and Cu(2)-N(7) (Figure 5.14).

Values of $\rho(\mathbf{r})$, $\nabla^2\rho(\mathbf{r})$, energy densities at the bond critical points, as well as Cu atomic charges and Lagrangian function integrated within their basins, are reported in Table 5.3.
For simplicity, the mean values between **2a** and **2b** are shown in Figure 5.14. Concerning intralayer interactions, both solid-state computations and experimental refinement indicate that Cu-N(tz) and Cu-N(Py) bonds have similar strength, showing almost no difference between the formally neutral pyridine (Py) and the charged tetrazolate ring (tz). Both are involved in a donor-acceptor interaction with copper atoms, indeed according to the ratio $|V_b|/G_b$, both Cu-N bonds are not purely covalent.

ρ_{bcp}	$\nabla^2\rho_{bcp}$	$\lvert V_b\rvert/G_b$
Cu(1)= 0.69 / *0.56*	Cu(1)= 8.52 / *10.86*	Cu(1)= 1.29 / *1.06*
Cu(2)= 0.70 / *0.55*	Cu(2)= 8.76 / *10.84*	Cu(2)= 1.30 / *1.05*
Cu(3)= 0.69 / *0.56*	Cu(3)= 8.83 / *10.82*	Cu(3)= 1.28 / *1.06*

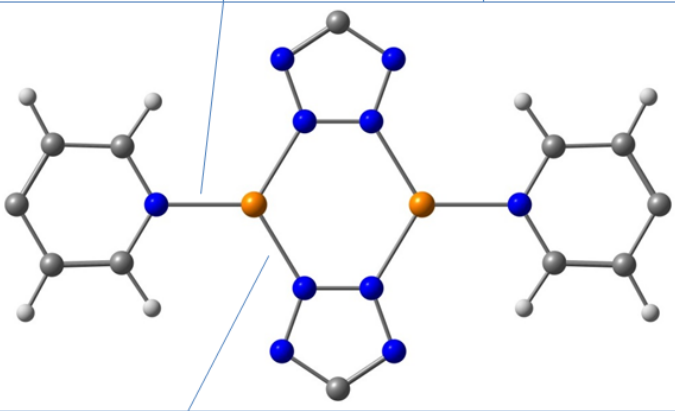

ρ_{bcp}	$\nabla^2\rho_{bcp}$	$\lvert V_b\rvert/G_b$
Cu(1)= 0.73 / *0.55*	Cu(1)= 9.34 / *11.09*	Cu(1)= 1.29 / *1.05*
Cu(2)= 0.74 / *0.55*	Cu(2)= 9.29 / *11.27*	Cu(2)= 1.29 / *1.05*
Cu(3)= 0.69 / *0.55*	Cu(3)= 8.70 / *11.19*	Cu(3)= 1.27 / *1.05*

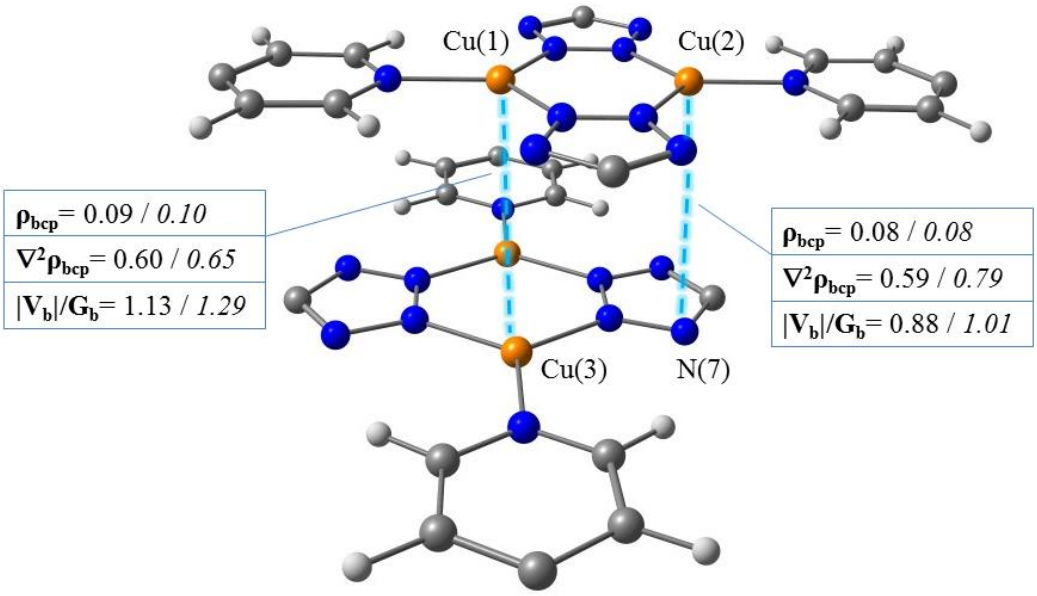

Figure 5.14. Experimental / *theoretical* values of the topological descriptors.

Table 5.3. Theoretical and experimental topological analysis.

	ρ(**r**) [e Å^{-3}]			$\nabla^2\rho$(**r**) [e Å^{-5}]		
BCP	**T**[a]	**2_a**	**2_b**	**T**	**2_a**	**2_b**
Cu(1)─N(2)$_{tz}$	0.55	0.74	0.73	11.09	9.53	9.15
Cu(1)─N(11)$_{Py}$	0.56	0.68	0.70	10.86	9.02	8.01
Cu(2)─N(1)$_{tz}$	0.55	0.72	0.75	11.27	9.66	8.91
Cu(2)─N(10)$_{Py}$	0.55	0.69	0.72	10.84	8.71	8.81
Cu(3)─N(6)$_{tz}$	0.55	0.69	0.69	11.15	8.51	8.58
Cu(3)─N(8)$_{tz}$	0.56	0.72	0.67	11.23	8.95	8.75
Cu(3)─N(5)$_{Py}$	0.56	0.72	0.65	10.82	9.47	7.91
Cu(1)─Cu(3)	0.10	0.09	0.09	0.65	0.57	0.62
Cu(2)─N(7)$_{tz}$	0.08	0.07	0.08	0.79	0.56	0.62

	Cu(1)			Cu(2)			Cu(3)		
	T	**2a**	**2b**	**T**	**2a**	**2b**	**T**	**2a**	**2b**
Q	0.66	1.06	0.99	0.69	1.07	0.93	0.68	0.96	1.03
L	1.47E-01	2.51E-01	1.24E-01	1.47E-01	2.35E-02	1.16E-01	1.47E-01	1.22E+00	7.81E-02

[a] T= theoretical.

About interlayer interactions, two bond critical points were found: one between metal atoms Cu(1) and Cu(3), and one between Cu(2) with the uncoordinated tetrazolic nitrogen atom N(7). $\rho(\mathbf{r})$, $\nabla^2\rho(\mathbf{r})$ and $|V_b|/G_b$ at the Cu(1)-Cu(3) bcp are comparable with theoretical values computed by Dinda[83] in dinuclear Cu^I complexes and other works[84]. Both from the experimental and theoretical point of view, the Cu-Cu interaction is confirmed to be extremely weak. However, the presence of a cuprophilic interaction is plausible, but not undisputed. Similar values of $\rho(\mathbf{r})$, $\nabla^2\rho(\mathbf{r})$ are found also in the Cu(2)-N(7) bond, but with an energy density ratio much closer to that of a ionic interaction. Both interlayer contacts, *i.e.* Cu(1)-Cu(3) and Cu(2)-N(7), are weak, but in the range of strength of π-π stacking interactions.[85,86]

Values of $\rho(\mathbf{r})$ and $\nabla^2\rho(\mathbf{r})$ from calculations and multipolar model are quite well in agreement, but small systematic differences are present possibly due to underestimation in the computation (given the small basis-set adopted) and/or to experimental overestimation (given the incompleteness of the multipolar model). The same considerations hold for the comparison of copper charges, +0.7 (computed) vs. +1.0/+1.1 (experimental).

To clarify the equivalence between the interactions Cu-N(tz) and Cu-N(Py), we additionally computed in gas-phase the Bader's charges of nitrogen atoms for the molecules pyridin-tetrazolate $Pytz^-$, pyridine Py and tetrazolate tz^- (Figure 5.15). Bader's analysis was carried out using AIMALL package.[87] The tetrazolate ring has the negative charge not uniformly delocalized, indeed it appears quite concentrated on the lateral nitrogen atoms (-0.71) instead of the terminals (-0.20). On the other hand, in the neutral pyridine ring, the nitrogen atom, due to its higher electronegativity, bears a notable negative charge (-1.10).

Concerning the molecule $Pytz^-$, the negative charged of the tetrazolate is partially delocalized also on the pyridine ring, increasing its basicity. The flow of electrons from the tetrazolate ring to the pyridine one is responsible of their equivalence of the interactions with copper atoms.

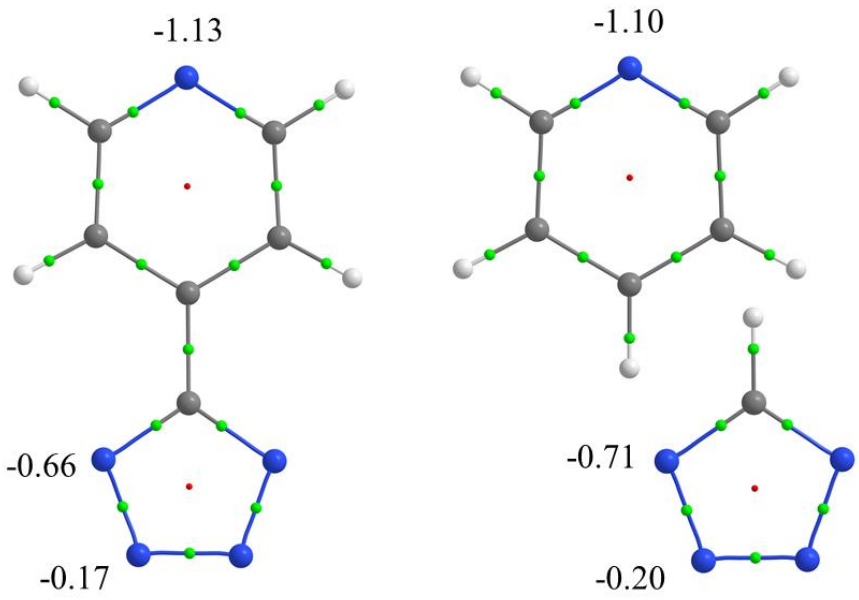

Figure 5.15. Molecular graphs of $Pytz^-$, Py and tz^- with relative nitrogen's charges.

We want to underline that due to the notable size of the system under investigation and to the complexity of the interlayer interactions, it was not possible to evaluate the non-covalent interactions (NCIs).[88]

5.3.4 Bonding partition

To further investigate the nature of the interaction in the azolate based MOFs, an energy decomposition analysis (EDA) was carried out.[89] The theory of the energy decomposition analysis (EDA) is treated and explained in Chapter 1.

The energy decomposition analysis was carried out on the fragments Cu_2^{2+}---$Py_2tz_2^{2-}$ ($Cu_2Py_2tz_2$), Cu^+---Py ($Cu_1Py_{1)}$ and Cu^+---tz^- (Cu_1tz_1), where Cu_2^{2+} is the Cu(I) dimer, Py is pyridine, tz^- is tetrazolate ring and $Py_2tz_2^{2-}$ is the ligand fragment around the copper dimer, as reported in Figure 5.16. The D_{2h} point group was used in the optimization of $Cu_2Py_2tz_2$, C_{2v} for Cu_1Py_1 and C_s for Cu_1tz_1.

The molecule $Cu_2Py_2tz_2$ coincides with the one used by Hao *et al.* for their TDDFT calculations[90]. Molecules were fully optimized and the nature of the minimum of energy was confirmed by frequencies calculations.

Moreover, to better understand the nature of the interactions between copper atoms and ligands, the interaction energy was further fragmented on its irreducible representation contributions. Those were then divided in three main groups, as suggested by Frenking *et*

al.: σ, $\pi_{\parallel}$ and $\pi_{\perp}$.[91] The first two contribute to the global σ character of the interaction, whereas only the last one describes the π-back-donation. The ratio electrostatic/orbitalic was used to evaluate the ionic/covalent character of the bond.[92] Results of the energy decomposition analysis are reported in Table 5.4.

For $Cu_2Py_2tz_2$, electrostatic is the leading term, being almost the 77% of the total interaction energy. This result is in agreement with previous works for similar systems[91] and is mainly due to the charged nature of the interacting fragments. Further, σ donation appears to give the main contribution in Cu-N bond, whereas the π-back-donation is just 28% of the global interaction. Comparing those results with the interactions between Cu^+ and Py or tz^-, the nature of Cu-N doesn't change, indeed in both case σ character is dominant. On the other hand, some difference is found in the ratio electrostatic/orbitalic between Cu_1tz_1 and Cu_1Py_1.

The first one has higher electrostatic character, again, due to the interaction between opposite charged fragments (Cu^+ and tz^-). Indeed, ΔE_{Els} term in Cu_1tz_1 is 114 kcal/mol more stabilizing than in Cu_1Py_1. ΔE_{Orb} is found as well higher (more negative) in the interaction with the tetrazolate ring, revealing a better orbitalic overlap. ΔE_{Prep} of Py, tz^- and Cu^+ are quite small, on the other hand, the preparation energy needed in the $Cu_2Py_2tz_2$ molecule is notably higher. Most of the energy is required for the formation of the dimer Cu_2^{2+}, which equals to 93.1 kcal/mol, whereas the preparation of the ligand fragment $Py_2tz_2^{2-}$ is of 75.6 kcal/mol. Nevertheless, ΔE_{Int} is always the dominant term, and so, all interactions produce a stable adduct.

However, a difference of almost 101 kcal/mol is observed in ΔE comparing Cu_1tz_1 with Cu_1Py_1. Finally, we report the energy level diagram from HOMO to HOMO-9 in Figure 5.16.

This diagram pinpoints that the main contribution to the valence molecular orbitals come from the copper atoms. The energy levels B_{3u} and B_{1u}, coinciding to HOMO-5 and HOMO-6, are very close in energy, but obviously not degenerate. In agreement with Hao *et al.*, LUMO level was found to be localized one the ligand.

Table 5.4. EDA terms for the interactions of Cu^{+} with different ligand's fragments.

	$Cu_2Py_2tz_2$	**Cu_1Py_1**	**Cu_1tz_1**
ΔE_{Prep}	168.7	0.3	1.9
	93.1 (Cu_2^{2+})		
	75.6 ($Py_2tz_2^{2-}$)		
ΔE_{Int}	-648.7	-72.2	-172.9
ΔE	-480.0	-71.9	-171.0
ΔE_{Pauli}	326.0	81.4	100.3
ΔE_{Els}	-736.8	-101.4	-215.3
ΔE_{Orb}	-224.9	-49.6	-56.2
ΔE_{Disp}	-12.9	-2.6	-1.7
%Els	76.6	67.1	79.3
%Orb	23.4	32.9	20.7
%σ	72.1	73.8	75.9
%π	27.9	26.1	24.1

D2h: $\sigma=B_{1u}$, A_g; $\pi_{\|}=B_{3g}$, B_{2u}; $\pi_{\perp}=B_{1g}$, B_{2g}, A_u, B_{3u}; C2v: $\sigma=A_1$; $\pi_{\|}=B_2$; $\pi_{\perp}=A_2$, B_1; Cs: $\sigma=A'$; $\pi_{\|}=A'$; $\pi_{\perp}=A''$.

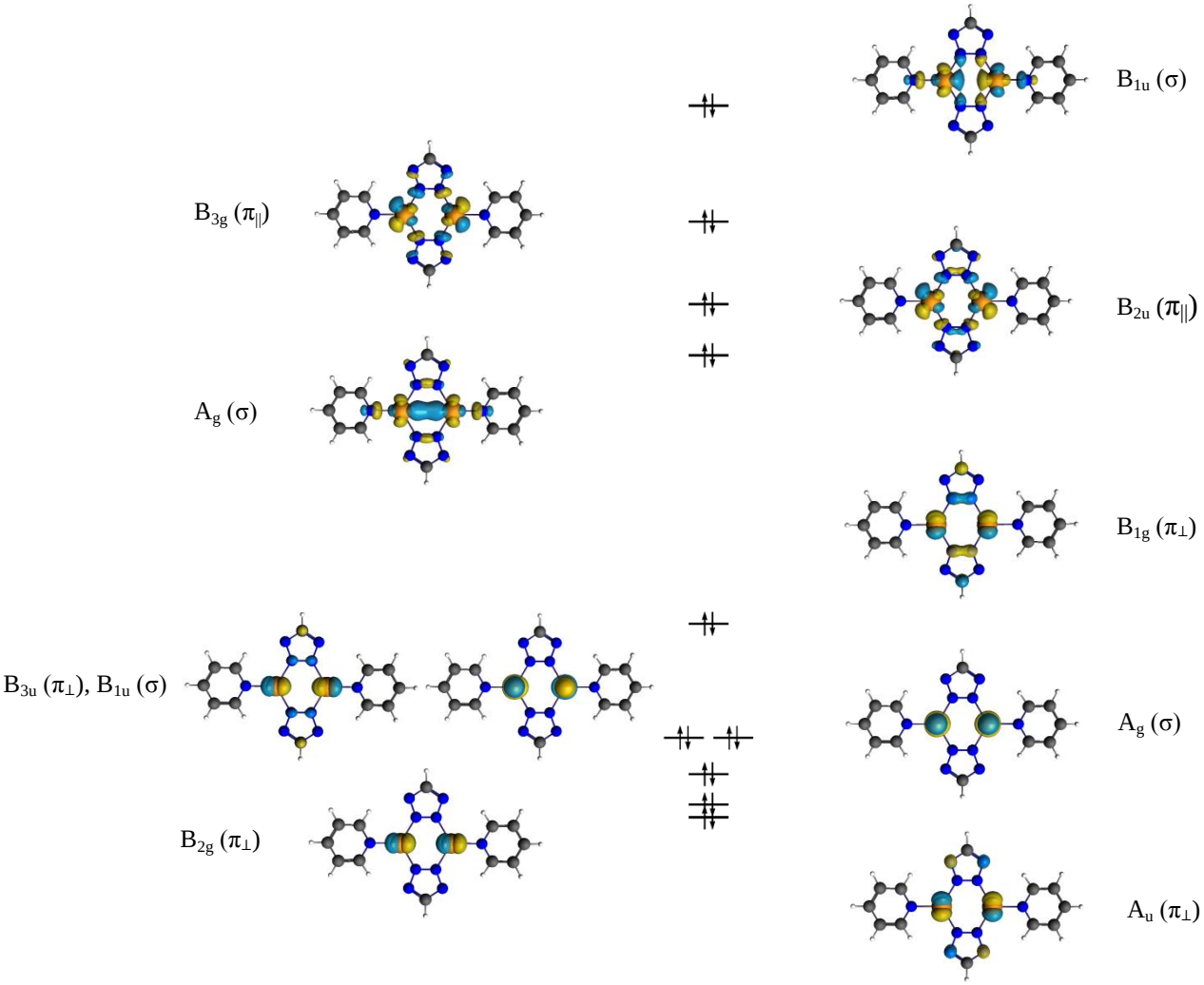

Figure 5.16. Molecular orbitals, view perpendicular to xy plane, iso-value 0.4

5.3.5 Dielectric properties

To extract the static dielectric constant and investigate the ionic and dipolar relaxation phenomena affecting this property, experiments usually focus on the range of frequencies between $1 \cdot 10^5 \div 1 \cdot 10^6$ Hz, which is the most interesting for the application in electronics.[45] At lower and higher frequencies other relaxations take place, like atomic and electronic resonance. Indeed, each relaxation mechanism has its own characteristic frequency (Figure 5.17). Electronic resonance is induced at high frequencies ($\approx 1 \cdot 10^{15}$ Hz), atomic resonance occurs in the region of Infrared $\approx 1 \cdot 10^{12}$ Hz, due to the stretching of ions opposite charged induced by the electric field. At lower frequencies, ca. $1 \cdot 10^6 \div 1 \cdot 10^9$, dipolar relaxation phenomena take place. It corresponds to the alignment of the randomly oriented molecular

and atomic dipole moments with the applied electric field, inducing a permanent dipole moment. At lower frequencies, slower mechanisms contribute to the dielectric constant.[93]

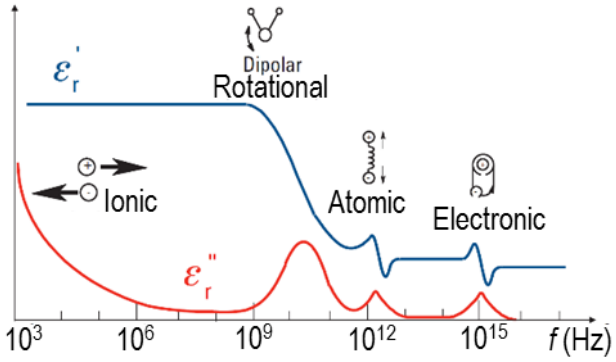

Figure 5.17. Resonance mechanisms and characteristic frequencies; ε'_r (real) and ε''_r (imaginary) parts of the relative permittivity.

The frequency dependence of the relative permittivity ε_r was measured at room temperature for **1** and **2** (Figure 5.18). At $1 \cdot 10^5$ Hz this value is equal 2.31 for **1**, and after the evacuation of ethanol, it decreases to 1.90. The linear trend of the signal of **1** till $1 \cdot 10^{-1}$ Hz indicates that the mobility of the dipole of the guest molecules is quenched, probably due to the constrained interaction with the framework and the absence of free space in the pores.

In **2**, the behavior is different. Already at $1 \cdot 10^2$ Hz an enhancement of ε_r is visible due to dipole relaxation of the few molecules of ethanol in the channels. Indeed, this is an additional proof of the not complete desolvation of **1**, consistent with the electron density removed with SQUEEZE from x-ray experiment. The few molecules retained in the structure have much higher degree of freedom, and so, relaxation phenomena are easier (see low frequencies in Figure 5.18). The static dielectric constant was then computationally evaluated through the Couple-Perturbed Kohn-Sham approach implemented in Crystal14. In order to evaluate the solvent's effect on the dielectric properties of the MOF, the same calculation was carried for **1**, and **2**. The three components of the diagonalized tensor (ε_i) and their averaged value, corresponding to the static dielectric constant for the material, are reported in Table 5.5.

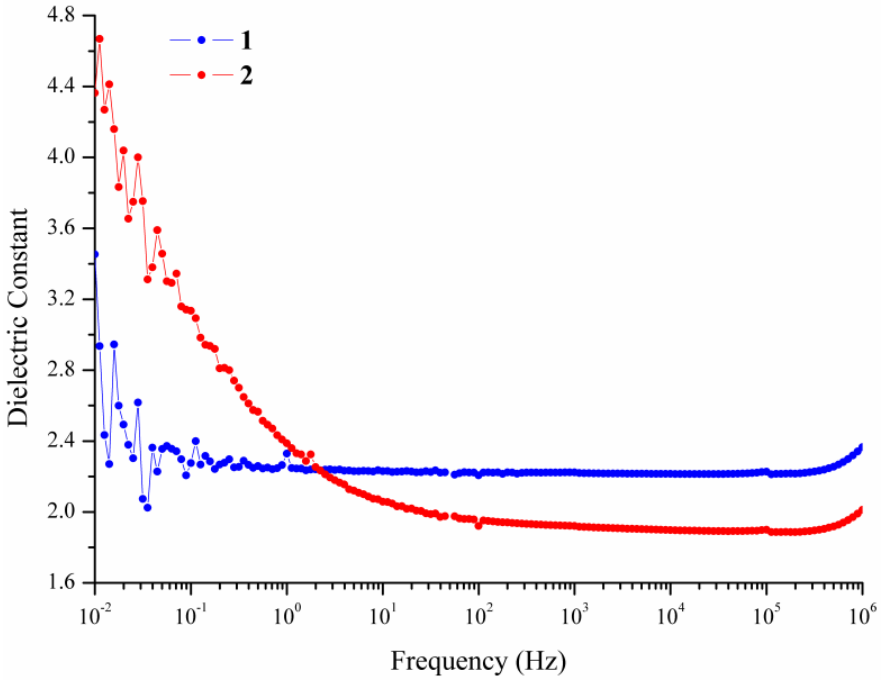

Figure 5.18. Frequency dependent dielectric constant.

Table 5.5. Eigenvalues of the dielectric tensor.

System	ε_1	ε_2	ε_3	ε_r
1	1.960	3.019	3.211	2.730
2	1.745	2.830	2.839	2.471

Surprisingly, the computed values of ε_r were much higher than the measured ones (Table 5.5). However, one of the three components of the tensor, *i.e.* ε_1, had an eigenvalue notably smaller than the other two, and much closer to the experimental one. A representative ellipsoid generated using the eigenvalues ε_i is reported together with the atomic coordinated of **1** and **2** in Figure 5.19. This addresses a strong anisotropy of the material's susceptibility. The two ellipsoids have both oblate shape, but differently oriented.

Indeed, in **2** the axis of lowest is orthogonal to the layers, corresponding to the crystal's planes (2,-2,-2) of **1** or (2,0,2) of **2**, the one where preferential orientation was measured with XRPD experiment. Indeed, the preferential orientation induced during the preparation of the pellet used for the impedance measurement influenced the observed dielectric behavior. The preferential orientation is parallel to direction of lower dielectric constant, so its component weighted more in the measurement and this explained the apparently smaller

value. The synergic combination of preferential orientation with the anisotropy of the dielectric tensor promoted the insulator character of this material a prepared in the pellet. In **2**, the presence of the solvent molecules strongly affects the dielectric property, producing both a reorientation of the minor axis of the tensor away from the normal to the layers, and an increment of the eigenvalues themselves. The loss of solvent reduces in modules ε_i, with a consequent improving of dielectric behavior of the system. To understand the effect of the solvent on the susceptibility of the frame, an investigation of the atomic polarizabilities is necessary.

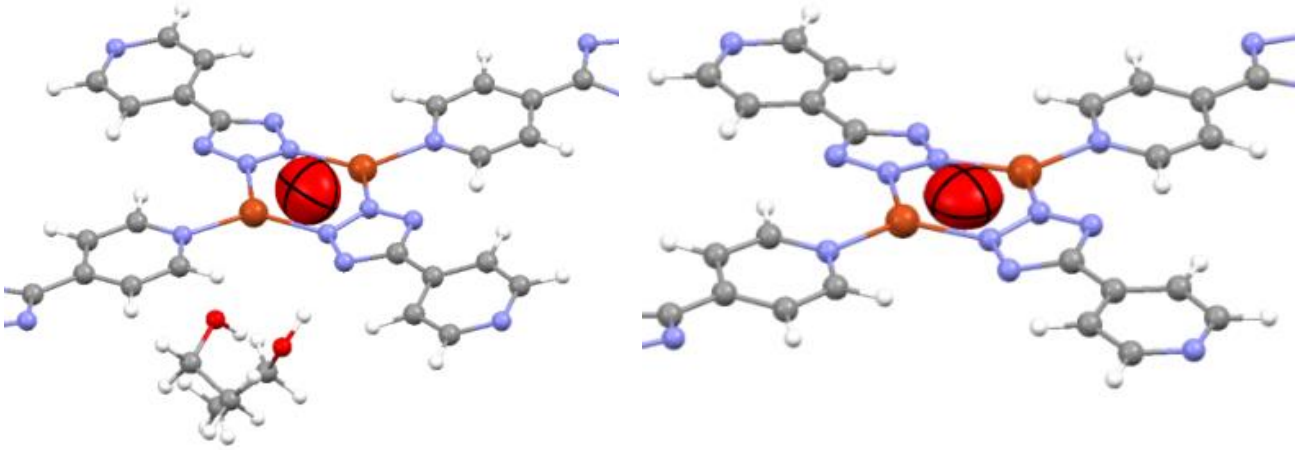

Figure 5.19. Ellipsoid of the dielectric tensor in **1** and **2**, calculated at the level of theory B3LYP-D/6-311G**; copper=orange, oxygen=red, nitrogen=blue, carbon grey, hydrogen=white.

5.3.6 Atomic and molecular polarizabilities

The evaluation of the atomic polarizabilities and the quantification of the contribution to the total susceptibility of the system from different part of the framework, *i.e.* metal, ligand and solvent, is possible by using *Polaber* program[94]. This software allows to compute the tensor components of atomic polarizability α_{ij} from each dipolar moment with respect to the applied electric filed (F):

$$\alpha_{ij} = \frac{\partial \mu_j}{\partial F_i} \qquad (5.3)$$

Wave-functions were calculated in gas-phase at zero electric field and under a field of 0.001 a.u. along the six directions ±**X**, ±**Y** and ±**Z**, as proposed by Krawczuk[95]. The same type of molecular fragments used for the energy decomposition analysis were generated from the optimized geometry of **1** and **2** in solid state, preserving the electroneutrality by capping the edging carbon atoms, as described above. The molecular fragments keep the name of the original periodic structures, *i.e.* **1** and **2**. In **1** a molecule of ethanol is present, having the same coordinates as in the solid state optimized structure. Wave-function were computed without relaxation of the geometry. Atomic partition and evaluation of dipole moments were carried out with AIMALL package.[87] The computed atomic polarization tensors represented as atomic ellipsoids are reported in Figure 5.20. Shape and size of the ellipsoids reflect the atomic polarizability behavior.

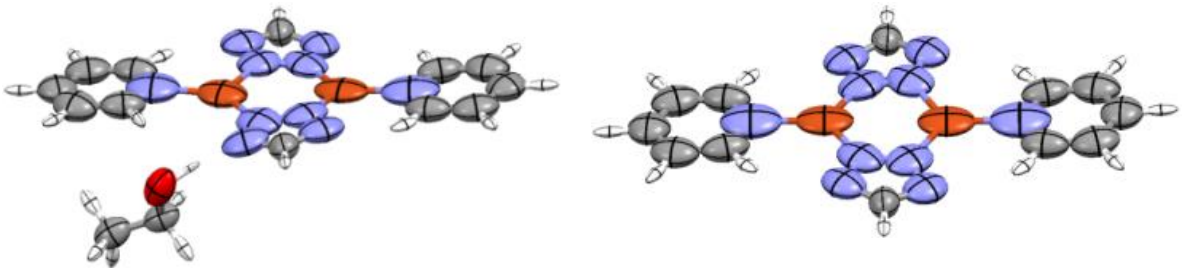

Figure 5.20 Atomic polarizabilities in molecular fragments of **1** and **2**, calculated at the level of theory B3LYP-D/6-311G**.

The preferential atomic polarization along the directions parallel to the layer is confirmed. In order to quantify the contribution to the total polarizability from the different part of the molecular system, fragments **1** and **2** were further partitioned into four sub-fragments: the copper atom Cu, the tetrazolate ring named tz, the pyridine ring named Py and the ethanol molecule EtOH. The six components of the symmetric polarizability tensor α_{ij} (i,j=1,2,3), the sub-fragment charges Q, the fragment polarization α_{iso} corresponding to the mean value of the three components of the diagonalized tensor and the polarizability density[96] α_{iso}/V, were computed and reported in Table 5.6. The volume V used for the evaluation of the polarizability density was obtained summing each atomic volumes. In

Figure 5.21 the values of α_{iso}/V for the copper atoms and tetrazolate group are plotted, distinguishing them between near and distant to the solvent molecule in the case of **1**.

Pyridine fragments were omitted, because their polarizabilities were not much affected by the presence of the guest (Table 5.6).

The presence of the ethanol molecule in **1** has a double effect on the polarizability α_{iso} and the polarizability density α_{iso}/V of the closer sub-fragment: a decreasing for metal atoms Cu(1), and an increasing for the tetrazolate ring tz(1).

However, the ethanol molecule does not affect much the global polarization of the molecular fragment (blue stars Figure 5.21), indeed it has almost the same value in **1** and **2**, meanwhile its individual components, *i.e.* Cu and tz, react differently (triangles and circles in Figure 5.21).

The increasing of the polarization of the tetrazolate ring closer to the EtOH is reasonably due to the instauration of the hydrogen bond interaction.

Moreover, both the tetrazolate rings in **1** shows a decrease of the total charge (more positive) compared to **2**, more pronounced in tz(1). However, no obvious correlation between sub-fragment's charges a polarizations appears (Table 5.6).

Indeed, even if copper atom is positively charged, and so "harder" compared with the tetrazolate ring, it has a higher polarizability density, at least in **2**, which decreases only for the metal atom closer to the guest molecule.

Further, in **1**, the solvent molecule is slightly negative charged (-0.055) leading to a framework positive charged.

In conclusion, α_{iso}/V value of the framework, referred only to the metal and ligand components, does not change in the presence of the solvent molecule. By extrapolating this finding to a periodic object, we can suppose that the decreasing of dielectric constant in the evacuated systems is due mainly to an increasing of the vacuum in the channels and not to a reorganization of the electron density of the framework.

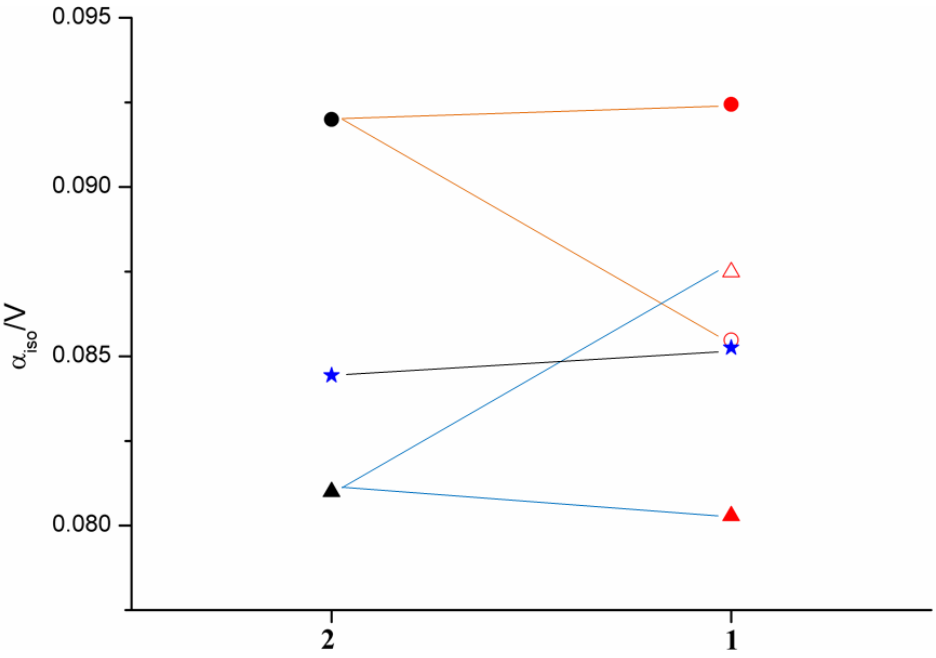

Figure 5.21. α_{iso}/V values for **1** and **2**; ●= Cu,▲=Tetrazolate ring, bold-symbol= atom/group distant from the solvent molecule, empty-symbol= atom/group near the solvent molecule; star = framework without solvent.

Table 5.6. Polarizabilities (a.u.) from single-point, level of theory B3LYP-D2/6-311G**.

1	**Q**	α_{11}	α_{22}	α_{33}	α_{12}	α_{13}	α_{23}	α_{iso}	α_{iso} /V
Cu(1)[a]	0.730	6.0	10.4	11.7	2.4	5.1	0.9	9.4	0.085
Cu(2)	0.728	5.8	11.0	13.5	3.4	5.7	2.0	10.1	0.092
tz(1)	-0.761	22.2	55.3	50.0	7.8	11.3	-0.1	42.5	0.087
tz(2)	-0.785	25.9	48.5	46.2	7.4	13.3	-6.7	40.2	0.080
Py(1)	0.073	42.2	70.3	71.2	13.7	22.7	3.9	61.3	0.086
Py(2)	0.070	38.5	74.8	71.9	15.5	21.8	9.4	61.7	0.085
EtOH	-0.055	29.0	33.8	30.7	-3.5	-0.1	5.6	31.2	0.061

2	**Q**	α_{11}	α_{22}	α_{33}	α_{12}	α_{13}	α_{23}	α_{iso}	α_{iso} /V
Cu	0.727	5.7	9.9	14.2	0.0	-6.5	0.0	9.9	0.092
tz	-0.793	24.7	54.1	43.4	0.0	-14.6	0.0	40.7	0.081
Py	0.066	38.9	65.4	82.0	0.0	-27.0	0.0	62.1	0.086

[a]Cu(1), tz(1), Py(1): closer to the solvent molecule; CuPT - Solvent.

5.4 Conclusions

The azolate-based Metal-Organic Framework (MOF) **1** was studied to understand the potential of this material as ultra-low dielectric constant material. The crystallinity of the solvated phase was retained after its activation and the structure of the unknown desolvated phase **2** was solved. Computations highlight the importance of dispersion corrections for a correct evaluation of the interlayer interactions. Indeed, no relevant stabilization comes from electrostatic and polarization effects.

Impedance spectroscopy analysis demonstrated that both **1** and **2** have very low dielectric constant values, in particular **2**, which, to the best of our knowledge, has the lowest value of static dielectric constant ever measured for this class of materials, equal to 1.90 at $1 \cdot 10^5$ Hz.

Theoretical calculation revealed the anisotropy of the dielectric properties while experiments showed the presence of a significant preferred orientation (due to platelet morphology). Indeed, only the combination of these two aspects allows such high dielectric performance. We showed that the guest molecules have a little effect on the overall polarizability of the framework since their effect on nearby tetrazolates is counterbalanced by that on nearby copper atoms. Thus, the lowering of the dielectric constant is mainly due the significant residual 'empty' spaces left by the evacuation of the solvent and not by the lack of solvent contributions to susceptibility.

Noteworthy, the investigated metal-azolate framework showed a remarkable mechanical strength upon desolvation despite its 2D nature. Accordingly, it would be worth to further investigate similar systems, particularly because of the synergic cooperation of anisotropic properties and the possibility to induce preferential orientation.

5.5 References

(1) Havemann, H.; Hutchby, J. A. High-Performance Interconnects: An Integration Overview. *Proc. IEEE* **2001**, *89* (5), 586–601.

(2) Maex, K.; Baklanov, M. R.; Shamiryan, D.; Iacopi, F.; Brongersma, S. H.; Yanovitskaya, Z. S. Low Dielectric Constant Materials for Microelectronics. *J. Appl. Phys.* **2003**, *93* (11), 8793–8841.

(3) Allan, A.; Edenfeld, D.; Joyner, W. H.; Kahng, A. B.; Rodgers, M.; Zorian, Y. 2001 Technology Roadmap for Semiconductors. *Computer (Long. Beach. Calif).* **2002**, *35* (1), 42–53.

(4) Grill, A.; Patel, V.; Rodbell, K. P.; Huang, E.; Baklanov, M. R.; Mogilnikov, K. P.; Toney, M.; Kim, H. C. Porosity in Plasma Enhanced Chemical Vapor Deposited SiCoH Dielectrics: A Comparative Study. *J. Appl. Phys.* **2003**, *94* (5), 3427–3435.

(5) Rouquerol, J.; Avnir, D.; Fairbridge, C. W.; Everett, D. H.; Haynes, J. H.; Pernicone, N.; Ramsay, J. D. F.; Sing, K. S. W.; Unger, K. K. Recommendations for the Characterization of Porous Solids. *Pure Appl. Chem.* **1994**, *66* (8), 1739–1758.

(6) Han, S. M.; Aydil, E. S. Reasons for Lower Dielectric Constant of Fluorinated SiO2 Films. *J. Appl. Phys.* **1998**, *83* (4), 2172–2178.

(7) Loboda, M. J. New Solutions for Intermetal Dielectrics Using Trimethylsilane-Based PECVD Processes. *Microelectron. Eng.* **2000**, *50* (1–4), 15–23.

(8) Jousseaume, V.; Gourhant, O.; Gonon, P.; Zenasni, A.; Favennec, L. Dielectric Constant of Porous Ultra Low-κ Thin Films. *J. Electrochem. Soc.* **2012**, *159* (5), G49.

(9) Gonon, P.; Sylvestre, A.; Meynen, H.; Van Cotthem, L. Permittivity and Conductivity of Low-Dielectric-Constant SiOC:H Films Deposited by Plasma-Enhanced Chemical Vapor Deposition. *J. Electrochem. Soc.* **2003**, *150* (3), F47.

(10) Grill, A. Plasma Enhanced Chemical Vapor Deposited SiCOH Dielectrics: From Low-k to Extreme Low-κ Interconnect Materials. *J. Appl. Phys.* **2003**, *93* (3), 1785–1790.

(11) Baklanov, M. R.; de Marneffe, J.-F.; Shamiryan, D.; Urbanowicz, A. M.; Shi, H.; Rakhimova, T. V.; Huang, H.; Ho, P. S. Plasma Processing of Low-κ Dielectrics. *J. Appl. Phys.* **2013**, *113* (4), 041101.

(12) Guo, X.; Jakes, J. E.; Banna, S.; Nishi, Y.; Shohet, J. L. Effects of Plasma and Vacuum-Ultraviolet Exposure on the Mechanical Properties of Low-k Porous Organosilicate Glass. *J. Appl. Phys.* **2014**, *116* (4).

(13) Usman, M.; Mendiratta, S.; Lu, K. L. Metal-Organic Frameworks: New Interlayer Dielectric Materials. *ChemElectroChem* **2015**, *2* (6), 786–788.

(14) Volksen, W.; Miller, R. D.; Dubois, G. Low Dielectric Constant Materials. *Chem. Rev.* **2010**, *110* (1), 56–110.

(15) Usman, M.; Lu, K. L. Metal–organic Frameworks: The Future of Low-κ Materials. *NPG Asia Mater.* **2016**, *8* (12), e333.

(16) Yaghi, O. M.; O'Keeffe, M.; Ockwig, N. W.; Chae, H. K.; Eddaoudi, M.; Kim, J. Reticular Synthesis and the Design of New Materials. *Nature* **2003**, *423* (6941), 705–714.

(17) Furukawa, H.; Cordova, K. E.; O'Keeffe, M.; Yaghi, O. M. The Chemistry and Applications of Metal-Organic Frameworks. *Science (80-.).* **2013**, *341* (6149), 1230444.

(18) Rosi, N. L.; Eddaoudi, M.; Kim, J.; O'Keeffe, M.; Yaghi, O. M. Advances in the Chemistry of Metal-Organic Frameworks. *CrystEngComm* **2002**, *4* (68), 401.

(19) Perry IV, J. J.; Perman, J. a.; Zaworotko, M. J. Design and Synthesis of Metal–organic Frameworks Using Metal–organic Polyhedra as Supermolecular Building Blocks. *Chem. Soc. Rev.* **2009**, *38* (5), 1400.

(20) Tranchemontagne, D. J.; Mendoza-Cortés, J. L.; O'Keeffe, M.; Yaghi, O. M. Secondary Building Units, Nets and Bonding in the Chemistry of Metal-Organic Frameworks. *Chem. Soc. Rev.* **2009**, *38* (5), 1257–1283.

(21) Eddaoudi, M.; Moler, D. B.; Li, H.; Chen, B.; Reineke, T. M.; O'Keeffe, M.; Yaghi, O. M. Modular Chemistry: Secondary Building Units as a Basis for the Design of Highly Porous and Robust Metal-Organic Carboxylate Frameworks. *Acc. Chem. Res.* **2001**, *34* (4), 319–330.

(22) Kitagawa, S.; Kondo, M. Functional Micropore Chemistry of Crystalline Metal Complex-Assembled Compounds. *Bulletin of the Chemical Society of Japan*. 1998, pp 1739–1753.

(23) Furukawa, H.; Kim, J.; Ockwig, N. W.; O'Keeffe, M.; Yaghi, O. M. Control of Vertex Geometry, Structure Dimensionality, Functionality, and Pore Metrics in the Reticular Synthesis of Crystalline Metal-Organic Frameworks and Polyhedra. *J. Am. Chem. Soc.* **2008**, *130* (35), 11650–11661.

(24) Eddaoudi, M.; Kim, J.; Rosi, N.; Vodak, D.; Wachter, J.; Keeffe, M. O.; Yaghi, O. M.; Eddaoudi, M.; Kimrn, J.; Rosi, N.; *et al.* Systematic Design of Pore Size and Functionality in Isoreticular MOFs and Their Application in Methane Storage Published by : American Association for the Advancement of Science Linked References Are Available on JSTOR for This Article : Systematic Design. **2002**, *295* (5554), 469–472.

(25) Li, C.; Du, M. Role of Solvents in Coordination Supramolecular Systems. *Chem. Commun.*

2011, *47* (21), 5958.

(26) Serre, C.; Surblé, S.; Mellot-Draznieks, C.; Filinchuk, Y.; Férey, G. Evidence of Flexibility in the Nanoporous Iron(III) Carboxylate MIL-89. *Dalt. Trans.* **2008**, No. 40, 5501–5506.

(27) Kitagawa, S.; Kitaura, R.; Noro, S. Functional Porous Coordination Polymers. *Angew. Chemie Int. Ed.* **2004**, *43* (18), 2334–2375.

(28) Li, H.; Eddaoudi, M.; O'Keeffe, M.; Yaghi, O. M. Design and Synthesis of an Exceptionally Stable and Highly Porous Metal-Organic Framework. *Nature* **1999**, *402* (November), 276–279.

(29) Han, S. S.; Mendoza-Cortés, J. L.; Goddard, W. A. Recent Advances on Simulation and Theory of Hydrogen Storage in Metal-Organic Frameworks and Covalent Organic Frameworks. *Chem. Soc. Rev.* **2009**, *38* (5), 1460–1476.

(30) Lee, J.; Farha, O. K.; Roberts, J.; Scheidt, K. A.; Nguyen, S. T.; Hupp, J. T. Metal-Organic Framework Materials as Catalysts. *Chem. Soc. Rev.* **2009**, *38* (5), 1450–1459.

(31) Liu, J.; Chen, L.; Cui, H.; Zhang, J.; Zhang, L.; Su, C.-Y. Applications of Metal–organic Frameworks in Heterogeneous Supramolecular Catalysis. *Chem. Soc. Rev.* **2014**, *43* (16), 6011–6061.

(32) Kreno, L. E.; Leong, K.; Farha, O. K.; Allendorf, M.; Van Richard P., D.; Hupp, J. T. Metal-Organic Framework Materials as Chemical Sensors. *Chem. Rev. (Washington, DC, United States)* **2012**, *112*, 1105–1125.

(33) Hu, Z.; Deibert, B. J.; Li, J. Luminescent Metal–Organic Frameworks for Chemical Sensing and Explosive Detection. *Chem. Soc. Rev.* **2014**, *43* (16), 5815–5840.

(34) Schneemann, A.; Bon, V.; Schwedler, I.; Senkovska, I.; Kaskel, S.; Fischer, R. A. Flexible Metal–organic Frameworks. *Chem. Soc. Rev.* **2014**, *43* (16), 6062–6096.

(35) Stavila, V.; Talin, A. A.; Allendorf, M. D. MOF-Based Electronic and Opto-Electronic Devices. *Chem. Soc. Rev.* **2014**, *43* (16), 5994–6010.

(36) Guo, M.; Cai, H. L.; Xiong, R. G. Ferroelectric Metal Organic Framework (MOF). *Inorg. Chem. Commun.* **2010**, *13* (12), 1590–1598.

(37) Kurmoo, M. Magnetic Metal–organic Frameworks. *Chem. Soc. Rev.* **2009**, *38* (5), 1353.

(38) Li, B.; Wen, H. M.; Cui, Y.; Zhou, W.; Qian, G.; Chen, B. Emerging Multifunctional Metal–Organic Framework Materials. *Adv. Mater.* **2016**, *28* (40), 8819–8860.

(39) Kuppler, R. J.; Timmons, D. J.; Fang, Q.-R.; Li, J.-R.; Makal, T. A.; Young, M. D.; Yuan, D.; Zhao, D.; Zhuang, W.; Zhou, H.-C. Potential Applications of Metal-Organic Frameworks. *Coord. Chem. Rev.* **2009**, *253* (23–24), 3042–3066.

(40) Kuc, a; Enyashin, a; Seifert, G. Metal-Organic Frameworks: Structural, Energetic, Electronic, and Mechanical Properties. *J. Phys. Chem. B* **2007**, *111*, 8179–8186.

(41) Zagorodniy, K.; Seifert, G.; Hermann, H. Metal-Organic Frameworks as Promising Candidates for Future Ultralow-κ Dielectrics. *Appl. Phys. Lett.* **2010**, *97* (25), 95–97.

(42) Ryder, M. R.; Donà, L.; Vitillo, J. G.; Civalleri, B. Understanding and Controlling the Dielectric Response of Metal–Organic Frameworks. *Chempluschem* **2018**, *83* (4), 308–316.

(43) Usman, M.; Lee, C.-H.; Hung, D.-S.; Lee, S.-F.; Wang, C.-C.; Luo, T.-T.; Zhao, L.; Wu, M.-K.; Lu, K.-L. Intrinsic Low Dielectric Behaviour of a Highly Thermally Stable Sr-Based Metal–organic Framework for Interlayer Dielectric Materials. *J. Mater. Chem. C* **2014**, *2* (19), 3762.

(44) Mendiratta, S.; Usman, M.; Luo, T.; Chang, B.; Lee, S.; Lin, Y.; Lu, K. Anion-Controlled Dielectric Behavior of Homochiral Tryptophan- Based Metal−Organic Frameworks. *Cryst. Growth Des.* **2014**, *14*, 1572–1579.

(45) Eslava, S.; Zhang, L.; Esconjauregui, S.; Yang, J.; Vanstreels, K.; Baklanov, M. R.; Saiz, E. Metal-Organic Framework ZIF-8 Films as Low-κ Dielectrics in Microelectronics. *Chem. Mater.* **2013**, *25* (1), 27–33.

(46) Park, K. S.; Ni, Z.; Côté, A. P.; Choi, J. Y.; Huang, R.; Uribe-Romo, F. J.; Chae, H. K.; O'Keeffe, M.; Yaghi, O. M. Exceptional Chemical and Thermal Stability of Zeolitic Imidazolate Frameworks. *Proc. Natl. Acad. Sci. U. S. A.* **2006**, *103* (27), 10186–10191.

(47) Zhang, J.; Zhang, Y.; Lin, J.; Chen, X. Metal Azolate Frameworks : From Crystal Engineering to Functional Materials. *Chem. Rev.* **2012**, *112*, 1001–1033.

(48) Yuan, S.; Feng, L.; Wang, K.; Pang, J.; Bosch, M.; Lollar, C.; Sun, Y.; Qin, J.; Yang, X.; Zhang, P.; *et al.* Stable Metal-Organic Frameworks: Design, Synthesis, and Applications. *Adv. Mater.* **2018**, *1704303*, 1–35.

(49) Tao, J.; Ma, Z. J.; Huang, R. Bin; Zheng, L. S. Synthesis and Characterization of a Tetrazolate-Bridged Coordination Framework Encapsulating D_{2h}-Symmetric Cyclic $(H_2O)_4$ Cluster Arrays. *Inorg. Chem.* **2004**, *43* (20), 6133–6135.

(50) Rowsell, J. L. C.; Spencer, E. C.; Eckert, J.; Howard, J. A. K.; Yaghi, O. M. Gas Adsorption Sites in a Large-Pore Metal-Organic Framework. *Science* **2005**, *309* (5739), 1350–1354.

(51) Bhadra, B. N.; Seo, P. W.; Khan, N. A.; Jhung, S. H. Hydrophobic Cobalt-Ethylimidazolate Frameworks: Phase-Pure Syntheses and Possible Application in Cleaning of Contaminated Water. *Inorg. Chem.* **2016**, *55* (21), 11362–11371.

(52) Demko, Z. P.; Sharpless, K. B. Preparation of 5-Substituted 1H-Tetrazoles from Nitriles in

Water. *J. Org. Chem.* **2001**, *66* (24), 7945–7950.

(53) Zhao, H.; Qu, Z. R.; Ye, H. Y.; Xiong, R. G. In Situ Hydrothermal Synthesis of Tetrazole Coordination Polymers with Interesting Physical Properties. *Chem. Soc. Rev.* **2008**, *37* (1), 84–100.

(54) Dincâ, M.; Yu, A. F.; Long, J. R. Microporous Metal-Organic Frameworks Incorporating 1,4- Benzeneditetrazolate: Syntheses, Structures, and Hydrogen Storage Properties. *J. Am. Chem. Soc.* **2006**, *128* (27), 8904–8913.

(55) Wang, F.; Yu, R.; Zhang, Q. S.; Zhao, Z. G.; Wu, X. Y.; Xie, Y. M.; Qin, L.; Chen, S. C.; Lu, C. Z. Solvent-Dependent Luminescent Cu(I) Framework Based on 5-(4-Pyridyl)Tetrazole. *J. Solid State Chem.* **2009**, *182* (9), 2555–2559.

(56) Wen, T.; Zhou, X. P.; Zhang, D. X.; Li, D. Luminescent Mechanochromic Porous Coordination Polymers. *Chem. - A Eur. J.* **2014**, *20* (3), 644–648.

(57) Liu, B.; Bai, L.; Lin, X.; Li, K.; Huang, H.; Hu, H.; Liu, Y.; Kang, Z. Crystal Engineering towards the Luminescence Property Trimming of Hybrid Coordination Polymers. *CrystEngComm* **2015**, *17* (7), 1686–1692.

(58) Li, F.; Lin, R.-B.; Wei, Y.-S.; Liao, P.-Q.; Bai, J.; Xue, W.; Zhang, W.-X.; Zhang, J.-P.; Chen, X.-M. Metal-Ion Controlled Solid-State Reactivity and Photoluminescence in Two Isomorphous Coordination Polymers. *Inorg. Chem. Front.* **2014**, *1* (2), 172.

(59) Li, M. X.; Zhang, Y. F.; He, X.; Shi, X. M.; Wang, Y. P.; Shao, M.; Wang, Z. X. Diverse Structures and Ferro-/Ferri-/Antiferromagnetic Interactions of Pyridyltetrazole Coordination Polymers with Polycarboxylate Auxiliary Ligands. *Cryst. Growth Des.* **2016**, *16* (5), 2912–2922.

(60) Ren, G.-J.; Liu, Y.-Q.; Liu, S.-J. Two Novel Metal-Organic Frameworks Based on Linear Dicarboxylic Acid and 5-(4-Pyridyl)Tetrazole. *J. Solid State Chem.* **2015**, *232*, 79–82.

(61) Zhang, J.-W.; Hu, M.-C.; Li, S.-N.; Jiang, Y.-C.; Zhai, Q.-G. Design of Highly Connected Cd-Tetrazolate-Dicarboxylate Frameworks with Enhanced CO_2/CH_4 and C_2 Hydrocarbons/CH_4 Separation Performance. *Cryst. Growth Des.* **2016**, *16* (11), 6430–6435.

(62) Nasani, R.; Saha, M.; Mobin, S. M.; Martins, L. M. D. R. S.; Pombeiro, A. J. L.; Kirillov, A. M.; Mukhopadhyay, S. Copper-Organic Frameworks Assembled from in Situ Generated 5-(4-Pyridyl)Tetrazole Building Blocks: Synthesis, Structural Features, Topological Analysis and Catalytic Oxidation of Alcohols. *Dalton Trans.* **2014**, *43* (26), 9944–9954.

(63) Macchi, P.; Bürgi, H. B.; Chimpri, A. S.; Hauser, J.; Gál, Z. Low-Energy Contamination of Mo Microsource X-Ray Radiation: Analysis and Solution of the Problem. *J. Appl.*

Crystallogr. **2011**, *44* (4), 763–771.

(64) Agilent Technologies: CrysAlisPRO Software System, Version 1.171.37.35g, Agilent Technologies UK Ltd, Oxford, UK,(2014).; Agilent Technologies: CrysAlisPRO Software system, version 1.171.37.35g, Agilent Technologies UK Ltd, Oxford, UK, (2014).

(65) Sheldrick, G. M. A Short History of SHELX. *Acta Crystallogr. Sect. A* **2008**, *64*, 112–122.

(66) Spek, A. L. PLATON SQUEEZE: A Tool for the Calculation of the Disordered Solvent Contribution to the Calculated Structure Factors. *Acta Crystallogr. Sect. C Struct. Chem.* **2015**, *71*, 9–18.

(67) Sheldrick, G. M. SHELXT - Integrated Space-Group and Crystal-Structure Determination. *Acta Crystallogr. Sect. A Found. Crystallogr.* **2015**, *71* (1), 3–8.

(68) Volkov, A.; Macchi, P.; Farrugia, L.; Gatti, C.; Mallinson, P.; Richter, T.; Koritsanszky, T. XD2016 - A Computer Program Package for Multipole Refinement, Topological Analysis of Charge Densities and Evaluation of Intermolecular Energies from Experimental and Theoretical Structure Factors, 2016.

(69) Volkov, A.; Macchi, P.; Farrugia, L.; Gatti, C.; Mallinson, P.; Richter, T.; Koritsanszky, T. XD2006 - a Computer Program for Multipole Refinement, Topological Analysis of Charge Densities and Evaluation of Intermolecular Energies from Experimental or Theoretical Structure Factors., 2006.

(70) Madsen, A. Ø.; Hoser, A. A. SHADE3 Server: A Streamlined Approach to Estimate H-Atom Anisotropic Displacement Parameters Using Periodic Ab Initio Calculations or Experimental Information. *J. Appl. Crystallogr.* **2014**, *47* (6), 2100–2104.

(71) Meindl, K.; Henn, J. Foundations of Residual-Density Analysis. *Acta Crystallogr. Sect. A Found. Crystallogr.* **2008**, *64* (3), 404–418.

(72) Dovesi, R.; Orlando, R.; Erba, A.; Zicovich-wilson, C. M.; Civalleri, B.; Casassa, S.; Maschio, L.; Ferrabone, M.; Pierre, M. D. La; Arco, P. D.; *et al.* CRYSTAL 14 : A Program for the Ab Initio Investigation of Crystalline Solids. *Int. J. Quantum Chem.* **2014**, No. 114, 1287–1317.

(73) Becke, A. D. Density-Functional Thermochemistry.III. The Role of Exact Exchange. *J. Chem. Phys.* **1993**, *98* (7), 5648.

(74) Lee, C.; Yang, W.; Parr, R. G. Development of the Colle-Salvetti Correlation-Energy Formula into a Functional of the Electron Density. *Phys. Rev. B* **1988**, *37* (2), 785–789.

(75) Grimme, S. Semiempirical GGA-Type Density Functional Constructed with a Long-Range Dispersion Correction. *J. Comput. Chem.* **2006**, *27* (15), 1787–1799.

(76) Doll, K.; Harrison, N. M. Chlorine Adsorption on the Cu(111) Surface. *Chem. Phys. Lett.* **2000**, *317*, 282–289.

(77) Doll, K.; Harrison, N. M. Theoretical Study of Chlorine Adsorption on the Ag(111) Surface. *Phys. Rev. B - Condens. Matter Mater. Phys.* **2001**, *63* (16), 2–7.

(78) Ferrero, M.; Rérat, M.; Orlando, R.; Dovesi, R. The Calculation of Static Polarizabilities of 1-3D Periodic Compounds. The Implementation in the CRYSTAL Code. *J. Comput. Chem.* **2008**, *29*, 1450–1459.

(79) Frisch, M. J.; Trucks, G. W.; Schlegel, H. B.; Scuseria, G. E.; Robb, M. A.; Cheeseman, J. R.; Scalmani, G.; Barone, V.; Mennucci, B.; Petersson, G. A.; *et al.* Gaussian09 Revision B.010. Gaussian, Inc.: Wallingford CT 2010.

(80) Te Velde, G.; Bickelhaupt, F. M.; Baerends, E. J.; Fonseca Guerra, C.; van Gisbergen, S. J. A.; Snijders, J. G.; Ziegler, T. Chemistry with ADF. *J. Comput. Chem.* **2001**, *22* (9), 931–967.

(81) E.J. Baerends, T. Ziegler, J. Autschbach, D. Bashford, A. Bérces, F.M. Bickelhaupt, C. Bo, P. M.; Boerrigter, L. Cavallo, D.P. Chong, L. Deng, R.M. Dickson, D.E. Ellis, M. van Faassen, L. Fan, T. H.; Fischer, C. Fonseca Guerra, M. Franchini, A. Ghysels, A. Giammona, S.J.A. van Gisbergen, A. W. G.; J.A. Groeneveld, O.V. Gritsenko, M. Grüning, S. Gusarov, F.E. Harris, P. van den Hoek, C.R. Jacob, H.; Jacobsen, L. Jensen, J.W. Kaminski, G. van Kessel, F. Kootstra, A. Kovalenko, M.V. Krykunov, E. van; Lenthe, D.A. McCormack, A. Michalak, M. Mitoraj, S.M. Morton, J. Neugebauer, V.P. Nicu, L.; Noodleman, V.P. Osinga, S. Patchkovskii, M. Pavanello, P.H.T. Philipsen, D. Post, C.C. Pye, W.; Ravenek, J.I. Rodríguez, P. Ros, P.R.T. Schipper, H. van Schoot, G. Schreckenbach, J. S. S.; M. Seth, J.G. Snijders, M. Solà, M. Swart, D. Swerhone, G. te Velde, P. Vernooijs, L. Versluis, L.; Visscher, O. Visser, F. Wang, T.A. Wesolowski, E.M. van Wezenbeek, G. Wiesenekker, S.K. Wolff, T. K.; *et al.* ADF2014, SCM, Theoretical Chemistry, Vrije Universiteit, Amsterdam, The Netherlands.

(82) Rabiller, P.; Souhassou, M.; Katan, C.; Gatti, C.; Lecomte, C. Accuracy of Topological Analysis of Gridded Electron Densities. *J. Phys. Chem. Solids* **2004**, *65* (12), 1951–1955.

(83) Dinda, S.; Samuelson, A. G. The Nature of Bond Critical Points in Dinuclear Copper(I) Complexes. *Chem. - A Eur. J.* **2012**, *18* (10), 3032–3042.

(84) Lepetit, C.; Fau, P.; Fajerwerg, K.; Kahn, M. L.; Silvi, B. Topological Analysis of the Metal-Metal Bond: A Tutorial Review. *Coord. Chem. Rev.* **2017**, *345*, 150–181.

(85) Navarro, A.; Fernández-Liencres, M. P.; García, G.; Granadino-Roldán, J. M.; Fernández-

Gómez, M. A DFT Approach to the Charge Transport Related Properties in Columnar Stacked π-Conjugated N-Heterocycle Cores Including Electron Donor and Acceptor Units. *Phys. Chem. Chem. Phys.* **2015**, *17* (1), 605–618.

(86) Rodríguez, J. I.; Matta, C. F.; Uribe, E. A.; Götz, A. W.; Castillo-Alvarado, F. L.; Molina-Brito, B. A QTAIM Topological Analysis of the P3HT-PCBM Dimer. *Chem. Phys. Lett.* **2016**, *644*, 55–66.

(87) AIMAll (Version 17.01.25), Todd A. Keith, TK Gristmill Software, Overland Park KS, USA, 2017 (Aim.Tkgristmill.Com).

(88) Johnson, E. R.; Keinan, S.; Mori-Sánchez, P.; Contreras-García, J.; Cohen, A. J.; Yang, W. Revealing Noncovalent Interactions. *J. Am. Chem. Soc.* **2011**, *132*, 6498–6506.

(89) Von Hopffgarten, M.; Frenking, G. Energy Decomposition Analysis. *WIREs Comput Mol Sci* **2012**, *2*, 43–62 doi: 10.1002/wcms.71.

(90) Liu, L.; Mi, W.; Hao, C.; Qiu, J. Theoretical Studies on How Excited State Hydrogen and Coordination Bonds Affect Luminescent Properties of Metal Organic Framework Cu_4(L) 4●2EtOH. *Inorg. Chem. Commun.* **2013**, *31*, 69–73.

(91) Tonner, R.; Heydenrych, G.; Frenking, G. Bonding Analysis of N-Heterocyclic Carbene Tautomers and Phosphine Ligands in Transition-Metal Complexes: A Theoretical Study. *Chem. - An Asian J.* **2007**, *2* (12), 1555–1567.

(92) Frenking, G.; Wichmann, K.; Fröhlich, N.; Loschen, C.; Lein, M.; Frunzke, J.; Rayón, V. M. Towards a Rigorously Defined Quantum Chemical Analysis of the Chemical Bond in Donor-Acceptor Complexes. *Coordination Chemistry Reviews*. 2003, pp 55–82.

(93) Microwave Electronics: Measurement and Materials Characterization, L. F. Chen, C. K. Ong, C. P. Neo, V. V. Varadan, Vijay K. Varadan, John Wiley & Sons, 2004.

(94) Krawczuk, A.; Pérez, D.; Macchi, P. PolaBer: A Program to Calculate and Visualize Distributed Atomic Polarizabilities Based on Electron Density Partitioning. *J. Appl. Crystallogr.* **2014**, *47* (4), 1452–1458.

(95) Krawczuk-Pantula, A.; Perez, D.; Macchi, P. Distributed Atomic Polarizabilities from Electron Density. 1. Motivations and Theory. *Trans Amer Cryst Ass* **2011**, 1–25.

(96) Dos Santos, L. H. R.; Krawczuk, A.; Macchi, P. Distributed Atomic Polarizabilities of Amino Acids and Their Hydrogen-Bonded Aggregates. *J. Phys. Chem. A* **2015**, 150324121940009.

Conclusions and outlook

In this thesis we focused on the theoretical and experimental characterization of chemical bonds in metal organic materials and investigated their correlation with material functionalities.

First, we developed a procedure based on reference states, which enables the comparison of two energy decomposition methods, such as the EDA[1–3] and the IQA[4]. We tested the feasibility of this protocol and proved that the two approaches converge towards the very same picture. Noteworthy, this procedure is unprecedented, and it brings new insight.

We investigated several science cases, encompassing metal organic clusters and polymers. We started with a peculiar case of conformational polymorphism of semi-interstitial metal carbonyl clusters.[5,6] Combination of computations and high resolution X-ray diffraction experiments provided a straightforward understanding of M-M and M-X interactions in these compounds and allowed to rationalize the observed polymorphism as due to the tradeoff between packing and molecular energies.

The combination of X-ray diffraction experiment at high-pressure together with topological analysis of the electron density on two iso-structural coordination polymers, CuFPT and AgFPT, revealed fundamental differences between Cu^{I} and Ag^{I} cations. Indeed, while potentially allowed in both derivatives compression induced true metallophilic interactions only in latter. Shading light on the differences between Cu^{I} and Ag^{I} cations, this work affords a better understanding of metallophilic interactions which are attracting more and more curiosity in different area.

The comprehension of materials properties through electron density analysis was the main goal of this thesis, and it fostered the study of dielectric properties of crystalline porous material (like MOFs) for their potential applications in microelectronics.[7] We proved the notable insulating behavior of a copper-tetrazolate MOF, giving a straightforward explanation of its dielectric performances. Moreover, we pinpointed that specific orientation enhances the performances of this 2D material, and potentially of many similar species.

The synergy between theoretical and experimental approaches is vital for the analysis of chemical bonds and correlation with materials functionalities. The new procedures and approaches we proposed in this thesis may be adopted within the relatively new field of *Quantum Crystallography* [8,9] where quantum mechanics and crystallography merge.

References

(1) Kitaura, K.; Morokuma, K. A New Energy Decomposition Scheme for Molecular Interactions within the Hartree-Fock Approximation. *Int. J. Quantum Chem.* **1976**, *10* (2), 325–340.

(2) Ziegler, T.; Rauk, A. Calculation of Bonding Energies by Hartree Fock Slater Method. *Theor. Chim. Acta* **1977**, *46* (1), 1–10.

(3) Von Hopffgarten, M.; Frenking, G. Energy Decomposition Analysis. *WIREs Comput Mol Sci* **2012**, *2*, 43–62 doi: 10.1002/wcms.71.

(4) Blanco, M. A.; Pendás, A. M.; Francisco, E. Interacting Quantum Atoms: A Correlated Energy Decomposition Scheme Based on the Quantum Theory of Atoms in Molecules. *J. Chem. Theory Comput.* **2005**, *1* (6), 1096–1109.

(5) Della Pergola, R.; Sironi, A.; Colombo, V.; Garlaschelli, L.; Racioppi, S.; Sironi, A.; Macchi, P. Periodical Trends in $[Co_6E(CO)_{16}]^-$ Clusters: Structural, Synthetic and Energy Changes Produced by Substitution of P with As. *J. Organomet. Chem.* **2017**, *849–850*, 130–136.

(6) Racioppi, S.; Della Pergola, R.; Colombo, V.; Sironi, A.; Macchi, P. Electron Density Analysis of Metal Clusters with Semi-Interstitial Main Group Atoms. Chemical Bonding in $[Co_6X(CO)_{16}]^-$ Species. *J. Phys. Chem. A* **2018**, *122*, 5004–5015.

(7) Usman, M.; Lu, K.-L. Metal–organic Frameworks: The Future of Low-κ Materials. *NPG Asia Mater.* **2016**, *8* (12), e333.

(8) Genoni, A.; Bučinský, L.; Claiser, N.; Contreras-García, J.; Dittrich, B.; Dominiak, P. M.; Espinosa, E.; Gatti, C.; Giannozzi, P.; Gillet, J. M.; *et al.* Quantum Crystallography: Current Developments and Future Perspectives. *Chem. - A Eur. J.* **2018**, *24* (43), 10881–10905.

(9) Matta, C. F. Quantum Crystallography: From the Intersection to the Union of Crystallography and Quantum Mechanics. *J. Comput. Chem.* **2018**, *39* (17), 1019–1020.

Acknowledgments

I express my gratitude to my supervisor Pierluigi Mercandelli and to Angelo Sironi. They gave me the opportunity to work in their research group, learning many things from their experience.

A special thank goes to Piero Macchi, for hosting me in its research group in Bern during my period abroad. His teaching and supervising were vital to complete this thesis.

Valentina Colombo, Roberto Della Pergola and Luigi Garlaschelli for their important contribute for the synthesis of the systems we investigated.

Michał Andrzejewski and Rebecca Scatena of the University of Bern. Michaeł Andrzejewski did the single-crystal X-ray characterization in high pressure, whereas Rebecca Scatena implemented the impedance spectroscopy facilities, enabling the evaluation of the dielectric constants.

Finally, the University of Milan for the scholarship and for the financial during in these three years.